Simulation Based Software and Hardware Development for the Active Reduction of Muon Induced Background in the Liquid Scintillator Detectors JUNO and OSIRIS

Dissertation
der Mathematisch-Naturwissenschaftlichen Fakultät
der Eberhard Karls Universität Tübingen
zur Erlangung des Grades eines
Doktors der Naturwissenschaften
(Dr. rer. nat.)

vorgelegt von
Axel Müller
aus Bad Saulgau

Tübingen
2022

Gedruckt mit der Genehmigung der Mathematisch-Naturwissenschaftlichen Fakultät der Eberhard Karls Universität Tübingen.

Tag der mündlichen Qualifikation:	14. April 2022
Dekan:	Prof. Dr. Thilo Stehle
1. Berichterstatter:	Prof. Dr. Tobias Lachenmaier
2. Berichterstatter:	Prof. Dr. Josef Jochum

Abstract

The Jiangmen Underground Neutrino Observatory (JUNO) is a 20 kton liquid scintillator neutrino detector currently under construction in southern China. Its main goal is the determination of the neutrino mass ordering by measuring the energy spectrum of reactor electron antineutrinos from nearby nuclear power plants. In addition, JUNO pursues a broad physics program by observing neutrinos from terrestrial and extra-terrestrial sources, including the sun, supernovae, the atmosphere and potentially dark matter. Besides the unprecedented energy resolution of $3\,\%\sqrt{E_{\mathrm{vis}}(MeV)}$, a detailed understanding and reduction of background signals in the detector is necessary. Among the main background sources are muon induced cosmogenic isotopes and radioactive contamination in the liquid scintillator. The first part of this thesis is dedicated to the rejection of cosmogenic background produced in events with multiple muons in the detector. For this event type, a dedicated algorithm is developed which aims to reconstruct the muon tracks in this event type with high precision and reliability. The performance of the algorithm is tested with simulated muon events and it is demonstrated that the method can contribute essentially to the rejection of cosmogenic background. In the second part of the thesis, the estimation of cosmogenic background and the development of a muon veto system for the JUNO pre-detector OSIRIS (Online Scintillator Internal Radioactivity Investigation System) is presented. The purpose of the sub-system is the monitoring of radioactive contamination in the liquid scintillator, before it is filled into the JUNO detector. As part of this thesis, the OSIRIS simulation framework is extended to address the production of cosmogenic isotopes in the detector, important features in the detector geometry and the components of the veto system. Based on comprehensive muon simulations, it is found that muon induced background contributes significantly to the OSIRIS sensitivity and its active rejection with a veto system is necessary. For that reason, detailed Monte-Carlo studies are conducted to determine the veto design which facilitates the maximum muon detection efficiency. Observed parameters are the number and positions of veto PMTs, the optical properties of the tank surfaces and the optical separation, the impact of dark counts and background on false trigger signals and potential incidents like PMT failure or aggravated water quality. Finally, it is shown that the anticipated veto design meets the requirements and rejects cosmogenic background efficiently.

Zusammenfassung

Das Jiangmen Underground Neutrino Observatory (JUNO) ist ein 20 kton Flüssigszintillator-Neutrinodetektor, der derzeit in Südchina aufgebaut wird. Für das Hauptziel des Experiments, der Bestimmung der Neutrino-Massenhierarchie, wird das Energiespektrum von Elektron-Antineutrinos aus nahegelegenen Kernkraftwerken gemessen. Darüber hinaus verfolgt JUNO ein umfangreiches Forschungsprogramm, in dem es Neutrinos aus terrestrischen und extraterrestrischen Quellen, unter anderem aus der Sonne, Supernovae, der Atmosphäre und potenzieller dunkler Materie beobachtet. Neben der beispiellosen Energieauflösung von $3\,\%\sqrt{E_{\mathrm{vis}}(MeV)}$ sind ein grundlegendes Verständnis der Untergrundsignale im Detektor und deren Reduzierung auf ein Minimum notwendig. Zu den wichtigsten Untergrundquellen zählen Myon-induzierte kosmogene Isotope und radioaktive Verunreinigungen im Flüssigszintillator. Der erste Teil dieser Arbeit widmet sich der Unterdrückung des kosmogenen Untergrunds, der bei Ereignissen mit mehreren Myonen im Detektor erzeugt wird. Für diese Art von Ereignissen wurde ein entsprechender Algorithmus entwickelt, der die Spuren aller Myonen in solchen Ereignissen mit hoher Präzision rekonstruiert. Die Leistungsfähigkeit des Algorithmus wurde mit simulierten Myon-Ereignissen getestet und es wird gezeigt, dass die Methode wesentlich zur Unterdrückung des kosmogenen Untergrunds beitragen kann. Im zweiten Teil der Arbeit wird die Abschätzung des kosmogenen Untergrunds und die Entwicklung eines Myon Vetosystems für den JUNO Vordetektor OSIRIS (Online Scintillator Internal Radioactivity Investigation System) vorgestellt. Dessen Hauptziel ist die Bestimmung radioaktiver Verunreinigungen im Flüssigszintillator, bevor dieser in den JUNO-Detektor gefüllt wird. Um die Produktion kosmogener Isotope, wichtige Bestandteile der Detektorgeometrie und die Komponenten des Vetosystems zu untersuchen, wurde das OSIRIS-Simulations Framework erweitert. Basierend auf umfassenden Myon-Simulationen wurde festgestellt, dass der Myon-induzierte Untergrund eine entscheidende Rolle für die Sensitivität von OSIRIS spielt und dessen aktive Unterdrückung mit einem Vetosystem notwendig ist. In Folge dessen wurden detaillierte Studien durchgeführt, um ein leistungsfähiges und effizientes Vetosystem für die Myonendetektion zu konstruieren. Die maßgeblichen Parameter sind die Anzahl und Position der PMTs, die optischen Eigenschaften der Tankoberflächen und der optische Abschirmung, der Einfluss von Dunkelzählrate und Untergrund auf falsche Triggersignale und mögliche Ereignisse wie PMT-Ausfälle oder beeinträchtigte Wasserqualität. Abschließend wird gezeigt, dass das gefundene Vetodesign die Anforderungen erfüllt und kosmogenen Untergrund effizient unterdrückt.

Contents

1. Introduction

In this thesis, analyses and methods for the muon induced background rejection in the JUNO experiment and the associated OSIRIS detector are presented. The elaborated subjects attend to the development of software structures with respect to muon track reconstruction in the JUNO detector as well as the simulation and analysis of muon induced background and the development of a corresponding veto system design for the OSIRIS detector. The overal objective of this research is the reduction of background signals in the JUNO detector, which is crucial for the successful accomplishment of its various physics goals.

Since the first discovery of neutrinos by Cowan and Reines, the field of neutrino physics became a crucial element of particle physics. With the identification of the three neutrino flavors and the associated flavor mixing, neutrino physics became one of the key aspects for the research of physics beyond the standard model of particle physics (SM). For the determination of the nature of neutrino mixing and the oscillation parameters, numerous experiments were established around the world. Based on their ground-breaking results, neutrinos and their characteristics are well described, however a few fundamental parameters and properties are still to be determined, with major impact on the description of physics beyond the SM. Besides fundamental particle physics, neutrinos are detected for probing the nature of various sources, like the Earth's core and the sun, but also at larger scales like Super Novae and possible Dark Matter.

While neutrino experiments of the latest generation were mainly designed for answering specific questions of the neutrino nature, the next generation experiments are planned and designed as multi purpose detectors with a broad scientific program. One of them is the Jiangmen Underground Neutrino Observatory (JUNO) a 20 kton liquid scintillator detector, currently constructed in the south Chinese province Guangdong. Its main goal is the determination of the neutrino mass ordering with a significance of $3-4\,\sigma$, by measuring the energy spectrum of electron antineutrinos emitted in two nuclear power plants at a distance of ~ 53 km. Among the numerous further experimental goals are the precise flux measurement of solar ^{7}Be and ^{8}B neutrinos, the detection of a large neutrino sample of a potential nearby supernova and the high precision measurement of the neutrino oscillation parameters. With its unprecedented liquid scintillator target volume and the anticipated energy resolution of $3\,\%\sqrt{E_{\mathrm{vis}}[MeV]}$, JUNO aims to set new standards in the field of neutrino physics.

The large detector volume and the corresponding mass of liquid scintillator material also

bear new aspects of background control, which require sophisticated strategies and elaborate measurement setups. Due to the relatively shallow overburden of $\sim 700\,\mathrm{m}$ of rock and the extensive detector dimensions, the expected muon rate in the detector is $\sim 4\,\mathrm{Hz}$. In order to reject the corresponding cosmogenic background, which can not be distinguished from the reactor neutrino signal, an advanced veto strategy is required which is based on the precise track reconstruction of muons. While the tracking of single muon tracks is covered by several approaches with high accuracy, the track reconstruction in multi-muon events, which have a non-negligible share, is very challenging and requires adapted methods. In this thesis, the prototype of a newly developed multi track reconstruction is presented. The method is considered as initial and fast reconstruction stage to identify the rough track parameters, on which more sophisticated algorithms can be based on.

Besides cosmogenic isotopes which are the major background source for the detection channel of the reactor neutrinos, intrinsic contamination of the liquid scintillator can mimic neutrino signals, especially for low-energetic solar neutrinos. The major contributors are isotopes of the ^{238}U and ^{232}Th decay chains. In sophisticated facilities, the liquid scintillator components are processed and purified to reduce radioactive contamination to a minimum. To monitor the purification performance and determine the contamination level in the scintillator, the Online Scintillator Internal Radioactivity Investigation System (OSIRIS) was proposed as a measurement facility in the scintillator filling line of JUNO. Due to the expected low count rates, the background control is of great importance. Besides external gamma photons, cosmogenic isotopes are expected to add a significant contribution to the background rate and thus require dedicated counter-measures. The determination of the cosmogenic background contribution to the signal is one aspect of this work. Therefor, extensive simulations are performed to determine the potential of secondary neutrons and heavier isotopes to imitate the sought BiPo coincidence signals.

To reject the cosmogenic background in OSIRIS, a dedicated veto system is required. Based on the results of the preceding simulations of cosmic muons and their secondary particles, the required detection efficiency of a veto system is determined. The final chapter of this thesis describes the simulation based design process of the OSIRIS muon veto system. Based on simulations, the ideal photomultiplier tube (PMT) positioning and materials for the veto components are determined, but also the optimized trigger model, with regards to the dark count rates of the PMTs and background induced signals.

Outline

In chapter 2 of this thesis, the development of neutrino physics and current open questions in the field of neutrino oscillations are presented. Chapter 3 describes the general setup and functionality of the JUNO experiment and summarizes the main aspects of its scientific program. In chapter 4, the JUNO muon veto strategy and the newly developed muon bundle track reconstruction algorithm are presented. The OSIRIS detector is described in chapter 5, followed by the description of its implementation in the dedicated simulation framework in chapter 6. Based on extensive muon simulations with the framework, the expected cosmogenic background is calculated in chapter 7. With these results, the required veto efficiency is calculated. In chapter 8, the veto design parameters are tested with respect to their impact on the muon detection efficiency and the final design is outlined. The thesis in hands is concluded by chapter 9, where a summary of the work and the results is given, followed by an outlook of the impact on the JUNO experiment.

2. Neutrino physics

With their exceptional and elusive character, neutrinos not only have a special place in the SM, but also issue scientists a peculiar challenge since their postulation. In this chapter, the historical background of neutrino physics and the classification of neutrinos in the SM is outlined (section 2.1), followed by the detailed description of neutrino flavor oscillations (section 2.2). The chapter is concluded with a summary of the current experimental status in the neutrino oscillation field and general open questions in neutrino physics (section 2.3).

2.1 Neutrinos in the Standard Model of particle physics

The neutrino was established as a hypothetical particle in 1930 by W. Pauli to explain the continuous energy spectrum of the β-decay, which was discovered in experiments. The neutrino, as a chargeless spin-$\frac{1}{2}$ particle emitted with the electron from the nucleus during the β-decay, would share the decay energy with the electron and thus explain the measured energy distribution without breaking the law of energy and momentum conservation [1]. Four years later, after the discovery of the neutron by J. Chadwick [2], E. Fermi defined the processes of the β-decay more precisely, based on the nucleus model of W. Heisenberg, in which atomic nuclei are composed of protons and neutrons. In the newly described β-decay model, a neutron decays into a proton via the emission of an electron and an antineutrino:

$$\mathrm{n} \rightarrow \mathrm{p} + \mathrm{e}^- + \bar{\nu}_\mathrm{e} \tag{2.1}$$

Furthermore, Fermi also described the reversal process where a neutron is created from a proton via the absorption of an antineutrino and the emission of a positron [3]:

$$\bar{\nu}_\mathrm{e} + \mathrm{p} \rightarrow \mathrm{e}^+ + \mathrm{n} \tag{2.2}$$

This process is now known as inverse beta-decay (IBD) and its cross-section was estimated by Bethe and Peierls in 1934 with $\sigma < 1{\times}10^{-44}\,\mathrm{cm}^2$ [4]. In 1956, C. L. Cowan and F. Reines could identify antineutrinos from a nearby nuclear reactor via the detection of the products of the IBD. Details on this coincidence detection method, which allowed an effective background discrimination, will be given in section 3.5.1. Based on the measurement results, the scientists calculated the cross section for the IBD process as $\sigma = 6.3 \times 10^{-44}\,\mathrm{cm}^2$ with

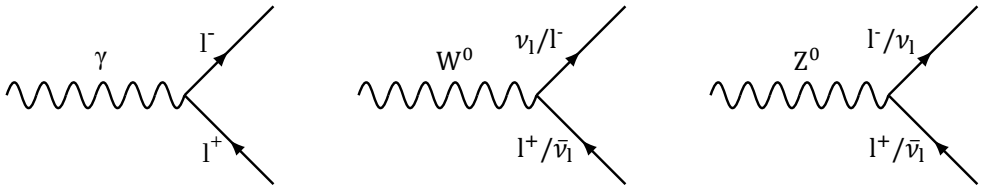

Figure 2.1: Coupling processes of the electroweak interaction. Left: A photon coupling to a pair of charged leptons. **Middle**: A W^--Boson coupling to a lepton with negative/positive charge and an anti-neutrino/neutrino of the according generation. **Right**: A Z^0-Boson coupling to a pair of leptons of opposite lepton number.

an uncertainty of 25 % [5]. About a decade later in 1962, a second kind of neutrino was found at the Brookhaven National Laboratory. The AGS neutrino experiment observed neutrinos from decaying pions produced in an accelerator:

$$\begin{aligned} \pi^+ &\rightarrow \mu^+ + \nu_\mu \\ \pi^- &\rightarrow \mu^- + \bar{\nu}_\mu \end{aligned} \tag{2.3}$$

In the target material they found that the neutrinos produced only muons but not electrons which lead to the assumption that the newly found neutrinos must be different from the ones involved in the β-decay. The denotation ν_e and ν_μ was introduced for the electron and muon neutrino [6]. After the discovery of the τ-lepton in 1975 [7] it was assumed that also a neutrino partner for this lepton should exist. This assumption was supported by the results of the ALEPH experiment at CERN which investigated the the decay of the Z^0-Boson and calculated the number of active neutrino generations associated with the weak interaction with $N_\nu = 3.3 \pm 0.3$ [8]. This result was later refined by a combined analysis with other collaborations to $N_\nu = 2.9840 \pm 0.0082$ [9]. More than two centuries after the discovery of the τ-lepton, the associated neutrino ν_τ was detected at the DONUT experiment in the decay of D_S-mesons

$$D_S \rightarrow \tau + \nu_\tau \tag{2.4}$$

from the Tevatron accelerator and identified by detecting τ-leptons similar to the detection of the ν_μ [10].

In 1957, the group of C. S. Wu published results on the experimental test of parity conservation in β-decay events where they showed that in weak interactions parity is maximally violated. In the experiment, the emission direction of electrons was detected relative to the spin direction of the mother nucleus. The strong dependence on the orientation of the nucleus implied that only left-handed particles and right-handed antiparticles couple to the $W^\pm$-bosons of the weak interaction [11]. The theoretical foundation was set by Tsung-Dao Lee and Chen Ning Yang, who tried to find an explanation for the anomaly in the decay of neutral kaons [12]. Based on this finding, M. Goldhaber investigated the helicity of neutrinos via the measurement of the polarization of photons emitted after the weak decay of ^{152m}Eu to ^{152m}Sm from which the helicity $h = \vec{s} \cdot \vec{p}$ (where $\vec{s}$ is the spin of ν and $\vec{p}$ is the momentum of ν) of the neutrinos can be derived. The result with $h_\nu = -1.0 \pm 0.3$ implies that neutrinos (anti-neutrinos) are exclusively left-handed (right-handed) particles (antiparticles) [13].

Based on these findings, the SM describes the three discovered neutrinos ν_e, ν_μ and ν_τ as massless, left-handed leptons organized in three generations together with their corresponding leptonic partners e^-, μ^- and τ^-. The description is identical for the antiparticles,

except for the helicity. The three generations of leptons couple to the gauge bosons of the electroweak interaction $W^{\pm}$ and Z^0 for the weak component and the massless photon for the electromagnetic component, which only couples to charged particles (see figure 2.1). The charged current coupling to the gauge bosons $W^{\pm}$ is restricted to the emission of a charged lepton of the same family, whereas in the neutral current coupling the charge of the lepton is conserved [14]. Due to the high masses of the weak gauge bosons ($m_{Z^0} = (91.187 \pm 0.002)\,\mathrm{GeV}, m_{W^{\pm}} = (80.379 \pm 0.012)\,\mathrm{GeV}$), the weak interaction has only a short interaction range [15].

2.2 Neutrino flavor oscillations

The theoretical concept of neutrino oscillations was already established before experimental data pointed towards neutrino characteristics which could not be described with the SM at that time. Although the oscillation theory did not consider flavor mixing, the concept could be adapted to explain the observation of experiments detecting neutrinos of solar origin.

2.2.1 Solar neutrino deficit

The standard solar model (SSM) is a quasi-static description of the physical processes in the sun depending on the directly observable boundary conditions like luminosity and radius and indirect parameters like its age and isotope composition. Beside the description of e.g. the solar evolution and the energy transport, the SSM also allows to make clear predictions on the energy production of regular stars by the fusion of chemical elements. The main process in the sun is the so called proton-proton-reaction chain (pp-chain). The pp-chain can be summarized by the net fusion reaction of four protons to a He nucleus, two electrons, two electron neutrinos and the released energy Q:

$$4\mathrm{p}^+ \rightarrow {}^4_2\mathrm{He}^{2+} + 2\nu_\mathrm{e} + 2\mathrm{e}^+ + \mathrm{Q} \tag{2.5}$$

Depending on the reaction chain and its corresponding fusion process, a broad spectrum of neutrinos with various energies is produced in the sun. The other important fusion reaction in stars is the carbon-nitrogen-oxygen cycle (CNO-cycle) which is a catalytic process with the net formula

$$4\mathrm{p} + 2\mathrm{e}^- \rightarrow {}^4_2\mathrm{He} + 2\mathrm{e}^+ + 2\mathrm{e}^- + 2\nu_\mathrm{e} + \mathrm{Q} \rightarrow {}^4_2\mathrm{He} + 2\nu_\mathrm{e} + \mathrm{Q}. \tag{2.6}$$

The eponymous elements of the cycle serve as catalytic partner. The CNO-cycle contains minor branches with differing intermediate steps. In these sub-branches, further neutrino reactions occur which appear in the solar neutrino spectrum. In the sun the pp-chain is the dominant process, whereas the CNO-cycle becomes more important for heavier stars which burn at higher central temperatures. The processes involving neutrino production are listed in table 2.1. They are separated in two-body and three-body processes which affects the energy distribution of the given neutrinos.

With the previous results in neutrino detection from nuclear reactors, solar neutrinos became more interesting as messenger particle to explore the processes in the sun's core. In the beginning of the detection of solar neutrinos, the measurement principle was based on radiochemical methods since the direct detection of the IBD signature was technically not realizable at this time, due to the small energies of the neutrinos. The first experiment by the team of R. Davis, called Homestake experiment after the name of the mine it was located in, started operation in 1967 and was based on the reaction

$$\nu_\mathrm{e} + {}^{37}\mathrm{Cl} \rightarrow {}^{37}\mathrm{Ar} + \mathrm{e}^- [17]. \tag{2.7}$$

Table 2.1: Solar neutrino production processes from pp-chain and CNO-cycle with the associated neutrino energy and the calculated flux at one astronomical unit. The neutrino energy of the ^{7}Be reaction depends on the energy level of the ^{7}Li daughter nucleus. Data from [16].

Name	Reaction	Neutrino energy (MeV)	Flux ($1 \times 10^{10}\,\mathrm{cm^{-2}s^{-1}}$)
pp-chain			
pp	$\mathrm{p} + \mathrm{p} \rightarrow {}^2\mathrm{H} + \mathrm{e}^+ + \nu_\mathrm{e}$	≤ 0.42	$5.9(1 \pm 0.01)$
pep	$\mathrm{p} + \mathrm{e}^- + \mathrm{p} \rightarrow {}^2\mathrm{H} + \nu_\mathrm{e}$	1.44	$0.014(1 \pm 0.02)$
^{7}Be	${}^7\mathrm{Be} + \mathrm{e}^- \rightarrow {}^7\mathrm{Li} + \nu_\mathrm{e}$	0.86(90%)/0.38(10%)	$0.49(1 \pm 0.12)$
^{8}B	${}^8\mathrm{B} \rightarrow {}^8\mathrm{Be} + \mathrm{e}^+ + \nu_\mathrm{e}$	≤ 15	$5.8 \times 10^{-4}(1 \pm 0.23)$
hep	${}^3\mathrm{He} + \mathrm{p} \rightarrow {}^4\mathrm{He} + \mathrm{e}^+ + \nu_\mathrm{e}$	≤ 18.77	$8 \times 10^{-7}(1 \pm 0.2)$
CNO-cycle			
^{13}N	${}^{13}\mathrm{N} \rightarrow {}^{13}\mathrm{C} + \mathrm{e}^+ + \nu_\mathrm{e}$	≤ 1.2	$0.06(1 \pm 0.4)$
^{15}O	${}^{15}\mathrm{O} \rightarrow {}^{15}\mathrm{N} + \mathrm{e}^+ + \nu_\mathrm{e}$	≤ 1.73	$0.05(1 \pm 0.4)$
^{17}F	${}^{17}\mathrm{F} \rightarrow {}^{17}\mathrm{O} + \mathrm{e}^+ + \nu_\mathrm{e}$	≤ 1.73	$6 \times 10^{-4}(1 \pm 0.4)$

with a neutrino energy threshold of 0.814 MeV. The evidence for a neutrino capture reaction in the detector was realized by extraction and detection of ^{37}Ar atoms, which undergo electron capture decay with a half-life of $\tau_{1/2} \approx 35\,\mathrm{d}$ via

$$^{37}\mathrm{Ar} + \mathrm{e}^- \rightarrow {}^{37}\mathrm{Cl} + \nu_\mathrm{e}. \tag{2.8}$$

The detection of the characteristic x-ray photons that accompanies this process is a signature for the detection of a decaying ^{37}Ar atom and thus for the capture of a neutrino. The process in equation 2.7 is not allowed for solar muon and tau neutrinos because the energy of the neutrinos is too small to produce the respective partner-leptons. Due to the energy threshold, only solar ^{7}Be, ^{8}B, pep and hep neutrinos could be detected (see table 2.1). After a measurement period of about 25 years the results stated a detected neutrino rate of $R = (2.56 \pm 0.16(sys.) \pm 0.16(stat.)) \cdot 10^{-36}\mathrm{s}^{-1}$ per taget atom (SNU) which was a strong contradiction to the prediction of the SSM with $R_{SSM} = (9.3 \pm 1.3)\,\mathrm{SNU}$ [17].

The GALLEX experiment was based on the same detection principle, but used ^{71}Ga as target material. The energy threshold of 233 keV allowed to detect solar neutrinos of almost the entire spectrum, even a part of the low-energetic pp-neutrinos. After more than four years of measuring the solar neutrino flux, the results showed a similar discrepancy to the theoretical predictions as the Homestake experiment with only $(57 \pm 15)\,\%$ of the predicted neutrino flux [18]. Both experiments have in common that they detect neutrinos only via a charged current interaction so only electron neutrinos could be detected.

The Japanese experiment Super-Kamiokande detects neutrinos via the elastic scattering with electrons which allows to detect neutrinos from all three light generations. The benefits of this detection mechanism is that it could identify the direction of the neutrinos and could reconstruct the events and their energies in real-time, but the energy threshold for neutrinos of 4.5 MeV limits the experiments to detecting ^{8}B neutrinos only. According to the radiochemical experiments, Super-Kamiokande also found a deficit in the solar neutrino flux compared to the SSM with a portion of $(45.1 \pm 1.6)\,\%$ [19].

In order to find an explanation for the reduced solar neutrino flux, several ideas were pursued. On the one hand, the predictions of the SSM could be flawed by the assumption of wrong cross-sections, temperatures or opacities in the sun. However, no changes in the solar or nuclear models could finally conciliate the detected neutrino fluxes and energy spectra

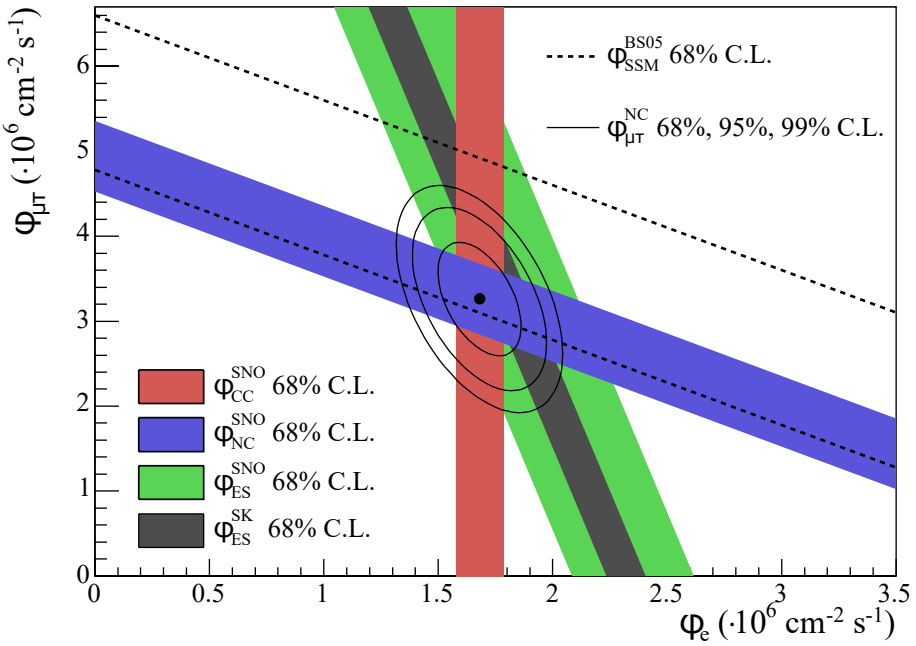

Figure 2.2: Solar neutrino fluxes from ^{8}B detected on earth separated in charged current results (red), neutral current results (blue) and elastic scattering results from SNO (green) and Super Kamiokande (black). The black scattered line indicates the prediction of the SSM. The appearance of muon and tau neutrinos is the proof for the oscillation of solar electron neutrinos. Figure from [20].

of all experiments [15]. On the other hand, the idea of flavor oscillations of neutrinos was discussed which based on the theoretical deliberations of B. Pontecorvo.

In 2001, the Sudbury Neutrino Observatory (SNO) found the first experimental evidence for neutrino flavor conversion and thus could solve the solar neutrino problem. The SNO detector was a real-time Cherenkov detector based on heavy water (D_2O) with an energy threshold of 3.5 MeV, allowing the detection of solar ^{8}B neutrinos via charged current and, for the first time, neutral current interaction. This innovation made it possible to detect a non-electron neutrino component in the solar neutrino flux (see figure 2.2), thus proofing the principle of neutrino flavor mixing and solving the solar neutrino deficit [20].

2.2.2 Neutrino oscillation theory

Similar to the mixing of neutral kaons, described in 1955 by Gell-Mann and Pais [21], B. Pontecorvo proposed the oscillation of neutrino states, however originally as neutrino to antineutrino oscillation [22, 23]. Later, the idea was refined to neutrino flavor oscillations by the Japanese Physicists Maki Nakagawa and Sakata [24] and Pontecorvo [25]. The conditions for neutrino flavor oscillations are that the weak flavor eigenstates and the mass eigenstates of the neutrinos are not identical and that the mass of neutrinos is non-zero. The described flavor mixing does not conserve individual lepton numbers, but the total lepton number. In the following section, the phenomenon of neutrino flavor oscillation is described in quantum mechanical terms in general, and in the two- and three-neutrino case, following [26, 27, 15].

General description

Under the assumption of neutrino flavor mixing, the n orthonormal flavor eigenstates ν_α ($\bar{\nu}_\alpha$) are connected to the n orthonormal mass eigenstates ν_j ($\bar{\nu}_j$) by the unitary $n \times n$

mixing matrix U[1] corresponding to

$$|\nu_\alpha\rangle = \sum_j^n U_{\alpha j} |\nu_j\rangle \text{ and } |\bar{\nu}_\alpha\rangle = \sum_j^n U^*_{\alpha j} |\bar{\nu}_j\rangle . \tag{2.9}$$

For neutrinos as Dirac particles, the $2n^2$ parameters of the mixing matrix U can be parameterized with $\frac{1}{2}n(n-1)$ neutrino mixing angles[2] and $\frac{1}{2}(n-1)(n-2)$ CP-violating phases (see 2.3.3). Assuming a relativistic neutrino with momentum p emitted at position $x(0) = 0$ at time $t(0) = 0$, its mass eigenstate $|\nu_j\rangle$ evolves in time with

$$|\nu_j(x,t)\rangle = \exp\left(i(p_j x - E_j t) |\nu_j\rangle\right) . \tag{2.10}$$

The state of a propagating neutrino generated in a weak interaction in the flavor state ν_α can thus be described with

$$|\nu(x,t)\rangle = \sum_j^n U_{\alpha j} |\nu_j(x,t)\rangle = \sum_{j,\beta}^n U_{\alpha j} U^*_{\beta j} \exp\left(i(p_j x - E_j t) |\nu_\beta\rangle\right) . \tag{2.11}$$

In order to allow neutrino flavor oscillation from an initial flavor state ν_α to a different final state ν_β, the neutrino mass eigenstates must be assumed to be different. The probability for this transition is given by the absolute square of the transition amplitude for the flavor conversion:

$$\begin{aligned} P(\nu_\alpha \to \nu_\beta)(t) &= \left|A(\nu_\alpha \to \nu_\beta)^2\right| = |\langle \nu_\beta | \nu(x,t)\rangle|^2 \\ &= \sum_{j,k}^n U_{\alpha j} U^*_{\alpha k} U_{\beta j} U^*_{\beta k} \exp\left(i(E_j - E_k)t\right) . \end{aligned} \tag{2.12}$$

Here, the assumption of relativistic neutrinos was made where the energy of the mass eigenstate can be approximated with $E_j = \sqrt{m_j^2 + p_j^2} \simeq p_j + \frac{m_j^2}{2p_j} \simeq E + \frac{m_j^2}{2E}$ for $p_j \gg m_j$.

By changing the dependence of the state probability from time t to flight distance L via $L = ct$, equation 2.12 can be written in general as

$$\begin{aligned} P(\alpha \to \beta)(E,L) = \delta_{\alpha,\beta} &- 4 \sum_{j<k}^n \Re\left(U_{\alpha j} U^*_{\alpha k} U_{\beta j} U^*_{\beta k}\right) \sin^2\left(\frac{\Delta m^2_{jk}}{4}\frac{L}{E}\right) \\ &+ 2 \sum_{j<k}^n \Im\left(U_{\alpha j} U^*_{\alpha k} U_{\beta j} U^*_{\beta k}\right) \sin\left(\frac{\Delta m^2_{jk}}{2}\frac{L}{E}\right) . \end{aligned} \tag{2.13}$$

The oscillation probability essentially depends on the difference of the squared masses of the neutrino mass eigenstates $\Delta m^2_{jk} = m^2_j - m^2_k$ from which follows that in the case of neutrino oscillation at least one mass eigenstate is non-zero and that there are non-diagonal terms in U. The formalism is also valid for the mixing of antineutrinos ($\bar{\nu}_\alpha \to \bar{\nu}_\beta$) by making the transformation $U \to U^*$. Thus, the first term of 2.13 is CP invariant, whereas the second term has opposite sign for neutrinos and antineutrinos.

[1] called PMNS matrix, according to the inventors Pontecorvo, Maki, Nakagawa and Sakata
[2] according to angles of an n-dimensional rotation matrix

Two flavor oscillations

When neutrino oscillations were established, only two states were considered, initially the oscillation between particle and antiparticle and, until the discovery of the τ-lepton, between electron and muon generation. Since former neutrino oscillation experiments were not sensitive enough, their results can be interpreted with two-flavor model, which can be described with one mixing angle Θ and the squared mass difference $\Delta m^2 = m_2^2 - m_1^2$. The two-flavor mixing matrix is thus defined by

$$\begin{pmatrix} \nu_\alpha \\ \nu_\beta \end{pmatrix} = \begin{pmatrix} \cos\theta & \sin\theta \\ -\sin\theta & \cos\theta \end{pmatrix} \begin{pmatrix} \nu_1 \\ \nu_2 \end{pmatrix}, \tag{2.14}$$

with the neutrino flavor eigenstates ν_α and ν_β and the neutrino mass eigenstates ν_1 and ν_2.

Following equation 2.12, the transition probability is given by

$$P(\alpha \to \beta) = |U_{\alpha1}U_{\beta1}|^2 + |U_{\alpha2}U_{\beta2}|^2 + 2\left(U_{\alpha1}U_{\alpha2}U_{\beta1}U_{\beta2} \cdot \Re\left(\exp\left(-i\frac{\Delta m^2}{2}\frac{L}{E}\right)\right)\right) \tag{2.15}$$

$$= 2 \cdot \cos^2(\Theta)\sin^2(\Theta) \cdot \left(1 - \cos\left(\frac{\Delta m^2}{2}\frac{L}{E}\right)\right) \tag{2.16}$$

$$= \sin^2(2\Theta)\sin^2\left(\frac{\Delta m^2}{4}\frac{L}{E}\right). \tag{2.17}$$

From equation 2.17 follows that the amplitude of the neutrino oscillation probability is defined by the mixing angle Θ and the oscillation frequency by the difference of the mass eigenstates.

Three flavor oscillation

With the more sensitive neutrino oscillation experiments of the next generation, like JUNO, the mixing of all three neutrino flavors $(\nu_e, \nu_\mu, \nu_\tau)$ and mass eigenstates (ν_1, ν_2, ν_3) of the SM must be considered. For Dirac neutrinos, the mixing matrix U can be parametrized by three mixing angles (Θ_{jk} with $jk = 12, 13, 23$) and one CP violating phase δ as

$$U = \begin{pmatrix} 1 & 0 & 0 \\ 0 & c_{23} & s_{23} \\ 0 & s_{-23} & c_{23} \end{pmatrix} \begin{pmatrix} c_{13} & 0 & s_{13}e^{-i\delta} \\ 0 & 1 & 0 \\ -s_{13}e^{i\delta} & 0 & c_{13} \end{pmatrix} \begin{pmatrix} c_{12} & s_{12} & 0 \\ -s_{12} & c_{12} & 0 \\ 0 & 0 & 1 \end{pmatrix}, \tag{2.18}$$

where $c_{jk} = \cos(\Theta_{jk})$ and $s_{jk} = \sin(\Theta_{jk})$ [28]. In contrast to the oscillation probability in the two-flavor case, also the signs of the squared mass differences must be considered. According to equation 2.13 the flavor oscillation probability in this case is given by

$$P(\nu_\alpha \to \nu_\beta) = \delta_{\alpha,\beta} - 4\sum_{jk} \Re(U_{\alpha j}U^*_{\alpha k}U_{\beta j}U^*_{\beta k})\sin^2\left(\frac{\Delta m^2_{jk}L}{4E}\right) + 4\sum_{jk} \Im(U_{\alpha j}U^*_{\alpha k}U_{\beta j}U^*_{\beta k})\sin\left(\frac{\Delta m^2_{jk}L}{4E}\right)\cos\left(\frac{\Delta m^2_{jk}L}{4E}\right). \tag{2.19}$$

The three mixing angles Θ_{12}, Θ_{13} and Θ_{23}, the two mass differences Δm^2_{21} and Δm^2_{31} ($\Delta m^2_{32} = \Delta m^2_{31}$ - Δm^2_{21}) and the CP-violating phase δ are the six independent parameters to describe neutrino flavor mixing. Their determination was and still is subject of numerous experiments, which will be described in section 2.3.1.

Neutrino oscillations in matter

The previous considerations only cover neutrino oscillations in vacuum. However, the oscillation probability of neutrinos in matter is strongly affected by the weak interaction with present electrons. While electron neutrinos interact via the charged and neutral current interactions, muon and tau neutrinos only undergo neutral current interactions at low energies. The increased interaction cross-section for electron neutrinos can be described with an additional potential which leads to the modification of the mixing angle depending on the electron density N_e according to

$$\sin^2(2\Theta_{mat}) = \frac{sin^2(2\Theta_{vac})}{(\cos(2\Theta_{vac}) - A)^2 + sin^2(2\Theta_{vac})} \text{ with } A = 2\sqrt{2}G_F N_e E_\nu, \tag{2.20}$$

with the Fermi constant G_F and the neutrino energy E_ν. In the case of high electron density, like in the core of the sun, where the electron neutrinos are produced, the mixing angle is maximal ($\Theta_{mat} \approx 90°$). While in vacuum ν_1 is similar to ν_e, the large mixing angle leads to an inversion of the neutrino flavor with $\nu_2 \approx \nu_\mathrm{e}$. Due to the large extent of the sun, the electron density decreases slowly compared to the oscillation length. Thus, Θ_{mat} approaches Θ_{vac} adiabatically, leading to an increased probability for a neutrino to be in the state ν_μ. This matter induced resonant enhancement of the neutrino mixing is called MSW-effect [3] and could be identified for high energetic neutrinos by SNO and KamLAND [29]. For low energetic neutrinos the MSW-effect is negligible and thus the flavor mixing can be described with vacuum oscillations. The transition between the vacuum oscillation and the matter oscillation regime lies in the region of $1 - 3\,\mathrm{MeV}$ and is subject of current neutrino experiments [30].

2.3 Experimental status of neutrino oscillations

The observation of neutrino flavor oscillations showed that the basic description of the SM is not sufficient to describe all observations. In order to facilitate a detailed extension of the SM or to find processes beyond the current understanding of particle physics, substantial experimental efforts are made to observe the characteristics of neutrinos.

2.3.1 Measurement of the oscillation parameters

Neutrino oscillation experiments can be divided in *appearance* experiments, where it is searched for neutrinos of a different flavor compared to the emitted neutrino flavor at the source, and *disappearance* experiments, where a reduced flux of neutrinos of a specific flavor is observed in the detector compared to the initial flux in the source. In both cases, intense and well understood sources and large detector volumes are required to achieve significant measurement results, due to the small cross-sections of neutrino interactions with matter. As mentioned in section 2.2.2, the six observable independent parameters are the three mixing angles Θ_{12}, Θ_{13} and Θ_{23}, two of the three mass differences Δm^2_{21}, Δm^2_{31} and Δm^2_{32} and the CP-violating phase δ. Which parameters are accessible for a particular experiment depends on the energy and flavor of the source neutrinos and the baseline to the detector. For historical reasons Θ_{12} and m^2_{21} are called *solar* mixing angle and mass splitting, Θ_{23} and m^2_{32}/m^2_{31} are called *atmospheric* mixing angle and mass splitting, and Θ_{13} is called *reactor* mixing angle.

[3] after the physicists Michejew, Smirnov and Wolfenstein

Solar neutrinos

With the detailed measurement of the electron neutrino component in the solar neutrino flux, SNO could not only solve the solar neutrino problem. In combination with the measurements of Super-Kamiokande and the findings of the KamLAND experiment, the solar vacuum oscillation parameters Θ_{12} and m^2_{12} and the proportion of the matter induced MSW-effect in the observed energy regions could be determined [29]. With Borexino, the solar ^{7}B neutrino flux can be investigated. The detector is a 300 t ultra-pure liquid scintillator detector with an energy threshold of 190 keV and an energy resolution of 5%@1 MeV, enabling the detection of solar pp, pep and ^{7}Be neutrinos, via the elastic scattering with electrons. With the measurement of the respective neutrino fluxes, the portion of the matter induced neutrino oscillation is investigated at the low energy edge of the transition region. [31].

Atmospheric neutrinos

Atmospheric neutrinos are secondary particles of cosmic rays interacting with atoms of the Earth's atmosphere. The main production channels are via charged pions or kaons that decay, among others, into two muon neutrinos and one electron neutrino. While the prediction of the total flux from simulations can vary up to 20 %, the ratio of fluxes between the different flavors is known much more precisely. The neutrino energy spectrum follows a power law distribution with $dN/dE \propto E^{-3.7}$ and ranges from below GeV to a few hundred TeV [32] and the baseline from creation to detection from around 10 km (for downward going neutrinos) up to 1.3×10^4 km for upward-going neutrinos which cross the entire earth, depending on the zenith angle.

Even before the detection of flavor mixing with solar neutrinos, Super-Kamiokande found conclusive proof for the oscillation of atmospheric neutrinos. The water Cherenkov detector contains 50 kt of ultra-pure water, in which neutrinos produce leptons of corresponding flavor via the charged current interaction. In the case of atmospheric neutrinos, these leptons are mainly electrons and muons, which can be distinguished clearly in the detector. The real-time measurement of neutrinos allowed Super-Kamiokande to investigate the flux of atmospheric neutrinos in dependence of the zenith angle and thus the baseline. While for electron neutrinos no deviation from the expected flux was observed, the muon neutrino flux was distinctly reduced, which was an evidence for the oscillation to tau neutrinos. Recently, Super-Kamiokande and the IceCube experiment reported the detection of tau neutrino appearance in the atmospheric neutrino flux [33, 34]. The analysis of the atmospheric neutrino flux allows the investigation of the atmospheric oscillation parameters Θ_{23} and $\left|\Delta m^2_{32}\right|$.

Accelerator neutrinos

An alternative source to study $\nu_\mu \rightarrow \nu_\tau$ oscillations (and also others) are particle accelerators, where pions and kaons are produced with a high energy proton beam. Using focusing devices, the dominant component in the beam of neutrino or antineutrino and the direction of the beam focus can be manipulated. By setting the ratio of the neutrino energy and the baseline to the neutrino detector (L/E) carefully, a selected window of the oscillation parameter space can be investigated. In long-baseline experiments with neutrino energies around 1 GeV and baselines up to 1000 km the atmospheric mass splitting can be investigated. The results from experiments like Tokai-to-Kamioka (T2K) with a baseline of $L = 295$ km and NOvA with a baseline of 810 km are in good agreement with the results of the atmospheric neutrino oscillation search [35, 36]. Future experiments are under preparation, like the Deep Underground Neutrino Experiment (DUNE) [37] and Hyper-Kamiokande [38], the successor detector of Super-Kamiokande, in combination with the

Japan Proton Accelerator Research Complex (J-PARC). These can provide high precision measurements of the neutrino mixing parameters.

Reactor neutrinos

With about 2×10^{20} $\bar{\nu}_e$ per second, nuclear reactors are the most intense human-made source of neutrinos up to the MeV energy region. On average, six neutrinos and 200 MeV of energy are released per fission of the isotopes ^{235}U, ^{238}U, ^{239}Pu and ^{239}Pu in a reactor, so the neutrino flux can be determined from the thermal power of the reactor [30]. Reactor neutrino experiments detect electron antineutrinos via the IBD channel with large liquid scintillator detectors. The detection of muon and tau antineutrinos is energetically not possible and thus, the disappearance of electron antineutrinos in the reactor neutrino flux is investigated to study flavor oscillations. Depending on the distance of the detector to the nuclear reactor, different parameter spaces of the oscillation can be tested. Experiments with a baseline in the order of 100 km are sensitive to a mass splitting of $\Delta m^2 = 10^{-4} - 10^{-5}\,\mathrm{eV}^2$, whereas baselines with ~ 1 km allow to investigate $\Delta m^2 = 10^{-2} - 10^{-3}\,\mathrm{eV}^2$. First observation of neutrino disappearance was made by KamLAND, an experiment with a 1 kt ultra-pure liquid scintillator detector with an average baseline to the reactor of ~ 180 km. The measured values for the mixing angle Θ_{12} and the mass splitting Δm^2_{21} deviate slightly from the solar measurements with SNO [39]. The following generation of reactor neutrino experiments, Double CHOOZ [40], Reno [41] and Daya Bay [42], was optimized to measure the mixing angle Θ_{13}, with a baseline of ~ 1 km and a second detector close to the reactor to measure the non-oscillated neutrino flux directly. All experiments could significantly detect the electron antineutrino disappearance and thus a non-zero value of Θ_{13}. In the latest analyses of Daya Bay [43] and Reno [44] further constrains on the mixing angle Θ_{13} and the absolute value of the mass difference Δm^2_{32} could be made. Further improvements on the precision measurements of the neutrino mixing parameters will be provided by JUNO, described in detail in chapter 3.

2.3.2 Neutrino mass ordering

With the measurement results of the neutrino oscillation experiments, only the absolute values of the squared mass splittings can be determined. Only for the solar mass splitting, the ordering of the two neutrino mass eigenstates could be identified with

$$m_2 > m_1 \Rightarrow \Delta m^2_{21} > 0 \tag{2.21}$$

by the MSW effect [45]. By convention the mass eigenstate with the highest admixture of electron flavor is allocated to m_1. This allows two scenarios for the position of the mass eigenstate m_3 with $(m_1 < m_2 < m_3)$ or $(m_3 < m_1 < m_2)$, which are called Normal neutrino mass ordering (NO) or Inverted neutrino mass ordering (IO) (see figure: 2.3). Due to the small difference of m^2_{31} in the two scenarios, the measurements of the latest experiments are not sensitive enough to determine the sign of the atmospheric mass splitting. Latest combined fit values favor the normal mass ordering at the level of $1.3 - 3.2\sigma$ [46].

Depending on the neutrino mass ordering, the values for the neutrino oscillation parameters can be derived from a global fit of the existing experiment results. The fit results are stated in table 2.2. Current open questions, beside the actual mass ordering, are the octant of Θ_{23} and the existence of CP violation in the neutrino sector. Although non-zero values are currently favored, conservation ($\delta_{CP} = 0°$ or $180°$) is still not excluded at the level of $1 - 2\sigma$[15]. The determination of these values is highly sensitive to the sign of Δm^2_{31} and thus the neutrino mass ordering.

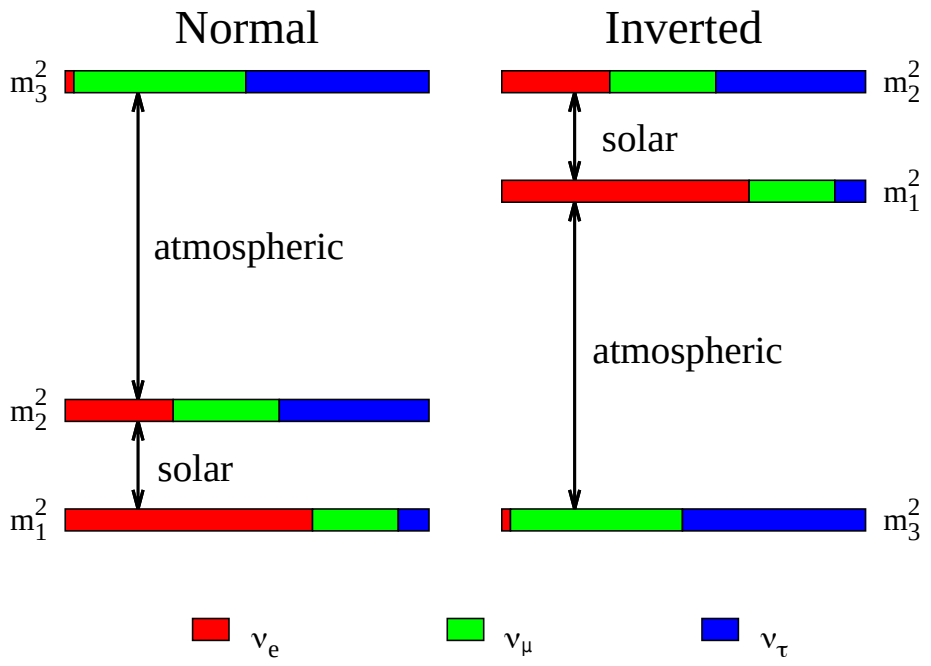

Figure 2.3: Illustration of normal and inverted mass ordering. By definition, m_1 is allocated to the mass eigenstate with highest admixture of electron flavor. The definition of the atmospheric mass splitting depends on the ordering with $\Delta m^2_{atm} = \Delta m^2_{3l}$ (NO: $l = 2$ or IO: $l = 1$). Adapted from [30].

In order to determine the neutrino mass ordering, experimental efforts with different approaches are currently in the planning and construction phase. For the accelerator experiments, DUNE is most promising [37], a 1300 km long baseline experiment. Also atmospheric neutrino experiments of the next generation aim to determine the mass ordering, for example the IceCube extension Precision IceCube Next Generation Upgrade (PINGU) [47] together with the IceCube upgrade [48]. The only direct detection channel of the neutrino mass ordering is the medium-baseline detection of reactor neutrinos, where JUNO is the only planned experiment in the near future. Studies show, that combined analyses of JUNO and PINGU will be able to determine the mass ordering with a significance of 5σ within a measurement time of three years [49]. Details on the measurement principle will be given in section 3.6.

2.3.3 Open questions in neutrino physics

With the observation of neutrino flavor oscillations, the fact of neutrinos being massive was established, which raised further questions on the SM and motivated to test further non-SM theories. These are shortly presented in this section.

CP-violation in neutrinos

The CP symmetry of fundamental particles describes the connection of particles and antiparticles, as expected in the SM. However violation of the symmetry was observed in the quark sector which could partially explain the observed particle-antiparticle imbalance in the universe. Similar to the CP violation in quark mixing, it might be present in neutrino mixing as well, implemented with the complex phase δ_{CP}. The investigation of the CP violating phase δ_{CP} is accessible with the observations of the oscillations of muon neutrinos to electron neutrinos and the corresponding antineutrino oscillations at accelerator experiments. Latest constraints on δ_{CP} come from T2K and NOvA with $\delta_{CP} = [-3.41, -0.03]$ for NO and $\delta_{CP} = [-2.54, -0.32]$ for IO (both at 3σ), excluding the CP conservation with

Table 2.2: Oscillation parameters for the three-neutrino case obtained from global analyses. The values depend on the assumption of normal or inverted ordering. Δm_{3l} is defined as largest difference between the mass eigenstates: $\Delta m_{3l} = \Delta m^2_{31} > 0$ (NO) or $\Delta m_{3l} = \Delta m^2_{32} < 0$ (IO). Data from [50, 51].

Parameter	Neutrino mass ordering		Experiment
	Normal	Inverted	
	best fit $\pm 1\sigma$		
$\sin^2\Theta_{12}$	$0.310^{+0.013}_{-0.012}$	$0.310^{+0.013}_{-0.012}$	Solar
$\sin^2\Theta_{23}$	$0.563^{+0.018}_{-0.024}$	$0.565^{+0.017}_{-0.022}$	Atmospheric
$\sin^2\Theta_{13}$	$0.02237^{+0.00066}_{-0.00065}$	$0.02259^{+0.00065}_{-0.00065}$	Reactor medium baseline
δ_{CP} (°)	221^{+39}_{-28}	282^{+23}_{-25}	Accelerator long baseline
$\Delta m^2_{21}(1\times10^{-5}\,\mathrm{eV}^2)$	$7.39^{+0.21}_{-0.20}$	$7.39^{+0.21}_{-0.20}$	Reactor long baseline
$\Delta m^2_{3l}(1\times10^{-3}\,\mathrm{eV}^2)$	$2.528^{+0.029}_{-0.031}$	$-2.510^{+0.030}_{-0.031}$	Accelerator long baseline

99.73% [52]. Leptogenesis, which is based on the CP violation, is one approach to explain the matter abundance in the universe [53].

Majorana neutrinos

Fermions, which are their own antiparticle are called *Majorana* particles[4]. Since neutrinos are the only uncharged fermions in the SM, they are eligible candidates, however no evidence for the Majorana character of the neutrino was found yet. If neutrinos were Majorana particles, equation 2.18 has to be complemented by a further matrix, containing two CP violating Majorana phases α_1 and α_2 [54]:

$$\begin{pmatrix} e^{i\frac{\alpha_1}{2}} & 0 & 0 \\ 0 & e^{i\frac{\alpha_2}{2}} & 0 \\ 0 & 0 & 1 \end{pmatrix} \tag{2.22}$$

Contrary to the Dirac CP-violating phase δ_{CP}, these phases have no impact on the neutrino oscillation probabilities. The effective Majorana neutrino mass, defined as $\langle m\rangle_{ee} = \left|\sum_{i=1}^{3}\left(U_{ei}^2 m_i\right)\right| = \left|\sum_{i=1}^{3}\left(|U_{ei}|^2 e^{\alpha_i} m_i\right)^2\right|$, is sensitive to all three light neutrino mass eigenstates and thus directly to the mass ordering. The only currently possible experimental evidence to probe the Majorana character of the neutrino is via the neutrinoless double-beta decay of elements like ^{76}Ge, which is observed by the GERmanium Detector Array (GERDA) and the Large Enriched Germanium Experiment for Neutrinoless $\beta\beta$ Decay (LEGEND). In the case of an inverted ordering, the Majorana mass is constrained to $\langle m\rangle_{ee} \geq 0.01\,\mathrm{eV}$, which would allow next generation experiments, like LEGEND, to detect the neutrinoless double-beta decay [30]. The non-observation of this rare event by the recently completed GERDA experiment so far limits its half-life to $T^{0\nu\beta\beta}_{1/2} \geq 1.8\times10^{26}\,\mathrm{yr}$ and the effective neutrino mass to $\langle m\rangle_{ee} \leq 79-180\,\mathrm{meV}$ [55]. The LEGEND experiment will aim for a discovery potential at a half-live limit of $T^{0\nu\beta\beta}_{1/2} \approx 1\times10^{28}\,\mathrm{yr}$ and an effective Majorana mass region of $15-50\,\mathrm{meV}$ [56].

Sterile neutrinos

Although the oscillation results can be explained very precisely with three neutrino generations, some anomalies point towards the existence of further neutrino states which do

[4] Otherwise they are called *Dirac* particles

not interact via the weak force but could be involved in neutrino mixing [30]. These particles are called sterile neutrinos and would expand the mixing matrix U (see 2.18) to a $(3 + N) \times (3 + N)$ matrix with N sterile neutrinos [15]. Since sterile neutrinos only interact gravitationally, they can not be detected directly, but they could be identified by oscillation experiments by precisely determining the elements of the (3×3) mixing matrix, which would not be unitary in the case of further neutrino states. Recent global analyses of neutrino oscillation reveal significant differences between different data sets, especially for results from appearance and disappearance experiments. The global data set rules out sterile neutrinos in a 3+1 scenario at the level of 4.7σ [57], however future experiments, with improved sensitivity will be able to investigate the mixing parameters with high precision and thus could be able to prove the theory of sterile neutrinos.

The absolute neutrino masses

In order to conciliate massive neutrinos with the SM, expansions are necessary, depending on the nature of the neutrino. In the simplest case of neutrinos being Dirac particles, a right-handed (left-handed) neutrino (anti-neutrino) is introduced to formulate a Dirac neutrino-mass term with a Yukawa coupling to the Higgs field, corresponding to the other fermions of the SM. Although the existence of massive neutrinos is proven by oscillation experiments, the mass of neutrinos is not determined yet. There are many different experimental approaches to determine the neutrino masses, for example via the observation of the neutrinoless double beta-decay, as mentioned above. From analyses of the cosmic microwave background (CMB) and structure formation in the universe, model dependent upper limits on the sum of neutrino mass eigenstates have been derived. Depending on the data sets and analyzing methods the most robust constraints come from the Planck satellite with $\sum_i m_i \leq 0.26\,\mathrm{eV}$ [58]. The only model independent way to determine the neutrino mass experimentally is via the energy-momentum relation in neutrino involved reactions. Most recent constraints are obtained by the KATRIN experiment, which observes the kinematics of electrons from the β-decay of tritium and thus the rest mass of the antielectron neutrino $m^2_{\bar{\nu}_\mathrm{e}} = |U_{\mathrm{e}1}|^2\, m_1^2 + |U_{\mathrm{e}2}|^2\, m_2^2 + |U_{\mathrm{e}3}|^2\, m_3^2$. The most recent limit, after a measurement time of 4 weeks, is $m_{\bar{\nu}_\mathrm{e}} < 1.1\,\mathrm{eV}$ (90 % c.l.). After the full science run of 5 years the sensitivity on the electron neutrino mass is expected to be 200 meV (90 % c.l.) [59, 60].

3. The JUNO Experiment

JUNO, the Jiangmen Underground Neutrino Observatory, is a 20 kt liquid scintillator detector with a broad range of experimental goals in the field of neutrino physics. The collaboration consists of 670 members from 78 institutions in 18 countries and was founded in 2008 as a follow-up of the Daya Bay experiment. Initial excavation works started in 2015 and are currently about to be completed. The detector is planned to be fully setup to be ready for data taking by June 2023. The location of the experimental site and the design of JUNO are optimized for the determination of the neutrino mass ordering as the primary physics goal. In this chapter, the location (section 3.1) and the general setup of the JUNO experiment (section 3.2) is presented, together with a detailed description of the utilized liquid scintillator (section 3.3) and the corresponding energy resolution (section 3.4). Subsequently, signal characteristics and the associated backgrounds are explained (section 3.5), followed by selected aspects of the scientific program of JUNO (section 3.6). Conclusively, the JUNO simulation framework (section 3.7), the liquid handling system together with OSIRIS (section 3.8) and TAO (section 3.9) are shortly presented.

3.1 Experimental site

In order to optimize the detector for the primary goal of JUNO, the determination of the neutrino mass ordering by detecting reactor electron antineutrinos, the actual experimental site was chosen carefully to address the requirements. The significance for the distinction of the scenarios NO and IO with JUNO is maximized at the first solar oscillation minimum, where the superposition of the reactor and solar oscillation frequencies allows to distinguish the impact on the detected reactor antineutrino energy spectrum. For neutrino energies in the range of $1 - 8\,\mathrm{MeV}$, this corresponds to a distance of $\sim 53\,\mathrm{km}$ between the detector and the source. Due to the small interaction cross-section of low energy antineutrinos with matter, not only a large detector volume, but also powerful reactors are required to achieve a sufficient antineutrino flux for a statistically significant result [30].

A suitable location was found in the Guangdong province in China, close to the city Jiangmen, where a detector with the required measurements and the accompanying infrastructure can be located. In the surrounding area, two commercial nuclear power plants are fully operating since 2020 and in medium-terms, no further plants are envisaged. The Yangjiang power plant, consisting of six reactors with $2.9\,\mathrm{GW_{th}}$ thermal power each and the Taishan power plant, with two reactors and respectively $4.59\,\mathrm{GW_{th}}$ provide a total power of $26.55\,\mathrm{GW_{th}}$ at the beginning of data taking with JUNO. In the following it will

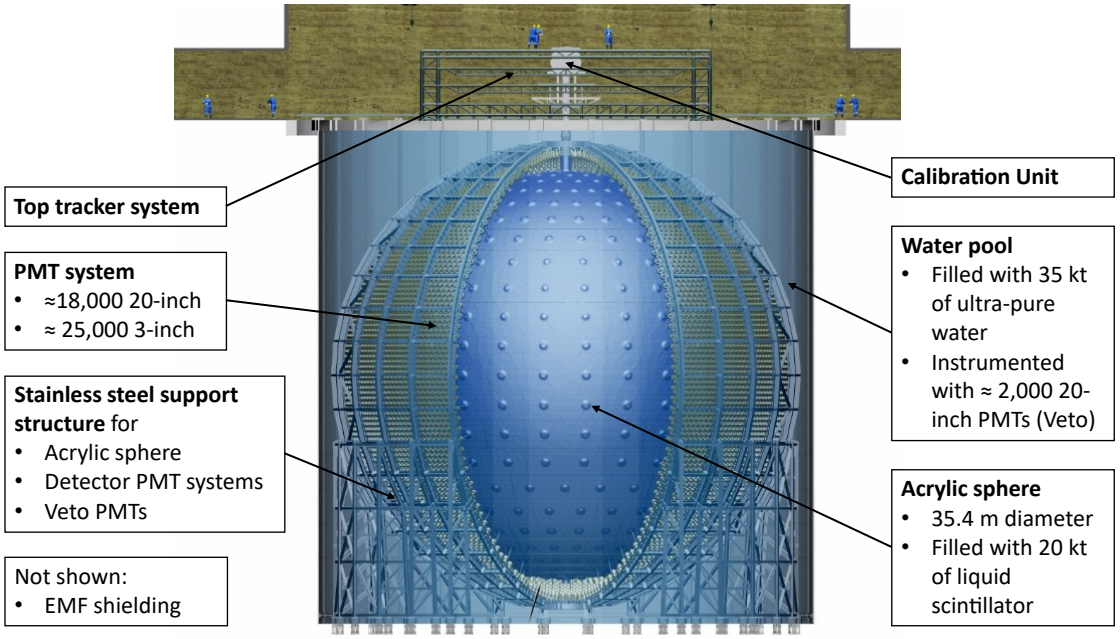

Figure 3.1: Overview of the JUNO main detector, which will be installed in a cavern with $\sim$ 700 m overburden. The PMTs of the central detector system will be mounted in a distance of $\sim$ 19.6 m to the center of the acrylic sphere. The EMF shielding consists of concentric wire rings to compensate the earth's magnetic field.

be expanded to 4 reactor cores, increasing the total thermal power to 35.73 GW_{th}. In order to avoid dephasing of the neutrino fluxes from different reactor cores and thus interference distortions in the oscillation pattern, equal distance to all reactor cores is very important. For JUNO the maximum distance difference between two reactor cores is $\sim$ 0.5 km. Further nuclear power plants in Daya Bay and Huizhou with distances larger than 200 km are expected to contribute with 2.8 % to the total electron antineutrino flux [30]. Due to the absence of mountains in the target area, which could contribute to the shielding from cosmic radiation, the experiment is planned to be deployed in an underground laboratory, with a total overburden of 679 m or 2000 m.w.e. [61]. The resulting muon flux in the JUNO central detector is predicted with a flux of 0.0037 $Hz \cdot m^{-2}$ and a mean muon energy of 209 GeV[61].

3.2 JUNO detector

The key component of JUNO is the central detector, although, the respective sub-systems are crucial for the operation of the experiment. As depicted in figure 3.1, the central detector will be erected into a cylindrical cavern filled with ultra-pure water to detain external backgrounds from the surrounding rock material and which will be used as an active muon veto system. The cavern has a diameter of 43.5 m and a height of 44.5 m. In the center of the cavern, the 20 kt liquid scintillator neutrino target is contained by an acrylic sphere with a diameter of 35.4 m and a thickness of 12 cm. The deposition of energy in the liquid scintillator results in the creation of scintillation and Cherenkov photons. The acrylic sphere has a total mass of $\sim$ 600 t and consists of 265 modules with a respective size of $\sim 3\,m \times 8\,m$ to facilitate the transport and the setup underground [62]. Furthermore it must meet strict requirements on stability, also in the case of a potential earthquake, radiopurity and transparencys.

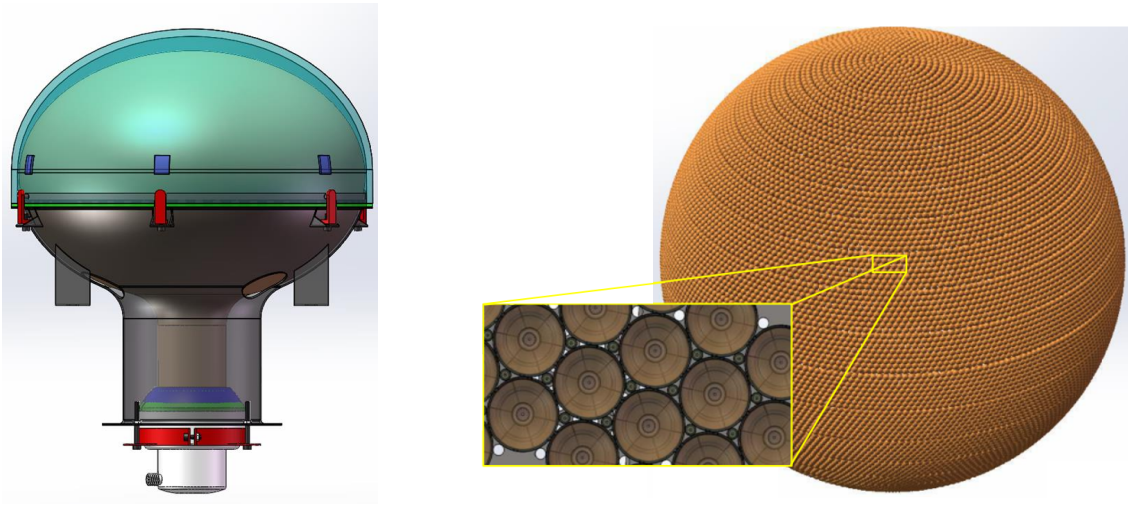

Figure 3.2: Rendered models of the Hamamatsu 20-inch PMTs and the mounting in the central detector. Left: CAD drawing of the 20-inch Hamamatsu PMT including the explosion protection and the base. **Right:** Target PMT arrangement in the central detector with the small PMTs in the gaps of the large PMTs. From [71] and [72].

The JUNO PMTs

Going further outside, the central detector PMTs are the next major component. With these, the photons, which are created in the liquid scintillator, are detected. Each PMT is installed as part of a module in a distance of 19.6 m from the detector center. Between the PMTs and the acrylic sphere, the ultra-pure water acts as a buffer to shield the central detector from external gamma radiation from the PMTs (see table 3.1). In JUNO, three different PMT types are attached to the stainless steel frame. The first of the two independent central detector PMT arrays is instrumented with 20-inch PMTs: approximately 5000 of the dynode-type R12860 HQE from Hamamatsu [63] and approximately 13000 of the micro-channel plate (MCP)-type by Northern Night Vision Technology Ltd. (NNVT) [64]. The second PMT array is instrumented with about 25000 3-inch dynode type PMTs, (XP72B22 from HZC Photonics [65]). Details about the large PMT specifications are listed in table 3.1. The small PMTs are mounted in the gaps between the large PMTs which leads to a total coverage of more than 75 % [66]. The parallel operation of the two systems makes the JUNO detector a double calorimetric system, which allows independent and comparable measurements of the same events. Additionally, the small detection area of the small PMTs results in the detection of mainly single photons, even from light intense events like throughgoing muons. This allows for a cross-calibration of the large PMTs which experience a variation in the detection of photons within two orders of magnitude and underlie strong nonlinearities for higher count rates [67]. Via read-out cables, three PMTs are connected to an underwater box, in which the high voltage supply and the data processing unit are housed. The digitized data is then transmitted to the JUNO back-end electronics [68, 69]. In a similar way, 128 small PMTs are connected to a designated underwater electronics box [70].

In order to prevent major damage to the PMT array due to single imploding tubes, which might cause a chain reaction, an additional implosion protection is applied to each PMT. It is realized with an acrylic half-sphere, which is installed in front of the PMT cathode and a stainless steel half-sphere in the back to contain potential shock waves in the water [73].

Table 3.1: PMT performance requirements for both 20-inch types. The minimum and maximum limits are valid for each individual PMT, the typical values are the required average value for the respective PMT batch. Data from [74].

Parameter		PMT type	Min.	Typical	Max.
PDE @ 420 nm		both	24.0 %	27.0 %	-
DCR @ 0.25 PE		Hamamatsu	-	20 kHz	50 kHz
		NNVT	-	-	100 kHz
TTS (FWHM)		Hamamatsu	-	2.7 ns	3.5 ns
		NNVT	-	12.0 ns	15.0 ns
Peak/Valley ratio for single PE		Hamamatsu	2.5	3.0	-
		NNVT	2.5	3.5	-
QE non-uniformity		both	-	5.0 %	15.0 %
Radioactive contamination	^{238}U	Hamamatsu	-	-	400 ppb
		NNVT	-	-	50 ppb
	^{232}Th	Hamamatsu	-	-	400 ppb
		NNVT	-	-	50 ppb
	^{40}K	Hamamatsu	-	-	40 ppb
		NNVT	-	-	20 ppb

Since the repair or the replacement of malfunctioning PMTs is not possible once the detector is filled, their durability and the stability of the performance are of major importance. For that reason, a dedicated acceptance test procedure was developed. The testing site was established in Zhonhshan, China and started data taking in 2017. In the first station, not only the general functionality of each PMT is tested, but also individual parameters like the photon detection efficiency, the dark count rate, transit time spread (TTS) etc., which are crucial for the aimed sensitivity of the JUNO detector [74]. In the second testing station, a selected sample of all PMTs is investigated in more detail to get a better understanding of their spatial photon detection efficiency and further systematic uncertainties [75]. Currently, the last PMT batches from the vendors are to be examined, before the second testing phase with the PMTs together with the glued base is initiated.

The acrylic sphere and the two PMT-systems are mounted to the stainless steel frame, which also contains the optical separation, a foil to separate the volume that is observed by the PMTs from the outside to minimize the amount of detected photons, that are not produced in the liquid scintillator volume. Furthermore, the compensation system of the earth magnetic field is installed to the frame, sixteen pairs of circular coils, concentrically arranged around the central detector axis to reduce the magnetic field at the positions of the PMTs to about 10 μT. Without the reduction of the external magnetic field, the PMT photon detection efficiency is assumed to be only 30 % of the nominal value, whereas with magnetic field compensation, the efficiency is > 90 % [76].

Auxiliary systems

The volume outside of the stainless steel frame is instrumented with approximately 2400 MCP-type PMTs, to detect Cherenkov photons from muons traversing the water pool. The surface of the entire veto volume, the cylindrical cavern and the outside of the steel frame are covered with Tyvek sheets to increase the light detection of the veto PMTs. The positions of the latter are optimized to increase the muon detection efficiency, for which a value of ≥ 95 % is expected, based on simulations [77]. A further component of the

experiments muon detection system is the Top Tracker, which is located above the central detector. It consists of three layers of plastic scintillator strips that cover around 60 % of the cylinder base area of the cavern. Based on simulations, it is estimated that one third of the cosmic muons crosses the top tracker area and due to the high detection efficiency and the layered array, the muon track progression can be reconstructed very precisely. Besides the actual contribution to the experiments muon veto, the Top Tracker is mainly used to calibrate and verify the muon reconstruction results of the water pool veto system and the central detector [78].

The calibration system of JUNO comprises several independent sub-systems to monitor and verify the status of the detector. Different calibration sources for neutrons and gamma photons but also diffuse, pulsed UV light can be deployed along the central axis of the detector. Due to the large dimensions of the detector volume, the system is extended by an additional guide tube system that circles the acrylic sphere along a longitudinal path and allows the calibration with MeV-scale gamma photons close to the detector edge. To enable the spatially extended placement of radioactive sources inside the detector, a cable loop system is envisaged, which consists of several anchor points between which cables are stretched. Along the latter, radioactive sources can be moved through the sensitive volume. More details on the sub-systems and the foreseen calibration campaign are presented in [79]. Additionally the laser system AURORA is installed outside the acrylic sphere to monitor the liquid scintillator transparency and the optical attenuation components. The laser sources are mounted on precisely adjustable termination holders and by detecting the emitted light with opposite PMTs , conclusions can be drawn about the optical properties of the liquid scintillator [80].

3.3 Liquid scintillator

The JUNO liquid scintillator is a derivative of the unloaded scintillation material utilized in the buffer volume of the Daya Bay experiment, with adaptions in the composition of the ingredients to address for the increased dimensions [66, 82]. The solvent LAB is an organic compound featuring a benzene ring and constitutes the major component of the neutrino target material [30]. In addition, two supplements are dissolved in the LAB to increase the scintillation and light propagation efficiency: PPO (3 g/L) and bis-MSB(15 mg/L). The deposited energy of charged particles, usually via excitation or ionization processes in matter, leads to an excited state of the benzene ring electron configuration of LAB molecules at the place of the energy deposition. The absorbed energy is transferred to the PPO molecules dominantly via a non-radiative process, a dipole-dipole interaction of the molecules and a subordinate radiative process, where LAB emits a photon in the range of approximately 280 nm, which is then absorbed by PPO. The PPO photo emission spectrum is shifted to longer wavelengths compared to the spectrum of LAB and overlaps with the absorption spectrum of bis-MSB. The emission spectrum of the latter is again shifted to higher wavelengths in the range of 430 nm, where the JUNO PMTs have their maximum sensitivity (see figure 3.3). As the wavelenghts of photons emitted from excited states of LAB and PPO overlap with the absorption window of LAB, the optical transparency of the scintillator for these photons is low. Together with sophisticated purification efforts, the wavelength shift of the scintillation photons to approximately 430 nm increases the absorption length drastically to $\sim$ 60 m. Together with a Rayleigh scattering length of $\sim$ 30 m the resulting absorption length of the liquid scintillator is $\sim$ 20 m for photons with a wavelength of 430 nm. Increased attenuation in the scintillation medium would result in a strongly reduced number of detected photons, especially from the center of the target volume, and thus deteriorate the energy resolution of the detector [83].

The number of emitted photons is about 10^4 photons per MeV of deposited energy in LAB. With the spatial and temporal distribution and the number of detected photons,

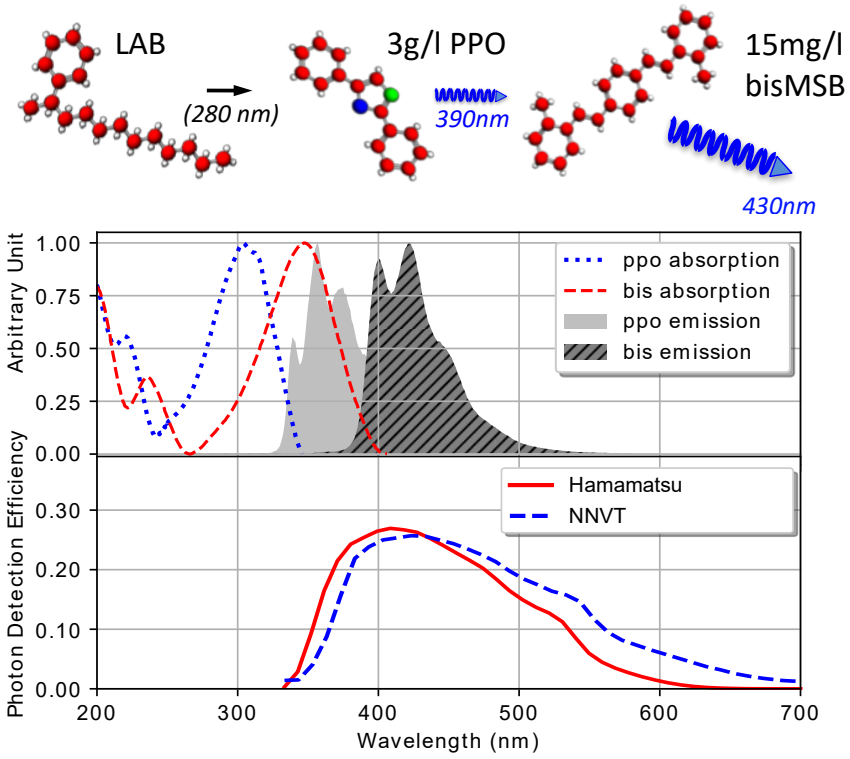

Figure 3.3: Radiation spectrum of the liquid scintillator components. In the first panel, the molecular structure of linear alkylbenzene (LAB), 2,5-diphenyloxazole (PPO) and p-bis-(o-methylstyryl)-benzene (bis-MSB) are depicted, together with their proportion in the liquid scintillator and the wavelength of the emitted gamma photon. The de-excitation of LAB is mainly non-radiative. In the second panel, the absorption and emission spectra of the two admissions are delineated, depending on the wavelength. As shown in the third panel, the wavelength dependent photon detection efficiency of the PMTsis maximum at the peak of the bis-MSB emission spectrum. From [81].

the deposited energy, the vertex and the track progression of a particle in the detector can be determined [66]. However, the dependence of the number of emitted photons and the deposited energy as well as the emission time spectrum depend on the particle type and its energy. As the energy deposition density in the liquid scintillator has a direct impact on the photon emission, the light yield is not linear with respect to the deposited energy. Heavy particles, like protons or helium nuclei, lead to an increased ionization density along their trajectory through the scintillator, which causes a decreased light emission when compared to lighter particles like electrons. This saturation effect is called *quenching* and is described semi-empirically by *Birk's law* [84]:

$$\frac{dL}{dx} = L_0 \frac{dE/dx}{1 + k_B \cdot dE/dx}, \tag{3.1}$$

with the luminescence of the particle L, the expected luminescence for a minimum-ionizing particle L_0 and the material and particle specific Birk's constant k_B. Besides the light yield, also the time profile of the light emission is depending on the type of the traversing particle and the scintillator composition. The scintillator molecules are excited to different states with different decay time constants along the track. The probability density function for the photon emission time of the scintillator material can be described with the sum of the weighted contributions of the different excited states to the emission probability over time:

$$f_{pd}(t, \tau, w) = \sum_{i=1}^{n} \frac{w_i}{\tau_i} \exp(-t/\tau_i), \tag{3.2}$$

with weights w_i and time constants τ_i [85]. The impact of the particle type on the population of the excited molecule states leads to slightly different photon detection spectra and thus allows for the discrimination based on pulse shapes [86]. The current description of the liquid scintillator implemented in the JUNO and OSIRIS detector simulations includes three components and is based on measurements in one of the Daya Bay detectors. The weights and time constants of the components are listed in table 3.2.

3.4 Energy resolution

The energy resolution of the system is essential for the success of the intended physics program, in particular the determination of the neutrino mass ordering, as the detailed features of the oscillation spectrum contain the required information (see section 3.6). To achieve the required sensitivity on the mass ordering determination, the energy resolution must not be worse than the ratio of the fast reactor oscillation frequency, which is

Table 3.2: Scintillator specific light emission properties implemented in the JUNO simulation framework and depending on the particle type. The time constants and weights determine the time profile of the scintillation light emission as defined in 3.2. The differences in the second and third component allow to distinguish particles via pulse shape discrimination.

	Decay component 1		Decay component 2		Decay component 3	
Particles	w_1	τ_1(ns)	w_2	τ_2(ns)	w_3	τ_3(ns)
γ, e^-, e^+	0.799	4.93	0.171	20.6	0.03	190.0
n, p	0.65	4.93	0.231	34.0	0.119	220.0
α	0.65	4.93	0.228	35.0	0.122	220.0

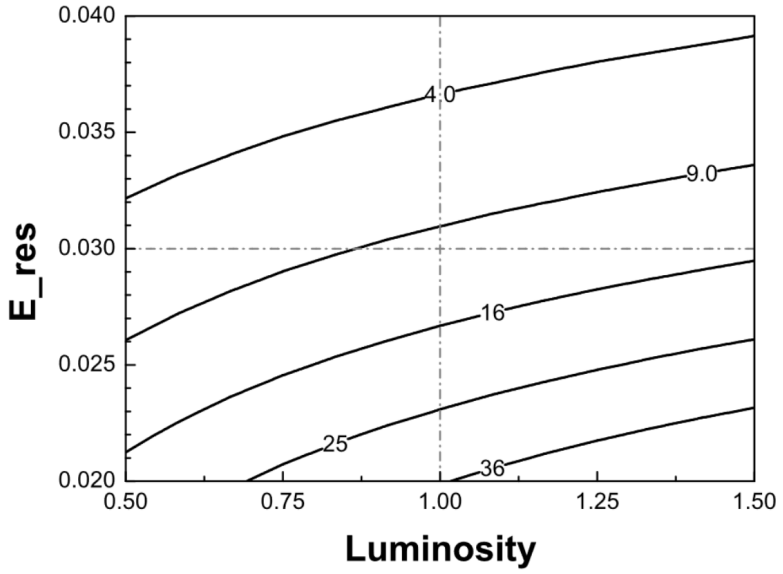

Figure 3.4: JUNO mass ordering sensitivity plot in dependence of the luminosity and the energy resolution. The luminosity is defined as the product of measurement time and detection efficieny. Luminosity = 1.0 represents a measurement time of 6 years and 80 % signal detection efficiency. The contour lines represent equal levels of the mass ordering sensitivity $\Delta\chi^2_{\mathrm{MO}}$. The dashed lines show the design parameters. From [30]

.

determined by Δm^2_{31} and Δm^2_{32}, and the slow solar oscillation frequency, driven by Δm^2_{21}:

$$\frac{\Delta m^2_{21}}{\Delta m^2_{\mathrm{ee}}} \sim \frac{7.39 \times 10^{-5}\,\mathrm{eV}^2}{2.53 \times 10^{-3}\,\mathrm{eV}^2} \sim 3\,\%, \tag{3.3}$$

with the effective squared mass difference

$$\Delta m^2_{\mathrm{ee}} = \cos^2\Theta_{12} \cdot \Delta m^2_{31} + \sin^2\Theta_{12} \cdot \Delta m^2_{32} \tag{3.4}$$

and the neutrino oscillation parameters from table 2.2 [30]. The energy resolution of JUNO is mainly governed by the photon-electron statistics, which is a combination of the PMT photocathode coverage ($\geq 75\,\%$), the PMT quantum efficiency ($\geq 35\,\%$), and the scintillation light attenuation length ($\geq 20\,\mathrm{m@430\,nm}$). Together with the 10^4 scintillation photons per MeV of deposited energy in the scintillator [87], this translates to a photon statistics of 1200 PE per deposited MeV, which corresponds to an energy resolution, based on photon statistics, of $\sigma = \frac{1}{\sqrt{1200}} \sim 3\,\%$. In figure 3.4, the JUNO mass ordering sensitivity depending on the energy resolution and the luminosity (combination of measurement time and detection efficiency), is depicted as a contour plot.

In order to address further impacts on the detector resolution and classify them realistically, the detector energy resolution can be described with a generic parametrization:

$$\frac{\sigma_E}{E} = \sqrt{\left(\frac{a}{\sqrt{E}}\right)^2 + b^2 + \left(\frac{c}{E}\right)^2}, \tag{3.5}$$

with the visible energy $E(MeV)$. The photon-statistic is expressed by the first term, effects like detector non-uniformity, vertex resolution and the PMT charge resolution are consolidated in the summand b and energy independent contributions like dark noise from PMTs and electronics are described by the third term. The three parameters are weighted based on results from Monte Carlo simulations with $a : b : c = 1 : 1.6 : \frac{1}{1.6}$ and are accessible in the final experiment by calibrations and results from Daya Bay [30].

3.5 Neutrino signal and background

3.5.1 IBD signal from reactor antineutrinos

The primary focus of JUNO is on the detection of electron antineutrinos from the surrounding nuclear power plants in a distance of $\sim 53\,\text{km}$, which are emitted from unstable fission fragments in the subsequent β-decay. The majority of the thermal power and the antineutrinos are produced in the initial fission of the reactor fuel isotopes ^{235}U, ^{238}U, ^{239}Pu and ^{241}Pu. As depicted in figure 3.5, where the neutrino fluxes are broken down by the isotopes, the spectrum of reactor antineutrinos reaches up to an energy of around 9 MeV and can be calculated based on the thermal power of the reactors with an expected uncertainty of $2-3\,\%$ [30].

In the JUNO detector, antineutrinos are detected via the IBD reaction (see section 2.1 and figure 3.5), which allows the reconstruction of its energy. The antineutrino interacts with a proton of the scintillator target, creating a positron and a neutron. The threshold energy is 1.806 MeV. After depositing its energy in the scintillator volume, the positron annihilates with an electron into two gamma photons with 511 keV each. The process unfolds within nanoseconds and represents the prompt signal of the IBD. Due to the kinematics of the reaction, the positron carries the bulk of the initial neutrino energy, facilitating the precise reconstruction of the latter. The neutron scatters on protons in the target until it thermalizes. The corresponding low energy depositions are not noticeable in the detector. The thermalized neutron can be captured by a proton, which leads to the emission of a 2.2 MeV gamma photon. The neutron is captured in average about $200\,\mu\text{s}$ after its emission and thus forms the delayed signal. The cross-section for the IBD process is energy dependent and also depicted in figure 3.5. Due to the composition of two related signals, strict cuts can be applied to the IBD event reconstruction, which leads to an efficient discrimination of background signals. Based on the assumed thermal power of the nearby reactors and the detector properties, the expected IBD rate from reactor antineutrinos is 83 events per day [30].

Background signals

Accidental coincidences

The rate of the accidental background signals R_{acc} depends on the rates of single events in the detector that can imitate the prompt R_{prompt} or the delayed $R_{delayed}$ signature of the IBD signal and the chosen coincidence time window ΔT_{coinc} with $R_{acc} = R_{prompt} \cdot R_{delayed} \cdot \Delta T_{coinc}$. The coincidence time window is adjusted to minimize the accidental background rate and maximize the number of IBD events. In the case of JUNO it is currently assumed to be at $\Delta T_{coinc} = 1\,\text{ms}$. The prompt component of the accidental coincidence signal is mainly due to energy depositions of radioactive isotopes in the surrounding rock and the glass of the PMTs. Although the majority of the external gamma photons is absorbed in the buffer volume around the acrylic vessel, a residual amount can reach the outer parts of the scintillator volume. For that reason, the fiducial volume cut, which rejects the outermost region of the detector per se, is very effective for the removal of external gamma signals (see table 3.3) [30].

The delayed signal is mainly imitated by gamma photons from external radioactiv sources. Based on Monte Carlo simulations, the rate of external gamma photons in the fiducial volume is 7.6 Hz, with about $8\,\%$ in the energy region of a neutron capture, resulting in ~ 410 random coincidences per day after the fiducial volume cut. A further source for the delayed IBD-signal, are neutrons and isotopes produced by cosmic muons in the liquid scintillator, which either are actually captured at hydrogen (neutrons) or deposit energy in the respective energy range (isotopes). The accidental coincidences of external gamma

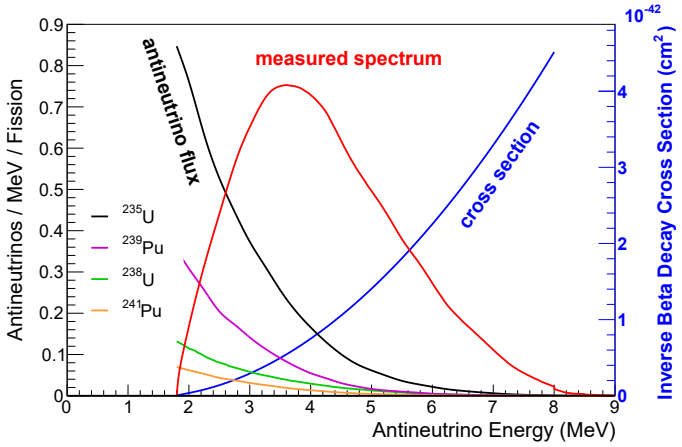

Expected IBD-spectrum

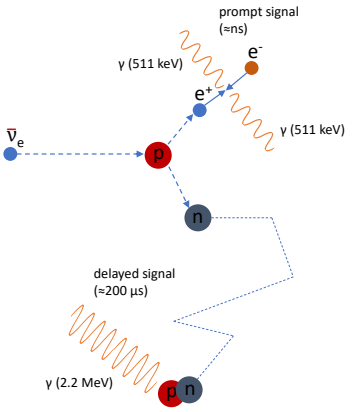

IBD coincidence signal

Figure 3.5: Reactor antineutrino IBD-spectrum in the JUNO detector. **Left:** In black, the expected antineutrino flux at the JUNO site is shown alongside with its constituents from the decays in the nuclear reactors. Together with the energy dependent IBD cross-section (blue), the expected spectrum is calculated (red). Figure from [30]. **Right:** The schematic process of an IBD-event in the detector starts with the initial neutrino interaction with a proton, resulting in the creation of a positron and a neutron. Both particles deposit energy in the liquid scintillator and finally lead to the creation of gamma photons with characteristic energy.

photons and cosmogenic secondary particles are stated with a rate of 340 events per day, but can be supressed efficiently with spatial and temporal distance cuts. Besides cosmogenic neutrons, which are created in hadronic and electromagnetic showers, the cosmic muons can create free neutrons via the spallation of atoms in the scintillator material. With a rate of 1.8 Hz, the spallation neutrons lead to accidental coincidence rate of ~ 45 events per day. Although the raw background from accidental coincidences exceeds the rate of detected reactor neutrinos by more than one order of magnitude, the application of further cuts allows to reduce it to below one count per day (see section below) [30].

Cosmogenic isotopes and fast neutrons

Cosmic muons and secondary particles in subsequent showers can interact with carbon nuclei in the liquid scintillator and produce radioactive isotopes with $Z \leq 6$ and neutrons via hadronic and electromagnetic processes. While most of the decaying cosmogenic isotopes contribute to the accidental background, ^{8}He and ^{9}Li can efficiently mimic the coincidence signature of the IBD-reaction in the JUNO detector. Both isotopes have a decay branch in which first an electron is emitted in a β-decay and leaves behind an excited nucleus, which immediately emits a neutron. The Q-value to the ground state of the β-decay is 8.63 MeV for ^{8}He and 11.94 MeV for ^{9}Li. Thus, they can pass the energy cut of the gamma signal of the IBD. As the signal of the emitted neutron is also indistinguishable from the delayed IBD signature, ^{8}He and ^{9}Li are the most serious correlated background for the reactor antineutrinos detection. The production cross-section was modeled empirically to depend on the mean energy of muons E_μ arriving at the detector with $\sim E_\mu^{0.74}$, where together with the measured production cross-sections in the KamLAND detector, the predicted number of muon induced isotopes is 150 for ^{9}Li and 50 for ^{8}He. With the branching ratio for decays including neutron emission (^{9}Li : 51 % and ^{8}He : 16 %) and the IBD coincidence cuts, the expected rate of cosmogenic IBD-like events is 71 events per day [30]. This rate was calculated for the initially planned position of the detector, which later had to be shifted

by $\sim 60\,\mathrm{m}$ due to technical issues in the excavation of the cavern. The changes caused a reduced overburden for the detector which leads to an increased expected muon rate (from $0.003\,\mathrm{Hz/m^2} \rightarrow$ to $0.0037\,\mathrm{Hz/m^2}$) and a decreased mean energy of the muons arriving at the detector (from $215\,\mathrm{GeV} \rightarrow$ to $209\,\mathrm{GeV}$) [61]. Taking into account the increased muon flux, the expected rate of IBD-signatures from ^{8}He and ^{9}Li increases to 94 events per day. Hence, for both the old and the estimated new cosmogenic background rate, the expected signal to background ratio is in the same order of magnitude.

Although the cosmogenic background is indistinguishable from the actual signal from reactor antineutrinos, a sophisticated muon track reconstruction allows to reduce the background rate to below two counts per day. Here, the correlation of the muon track and the isotope production position as well as the relatively short half-lives, compared to the production rate, of ^{8}He (0.119 s) and ^{9}Li (0.178 s) are exploited. The lateral distance of the cosmogenic isotopes to the initial muon track is distributed exponentially. The rejection of a cylindrical volume with a radius of 3 m from the muon track axis for 1.2 s allows to veto the majority of the signals from the cosmic background. Due to the large detector volume and the muon event rate of $\sim 4\,\mathrm{Hz}$, vetoing the entire detector after a muon event would raise the dead-time to almost 100 % and inhibit the anticipated physics program. Therefore, the required muon track reconstruction efficiency for muons in the detector is 99 % and only in cases, where the muon track could not be reconstructed properly or the muons exclusively traverse the water volume, the entire detector is vetoed. After applying the coincidence cuts and especially the efficiency of the full muon veto strategy, an expected background rate of 1.6 events per day from cosmic muons is expected [30]. More details about the muon track reconstruction are provided in chapter 4.

Another aspect of the cosmic muon induced background are fast neutrons, produced in the surrounding rock or the water pool volume. Muons that do not traverse the central detector or only a small part of the water Cherenkov veto volume cannot be registered, however the high energetic neutrons produced in showers and spallations still can reach the detector volume. By scattering off a proton in the liquid scintillator and subsequently being captured, the fast neutrons are capable to imitate the IBD signal. After applying the fiducial volume cut, the expected rate of fast neutron induced background is 0.1 events per day [30].

Besides fast neutrons, ^{8}He and ^{9}Li, other radioactive isotopes with $Z \leq 6$ are produced in the liquid scintillator that cannot imitate the IBD signal solely but contribute to the accidental background. Although they are mainly rejected by the coincidence cuts, the muon veto also has an impact on the accidental background (see table 3.3) [30].

$^{13}\mathbf{C}(\alpha, n)^{16}\mathbf{O}$

Despite the sophisticated purification strategy, contaminations with uranium and thorium are not fully avoidable in the liquid scintillator material and the acrylic vessel. The α-particles from the decay chains (details in section 5.1) can interact with naturally abundant ^{13}C in the scintillator. The reaction $^{13}\mathrm{C}(\alpha, n)^{16}\mathrm{O}$ can lead to a correlated background signal, if the emitted neutron is fast enough to scatter off a proton and deposit enough energy, or a gamma photon is emitted from the excited ^{16}O. The expected background rate of this reaction is estimated with 0.05 events per day for a contamination level of $1 \times 10^{-15}\,\mathrm{g/g}$ of ^{238}U and ^{232}Th, which are the specified upper limits for the reactor antineutrino detection. However a recent publication indicates that the $^{13}\mathrm{C}(\alpha, n)^{16}\mathrm{O}$-cross-sections are overestimated, which would result in a substantially smaller background rate [30, 88].

Table 3.3: Expected efficiency of the antineutrino selection cuts on the IBD signal and background rates. Empty cells indicate the combined results of multiple consecutive cuts. For the cut efficiency of the muon veto, a muon track reconstruction efficiency of 99 % is assumed. Data from [30].

Selection	IBD efficiency	IBD	Geo-neutrinos	Accidental coincidences	^{9}Li/^{8}He	Fast neutrons	(α, n)
				events per day			
		83	1.5	5.7×10^4	84	-	-
Fiducial vol.	91.8 %	76	1.4		77	0.1	0.05
Energy cut	97.8 %			410			
Time cut	99.1 %	73	1.3		71		
Vertex cut	98.7 %			1.1			
Muon veto	83.0 %	60	1.1	0.9	1.6		
Combined	73.0 %	60			3.8		

Geo-neutrinos background

Although geo-neutrinos are part of a dedicated physics program in JUNO, they must be considered as background for the reactor antineutrino detection. The neutrinos are produced in decays of thorium and uranium in the earth's crust and mantle, which add up to an expected rate of 1.5 events per day (Th: 23 %, U: 77 % [30]). Since the endpoint energy of the geo-neutrino spectrum is distinctly lower than the reactor antineutrino spectrum, they only contribute to the background in the low-energy region. Applying the IBD coincidence cuts, the rate is reduced to 1.1 events per day and by investigating the geo-neutrino flux with JUNO itself, the actual rate and spectrum shape uncertainty is expected to be reduced sufficiently [30].

Background suppression

In order to discriminate the detector signals of reactor antineutrinos from the various background signals, several cuts are applied. Especially the accidental background of uncorrelated single events can be suppressed efficiently with cuts on the fiducial volume, the vertex correlation of the two consecutive events of the IBD and the time difference of the prompt and the delayed signal. The rejection of cosmogenic backgrounds relies on the track reconstruction of the causal muons to veto parts of the the traversed volume (details about the muon track reconstruction are given in chapter 4). The fiducial volume cut rejects the outermost 0.7 m of the liquid scintillator target. Besides that, coincidence cuts are applied to exploit the characteristics of the IBD-signal. The accepted energy window for the prompt signal, which is a direct measure for the neutrino energy is defined from 0.7 MeV to 12.0 MeV. The delayed energy window is adjusted to the detection of the gamma photon, released after the neutron capture, with an accepted energy interval from 1.9 MeV to 2.5 MeV. Finally, the correlation of the two signals is considered with a distance cut of up to 1.5 m and a maximum time interval of 1.0 ms between the two signal components. With the muon veto strategy, the expected signal to background ratio can be increased from $\sim 1:1$ (after the other cuts) to 60 : 1.6 [30]. The impact of the cuts is listed in table 3.3. Additionally, the materials of the detector and the liquid scintillator itself are subject to strict limits regarding contamination with radioactive isotopes to reduce accidental background coincidences and the creation of correlated background.

3.5.2 Elastic neutrino-electron scattering channel

Also neutrinos from other sources than reactors can be detected by JUNO: from Supernovae, the sun and neutrinos created in the earths crust and in the atmosphere in cosmic rays. Here, not only electron antineutrinos create signals in the target volume via the IBD. Also electron neutrinos as well as muon and tau (anti)neutrinos can be detected. The interaction is via neutral current interactions with protons or carbon atoms of the scintillator material or elastic scattering with electrons, depending on the neutrino energy and the related cross-section. However, for electron antineutrinos the cross-section is small compared to the IBD.

The elastic scattering of neutrinos of all flavors off electrons in the scintillator facilitates the detection of solar neutrinos:

$$\nu_{e,\mu,\tau} + e^- \rightarrow \nu_{e,\mu,\tau} + e^-. \tag{3.6}$$

Unlike for the IBD reaction, the elastic scattering does not result in a coincidence signature in the detector, but appears as a single event. Furthermore, only a fraction of the initial neutrino energy is transferred to the electron, resulting in a continuous electron recoil spectrum, even for mono-energetic neutrino fluxes.

Due to the quasi point-like energy deposition and the isotropic emission of scintillation photons, also the initial direction of the neutrinos is hardly reconstructable, making them indistinguishable from intrinsic β- or γ-decays in the sensitive volume. Especially the detection of low-energetic neutrinos via the elastic scattering channel is thus affected by internal radioactive contaminations. For the detection of solar neutrinos via elastic scattering, the contamination level has to be below 1×10^{-16} g/g (baseline) or even 1×10^{-17} g/g (ideal) [30]. The corresponding signal to background ratio is 1 : 3 (baseline) or 2 : 1 (ideal), respectively. In addition, cosmogenic isotopes such as ^{11}C, ^{10}C and ^{11}Be create a further background component for high energy solar neutrinos. With live-times between ~ 20 s and ~ 30 min, the same veto strategy as for the IBD signal is not applicable. For that reason, their production yield and the resulting energy spectra must be measured and subtracted from the total spectrum. Also electron antineutrinos from the surrounding nuclear power plants can interact in the detector via the elastic scattering channel. Their contribution is estimated with ~ 10 events per day in the energy region from 1 to 8 MeV. By measuring the IBD channel precisely, they can be subtracted statistically [30].

3.6 JUNO physics program

The JUNO experiment pursues a large variety of physics goals by the detection of neutrinos. In the following section, the identification of the neutrino mass ordering, the detection of neutrinos from the sun and supernovae, the precision measurement of neutrino oscillation parameters and the indirect search for dark matter are discussed shortly. Beyond that, the measurement of geo-neutrinos, sterile neutrinos and more exotic topics like nucleon decays and the search for Lorentz invariance violation are comprised by the broad physics program of JUNO.

Identification of the neutrino mass ordering

The main goal of the JUNO physics program is the model independent determination of the neutrino mass ordering by precision measurements of the oscillated reactor antineutrino spectrum. With the thermal power of ~ 36 GW from the surrounding nuclear power plants, the expected rate of detected antineutrino events in the JUNO detector is 83 counts per day [30]. The expected unoscillated spectrum is depicted in figure 3.6, according to the product

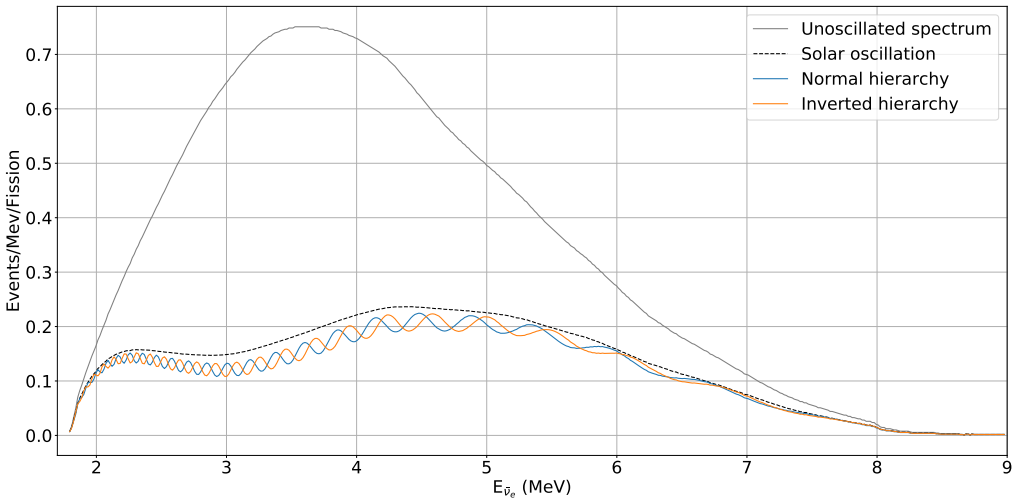

Figure 3.6: Expected reactor antineutrino spectrum in the JUNO detector for the case without neutrino oscillation (grey line), solar oscillation only (dashed) and the oscillation spectra for the NO (blue) and the IO (orange).

of the expected on-site neutrino flux and the neutrino detection cross-section depicted in figure 3.5. Based on equation 2.19, the vacuum electron (anti-)neutrino survival probability can be written as

$$P_{\bar{\nu}_e \to \bar{\nu}_e} = 1 - \cos^4(\Theta_{13}) \sin^2(2\Theta_{12}) \sin^2(\Delta_{21}) - \sin^2(2\Theta_{13}) \left(\cos^2(\Theta_{12}) \sin^2(\Delta_{31}) + \sin^2(\Theta_{12}) \sin^2(\Delta_{32}) \right), \tag{3.7}$$

with $\Delta_{ij} = \Delta m^2_{ij} L/4E$ $(i,j = 1,2,3; i > j)$, the reactor-detector baseline L and the antineutrino energy E [30]. The survival probability is governed by two terms. The first term is dependent on the squared mass difference Δm^2_{21} defining the medium baseline *solar* oscillation. The dashed line in figure 3.6 represents the reduced neutrino flux, due to the solar oscillation term only. The second term describes the short baseline *reactor* oscillation which is governed by the squared mass differences Δm^2_{31} and Δm^2_{32}. By rewriting the expression

$$\cos^2(\Theta_{12}) \sin^2(\Delta_{31}) + \sin^2(\Theta_{12}) \sin^2(\Delta_{32}) \tag{3.8}$$

$$= \frac{1}{2} \left(1 - \cos(\Delta_{31} + \Delta_{32}) \cos(\Delta_{21}) + \cos(2\Theta_{12}) \sin(\Delta_{31} + \Delta_{32}) \sin \Delta_{21}\right) [89], \tag{3.9}$$

the impact of the mass ordering on the survival probability can be highlighted with the expression$(\Delta_{31} + \Delta_{32})$, which is positive for NO and negative for IO. The resulting energy spectra are also depicted in figure 3.6. The effect of the mass ordering is a phase shift of the fast oscillation pattern. For the determination of the neutrino mass ordering by a χ^2-fit to the data, an energy resolution of better than $3\,\%/\sqrt{E(MeV)}$ is required, which is a key parameter for the JUNO detector design.

Taking into account the spatial distribution of the reactor cores, uncertainties connected to the reactor neutrino flux, uncertainties in the detector performance and the background distribution, a median sensitivity of $\sim 3\,\sigma$ is expected for a detector run time of six years. In figure 3.7, the sensitivity on the mass ordering discrimination in dependence of the effective squared mass difference Δm_{ee} (see equation 3.4) is depicted, respectively for the ideal (dashed) and the realistic case. The impact of the uncertainties, especially the actual reactor core distribution, causes a sensitivity degradation of $\Delta\chi^2 \sim 5$ [30]. Beyond that, the spectral measurement of reactor neutrinos contributes to the overall mass ordering sensitivity in combination with other experiments as already mentioned in section 2.3.2.

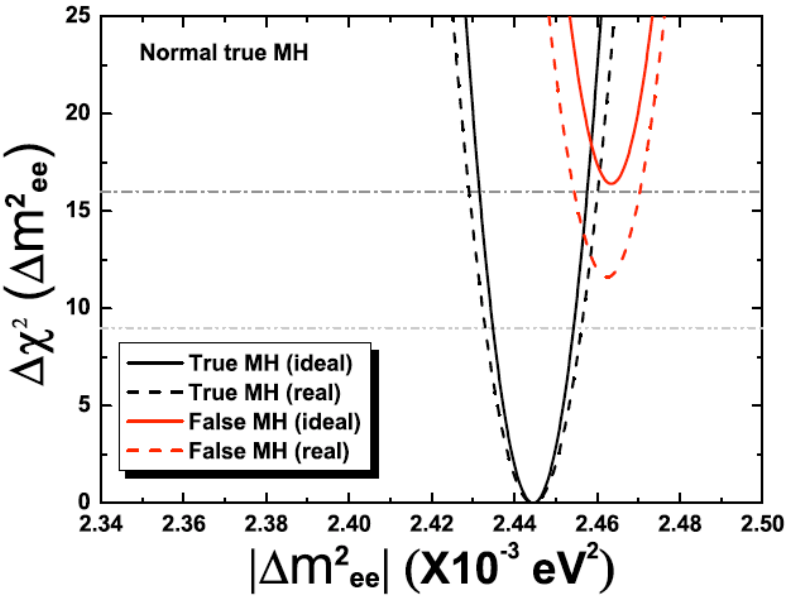

Figure 3.7: Comparison of the JUNO mass ordering sensitivity for the ideal and the real setting. The decreased sensitivity in the real case is mainly driven by different distances to the reactor cores. Figure from [30].

Solar neutrinos

Due to the very good energy resolution and the large detector volume of JUNO, the detection of solar neutrinos is possible with low statistical uncertainty. Especially the measurement of the low energetic ^{7}Be and the ^{8}B neutrino flux is of interest, as they allow the access to open questions in the SSM. As described in 3.5.2, neutrinos of all three flavors can be detected via the elastic scattering off electrons, which results in a quasi point-like energy deposition with a continuous energy spectrum, also for mono-energetic neutrino fluxes. As this signal is indistinguishable from β- and γ-decays, the determination of the solar neutrino flux is performed with a statistical analysis of the energy spectrum, making the radiopurity of the liquid scintillator the key parameter for the solar neutrino program.

In figure 3.8a, the expected neutrino fluxes and the single signal background spectra are displayed for the required liquid scintillator contamination level of 1×10^{-16} g/g for ^{238}U and ^{232}Th (assuming secular equilibrium). Additionally, the decay spectra of the respective secondary isotopes from cosmic muons are outlined. External backgrounds are neglected, as they are assumed to be removed with the fiducial volume cut. By comparing the contribution of the solar neutrino fluxes to the total spectrum, it is apparent that in the low energy regime only the ^{7}Be branch of the solar neutrino spectrum is observable as an edge at $\sim$ 665 keV for the expected background level. Assuming the ideal contamination level, the ^{210}Bi energy spectrum would be reduced by one order of magnitude allowing the detection of pep-neutrinos above 156 keV, where the threshold is determined by ^{14}C [30].

Via the same detection channel, but up to distinctly larger energies, the neutrino flux from the ^{8}B-branch is a further aspect of the solar physics program of JUNO. In the energy region below 5 MeV, the background is dominated by the decays of ^{208}Tl isotopes from the ^{232}Th decay chain and the elastic scattering of reactor antineutrinos. Above 5 MeV, the main background sources are secondary isotopes produced by cosmic muons. The majority of the cosmogenic isotopes can be rejected with the muon veto strategy of JUNO (see 4.1) except for the long-lived isotopes ^{10}C, ^{11}C and ^{11}Be. Their decay spectra are depicted in figure 3.8b, alongside the expected energy spectrum of solar ^{8}B-neutrinos in the detector.

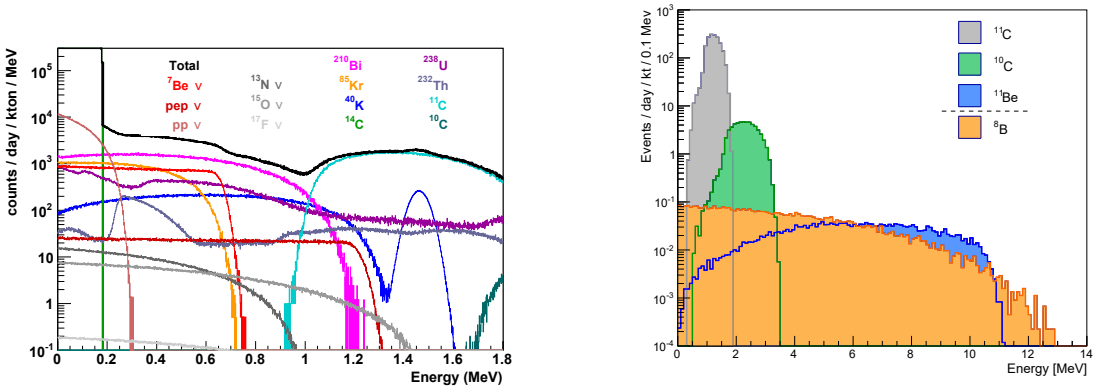

Low energy spectrum High energy spectrum

Figure 3.8: Solar neutrino and relevant background spectra for the low (left) and high (right) energy regions. The low energy spectrum assumes the baseline contamination level in the liquid scintillator (with 1×10^{-16} g/g U/Th). For the high energy spectrum, the cosmogenic background could be further reduced by applying three-fold coincidence cuts (see text). Figures from [30].

By additionally registering the capture signal of neutrons, which are produced together with the cosmogenic isotopes, a threefold coincidence of muon track, neutron capture and isotope decay can be used to identify and thus remove the respective background.

The measurement of the solar neutrino flux, especially from the distinct branches with low statistical uncertainty allows to access key parameters of the SSM and the MSW effect. Especially the solution for the recent solar metallicity problem might benefit from the high precision measurement of the flux of ^{7}Be and ^{8}B neutrinos as the proposed solar models predict different ratios. Determining the ratio of the neutrinos fluxes and comparing it to the current models allows to make statements about the surface heavy-element content and the potential contribution of the CNO-cycle, which was detected by Borexino recently [90]. A further open question is the transition between the vacuum-oscillation and matter-oscillation dominated regions, which are separated at around $1-3$ MeV (see section 2.2.2). By exploiting the continuous energy spectrum of the ^{8}B-neutrinos up to ~ 13 MeV, the MSW-modulated energy dependence can be studied to confirm the anticipated continuous transition between the vacuum and matter related solar neutrino survival probabilities [30]. Furthermore, based on the high precision measurements of Δm^2_{21} and Θ_{12} (see following section), matter effects beyond the SM can be analyzed. Hints for these non-standard neutrino interactions (NSI) come from the discrepancies between solar and reactor neutrino experiments. In combination with other experiments like DUNE and Hyper-Kamiokande new limits on the NSI parameters can be set by studying their effect on neutrino oscillation in the Sun and the Earth as well as on the day-night-asymmetry of the neutrino flux [91, 92].

Precision measurements of oscillation parameters

The requirements that dictated the design and the location of the JUNO detector to determine the neutrino mass ordering additionally allow to extract the neutrino mixing parameters Θ_{12}, Δm^2_{21} and $|\Delta m^2_{ee}|$ with unprecedented precision. The fact that JUNO simultaneously observes the atmospheric and solar oscillation patterns and the excellent energy resolution allow to measure the oscillation parameters with a precision of less than 1 %. In table 3.4, the current global analysis values and their precision are stated alongside the expected precision after including the oscillation parameters determined with JUNO for the current setup and with additional systematics, such as bin-to-bin

energy uncertainties, nonlinearities in the energy scale and the impact of background signals. Additionally, the precision measurements allow to test the standard three-neutrino paradigm and to narrow down the parameter space of the effective mass $|m_{ee}|$ of the neutrinoless double beta decay [30].

Supernova neutrinos

The detection of neutrinos from the supernovae SN 1987A was a major achievement in astroparticle physics. Measuring a neutrino burst from a nearby supernova with JUNO would be of huge benefit for the astrophysics and multi messenger community. Compared to the 12 elastic scattering events detected by Kamiokande II in 1987 [93], JUNO would register 5000 events via the IBD-channel, 2000 events from elastic all-flavor neutrino-proton scattering and 300 events from neutrino-electron scattering for a supernova in the galactic distance of 10 kpc [30]. Due to the high event rate in a time of ∼10 s, backgrounds are no major concern. However the standard data acquisition procedure, which is optimized for the detection of reactor antineutrinos, is not sufficient for the large IBD rates of up to 100 Hz and must be adapted accordingly [94]. With these caveats currently being addressed, the detection of a supernova neutrino burst with JUNO would help to clarify the neutrino driven explosion mechanism and the nucleosynthesis and it would act as an early warning for such events for the multi messenger community.

Additionally, the diffuse neutrino flux of all core-collapse events in the visible universe in the past might be measured, or at least new limits could be provided. The pulse shape discrimination capability of JUNO allows to efficiently reject atmospheric neutrinos and thus reducing the major background source of the diffuse supernova neutrino background (DSNB). At the current stage, a positive signal with a significance of $3\,\sigma$ is anticipated within 10 years containing information about the rate of star formation, the average energy spectrum of neutrinos from supernovae and also the rate of failed supernovae. In the case of no detected signal, a significantly improved limit can be achieved [30].

Neutrinos from dark matter

The unprecedented detector properties of JUNO allow for the indirect dark matter search via the detection of neutrinos from dark matter self-annihilation. This process would be visible via a mono-energetic excess in the energy range from 10 MeV to 100 MeV, beyond the given background levels. The major background sources are the reactor antineutrino flux in the low energy regime and neutrinos from the DSNB and atmospheric neutrino events as well as cosmogenic isotopes produced by muons in the detector. The pulse shape discrimination capability of JUNO helps to distinguish a potential dark matter signal from background events. For JUNO it is anticipated to increase the sensitivity of the dark matter annihilation cross section by a factor of 3 to 10 in the mass range from 15 MeV to 100 MeV compared to previous neutrino experiments like Super-Kamiokande or KamLAND (see figure 3.9) [95].

Table 3.4: Expected precision improvement for the solar oscillation parameters and Δm^2_{ee} with JUNO results. The systematics contain uncertainties of the energy scale and binning as well as contributions from several background sources. Data from [30].

Oscillation	Global analyses		JUNO precision	
parameter	value	precision ($1\,\sigma$)	nominal	with systematics
Δm^2_{21}	$7.42 \times 10^{-5}\,\mathrm{eV}^2$	2.8 %	0.24 %	0.59 %
Δm^2_{ee}	$2.514 \times 10^{-3}\,\mathrm{eV}^2$	1.4 %	0.27 %	0.44 %
$\sin^2(\Theta_{12})$	0.304	4.1 %	0.54 %	0.67 %

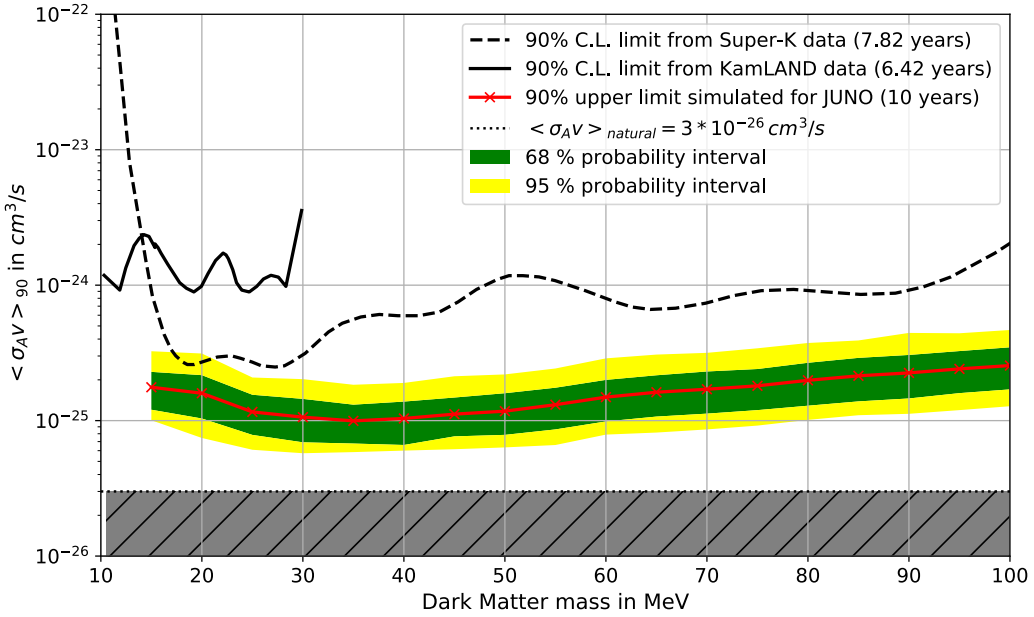

Figure 3.9: 90 % upper limit on the total dark matter self-annihilation cross-section from the JUNO experiment in comparison with the current limits from Super-Kamiokande and KamLAND. Figure from [95].

3.7 JUNO simulation framework

In order to make estimations about the detector performance and sensitivity for the preliminary design process and the preparatory development of reconstruction algorithms, the implementation and application of a detailed simulation framework is inevitable. The basis of the JUNO simulation package is the software framework SNiPER (Software for Non-collider Physics ExpeRiments) [96], which is dedicated to the requirements from nuclear reactor neutrino and cosmic ray experiments with the goal to provide efficiency and flexibility within the execution of tasks. It provides the communication between external software components, job execution control, event configuration etc. Especially the capability to keep the temporal correlations of events in the data buffer as well as the event splitting and mixing is valuable for the JUNO simulations. As SNiPER is not specifically dedicated to JUNO, the experiment related software parts are combined in the so called *offline* package, which are administrated by SNiPER and combined with external software packages like ROOT [97], CLHEP [98] and geant4 [99].

The detector simulation, containing the definition of the geometry, the physics processes, event propagation etc. is the first stage of the offline package. For the initialization of physical events, it provides several geant4 based interfaces to set the user defined parameters but can also handle the output of the various event generators, implemented by the collaboration. The physics processes and the propagation of the event particles and the eventually produced secondary particles is managed by default geant4 classes. Besides the Monte Carlo truth, the photon hit times at each PMT and other custom parameters are saved in a dedicated ROOT data tree [100].

In the following step, the electronics simulation, the detector response is simulated. Therefore, the photon hit times for each PMT are transformed into waveforms, which represent the expected output of the DAQ in the later experiment. The transformation also considers the properties of the PMTs such as dark count rate, TTS and pre- and after-pulses (see table 3.1) and of the JUNO electronics like trigger schemes, saturation and electronic noise [100].

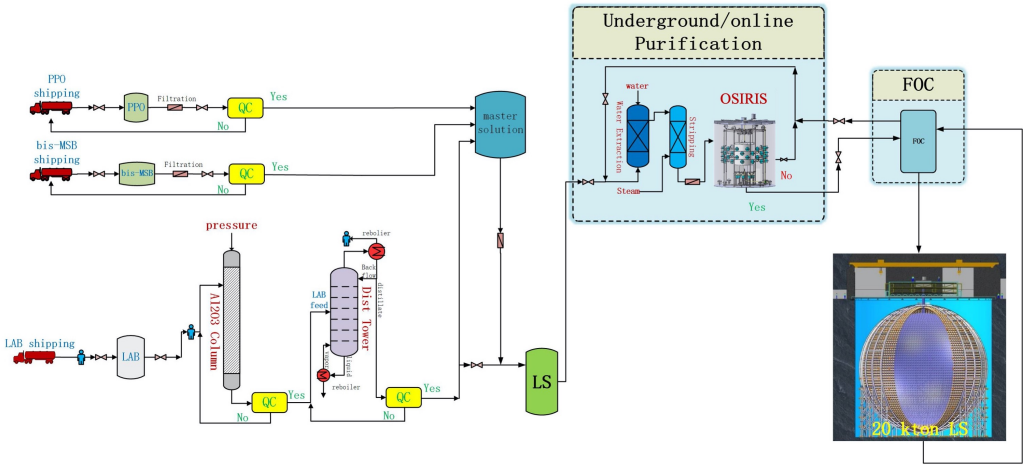

Figure 3.10: Layout of the JUNO scintillator filling and purification system. The delivery and initial purification of the liquid scintillator components is conducted above ground before it is lead to the underground facilities, where the second purification system and OSIRIS are located in the liquid scintillator hall. OSIRIS is the final component of the filling line with the task to monitor the scintillator radiopurity, before it is filled into the central detector.

The third stage of the offline package combines the reconstruction algorithms for different event types. Therefore, the waveform (from the electronics simulation or later from the DAQ) is analyzed with different approaches like deconvolution [101] or waveform fitting and integration methods [102]. Based on the processed waveforms, the requested event reconstruction is performed, which contains the energy and vertex reconstruction algorithms for point like events [103, 104] and track reconstruction for e.g. muons (see chapter 4).

3.8 Liquid handling system and OSIRIS detector

With 20 kt of liquid scintillator, JUNO distinctly exceeds comparable previous experiments by means of the target material volume. Accordingly, the production, processing and quality assurance of the liquid scintillator material are challenges at a completely new level and require careful planning. In figure 3.10, the JUNO liquid handling system is schematically depicted, with the above ground and underground components. The LAB will be shipped to the experiment site in batches of $\sim$ 5 kt. Before mixing it with the solutes PPO and bis-MSB, the LAB will pass through the initial purification above ground, consisting of adsorption in an aluminum oxide column, distilation, water extraction and nitrogen purging. After the quality control, equipped with small-scale detectors to identify impurities and monitor the attenuation length, the liquid scintillator is transported to the underground scintillator hall, where the second purification stage is located, which is foreseen to conduct the loop-mode purification [66]. Furthermore, the OSIRIS detector, a detector installed in the liquid scintillator handling line and designed for the monitoring of the radiopurity of the target material will be located in the liquid scintillator hall. More information about OSIRIS is given in chapter 5.

3.9 Taishan Antineutrino Observatory

The Taishan Antineutrino Observatory (TAO) is a satellite detector of JUNO located $\sim$ 30 m from a reactor core of the Taishan nuclear power plant in Guangdong. It was established as a part of the JUNO experiment after the analysis of the potential impact of fine structures in the reactor antineutrino flux on the determination of the neutrino mass

ordering [105]. With TAO as a reference detector, the determination of the unoscillated spectrum of the reactor antineutrinos allows to distinguish oscillation patterns from reactor fine structure patterns in the JUNO detector and thus to increase the precision on the mass ordering and oscillation parameter determination. However, the required energy resolution of TAO must be equal or even better than for JUNO.

For that reason, TAO aims to detect about 4500 photo electrons per deposited MeV in its liquid scintillation target of $\sim 10\,\mathrm{m}^3$ [106]. TAO will be instrumented with silicon photomultipliers (SiPMs) with a photo detection efficiency of $> 50\,\%$ and almost full coverage ($\sim 95\,\%$). In order to keep the the dark noise of the SiPMs at a low level, the detector will operate at $-50\,^\circ\mathrm{C}$, which, however, requires adjustments in the liquid scintillator composition compared to JUNO. To increase the neutrino detection efficiency further, and simultaneously improve the background discrimination, the liquid scintillator will be doped with gadolinium. Besides the main goal of providing an unoscillated reference spectrum of reactor neutrinos for JUNO, TAO can contribute to analyses of the evolution of isotope composition in the reactor fuel and neutron-rich isotopes. Additionally, TAO can search for light sterile neutrinos with a mass scale of $\sim 1\,\mathrm{eV}$.

4. Muon bundle reconstruction for JUNO

The efficient rejection of cosmogenic background in JUNO is essential for the success of its experimental goals. Due to the large dimensions of the target volume, a naive muon veto would cause severe dead time of the detector and is not applicable. For that reason, a veto strategy is developed (section 4.1), based on the reconstruction of the muon tracks in the detector. Beyond the reconstruction of single muon events, for which various approaches exist, the track reconstruction of events with multiple muons in the detector at the same time (so called bundle events) is required to achieve the design sensitivity of JUNO. The development of an algorithm which determines the muon entry and exit points into and out of the detector and allocates the associated tracks is described in this chapter. First, the characteristics of bundle events, their simulation with the JUNO software framework and the reconstruction principle are described (section 4.2). Following, the reconstruction algorithm is applied to the simulated muon bundle events and the reconstruction performance is determined (section 4.3). Finally, the integration to the offline framework and possible improvements are discussed (section 4.4).

4.1 JUNO muon reconstruction strategy

For liquid scintillator experiments like JUNO, muon induced secondary particles or nuclei are one of the main background sources as their signals cannot be distinguished from the searched IBD signal. Following the description in section 3.5.1, the expected background rate is on the same level as the IBD signal rate from the nuclear power plants. In order to reduce the cosmogenic background contribution in particle experiments, typically the fiducial volume is vetoed after the detection of a muon event. With respect to the life-times of the relevant isotopes, the veto time in JUNO is set to $t_{veto} = 1.2\,\mathrm{s}$ [30]. However, due to the large detector volume of JUNO, the muon rate in the liquid scintillator volume is $R_\mu = 4.7\,\mathrm{Hz}$ [107]. Thus, the vetoing of the entire fiducial volume after each muon would lead to a detector dead-time of 100% and is not applicable.

In order to reject muon induced background without sacrificing the majority of the active detector volume, the spatial and temporal correlation of the secondary particles and nuclei to the initial muon track can be exploited. In analyses of predecessor experiments like Double Chooz [108], Borexino [109], KamLAND [110], Daya Bay [111] and at CERN [112] where the muon tracks and the muon induced production of particles were reconstructed, the typical distance of the secondaries to the inital track was determined. With the knowledge about the track of the muons in the experiment, cylindrical volumes with the

radius r_{veto} around the tracks can be vetoed for the specific time t_{veto}, while keeping the remaining volume active.

The water buffer volume of JUNO, which surrounds the detector volume, is instrumented with $\sim$ 2000 PMTs to detect the Cherenkov light of cosmic muons in the water. However, the low density of PMTs and the small number of created photons, compared to experiments where the buffer is filled with scintillating material, is not sufficient to provide the required photon statistics for the full reconstruction of muon tracks. For that reason, the signals from the water PMTs are used as trigger signal for muon events and for the identification of muons that exclusively go through the buffer volume. The track reconstruction for muons which traverse the liquid scintillator volume is performed with the signals of the central detector PMTs.

The most abundant muon event type in the central detector contains only one muon (see table 4.1). For the single muon track reconstruction in JUNO, several already established and newly developed algorithms are prepared and tested within the JUNO simulation environment. The methods for single through-going or stopping muons utilize the first hit time distribution of the two PMT-systems (20-inch and 3-inch PMTs) of the central detector. The *fastest light* algorithm is based on the minimization of time residuals where the photon hit times at the PMT i of a given muon track hypothesis (t_i^{pre}) are compared to the observed first hit time (t_i^{obs}). The hit time in this model is composed by the sum of the muon flight time, the photon emission time and the photon time of flight from the emission point to the detecting PMT. By minimizing the expression

$$\chi^2 = \sum_{i=0}^{n_{PMT}} \left(\frac{t_i^{\mathrm{obs}} - t_i^{\mathrm{pre}}}{\sigma_i} \right), \tag{4.1}$$

where the time difference is summed up over the numer of all hit PMTs n_{PMT} with respect to the uncertainty of the measured hit-time σ_i, the best fitting muon track can be found. The accuracy obtained with this method is expected to be up to 3 cm in spatial and 0.5 ° in angular resolution (the reconstruction quality parameters are explained in detail in section 4.3 and in [113]).

The *geometrical model* algorithm also analyzes the first hit time distribution of the PMTs, but additionally exploits the characteristic temporal evolution of the "first light" front. Due to the high muon velocities ($v_\mu \approx c$), the scintillation light propagation has a conical geometry around the muon track, which leads, together with the spherical detector design, to rings of PMTs which detect the first light of the muon track in a given time window. From the propagation of the light front in the detector, the track parameters can be obtained with a likelihood fit. A full simulation of an extensive muon sample, involving the simulation of the read-out electronics of JUNO, shows that a spatial resolution of 20 cm and an angular resolution of 1.6 ° [114] can be achieved.

A third and more sophisticated method is the *topological reconstruction*, which provides a detailed "picture" of the muon track and exceeds the sole reconstruction of geometrical track parameters, but requires large computational effort. It takes into account the hit-time and charge information of each PMT to calculate three-dimensional probability maps of photo emission which is proportional to the energy deposition at each position in the liquid scintillator. By recursively using the obtained results as a prior of the following iteration, the spatial grid can be refined to improve the reconstruction resolution. The dependence on the exact photon emission demands high standards of the knowledge about the creation and propagation of photons in the detector, the characteristics of the PMTs and the optical model of the materials [115]. Besides the precise track reconstruction, regions of increased energy deposition can be recognized which helps to identify particle cascades along the muon track, where an increased amount of secondary particles is produced [87].

The above mentioned muon rate of $R_\mu = 4.7\,\text{Hz}$ in the liquid scintillator volume of JUNO includes not only single muon tracks, but also so called bundles, multiple muon tracks that traverse the detector. Although in most cases only one of the bundle muons hits the detector, in 8.3% of the events, two or more muons traverse the detector at the same time caused by the large extent of the experiment. The rate and abundance depending on the muon bundle multiplicity in the liquid scintillator volume is listed in table 4.1.

Muon events with an imprecise track reconstruction are rejected via a full detector veto which reduces the effective sensitive volume an thus the detector efficiency. The anticipated track reconstruction efficiency in [30] is $\geq 99\,\%$ for all muon events, which is required for the neutrino mass ordering sensitivity of JUNO (see section 3.5.1). To achieve the reconstruction efficiency goal, it is required that all single muon events and the majority of the bundle events with up to three muons in the detector are well reconstructed.

4.2 Muon bundle reconstruction

In contrast to single muons, the reconstruction of muon tracks in a bundle is aggravated and the already implemented and approved algorithms can not be simply applied, as the detector signal of multiple muon tracks can not be processed correctly. In order to test several reconstruction approaches, the algorithm that is presented in this thesis is developed outside of the JUNO offline framework as an independent software project, written in *python*. The goal is to examine a method for a robust and fast initial reconstruction of muon bundles, on which more sophisticated approaches can be based on. Therefor, the pulse shape analysis must be extended to be applicable for bundle events (currently under development in the collaboration).

4.2.1 Characteristics of bundle events in the detector

A bundle of muons is created in a collision in the atmosphere, induced by a cosmic ray particle. Due to the mutual origin and the long baseline to the detector, the resulting muon tracks arrive on the experimental site on an approximately flat plane with almost parallel track alignment. Only in rare cases, two independent muons traverse the detector simultaneously, which would result in non-parallel tracks. These events are not considered in the following analysis, as they are expected to constitute $\leq 0.1\%$ of the bundle events only.

In the liquid scintillator volume, the muons create, besides Cherenkov photons, a large amount of scintillation photons with $\sim 1.5 \times 10^4\,\text{photons/cm}$ [87], [116]), making muons the brightest events in the detector. In contrast to Cherenkov radiation, scintillation

Table 4.1: Expected muon rate and multiplicity distribution in the JUNO central detector[107]. The numbers are derived from extensive muon simulations with MUonSImulationCode (MUSIC) simulations, which take into account the onsite muon flux, the landscape profile above the muon detector and the rock density [61].

Muon multiplicity in the central detector	Rate (Hz)	Abundance (%)
1	4.352	91.7
2	0.292	6.1
3	0.068	1.4
4	0.023	0.5
5 or more	0.011	0.2
total	4.746	100

photons are emitted isotropically from the position of the energy deposition. However, the refractive index n_{LS}, $v_{\mathrm{photon}} = \frac{c}{n_{\mathrm{LS}}}$ and the relativistic muons with $v_\mu \approx c$ lead to a conical fastest light front, emerging around the muon track, with the tip of the cone at the current muon position and an opening angle of $\Theta_\alpha = \arccos(\frac{1}{\beta n_{\mathrm{LS}}})$, with $\beta = \frac{v_\mu}{c}$. In figure 4.1, the temporal evolution for the light detection of a simulated muon event in the JUNO detector is depicted. The pictures show the amount of detected photons at the large PMTs in the detector within a time window of 5 ns at four different times. At the intersection positions (subfigures a (entry) and c (exit)) of the muon track and the liquid scintillator volume, the distance to the PMTs is minimal, resulting in a high number of detected photons within a very short time frame. In combination with the spherical arrangement of the detector PMTs, the first hit light front of the muon track light cone travels as a ring shaped pattern through the detector, which constitutes the intersection of a cone and a sphere, as shown in subfigure b. From the exit point of the muon, a second light front originates and merges with the initial light front (subfigure d).

In the case of multiple muons in an event, these rings partially overlap at a certain point of the progress of the event, which exacerbates or even inhibits the application of the single muon track reconstruction algorithms, as the first hit times detected at a PMT cannot be allocated to a specific muon track distinctly.

4.2.2 Event generation for the simulation

The muon reconstruction algorithms are developed and tested on the basis of simulated events, which are computed with the JUNO simulation framework (see section 3.7), a standalone application based on geant4 [117] [118]. For the simulation of muon events, a sophisticated event generator is implemented, which takes into account the expected onsite muon flux and topology (described in detail for the OSIRIS detector in section 6.2) and the experiment dimensions. Furthermore, it considers the expected onsite bundle multiplicity distribution (see table 4.1). The output files of the muon generator contain the initial position and direction parameters and the kinetic energy for the generated muon events in the HEP file format. As the output file of the muon generator contains a realistic sample of the expected muon events onsite, the majority of the events contain only one muon. According to the bundle size distribution, only $\sim 8.3\,\%$ of the events consist of multiple muon tracks that simultaneously traverse the detector volume. In order to achieve a sufficiently large number of muon bundle events for the development of a reconstruction algorithm and to reduce the simulation effort, the initial positions and momenta of the simulated bundle events are not created directly with the muon generator, however on the basis of its result.

For this purpose, a large sample of single muon events is generated with the JUNO muon generator. For the creation of bundle events with the specified multiplicty only, one of the generated muon events in the HEP files is selected randomly as initial position and momentum for the first muon of the bundle. Subsequently, random initial positions for the further muon tracks are generated within the ranges of the simulated volume. As the muon tracks of the bundle events must proceed in parallel, the momentum direction can be taken directly from the initial event. This process is repeated until the target multiplicity is reached with muon tracks that definitely hit the liquid scintillator volume of the detector. As a last step, the kinetic energy of the artificial muons is sampled from the predefined distribution (see figure 6.7) and the components of the momentum direction are respectively adjusted. The generated bundle events are stored in the HEP format and can be processed with the JUNO simulation framework. The advantage of the independent generation of bundle events is the simple manipulation of the bundle properties for the single muon tracks, such as the bundle size and restriction to certain volumes of the detector.

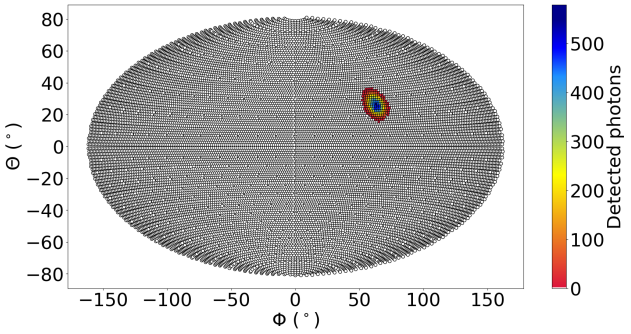

a) 25 ns

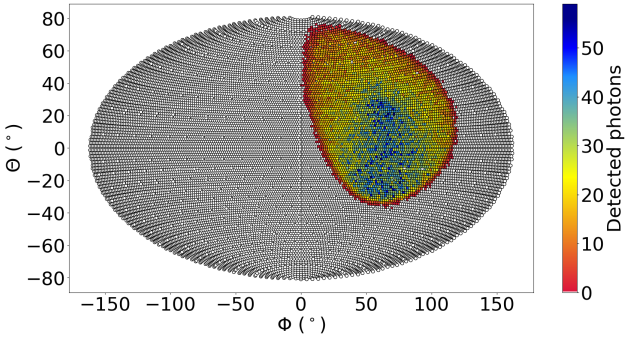

b) 100 ns

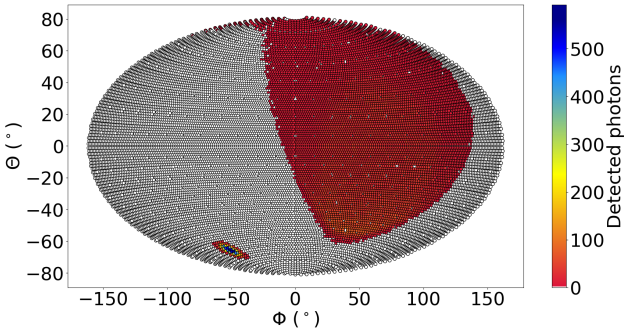

c) 130 ns

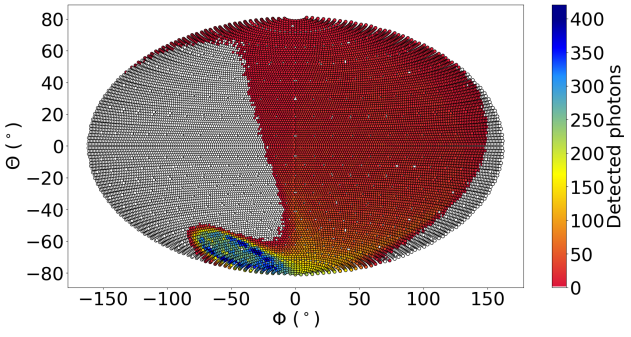

d) 145 ns

Figure 4.1: Exemplary light detection for a muon event in the central detector at different event times. Each frame shows the light detection within a time window of 5 ns. The circles represent the PMTs and the number of detected photons is represented by the color code (white is zero). The spherically arranged PMTs are depicted in Aitoff projection with the polar angle Θ and the azimuthal angle Φ. In figures 4.1a and 4.1c the small areas with high photon detection represent the muon entry and exit points. The cylindrical light front emitted around the muon track leads to the characteristic light detection distribution in the detector which spreads from the muon entry point (figures 4.1b -4.1d) and the exit point in figure 4.1d.

4.2.3 Simulation and data processing

The simulation of the muon events for the development and optimization of the bundle reconstruction algorithm was performed on the IHEP [1] computing cluster in Beijing, on which the most current version *J20v2r0* of the JUNO simulation framework was provided. As the large amount of simulated scintillation and Cherenkov photons of a full muon bundle event exceeds the hardware capacities (especially the memory per job that is available on the cluster (3.85 GB)), the optical simulation of muon events are split. Hence, the simulation of a specific event is interrupted, when a given memory threshold is reached and the data is stored in a file. Then the memory can be released and the event simulation is resumed. Although the simulation result is still stored in a single file, the tree structure is modified, compared to a regularly simulated event, which must be considered in the read-out of the data. As the resulting splitting of the muon track also affects the Monte Carlo truth which is required to review the quality of the reconstruction results, the simulation is repeated with the same initial parameters and random seed, but without the generation of optical photons.

As the development of the muon bundle reconstruction algorithm is realized independently from the JUNO software framework, the simulated data is pre-processed, to reduce the computation time for the actual reconstruction algorithm. With this modular setup, the read-out and processing of the simulated muon data is only performed once and the reconstruction algorithm can be initiated repeatedly with different parameters and settings.

First, the PMT positions are extracted from a GDML[2] file, in which for each simulated event the respective array is saved. From the Cartesian coordinates, the PMT positions in spherical coordinates and the transformation into the Hammer-Aitoff-projection are calculated and stored in a newly developed data class. Additionally the spherical PMT coordinates for shifted coordinate systems ($\Delta\Phi = 90°$, $\Delta\Theta = 180°$ and $\Delta\Phi = 90° + \Delta\Theta = 180°$ respectively) are stored, as they are required for the reconstruction approach. In order to verify the later reconstruction results, detailed information of the simulated muon tracks is required. Besides the initial vertex and the momentum direction of the muons, which can be deducted from the Monte Carlo truth, also the intersection points of the tracks with the scintillation containing volume are calculated. Here, additionally the differentiation between entry and exit point must be made, as the temporal succession of the bundle event reconstruction is not unambiguous. The calculated intersection points are additionally transformed into spherical coordinates. Concluding, the optical simulation data is extracted. It contains the specific ID of the detecting PMT and the respective detection time for each photon hit. The effect of the electronics and the PMT characteristics, is considered by the smearing of each photon detection time with the mean TTS of the respective PMT type. To improve the computing performance of the reconstruction algorithm, the hit times arrays, associated to each PMT ID, are sorted and the respective first hit times are determined.

4.2.4 Track reconstruction algorithm

The overlapping first hit time distributions of the different muon tracks in the bundle events inhibit the direct adaption of the sophisticated single muon reconstruction algorithms. Therefore, a more basic reconstruction strategy for bundle events is required. The presented algorithm searches for the intersection points of the muon tracks and the liquid scintillator volume and connects the respective points with parallel lines which exploits the defined track alignment of bundle muons. With this approach, also the entry and exit times of the respective muon tracks can be deduced with the first hit time of the PMT

[1] Institute of High Energy Physics
[2] Geometry Description Markup Language

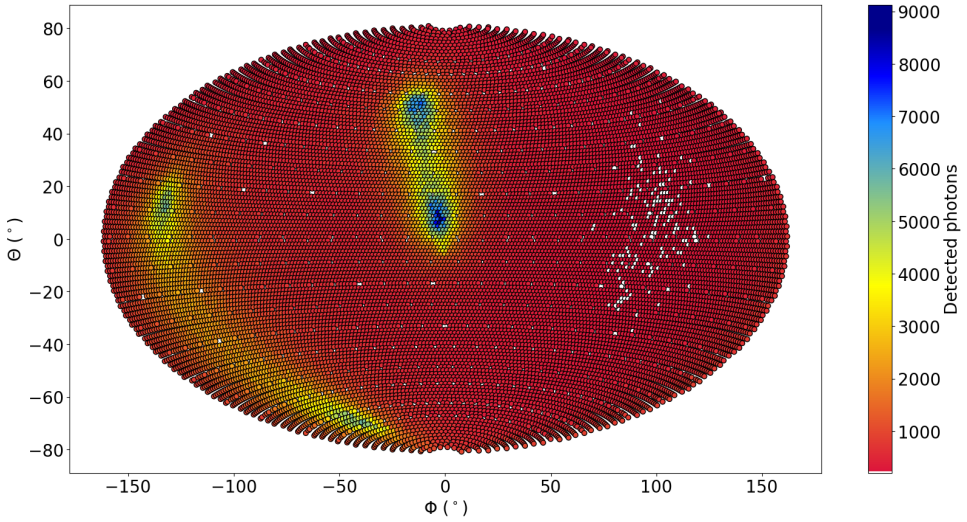

PMT depiction

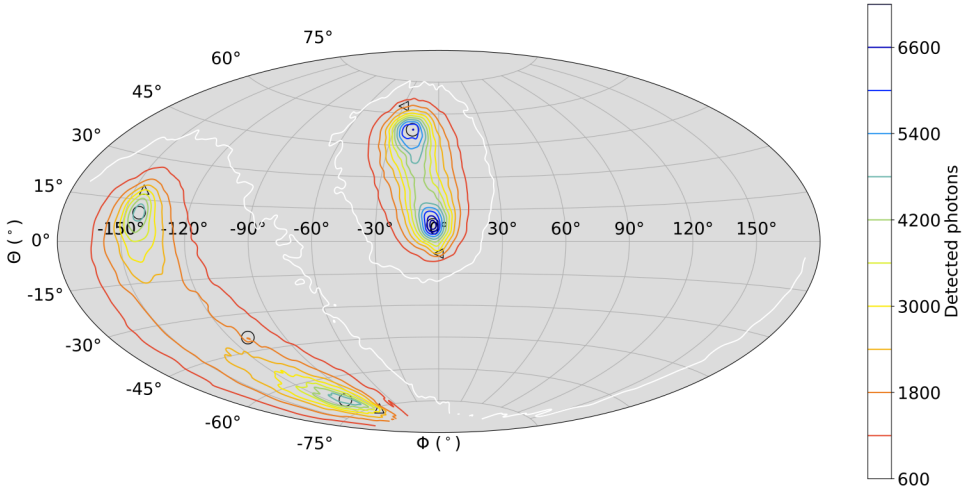

Contour depiction

Figure 4.2: Charge picture of an exemplary muon bundle event in the Hammer-Aitoff projection depiction. The muon entry and exit points are distinctly visible in both depictions. In the contour picture, the intersection points identified by the algorithm, are indicated by black circles. The true intersection points are depicted by pairs of black triangles, with the orientation indicating the allocation to the specific track. A further identified maximum is indicated by the black circle at ($\Phi \approx -110\,^\circ$, $\Theta \approx -40\,^\circ$), which does not belong to an intersection point.

which is closest to the computed intersection point. Furthermore, the algorithm is applicable to events with any bundle size and fast enough to reconstruct the events in realtime. The downside of this approach is that the reconstructed muon path is only described as a straight line between the two intersection points. Additionally, the algorithm is limited to events where all muons go through the central detector and are not stopped inside the liquid scintillator volume. However, the deviation of muon tracks from the anticipated straight lines has only minor effects on the reconstruction results and can be compensated by a slightly larger veto volume. Stopping muons are a rare event type with assumed 4 % of all bundle events and thus can be compensated with a full detector veto. Furthermore, advanced muon track reconstructions can use the information of the basic approach as input to determine the track inside the detector volume more precisely and thus increase the muon bundle reconstruction performance, both by the accuracy and by efficiency.

In order to identify the muon track intersection points with the scintillator volume, the photon detection distribution of the entire muon event for all PMTs is observed. The resulting "charge map" is depicted in figure 4.2 for an exemplary two muon event. Due to the short distance of the muon tracks to the PMTs at the entry and exit points, the scintillation light density is maximal there. An approach by a group in Beijing [119] is based on the fitting of two-dimensional Gauss distributions to the charge map to identify the local maxima. Although in most cases the positions of the found maxima match the true intersection points, further local maxima which do not represent a muon intersection point are found by the fit, due to the granularity of the detector. The intersection point detection strategy described in this section, also aims to identify the maxima in the charge picture, but is based on the analysis of the contour image of the charge map, shown in the lower image of figure 4.2. Here, areas of PMTs with equal charge are separated by the contour lines. The main advantage of the contour analysis resides in the reduced granularity of the charge picture and delivers further properties that can be useful for the event reconstruction, such as the quick detection and the shape of equal charge levels.

The contour images of the charge map of an event are created with the python function *contour*, implemented in the *matplotlib* module, that requires the coordinates of the PMTs from the Aitoff projection and the charge per PMT. The computation of the contour images for each simulated event is structured as a stand-alone script which allows to process the contour generation independently from the preceding data processing or the following reconstruction scripts. The function returns a class *QuadContourSet*, in which the image points of the calculated contour lines are stored. In order to consider contour lines close to the edge of the projection correctly, further contour images are computed with rotated coordinates (see above).

Based on the contour image of the charge distribution of the observed muon event, the entry and exit points of the muon tracks are reconstructed. In figure 4.2, the maxima in the charge distribution, located close to the true intersection points of the muon tracks (black triangles), are clearly recognizable. However, additional maxima which do not represent muon intersection points can be identified in the contour image, for example at position ($\Phi \approx -110\,^\circ$, $\Theta \approx -40\,^\circ$) in figure 4.2. For the determination of the maxima which are associated to the real muon intersection points, criteria are defined to identify them as such: for each contour line it is verified if it encompasses another contour line or if there is another contour line of the same level encompassed by the same contour line with a lower level, which would exclude it as a maximum. As this procedure is performed for the original and the rotated picture independently, in the following step the results of the two procedures are merged into a single set of reconstructed points. Therefor, the coordinates of the rotated picture are retransformed opposed to the initial transformation. For the

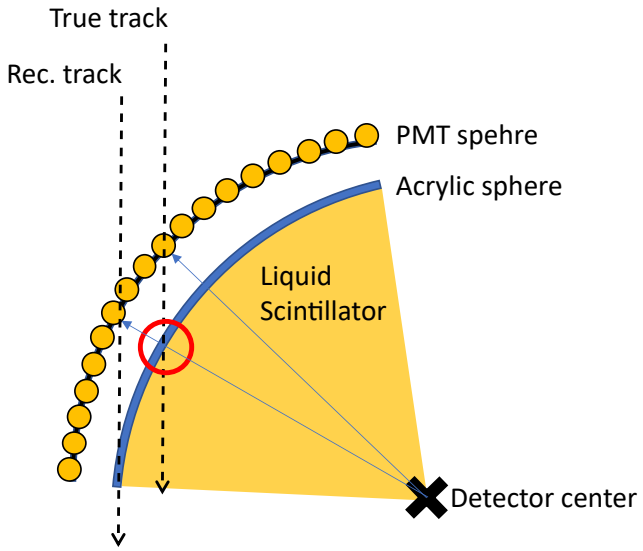

Figure 4.3: Geometry induced shift of reconstructed tracks due to the spherical geometry of the detector, the detected position of intersection points is shifted to larger values, depending on the distance of the true track to the detector center.

maxima in the combined picture, the position is calculated by

$$\vec{x} = \frac{1}{n} \sum_{i}^{n} \vec{x}_i \tag{4.2}$$

for all n points with coordinate $\vec{x}_i$ of the contour line with the highest contour level of the maximum. In figure 4.4a, the number of identified points for the two-muon data sample is depicted, for which $n = 4$ is the true value. Events with less identified points contain at least one muon track, which is close to the edge of the detector and produces one large charge maximum. Events with more identified maxima mainly contain at least one track which intersects the detector at the pole regions, where the less homogeneous PMT placement leads to a higher granularity of the charge picture. These falsely identified maxima can be rejected in the track allocation step (see below), but this increases the computational effort.

For each of the reconstructed points, the corresponding Cartesian coordinates are calculated and the associated intersection time is determined. Therefor, the PMT, which is closest to the identified maximum is determined and the registered first hit time of the PMT is allocated as muon intersection time. This value is corrected after the muon tracks are allocated to the muon intersection points to consider the distance between the emission and detection positions of the photons.

In order to assign the muon tracks for each bundle event, three independent algorithms were developed to allocate the muon tracks to the identified intersection points. In the first algorithm the parallelism of the tracks is exploited. Each identified maximum point is connected to the other points ($\vec{p}_a$ and $\vec{p}_b$) and the normalized direction vectors $\vec{x}_j = \frac{1}{|\vec{p}_b - \vec{p}_a|} \cdot \vec{p}_b - \vec{p}_a$ are calculated. With the knowledge about the bundle multiplicity n, the set of n connections is determined for which the highest grade of parallelism is found. Therefor the parameter p is calculated for each combination of n point connections

$$p = \sum_{k>l}^{n} \sum_{i=1}^{3} (x_{k,i} - x_{l,i})^2, \tag{4.3}$$

with the direction indices $j = k$, $l \leq n$ and the coordinates $i = x$, y, z. The combination for which p is minimal is chosen as result for the reconstruction.

The second method to allocate tracks to the entry and exit points is based on the reconstructed intersection times. Therefor, between each combination of intersection points the time of flight for relativistic muons is calculated by

$$tof_{i,j} = \frac{|\vec{r}_i - \vec{r}_j|}{c}, \tag{4.4}$$

with two reconstructed intersection points at the positions $\vec{r}_i$ and $\vec{r}_j$ and the speed of light in vacuum c. By searching for the minimum difference between the derived time of flight and the differences of the reconstructed intersection times $\Delta t = t_i - t_j$, pairs of points can be allocated to a track. As the bundle events consist of n tracks, the combination of allocated tracks with minimum $\tau = \sum_k^n (tof_k - \Delta t_k)$ is chosen.

The third track allocation algorithm is based on the contour image data of the deposited charge in the detector (figure 4.2), which exploits that the entry and exit point of a muon track are encompassed by joint contour lines. This mainly holds true for tracks traversing the detector close to the edge, which leads to increased charge deposition at PMTs located between the two points. To illustrate the algorithm, in figure 4.2 the charge picture for a two-muon event with one muon track close to the detector edge (intersection points marked with $\triangleleft$) and one rather centrally passing track (intersection points marked with $\triangle$) is depicted. The cohesive intersection point pairs are encompassed by multiple joint contour lines, with the number depending on the distance to the detector edge. Furthermore, even close non-cohesive intersection points from different muon tracks do not show this common feature so they can be distinguished with this algorithm. In the entire analysis, the lowest contour level (white) is not considered. This method was developed to resolve problems in the track allocation for two- muon bundle events in which both tracks have similar distance to the detector center. This leads to a parallelogram-like arrangement of the resulting intersection points, in which the track allocation via the parallelism approach is not unambiguous. In the third algorithm, the joint contour line with the highest level for every combination of point pairs is determined. In the case of n independent pairs of points, which share a joint encompassing contour level above a given threshold, the track allocation can be performed.

In order to find the best track allocation to the reconstructed points, the independent results of the three algorithms A_{para}, A_{tof} and $A_{contour}$ are analyzed in a dedicated algorithm. For $A_{para} = A_{tof} = A_{contour}$ (all algorithms get to the same allocation result) the track allocation is considered as unambiguous and $A_{reco} = A_{para}$. If this is not the case, but $A_{contour}$ returns n track allocations, the result is $A_{reco} = A_{contour}$. Otherwise, the performance parameters of the other two algorithms are considered, by comparing the parameters p and τ to defined limits. In case both parameters are below the limit, but return different results, the allocation result is $A_{reco} = A_{para}$, as the parallelism algorithm returns more precise results. If both parameters surpass the limit, the track reconstruction is considered as unsuccessful.

Due to the spherical array of the PMTs around the acrylic vessel, the PMTs closest to the muon intersection point with the scintillator volume detect most scintillation light. For that reason, the reconstructed points are projected on the PMT sphere with a straight line between the geometry center and the muon intersection point with the scintillator volume (see figure 4.3). This leads to a shift of the reconstructed tracks in relation to the true track. The magnitude of the shift depends on the distance of the muon track to the detector center. As the reconstructed track direction is not affected, the shift can be corrected for by calculating the true intersection points with the scintillator. Therefor,

Table 4.2: Events with $2n$ or more identified intersection points depending on the maximum muon track distance to the detector center. The detected events qualify for the subsequent track allocation algorithm. The detection efficiency of the algorithms decreases with increasing n and increasing radius of the observed detector volume.

Bundle size n	$2n$ or more identified intersection points (%)		
	Full sample	$r_\mu \leq 17\,\mathrm{m}$	$r_\mu \leq 16\,\mathrm{m}$
2	72.7	80.7	84.9
3	51.0	56.3	61.2
4	36.6	42.2	43.0

the intersection points of the reconstructed track with the acrylic sphere are calculated. The corrected muon track has the same direction as the originaly reconstructed track and passes the calculated intersection points. Furthermore, the corrected muon intersection time can be calculated by subtracting the time of flight for photons in water from the scintillator intersection point to the nearest PMT.

4.3 Bundle reconstruction performance

For the determination of the bundle reconstruction performance, three data sets are simulated with respectively $\sim$ 2000 two-, three- and four-muon bundle events. Only muon events in which all muon tracks traverse the JUNO liquid scintillator volume with a minimum track length of $l_{scint} \geq 10\,\mathrm{cm}$ were selcted for the determination of the reconstruction performance. As the muon bundle track reconstruction is based on the identification and allocation of the associated entry and exit points of the muons tracks into the detector, the capability to identify all intersection points of the bundle muon tracks determines the total reconstruction performance. For the allocation of the muon tracks in an n-bundle event, at least $2n$ points need to be identified. As shown in figure 4.4, the amount of events, which pass this criteria depends on the bundle size and the maximum distance of the muon tracks to the detector center in the bundle. In the two-muon data sample, for the majority of events four intersection points are identified. Furthermore, the dependence of identified points on the distance of the muon tracks is noticeable, as the distribution for smaller observed radii is shifted to higher multiplicities. While events with four or more points are hardly affected by the radius cut, events with less identified points are rejected. The distributions with three- and four-muon bundles are spread more widely and in the case of $n = 4$ do not show the clear peak at the corresponding target value $2n = 8$. Additionally, the reduction of events with less identified points than the target value induced by the radius cuts is less pronounced. This indicates that for these events the lower detection efficiency is mainly caused by close muon intersection points which can not be resolved particularly. In table 4.2, the amount of events with $2n$ or more identified intersection points is listed. It indicates, that the number of events, which qualify for the track allocation decreases with the bundle size and the distance of the muon tracks to the detector center.

For bundle events with n muons and $> 2n$ identified intersection points, the track allocation can be performed according to the procedure described above. The limit parameters of the parallelism and time-of-flight approach are derived from the mean values of the calculated values and set as $p_{thres} = 0.1$ and $\tau_{thres} = n \cdot 20\,\mathrm{ns}$. In table 4.3, the fractions of the applied allocation algorithm are listed for the bundle sizes $n = 2, 3, 4$. For all three data samples, mainly the parallelism algorithm is applied, followed by the time of flight algorithm. The contour algorithm has only a small impact on the two muon bundles and is negligible for

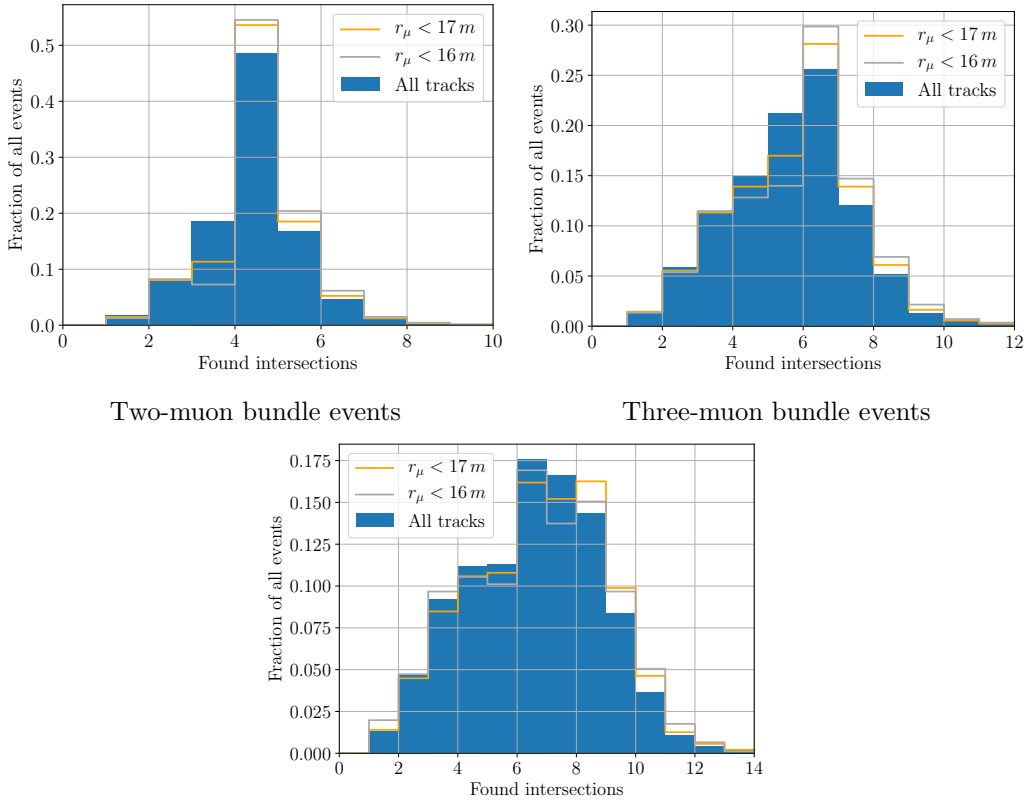

Two-muon bundle events

Three-muon bundle events

Four-muon bundle events

Figure 4.4: Number of identified muon track intersection points with the bundle reconstruction algorithm for two-, three- and four-muon events (blue bars). Additionally, the distributions for events containing only muon tracks with a selected maximum distance to the detector center are depicted (orange and grey lines).

Table 4.3: Distribution of the applied track allocation methods for the bundle sizes $n = 2, 3, 4$. The parallelism algorithm is dominant in all simulated samples. The fraction of unallocated tracks decreases with the bundle size.

	Fraction (%)		
Track allocation method	$n = 2$	$n = 3$	$n = 4$
$A_{para} = A_{tof} = A_{contour}$	4.9	0.1	0.0
$A_{contour}$	6.5	2.0	0.4
A_{para}	59.9	51.1	50.2
A_{tof}	19.2	43.0	44.9
Unallocated events	9.5	3.7	1.5

Table 4.4: Performance parameters of the reconstruction after the track allocation depending on the bundle size. The mean bias and variance over the entire radius is calculated (see figure 4.5). While the accuracy of ΔD decreases with increasing bundle size, it is relatively constant for α. Additionally, the number of contained events in different variance ranges around the mean value is listed.

Track parameter		$n = 2$	$n = 3$	$n = 4$
ΔD	Mean (mm)	-98.8	-183.3	230.0
	Variance (mm)	325.3	628.6	667.8
α	Mean (°)	0.82	0.93	0.8
	Variance (°)	0.52	0.49	0.41
Accepted range		Reconstructed events (%)		
	$\pm 1\sigma$	64.4	67.0	53.9
	$\pm 2\sigma$	91.8	90.4	79.8
	$\pm 5\sigma$	98.9	96.4	92.3

larger bundle sizes, as here the formation of isolated point pairs is suppressed, due to the number of total points. In general, the track allocation improves for larger bundles, as single outliers of a distinct track within an event can be corrected by the other tracks and thus have a smaller impact.

With the tracks allocated to the intersection points in each event, the reconstruction accuracy for tracks can be determined. The performance is determined in dependence of the true distance of the muon track to the detector center D_{true}. The reconstruction performance parameters for each track in a bundle are the difference of the true and reconstructed distance of the track to the center $\Delta D = D_{true} - D_{rec}$ and the angle α between the true and the reconstructed track. The parameters are calculated for each allocated track in bundles with $2n$ identified intersection points and successful track allocation. In figure 4.5, the distributions of ΔD and α for the three data sets are depicted. Aside the low statistic in the bins at small radii (geometrical reasons) and in the four muon data sample (reduced intersection point identification), the distribution bias for ΔD and α is flat over the radius of the detector, however the variance in the specific bins increases for larger bundles. The mean values are listed in table 4.4. While the dependence of the angular precision to the number of muons per event is subordinate, the mean and the variance of the distance parameter ΔD increases for larger bundle sizes.

Based on the mean value and the variance in each bin, the track reconstruction performance for the associated radius can be calculated. It is defined by the ratio of events with n reconstructed tracks to the number of events with $\geq 2n$ well reconstructed intersection points. According to [120], simulated tracks are considered as well reconstructed if the deviation of the reconstructed parameters ΔD and α is within two times the standard deviation in the associated bin. In [120], the allowed track parameter range is five times the standard deviation, which is not applicable for the bundle events, as the variance is too high. The amount of reconstructed events is listed in table 4.4. The reconstruction efficiencies for bundle events are 91.8 % for $n = 2$, 90.4 % for $n = 3$ and 79.8 % for events with $n = 4$.

The combination of the results from the intersection point detection (see table 4.2), the track allocation (see table 4.3) and the track reconstruction (see table 4.4) allows to define a total bundle reconstruction performance with the described method in dependence of the bundle size. In the steps two and three, only events are considered which pass preceding

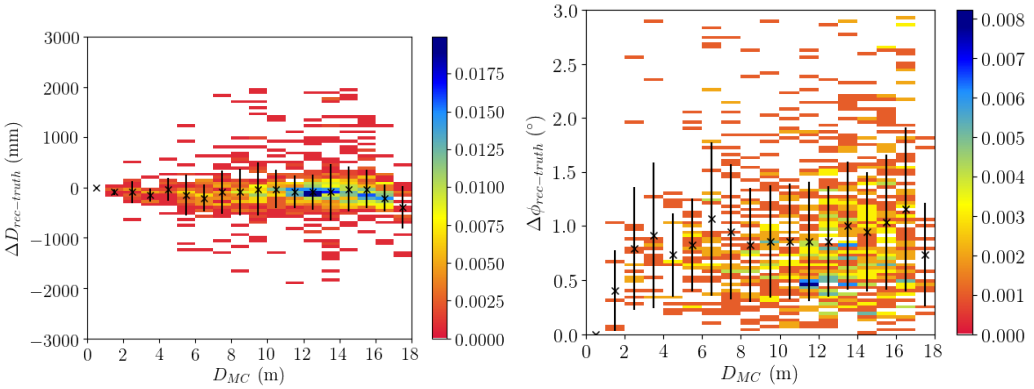

Two-muon bundle events: ΔD

Two-muon bundle events: α

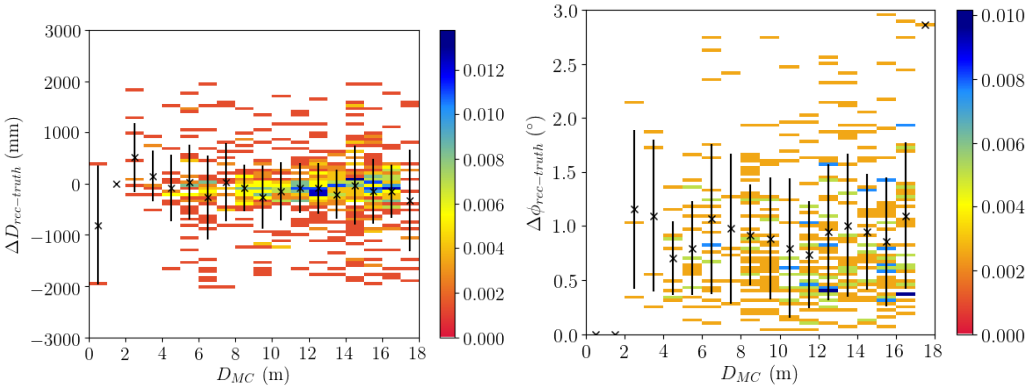

Three-muon bundle events: ΔD

Three-muon bundle events: α

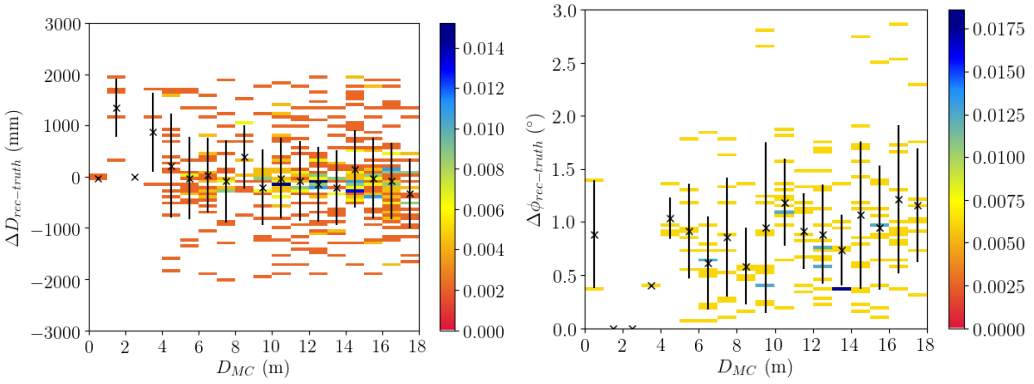

Four-muon bundle events: ΔD

Four-muon bundle events: α

Figure 4.5: Accuracy of the reconstructed track parameters for the three bundle sizes $n = 2, 3, 4$ for events with $\geq 2n$ identified intersection points. Each bin represents a range of 1 m of the true muon track distance to the detector center. The black crosses represent the mean values within each bin. For small radii and with increasing bundle size, less tracks are available for the reconstruction leading to an increased variance of the reconstructed values. The mean values and variances are listed in table 4.4.

Table 4.5: Total muon bundle reconstruction performance depending on the bundle size. It is calculated by the combination of the intersection point detection efficiency (table 4.2), the track allocation efficiency (table 4.3) and the track reconstruction efficiency (table 4.4) for a range of 2σ.

Bundle size	Reconstructed events (%)
2	59.8
3	44.3
4	28.8

reconstruction. The results listed in table 4.5 show a strong dependence of the bundle size and are mainly determined by the intersection point detection. In total, a rate weighted bundle event reconstruction with an efficiency of 52.9 % is achieved with the presented algorithm.

4.4 Conclusion

Based on the results in table 4.5 and regarding the anticipated bundle rates (see table 4.1), 52.9 % of the bundle events in the JUNO detector can be reconstructed with the required accuracy. Assuming perfect single muon event reconstruction, the total muon detection efficiency sums up to 96.1 %. Thus, and this is also valid for the current single muon reconstruction approaches[107], the design goal of 99 % [30] sufficiently well reconstructed muon events in the central detector is not achieved. Therefore, improved methods must be developed, especially to accurately reconstruct non-standard muon tracks, such as close-to-the-edge tracks. Compared with the reconstruction for single tracks, the muon bundle reconstruction algorithm shows a significantly reduced performance for both the detection of tracks and the accuracy for their reconstructed parameters. This can be explained with the aggravated conditions, due to the interference of multiple track signals and the simpler reconstruction method which does not consider scattering off muons and generally is more imprecise in the determination of the entry and exit positions of the muons. A potential way to improve the muon bundle reconstruction is the combination with sophisticated single muon algorithms, as described in section 4.1. This requires advancements in the analysis of the PMT signal waveforms which would allow to distinguish the first hit times of the light fronts of the different muon tracks. With this approach, and the input of the presented bundle reconstruction, the precision of the track parameters should be improved distinctly. The required developments are currently under development in the collaboration and can be expected to be applicable soon. The modular structure of the presented reconstruction algorithm enables to exchange distinct steps of the procedure with improved methods. Especially the intersection point detection, which shows the lowest performance, might be improved in the future with more precise approaches.

5. The OSIRIS pre-detector

The purpose of the OSIRIS detector is to monitor the radiopurity of the liquid scintillator for the JUNO experiment. It is installed in the scintillator filling and purification line and is designed for the detection of ^{238}U and ^{232}Th isotopes at the level of 1×10^{-16} g/g. In this chapter, the motivation to develop and install the OSIRIS detector is discussed (section 5.1), followed by the description of the setup and planned operation modes (section 5.2). Furthermore, the characteristic BiPo coincidence signal, which OSIRIS is searching for and the relevant background sources are described in detail (section 5.3). Finally, the anticipated OSIRIS sensitivity is presented (section 5.4).

5.1 Motivation

The success of the JUNO physics program (see section 3.6) relies on the detector performance and background discrimination capability. While the determination of the neutrino mass hierarchy strongly depends on the energy resolution of the detector, the detection of neutrinos via elastic scattering is mainly driven by the rate of background events. Especially the solar neutrino program for which the signal of the elastic neutrino-electron scattering is searched for, relies on a low internal contamination with radioactive isotopes, which imitate the event signature indistinguishably. As shown in section 3.8, the liquid scintillator material undergoes a strict purification procedure to reduce radioactive contamination, such as isotopes from the ^{232}Th and ^{238}U decay chains and ^{40}K. In table 5.1, the required contamination levels for the respective physics goals and for comparison, the achieved contamination levels in Borexino are displayed. Although the scintillator purification facilities are expected to operate at a high level, the scintillation contamination levels must be monitored to ensure that the average contamination of radioactive isotopes does not surpass the limits. As the lifetimes of the constituents of the ^{232}Th and ^{238}U decay chains are too long to be registered in a small sample within a reasonable time for the expected contamination levels, the OSIRIS detector with a scintillator volume of $\sim 18\,\mathrm{t}$ was introduced during the JUNO planning phase. The main goal of the OSIRIS detector is the determination of the scintillator contamination with the natural isotopes of the ^{232}Th and ^{238}U decay chains by tagging the fast coincidence decays of the isotope pairs ^{212}Bi – ^{212}Po (^{212}BiPo) and ^{214}Bi – ^{214}Po (^{214}BiPo), which are located towards the end of the two chains (see figure 5.1). Both coincidence signals are composed of a β-decay of the respective bismuth iostope, followed by the fast α-emission of the resulting polonium isotope [121].

Table 5.1: Liquid scintillator radiopurity requirements for JUNO for the IBD and solar physics program. For comparison, the experimental values achieved in Borexino are stated. [30, 121, 122].

	JUNO		Borexino
	IBD	solar	
Isotopes	g/g		
^{232}Th chain	1×10^{-15}	1×10^{-16}	$\leq 1 \times 10^{-18}$
^{238}U chain	1×10^{-15}	1×10^{-16}	$\leq 1 \times 10^{-18}$
^{210}Po	-	5×10^{-24}	$\leq 1 \times 10^{-25}$
^{40}K	1×10^{-17}	1×10^{-17}	$(2.7 \pm 0.1) \times 10^{-18}$

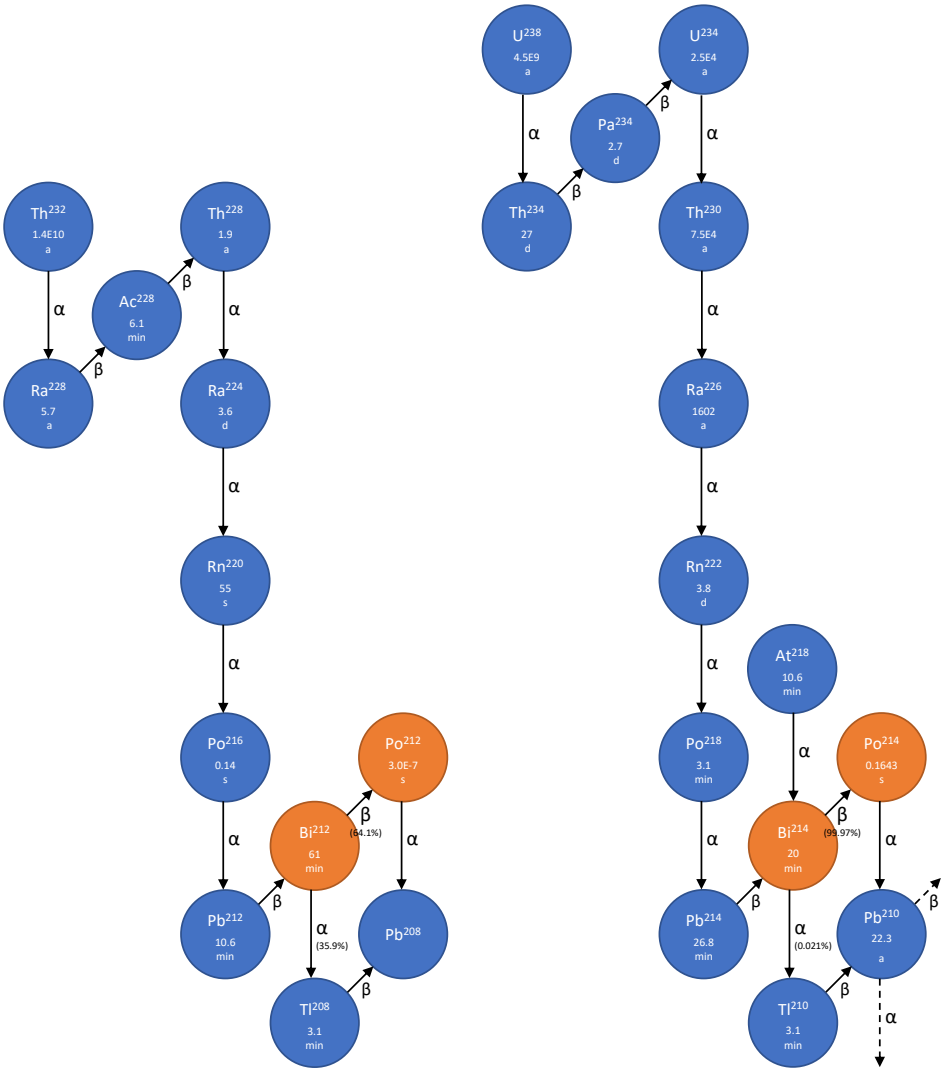

Figure 5.1: Decay chains of ^{232}Th and ^{238}U. α-decays are represented by vertical downward arrows, β-decays by diagonal arrows to the top right. In the case of multiple decay branches, the ratio is stated in percent. Below the isotope names, the half-life is noted. The possible gamma decays from excited states are not depicted. The orange marked isotopes and their corresponding decays are used in OSIRIS to derive the contamination of ^{232}Th and ^{238}U, assuming secular equilibrium. Data from [123].

Based on the secular equilibrium within the decay chains and the decay times of the participating isotopes of the BiPo coincidence, the detected rate of the coincidence signal can be used to calculate the total contamination of isotopes of the ^{232}Th and ^{238}U decay chains. The BiPo activity limits corresponding to the two considered JUNO contamination limits are presented in table 5.2. Due to the distinctly smaller sensitivity to ^{210}Po and ^{40}K, their determination requires increased volumina and measurement time, compared to ^{232}Th and ^{238}U.

5.2 Setup and operation modes

The OSIRIS detector will be installed at the end of the JUNO liquid scintillator purification line, to monitor the output of the mixing and purification plants before the scintillator is filled in the central detector (see figure 3.10). The OSIRIS setup will be placed at the rear end of the underground Liquid Scintillator Hall, which also houses the water extraction and steam stripping plants.

In figure 5.2, a realistic model of the OSIRIS detector system is depicted. In the center of the geometry, the cylindrical acrylic vessel is located. With a diameter and height of 3 m, the inner volume contains $\sim 21\,\mathrm{m}^3$, which corresponds to ~ 18 t of liquid scintillator. The acrylic wall thickness of 3 cm and the additional stiffeners on top and bottom provide sufficient stability, especially required during the filling process. The acrylic vessel is placed on a pedestal, which is part of a steel frame. The main purpose of the frame is the mounting of the PMT-systems, the laser calibration system and the optical separation (not shown, see section 8.2.3) [121]. The optical separation consists of several foil pieces, stretched between the legs of the steel frame. To shield the gaps between the horizontal PMTs, additional wires are mounted to the steel frame to fix the foil pieces. In order to reduce reflections on the inside and increase them on the outside of the optical separation, the foil is colored in black on the inside and white on the outside.

For the purpose of this work, a suitable material for the optical separation was searched. With the silage film *OK T200* a foil was found, which matches the given requirements. It is a bichromatic low density polyethylen (LDPE) foil, usually used in agriculture. LDPE is stated as a flexible and highly durable crystalline synthetic, only consisting of hydrogen and carbon [125]. The vendor states the foil thickness with 0.2 mm and a tear strength of $26.6\,\mathrm{N/mm}^2$ [126]. To test the suitability for the OSIRIS experiment, the material was reviewed for its durability in HPLC water, its contamination with radioactive isotopes and its optical properties.

The scintillation light produced in the central volume is detected by 64 20-inch Hamamatsu PMTs of the same type as used for the JUNO detector (see section 3.2). To achieve a good weighting between shielding gamma photons from radioactive contaminations in the glass and the number of detected scintillation photons, the PMTs are mounted at a distance of 1.3 m to the acrylic vessel. The PMT array consists of eight PMTs each above and

Table 5.2: Expected coincidence signal rates induced by scintillator contamination for the IBD and solar limits. From the actually measured ^{212}Bi – ^{212}Po (^{214}Bi – ^{214}Po) rate, the ^{232}Th (^{238}U) activity can be derived.

Decay chain	coincidence signal	Activity limit IBD	Activity limit solar
^{232}Th	^{212}Bi – ^{212}Po	1.2×10^{-8} Bq/kg	1.2×10^{-9} Bq/kg
^{238}U	^{214}Bi – ^{214}Po	0.4×10^{-8} Bq/kg	0.4×10^{-9} Bq/kg

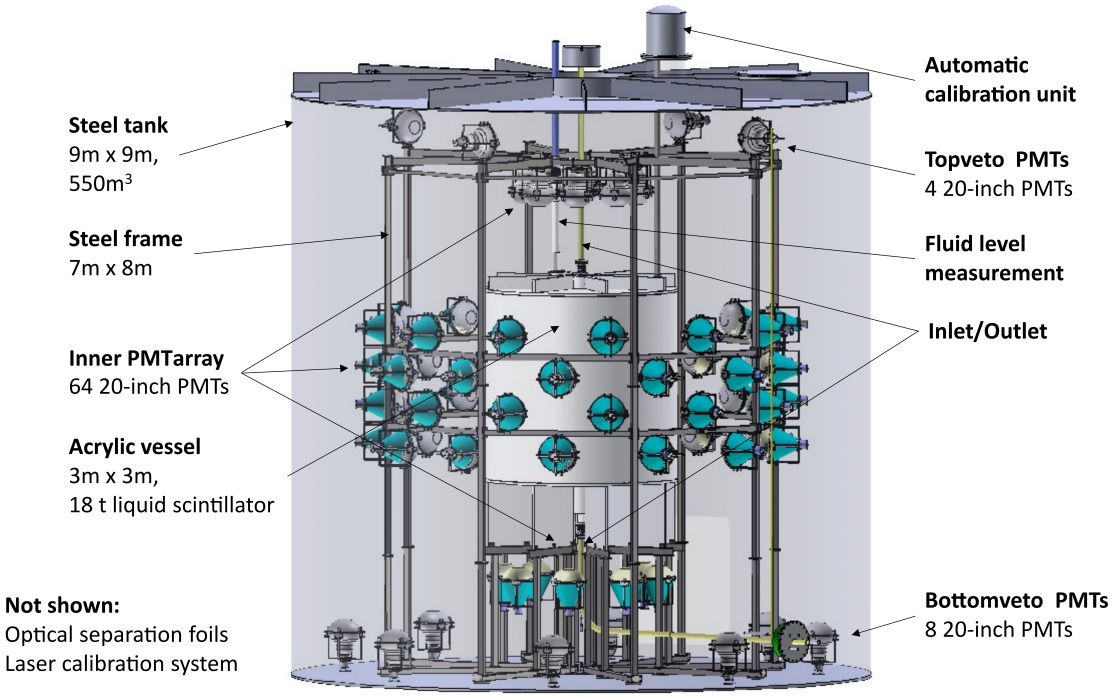

Figure 5.2: The OSIRIS detector layout. The central acrylic vessel contains $\sim$ 18 t of liquid scintillator material and is observed by 64 PMTs. The central detector PMTs are mounted on a steel frame which also holds the optical separation foil and the diffusors of the laser calibration system (not shown). To shield the liquid scintillator volume from gamma photons originating in the surrounding rock volume and the PMTs, the steel tank is filled with ultrapure water, which is instrumented with 12 additional PMTs to detect Cherenkov photons from traversing muons. On top of the steel tank, the automatic calibration unit is located, which is connected to the acrylic vessel via steel pipes and can deploy radioactive and photon sources into the scintillator volume. Adapted from [124].

below the target volume and four rings of 12 PMTs each around the the acrylic vessel. The PMTs are additionally shielded magnetically via steel cones (not shown, see section 6.1.2) [124]. This design leads to an optical coverage of 9 %, resulting in an estimated photo electron yield of ~ 280 PE/MeV deposited energy in the detector. For the OSIRIS detector, the novel iPMT (intelligent PMT) concept is applied, which combines the PMT and the associated electronics modules to a single device. Voltage supply, digitizer and control electronics are mounted directly at the base of the PMT and housed in a steel shell. Due to the digitization directly at the PMT, the signal quality is improved by reducing the cable length between the signal source and the digitization circuit [124].

The entire system is deployed in a steel tank of 9 m in height and diameter which is filled with ultrapure water. The tank walls are covered with black HDPE liner to prevent corrosion. To increase the muon veto efficiency (see section 8.2.3), the side walls and the bottom floor outside the steel frame are additionally covered with highly reflective Tyvek foil. The water volume offers a shielding of ≥ 3 m to reduce the gamma and fast neutron background from the surrounding rock. Additionally, the water volume is instrumented with 12 20-inch Hamamatsu PMTs to detect Cherenkov photons from muons in the volume between the steel frame with the optical separation and the steel tank. This allows for an active suppression of background signals from muon induced isotopes and neutrons in the scintillator volume. To increase the shielding from external upgoing gamma photons, the steel tank is erected on 3 layers of steel plates (~ 14 cm) to reject background from the rock and concrete below the detector [124].

In order to monitor the liquid scintillator properties and the PMT performance and to interpret the detected signals, two independent calibration systems are installed in the detector system. A laser calibration system is used for timing and charge calibration of the two PMT systems. Therefore, the beam of a pico-second laser is coupled into a fiber system, which distributes the light to 24 diffusor capsules that are mounted at the steel frame. Their broad light emission and the sufficient distance to the PMTs on the opposite side of the frame allows to calibrate multiple PMTs with a single diffusor. The diffusor positions are optimized to reach roughly similar illumination for all PMTs. This was verified using the simulation framework. The second calibration system is the Automated Calibration Unit (ACU), a source insertion system located on the top of the detector at a distance of 1.2 m to the central detector axis. It is used to deploy radioactive sources and an LED light source directly into the liquid scintillator volume. The radioactive sources (one carries a probe with ^{137}Cs, ^{65}Zn and ^{60}Co isotopes, the other with ^{40}K) are used to calibrate the energy scale of the detector and to monitor the properties of the liquid scintillator material. The LED system serves as an additional source for the PMT charge and time calibration. The source positions of the ACU, but also the detector in general can be observed with a CCD system installed on the steel frame [124].

Operation modes

The initial filling procedure of the OSIRIS detector foresees the replacement of the air in the acrylic vessel and the water tank with ultrapure nitrogen to remove radioactive contaminants like radon. In the next step, both volumes are filled with ultrapure water to prevent damages from hydrostatic pressure differences. In the final step, the acrylic vessel is filled with liquid scintillator from the top replacing the water.

During regular operation, the liquid handling system is designed to replace the liquid scintillator with a new batch without emptying the system. During filling of the JUNO central detector, OSIRIS will be operated in **continuous mode**, where liquid scintillator is filled continuously from the top at an increased temperature and drained at the bottom. A temperature gradient inside the acrylic vessel, induced by a flow of cold water in the steel

Table 5.3: Expected external radioactive contamination of the major OSIRIS components. The values are based on internal measurements in the JUNO collaboration. The resulting gamma flux is based on secular equilibrium. The gamma rate in the target (last column) is determined with the OSIRIS simulation framework. The values are taken from [120] with adaptions for the PMTs, to include the additional gamma flux from the magnetic shielding.

Detector component	Contamination level ^{40}K (Bq/kg)	^{232}Th (Bq/kg)	^{238}U (Bq/kg)	Total mass (kg)	Emitted gammas (s^{-}1)	Rate in target (s^{-}1)
Acrylics	2.7×10^{-4}	4.0×10^{-6}	1.2×10^{-5}	1.53×10^{3}	0.12	7.40×10^{-2}
Water	1.6×10^{-6}	3.0×10^{-7}	3.0×10^{-7}	5.41×10^{5}	1.23	8.40×10^{-3}
PMTs	2.12	1.75	4.82	8.62×10^{2}	18.7×10^{3}	2.19
Steel frame	2.7×10^{-1}	1.6×10^{-1}	2.4×10^{-2}	2.90×10^{3}	2.16×10^{3}	2.37×10^{-2}
Optical sep.	1.06	4.5×10^{-2}	9.7×10^{-2}	30	32.3	5.63×10^{-3}
Tank	2.6×10^{-1}	4.0×10^{-2}	7.0×10^{-2}	1.20×10^{4}	4.44×10^{2}	3.70×10^{-5}
Rock	220	123	142	6.20×10^{5}	5.82×10^{8}	3.75

tank, prevents mixing of old and new scintillator liquid. The exchange rate of $\sim 1\,\mathrm{t}$ per hour allows to monitor $\sim 15\,\%$ of the total liquid scintillator filled into the acrylic sphere of JUNO. In the case of a detection of increased contamination the JUNO filling process can be stopped without delay times.

During the commissioning phase of the purification plants, OSIRIS will be operated in **batch mode**, where the unchanged target volume will be observed for up to several weeks in order to reach the design-level sensitivity for ^{238}U and ^{232}Th contamination. In comparison, the sensitivity in continuous mode is lower than in batch mode, but still approaches the IBD level and allows the uninterrupted monitoring of the purification plants [124].

5.3 Signal and background

The selection of BiPo coincidence signals among the acquired detector data is based on four consecutive cuts: the fiducial volume cut, energy cuts on the two independent energy depositions of the BiPo signals and the cut on the time difference and distance between the two signals. More details and the chosen cut windows are described in section 7.2.1.

Gamma photons

The sensitivity of OSIRIS to determine the contamination of U/Th chain isotopes in the liquid scintillator is driven by the rate of background events, which imitate the coincidence signal. Assuming solar contamination levels, the expected BiPo rate is in the order of $\sim 1\,\mathrm{cpd}$. The main background in the OSIRIS detector is induced by random coincidences of uncorrelated gammas, which pass the coincidence cuts. The decay of both, external and internal radioactive isotopes contribute to the rate of energy depositing events in the detector. External background is dominated by gamma photons from ^{40}K and isotopes of the ^{232}Th and ^{238}U decay chains in the surrounding rock volume and the PMT glass. Internal background consists of the decay of isotopes from the uranium and thorium decay chains, other than bismuth and polonium, and contaminations with ^{40}K and ^{85}Kr. The expected contamination levels and rates of gamma photons in the liquid scintillator are listed in the tables 5.3 and 5.4, which show that external gamma background from the surrounding rock volume and the PMTs is dominant.

Table 5.4: Expected internal radioactive contamination and rate in the liquid scintillator from internal impurities. Based on insights from BOREXINO [127], the rates of ^{85}Kr, ^{210}Bi and ^{210}Po are increased by a factor of ten. From [120].

Isotope	Contamination	Rate in target (s^{-1})
^{40}K	1×10^{-17} g/g	4.7×10^{-5}
^{232}Th	1×10^{-16} g/g	7.4×10^{-6}
^{238}U	1×10^{-16} g/g	2.3×10^{-5}
^{85}Kr	3.12 cpd/t	6.6×10^{-4}
^{210}Bi	4.1 cpd/t	8.7×10^{-4}
^{210}Po	8×10^{2} cpd/t	1.7×10^{-1}

One further significant background source is based on the radon emanation into the water shield. ^{220}Rn from the thorium decay chain and ^{222}Rn from the uranium decay chain can emanate from all materials in the direct environment into the water and, due to convection, be transported close to the acrylic vessel and thus overcome the shielding. Assuming the worst case scenario with high radon contamination, its contribution to the gamma background is in the same range as from the surrounding rock and the PMTs, making it one of the dominant background sources with an estimated rate of ~ 3.5 gamma photons per second in the target volume. The resulting energy spectrum of gamma photons in the target volume is depicted in figure 7.12.

Cosmogenic isotopes

Due to the underground placement of the OSIRIS detector with 700 m of rock overburden, the muon flux and corresponding cosmogenic isotope production is reduced significantly. For the purpose of this work, the expected cosmogenic isotope production rates were calculated (see table 5.5). A similar list for JUNO is in [30]. The rates are the result of simulations with the OSIRIS simulation framework. 10^7 muon events in the entire detector volume were simulated, which corresponds to a measurement time of ~ 300 days. The production of secondary particles is based on the *QGSP_BERT_HP* physics list (more details in section 6.1.3), which allows comparison with other experiments (see section 7.1.3). The production rates are listed for isotopes produced in the liquid scintillator volume and do not contain e.g. neutrons which are produced outside the target volume and traverse into the acrylic vessel. The comparison with the results of the FLUKA simulation for JUNO in [30] show good agreement. With decay branches containing the emission of an electron and a neutron, ^{8}He and ^{9}Li are capable to imitate the BiPo signatures and require a dedicated veto system and strategy (see chapters 7 and 8). The other cosmogenic isotopes contain single decays and multi-particle decays, which however do not pass the BiPo coincidence cuts. Although they can deposit energy in the target volume, they are mostly negligible with respect to the sensitivity studies, as their production rates and decay times are very small compared to the signals of external gamma photons. For the sensitivity analyses in [120], only ^{10}C, ^{11}C and ^{14}C are considered, but still have a subordinate impact compared to gammas. The application of a muon veto, further reduces the background rates from short-lived (≤ 1 s) cosmogenic isotopes by up to 96 %, depending on the final veto strategy and the muon veto trigger.

In [128], additionally the neutron production from muons in the surrounding rock was investigated. As the muons do not pass the water volume, they can not be registered by the veto system. Still, the secondary neutrons can enter the target volume and be captured at a hydrogen or carbon atom. In the analyses, the simulation volume was extended to include the underground liquid scintillator hall and an increased rock volume

Table 5.5: Estimated production rate of cosmogenic isotopes in the OSIRIS target volume, derived from geant4 particle simulations based on the *QGSP_BERT_HP* physics list. The rate of neutrons is restricted to the production in the liquid scintillator. External neutrons entering the acrylic vessel are considered in chapter 7. The comparison with the FLUKA simulations in [30] for JUNO show good agreement. The Q values and half-lives are taken from [30].

Isotope	Q(MeV) and decay mode	$T_{1/2}$	Rate (per day)
^{3}H	0.0186 (β^-)	12.31 a	7.550
^{6}He	3.508 (β^-)	0.807 s	0.640
^{7}Be	$Q_{EC} = 0.862$ (10.4 % $\gamma, E_\gamma = 0.478$)	53.22 d	1.550
^{8}He	10.66 ($\beta^-\gamma$: 84 %), 8.63 ($\beta^- n$: 16 %)	0.119 s	0.013
^{8}Li	16.0 (β^-)	0.839 s	0.785
^{8}B	16.6 (β^+)	0.77 s	0.152
^{9}Li	13.6 (β^-: 49 %), 11.94 ($\beta^- n$: 51 %)	0.178 s	0.286
^{9}C	15.47 ($\beta^+ p$: 61.6 %), 8.63 ($\beta^+\alpha$: 38.4 %)	0.126 s	0.067
^{10}Be	0.556 (β^-)	1.5×10^6 a	2.332
^{10}C	2.626 ($\beta^+\gamma$)	19.29 s	1.021
^{11}Li	20.55 ($\beta^- n$: 83 %), ($\beta^- 2n$: 4.1 %)	0.008 75 s	< 0.003
^{11}Be	11.51 ($\beta^-\gamma$: 96.9 %), 2.85 ($\beta^-\alpha$: 3.1 %)	13.76 s	0.023
^{11}C	0.96 (β^+)	20.36 min	9.647
^{12}Be	11.708 ($\beta^-\gamma$: 99.5 %), ($\beta^- n$: 0.5 %)	0.0215 s	0.007
^{12}B	13.37 ($\beta^-\gamma$)	0.0202 s	0.660
^{12}N	16.316 ($\beta^+\gamma$)	0.011 s	0.074
^{13}B	13.437 ($\beta^-\gamma$)	0.0174 s	0.010
^{13}N	1.198 (β^+)	9.965 min	< 0.003
^{14}B	20.644 ($\beta^-\gamma$: 93.9 %), ($\beta^- n$: 6.1 %)	0.0126 s	< 0.003
^{14}C	0.156 (β^-)	5730 a	0.013
^{15}C	9.772 (β^-)	2.449 s	< 0.003
^{16}C	8.010 ($\beta^- n$)	0.747 s	< 0.003
^{16}N	10.42 ($\beta^-\gamma$)	7.13 s	< 0.003
^{17}N	8.680 ($\beta^-\gamma$: 5 %), 4.536 ($\beta^- n$: 95 %)	4.173 s	< 0.003
^{18}N	13.896 ($\beta^-\gamma$: 93 %), 5.851 ($\beta^- n$: 7 %)	0.62 s	< 0.003
Neutrons			326.31

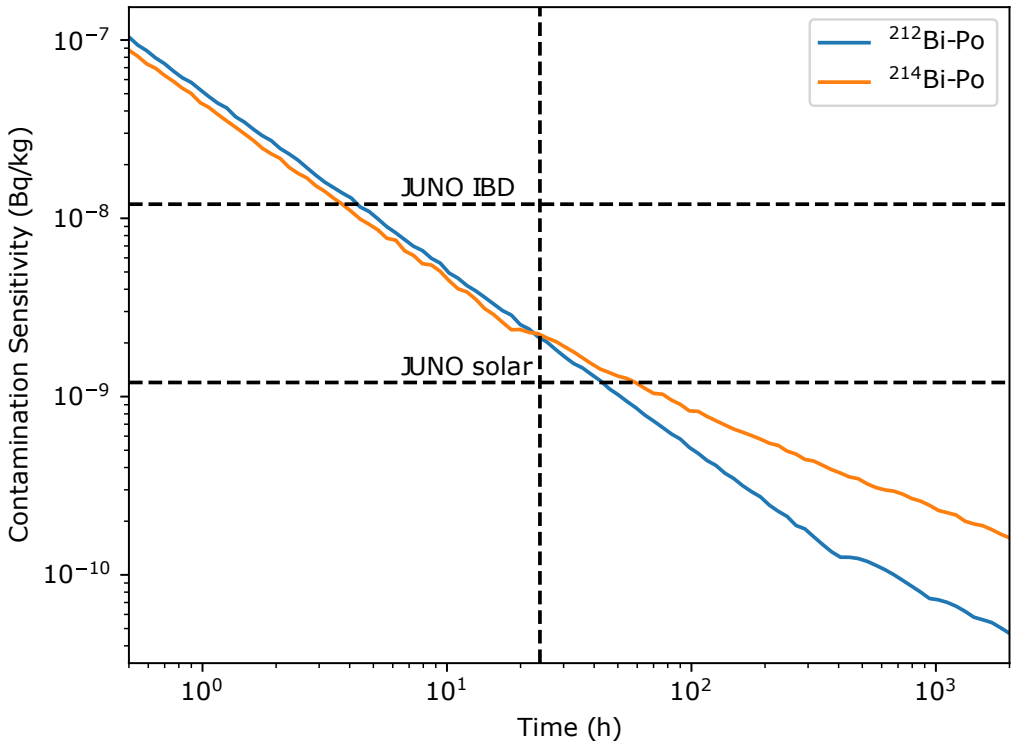

Figure 5.3: Sensitivity of OSIRIS to the ^{238}U (orange) and ^{232}Th (blue) contamination of the liquid scintillator depending on the measurement time. While the IBD limit requires a measurement time of several hours per scintillator batch, the limits for the solar physics program of JUNO requires several days. The vertical dashed line represents 24 h of measurement time. From [124].

with a minimum thickness of 10 m. The expected neutron rate in the target volume, based on simulations, is 4.7 per day resulting in $\sim$ 4 captures per day. Compared to the single gamma rates in the liquid scintillator, this background is also negligible for the sensitivity studies.

5.4 Sensitivity

The sensitivity of OSIRIS to a contamination of U/Th decay chain isotopes in the scintillator material is derived from the rate of the respective BiPo decay signals for which the coincidence rate $\dot{n}_{BiPo}$ exceeds fluctuations of accidental background coincidences $\dot{n}_{BG}$ on a 90 % confidence level. It depends on the total number of detected events n in a defined time interval T [124]:

$$n(T) = (\dot{n}_{BiPo} + \dot{n}_{BG}) \cdot T. \tag{5.1}$$

For short measurement times, the low signal rate inhibits Gaussian approximations and requires sophisticated methods to define sensitivity limits. The application of Feldman-Cousins limits tailored to the conditions in the OSIRIS experiment are described in [120]. The resulting OSIRIS sensitivity, in dependence of the measurement time, is depicted in figure 5.3.

With the assumption of secular equilibrium for the U/Th decay chains, the measured BiPo coincidence rate n_{BiPo} corresponds to the decay rate of U/Th decay chains elements and

can be directly translated to mass limits, as calculated in table 5.2. As shown by the sensitivity curves, the radiopurity level for the IBD physics program can be verified within several hours, however the solar contamination limits require a measurement time of more than one day. This general estimate of the sensitivity must be adapted to the conditions of the two operation modes, which are foreseen for OSIRIS: batch mode and continuous mode.

Batch mode

In the batch mode operation, the presence of correlated backgrounds, e.g. radon (^{220}Rn with $T_{1/2} = 55.6\,\mathrm{s}$ and ^{222}Rn with $T_{1/2} = 3.8\,\mathrm{d}$ [123]) contamination in the liquid scintillator, emanating from steel surfaces in contact with the scintillator material in the filling and purification line, must be considered additionally. The contamination with relatively short-lived Rn isotopes is not in secular equilibrium with the U/Th decay chains and has no impact on the JUNO physics program, but adds an additional source for BiPo signals in the OSIRIS detector. From estimations and measurements, the expected added signal rate from radon emanation sums up to $130 - 830$ BiPo signals per day for a fresh batch of liquid scintillator in the acrylic vessel [124]. The number of decays from additional radon will decrease exponentially, while the BiPo signal rate from U/Th decay chain contamination stays constant. By applying a time dependent fit, the upper limits on the OSIRIS sensitivity (90 % C.L.) can be derived from the fit uncertainty. To set an upper limit on the ^{238}U (^{232}Th) contamination in the scintillator, an expected measurement time of 7 (2.5) days is required to achieve the IBD sensitivity level, and 22 (6) days to achieve the solar sensitivity level for an initial radon contamination corresponding to 130 cpd [124].

Continuous mode

In order to get a handle on the additional radon background in the continuous mode, it is important to prevent mixing of the newly added scintillator with the material already in the acrylic vessel. Thereby, in combination with the relatively slow flow rate of $\sim 1\,\mathrm{m}^3/\mathrm{h}$, the BiPo signals from emanated radon decreases along the z-axis by 17 % (80 %) for ^{222}Rn (^{220}Rn). Similar to the analysis for the batch mode, the sensitivity limits at 90 % confidence level are $1.0 \times 10^{-15}\,\mathrm{g/g}$ ($3.0 \times 10^{-15}\,\mathrm{g/g}$) for ^{238}U (^{232}Th) in the ideal case. Thus, the continuous mode can not only raise an alert in the case of a malfunction in the scintillator filling and purification line, but also verify the IBD level contamination requirements continuously [124].

6. The OSIRIS simulation framework

In the design process of the OSIRIS experiment, the several detector components must be attuned to each other and the scientific goals. The dimensions of detector volumes, the positioning of the PMTs and the applicability of materials and surfaces must be planned carefully, as there will be no prior test setup of the detector before it is installed in the JUNO facility and after the installation, major changes of the design are aggravated. To ensure an operational detector design, but also to develop analysis and reconstruction algorithms in advance, the application of Monte Carlo simulations is indispensable. The foundations of the OSIRIS simulation framework were set by Paul Hackspacher, Sebastian Lorenz (both Johannes Gutenberg-Universität Mainz) and Christoph Genster (RWTH Aachen University) and further developed within the scope of this thesis. In the following chapter, the basic implementation of the simulation framework and the adatptions and developments with respect to the following chapters are described (section 6.1). These include alterations and refinements in the detector geometry and mateiral database, the description of the physics processes and the structure of the framework. Besides the main simulation framework, the muon event generator, which was newly developed within the context of this thesis, is described in detail with the underlying input data, the realistic event generation and the resulting expected muon flux in the OSIRIS detector (section 6.2).

6.1 Implementation of the OSIRIS experiment

In order to provide a unified simulation environment, the OSIRIS simulation framework was established, a singlethreaded C++ framework based on the simulation library Geant4, the analysis framework ROOT and the class library CLHEP. It is independent of the JUNO simulation framework, but shares parameters and definitions. To allow the parallel work of multiple developers, the code base is organized in a GitLab repository. The development of the OSIRIS detector regarding mechanical design, material selection, PMTs, calibration source positioning and background and sensitivity analyses are fully based on the simulation framework. For that reason, the simulation software is separated in different operation modes, which are specialized for certain tasks and thus have different input and output formats, constrained physics processes, or unique but very effective simulation methods (for details see section 6.1.4). The geometry and the description of physical processes and particle definitions are independent of the chosen mode.

6.1.1 Underlying software packages

The OSIRIS simulation framework combines simulation and data processing programs which are already established and well-tested in particle physics experiments. The OSIRIS framework is based on the Geant4 simulation framework and uses its program structure. ROOT and CLHEP classes and methods are applied mainly in the data output and the description of physical processes.

Geant4

Geant4 is a C++-based, object-oriented toolkit to simulate the interplay of particles and matter, used to design and develop and analyze data of physics experiments. It allows the definition of the detector geometry, the tracking of particles and physical processes, covering electromagnetic, hadronic and optical interactions. A variety of particles is available and can be set as primary particles with arbitrary starting conditions as the initial input of a simulation event. The definition of the geometrical structure, in which the physical processes take place, is realized via the arrangement of simple geometrical bodies, like boxes, tubes etc. These objects can be assigned with physical properties, such as the atomic composition of the material and the optical properties of surfaces and solids. With this initial conditions being set, each particle of the event, primary or secondary, is simulated separately until at least one user defined termination criteria is fulfilled. The propagation and validation of one particle is called track, which is divided into steps, the smallest unit of the particle transportation. At each step, the physics processes are evaluated and the simulation is adapted. By the definition of sensitive detector components, the detection of particles can be simulated and thus the generation of realistic event data. Due to the tight concatenation with ROOT, the scientific software toolkit of the European Organization for Nuclear Research (CERN) [97], the simulation data can be stored in a organized and user friendly data format [99].

ROOT

ROOT is a multi-platform C++-software framework designed for the demanding requirements in the data analysis of particle physics experiments. Mainly designed for the large data stream at the Large Hadron Collider, its basic and accessible implementation allows also other experiments to benefit. The vertically arranged ROOT data format is suitable for both, simulation and data taking and ensures the secure allocation of physical properties to the events and optimized access for statistical data analysis. Additionally, it offers a variety of implemented analysis and fitting methods and an advanced user interface to access the data conveniently [97].

CLHEP

CLHEP stands for Class Library in High Energy Physics and is a collection of C++-classes specialized for the data generation and analysis in high energy physics. The main goal is to provide basic methods and elements used in simulation and analysis frameworks with the goal to save development work and ensure comparability due to a common software basis. CLHEP is deeply incorporated in Geant4 and ROOT, but is also accessed directly in the OSIRIS simulation framework [98].

6.1.2 Implementation of the OSIRIS geometry

All design and material studies for the OSIRIS detector layout are based on simulations with the framework. To provide the same geometry to all developers, the current target detector design is implemented into the software framework as explicitly as possible. The

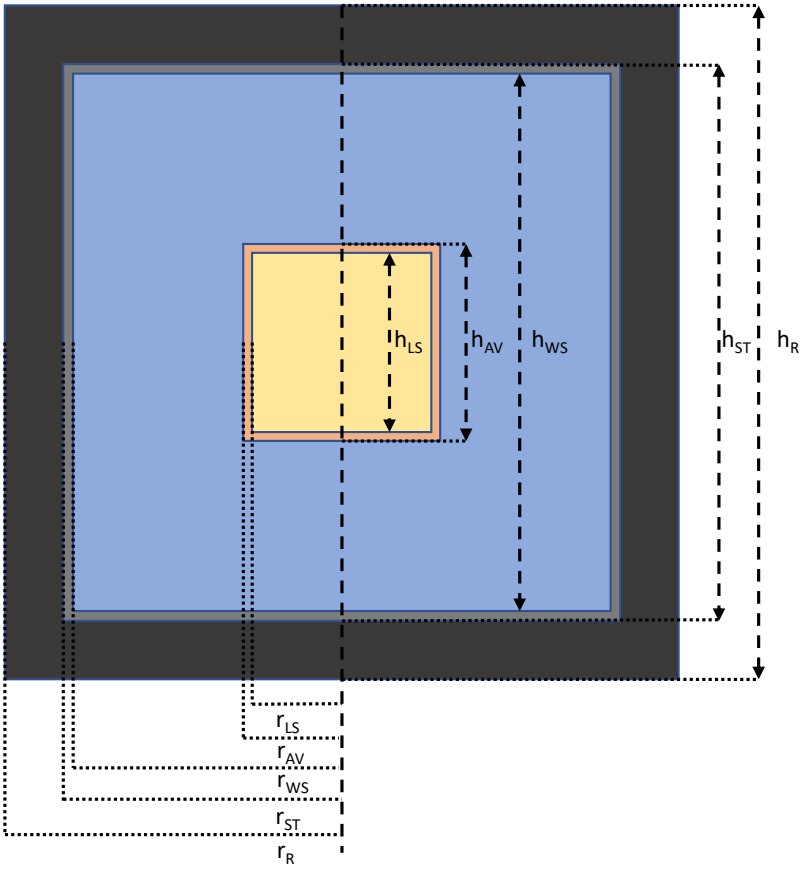

Figure 6.1: Schematic drawing of the OSIRIS detector geometry defining the alignment and dimensions of the main volumes. The thickness of the acrylic vessel and the steel tank are increased for reasons of visibility. The values of the dimensions of the implemented geometry are shown in table 6.1.

two main parameters which specify the geometry of the detector are the aimed sensitivity of OSIRIS, which defines the size of the sensitive detector volume and the available space in the underground Scintillator Hall of the JUNO facility. In the simulation, the main volumes are concentrically arranged cylinders where the dimensions of the scintillator volume and the containing steel tank define the dimensions of the further volumes. The scintillator volume is contained by an acrylic vessel with a thickness that adds up to the dimensions of the scintillator volume and thus defines its dimensions. In contrast, the measures of the surrounding water volume, in the simulations called *shield*, are defined by the inner radius and height of the steel tank. Outside of the steel tank, a rock volume is defined which is directly connected to the tank and is one of the source volumes for simulated external γ-radiation. Its dimensions are defined by the outer radius and height of the steel tank and the containing world volume which is compulsory for Geant4 simulations and defines the maximum limits of the simulation geometry. The conditional definition of the volume dimensions allows their convenient variation to analyze different settings, without the necessity to change the dimensions of each volume separately. The schematic description and the exact dimensions of the main volumes are shown in figure 6.1 and table 6.1.

In order to achieve simulation results comparable to real measurement results, the implemented geometry must approximate the experiment design as precisely as possible. In the case of the acrylic vessel (figure 6.2), additional acrylic pipes, for in- and outlet of the scintillator, the calibration with the auxilliary calibration unit (ACU) and the liquid level measurement are implemented. Since the pipes are partially defined outside the vessel,

Table 6.1: Dimensions of the main components of the OSIRIS detector. The acrylic vessel and the steel tank are actual detector components, whereas the other volumes are liquids or solids, defined by these geometries. Therefore, only the two have a defined thickness. A schematic visualization is shown in figure 6.1

Volume name	Height (mm)	Radius (mm)	Thickness (mm)
Liquid scintillator (LS)	3000	1500	-
Acrylic vessel (AV)	3060	1530	30
Water shield (WS)	8988	4494	-
Steel tank (ST)	9000	4500	6
Rock (R)	10200	5100	-

additional sub-volumes are implemented and associated with the material definition of the liquid scintillator, to simulate "filled" pipes. This detail has a noticeable impact on the simulation of background and calibration simulations and must not be neglected. To ensure the mechanical stability of the acrylic vessel during its transport, the setup and in operation, acrylic stiffeners on the top and the bottom of the tank are applied. To increase the distance of the acrylic tank, and thus the sensitive volume, to eventually radioactively contaminated materials, the acrylic stiffeners on the bottom are longer than on the top. At the end of the in- and outlet pipes inside the vessel, acrylic diffusor plates are installed to force a homogeneous mixing of the liquid scintillator. They are also included in the simulation geometry, mainly to study the impact on optical photons due to reflections and refraction.

In the simulations the photo detection is emulated via the implementation of geometries representing PMTs, equipped with sensitive areas. The placement of these PMTs in the experiment is realized via the mounting to a holding structure which is planned to be a stainless steel frame (see figure 6.3). In the simulations, the frame is modeled explicitly, according to the currently planned design, which allows the study of optical shadowing and reflection effects on the detection of scintillation light, but also detailed background analyses concerning radioactive contamination in the steel material. As discussed in chapter 8, the steel frame is also used to mount the optical separation foils, which are required to prevent false signals in either of the PMT systems. Furthermore, they reduce the reflection of scintillation photons at the surface of the steel tank and increase the detection efficiency of the muon veto system.

The central detector PMT system

The optical model of the OSIRIS framework is implemented explicitly and aims to reproduce the photon production of the actual experiment. In order to emulate the realistic detector behavior and event reconstruction, the PMT model is implemented extensively (see figure 6.4). Its simplified geometrical model consists of two concentric ellipsoids and a cylinder. The inner ellipsoid is implemented as a vacuum volume, while the outer one, and the cylindrical volume are associated to boron silicate, the glass material of the PMTs. The photo detection is emulated via the implementation of a sensitive, partial ellipsoid volume, aligned to the surface of the outer ellipsoid of the PMT model in the simulation according to the photocathode of the real PMT. In order to simulate the photon detection efficiency of the real PMTs, a wavelength dependent detection efficiency for the sensitive photocathode volume and reflection values for the glass material are stored in the OSIRIS material table of the simulation framework. The implementation of a sensitive volume allows to rise a flag in the simulation whenever a photon enters it so the ID of the detecting PMT and the detection time can be saved. In contrast to the Monte Carlo truth

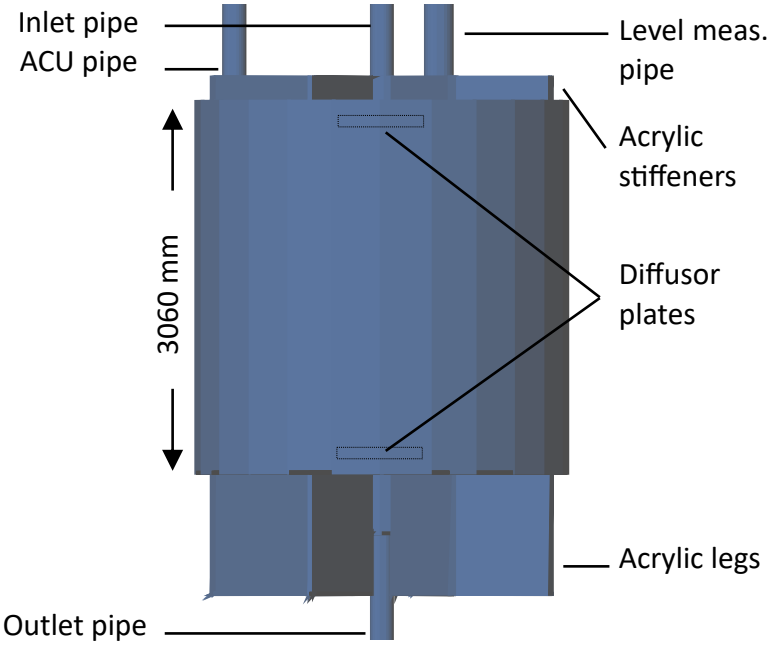

Figure 6.2: Detailed illustration of the acrylic components of the OSIRIS detector. The internal diffusor plates are indicated with dashed lines.

information, where the standard ROOT data structure is used, the storage of the photon hits is realized with a custom data format that facilitates the unsophisticated processing, e.g. the data analysis or the position and energy reconstruction. Therefore a standard C++ vector with the size of the number of implemented PMTs is initialized. Each of these elements is again a standard vector, but without predefined size. Whenever a hit is registered, the hit time is appended to the vector, with the index according to the ID of the PMT. This two-dimensional vector is written as custom structure to the ROOT output file.

In order to provide a magnetic shielding of the PMT in the experiment, it is partially incorporated in a Mu-metal housing. It is currently under design and construction at the JINR [1] in Dubna. The final layout is not yet finalized, but since the dimensions of the shielding have a massive influence on the detector performance, a rudimentary model of the planned magnetic shielding is implemented in the simulation framework. As shown in figure 6.4, the shielding consists of two hollow truncated cones and a back plate to close the entire volume and to keep out reflected light. Currently the thickness of the shield geometries is defined with 2 mm and the entire body is assigned with the already implemented stainless steel model as material. To increase the light collection, despite the reduced field of view caused by the shielding, the inner surface of the front cone part will be painted with a highly reflective color, which is also implemented in the simulation. Here, also the exact values and behavior is not known yet, so the optical model is defined with a solely diffuse reflective characterization and a wavelength independent reflection value of $R_b = 0.8$. In contrast, the outside of the metallic shield is defined with a diffuse reflection value of $R_w = 0.05$, which corresponds to a flat black painting, that is anticipated for the final design. Aside from the color, the length of the front cone of the shield compared to the tip of the PMT has a big impact on both, the magnetic shielding capability and the light detection efficiency. While a larger excess length improves the shielding and allows to omit a metallic mesh in front of the PMT, the field of view is increasingly reduced in

[1] Joint Institute for Nuclear Research

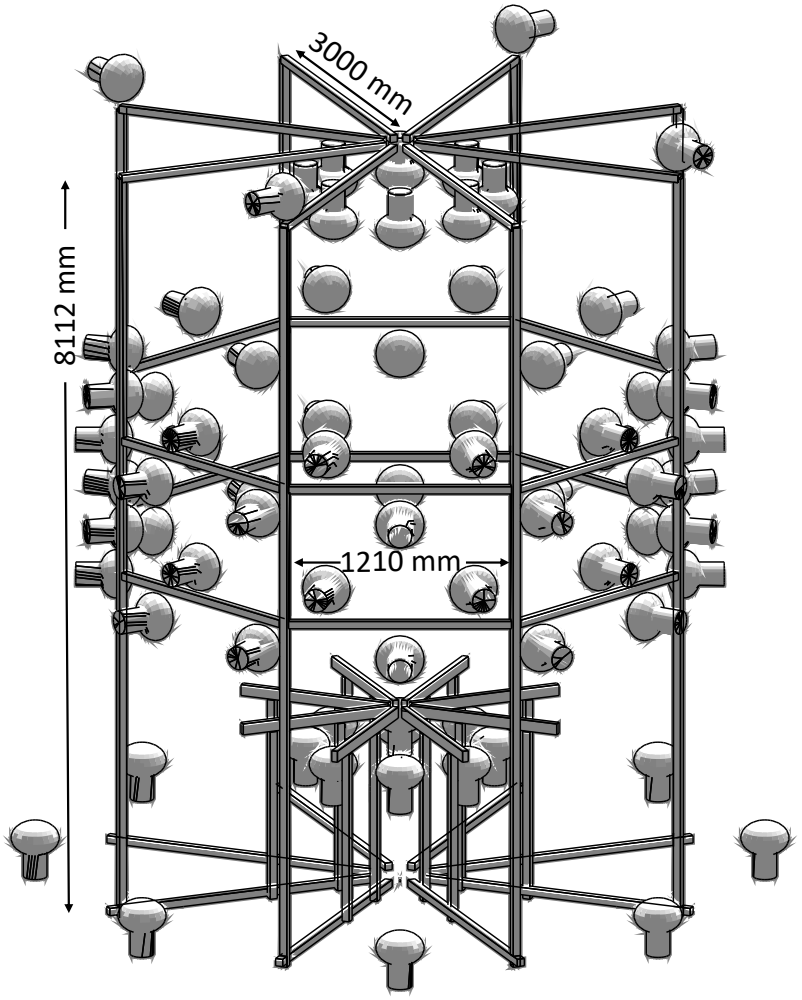

Figure 6.3: Detailed illustration of the stainless steel frame of the OSIRIS detector and the central and veto PMTs. The minimum distance between two opposite central detector PMTs (horizontal and vertical) is 5.66 m The bottom veto PMTs are place 10 cm above the the ground plate of the steel tank.

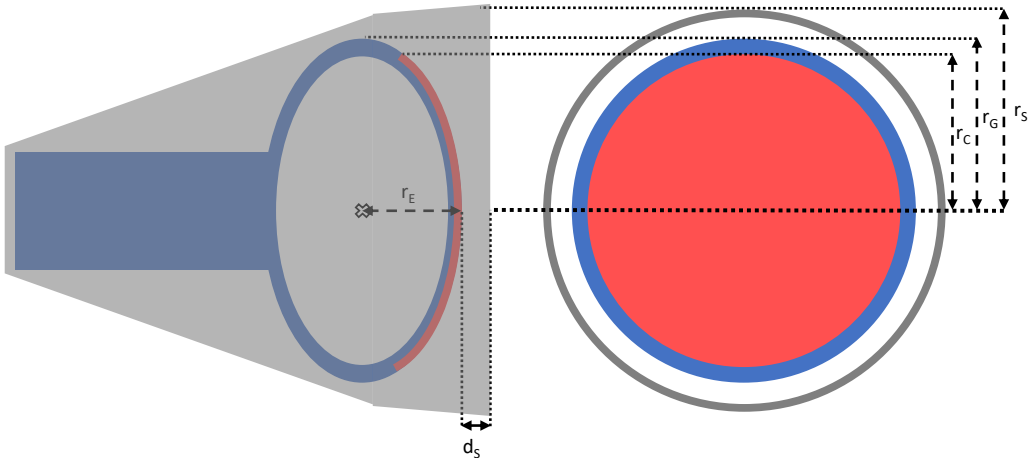

Figure 6.4: Schematic illustration of the OSIRIS simulation PMT model. The model consists of two concentric ellipsoids, representing the inner vacuum volume (left figure, white) and the outer glass volume, and a cylinder representing the PMT glass body (blue). On the front surface, an additional partial ellipsoid is implemented which is defined as a sensitive volume to represent the function of the photo cathode (red). Additionally, the model of the PMT magnetic shielding is overlaid, which is defined as a combination of two metallic truncated cones and an end cap to close the rear of the volume. The excess length of the shield compared to the tip of the PMT is adjustable in the simulations and object of sensitivity studies. Currently it is set to $d_S = 50\,\text{mm}$. The further dimensions of the implemented model are given in table 6.2.

size and thus the number of detected photons. To find the optimum setting, the excess length of the shield is implemented variably and can be set individually. The influence of the shield length on the light detection efficiency was analyzed for several settings and led to the result that a surplus of $d_S = 50\,\text{mm}$ results in a reasonable trade-off, where the magnetic shielding of the PMT is accomplished without the additional metallic mesh and enough light from events in the liquid scintillator volume is detectable to ensure a sufficient energy resolution.

As indicated in table 6.2, two scenarios for the OSIRIS detector geometry with respect to the used PMT model were originally under consideration. Initially it was planned to reuse 110 of the 10 inch PMTs Hamamatsu R7081 from the Double Chooz experiment, which was not possible, since the time plans of OSIRIS and the deconstruction of the Double Chooz experiment could not be brought in line. For that reason it was decided to utilize a PMT type, which is also used in the JUNO experiment, the R12860HQE from Hamamatsu. In order to compare former simulation results on background and sensitivity studies, both simplified models (see figure 6.4 and table 6.2) are implemented in the simulation framework.

Table 6.2: Dimensions of the two implemented PMT models. A schematic visualization is shown in figure 6.4.

Parameter	abbr.	HamR12860HQE (20”)	HamR7081 (10”)
Major half axis of the ellipsoid	r_G	254 mm	127 mm
Minor half axis of the ellipsoid	r_E	179 mm	60 mm
Projected cathode radius	r_C	230 mm	110 mm
Magnetic shield radius	r_S	282 mm	137 mm

In the OSIRIS simulation framework, PMTs are organized in sub-systems to set special preferences and attributes for different use cases, but also to allow an effective and distinct data production e.g. PMTs in the central detector system and in the veto system (see chapter 8). In the current version of the framework, the first sub-system contains all PMTs that observe the liquid scintillator volume. They are arranged in 4 rings with respectively 12 vertically placed PMTs and two rings with 8 PMTs each, above and below the acrylic vessel, as shown in figure 6.3. While the angular positions of the PMTs are fixed, the distance between the photo cathode and the surface of the acrylic vessel is adjustable. This parameter determines the covered solid angle on the one hand and the amount of background introduced by the PMTs (see chapter 5.3) on the other hand. The currently design value is $d_{PMT} = 1.3\,\mathrm{m}$, which leads to an energy resolution of $6.0\,\%/\sqrt{E(MeV)}$. The implementation of the steel frame is designed variably, so the geometry parameters are automatically adapted to the placement of the PMTs.

6.1.3 Implementation of the physical properties

Besides the geometry of the entire experiment, the physical particles and processes are also defined independently from the used simulation mode to provide comparable results. Nevertheless, it can be beneficial for some simulation scenarios to deactivate specific processes to improve the performance of the simulation framework. Therefore, and for the sake of clarity and expandibility, the "OSIRIS physics list", an inherited class from the Geant4 *G4VUserPhysicsList*, is structured modularly. A basic distinction is made between the definition of particles (baryons, bosons, ions, leptons and mesons) and the physical processes (decays, electromagnetic interactions, the behavior of optical photons and the physical processes for hadrons), for which both standard Geant4 classes are available that contain the relevant information. Additionally it is possible to extend and manipulate the processes to match the conditions of the simulated experiment. In the case of the OSIRIS framework, modifications were made for the optical model including the scintillation process and the transportation and capture of thermalized neutrons . Besides these internal adjustments, the input data for the Geant4 decay model was modified as well, to allow the realistic simulation of the decay of cosmogenic isotopes [118].

The optical model

The optical model describes the part of the physics list, which defines the propagation and the physical processes of photons in the optical wavelength regime. Since the detection of physical events in the OSIRIS and also JUNO detector is based on the detection of photons, generated by these events in the scintillator, but also in water via the Cherenkov effect, the exact description of optical properties is decisive for the quality and comparability of the simulation results. The Geant4 simulation framework provides several standard processes specifically tailored for optical processes, which are directly adopted to the OSIRIS physics list, such as Rayleigh scattering, Mie scattering, the light production via the Cherenkov effect and boundary processes. To activate the effects, the classes are called in the physics list. At each step of a particle track, the probabilities for all physical processes are evaluated and deployed depending on the energy and the material. In the case of optical photons, the refractive index of the traversed material, (of the two materials at a transition) defines the particle propagation. These values, but also the values for absorption and scattering are defined for each material in the code, accordingly to the material specifications from the JUNO simulation framework. Besides that, the reflectivity of surfaces can be defined explicitly, which allows a more detailed description of the reflective behavior.

Most of the implemented processes meet the requirements of the OSIRIS physics model, in terms of precision and integrity and are directly called in the physics list. As opposed to

this, the Geant4 models for the re-emission of photons after their absorption by a molecule and the scintillation process itself are not described explicitly enough and are implemented in custom classes, which are also callable in the physics list.

Re-emission of optical photons

Although the absorption of photons is implemented properly in Geant4, the possibility for a subsequent re-emission, which has a major effect on the optical behavior of the scintillator and thus the sensitivity, is not given in the simulation by default. To allow this physical process, the OSIRIS custom class *OSIRISOpAbsReemission*, which extends the Geant4 absorption class is implemented and callable in the physics list. It calculates the probability to re-emit a photon, after it was absorbed by a molecule in the current simulation step, based on the photon energy and the material parameters of the current volume. If the case is given, a new photon is generated with a uniformly diced energy (with the maximum at the energy of the absorbed photon), isotropic direction, random polarization and emission time depending on the material specific time constant for re-emission. This photon starts a new track and is propagated accordingly.

Custom scintillation process

To describe the scintillating material of JUNO and OSIRIS, the default scintillation process of the Geant4 simulation framework is not sufficient. It only provides two decay time constants, whereas LAB requires three to be characterized correctly and does not include quenching, an important feature of organic scintillators, which must be implemented for realistic simulation results (see section 3.3).

For that reason, the class *OSIRISScintillation* is implemented which replaces the default Geant4 class. It is callable in the physics list and can be adjusted, regarding the scintillation yield factor (default is 1.0) and whether quenching is activated (default is on). The scintillation class is called whenever a step of a charged particle track ends in a volume, whose associated material is defined as scintillating in its definition. From the deposited energy in the current step and the scintillation yield factor of the material, the mean number of expected scintillation photons is calculated. If quenching is activated this number is calculated in an explicit function which applies Birk's law (see equation 3.1) with a particle specific constant k_B taken into account. The actual number of photons emitted in this step is sampled from a Gaussian distribution with the number of mean photons as expectation value and the number of mean photons as width. If it is smaller than 10, it is sampled from a Poisson distribution. The temporal scintillation spectrum is modeled as the sum of three exponential distributions. For each of the time constants, the associated number of emitted photons is calculated to achieve a realistic distribution and for each a new optical photon particle is created with random direction, polarization, energy (sampled from a given spectrum) and a random emission time depending on the time constant.

Particle physics

As mentioned above, the implementation of particles and physical processes is separated in the OSIRIS physics class. After their definition, the utilized physics processes are allocated to each particle. During the simulation run, the currently tracked particle is then compared to the definitions in the physics list at each step and the allowed processes are calculated and activated. The implemented particles and the allocated Geant4 physics process classes are shown in table 6.3. The majority of the physical processes is implemented without modifications except for the capture and scattering processes of the neutron. Here, the applied process depends on the kinetic energy of the neutron, as well as the data set to which the process class accesses to.

The HEP event mode (see section 6.1.4) can be initialized with an alternative physics list, by calling the keyword at the start of the simulation. This external list is called *QGSP_BERT_HP*, which combines different models for particle generation and transport and which is also used for the production of cosmogenic isotopes in the JUNO simulation framework. Details are given in table 6.4 and section 7.1.3.

Modification of the ^{9}Li and ^{8}He decay schemes in Geant4

As shown in section 7.2.1, the decays of cosmogenic nuclei like ^{9}Li and ^{8}He can mimic the coincidence signal, investigated by OSIRIS and are thus a irreducible background source. To study their production and decay with simulations and the impact on the sensitivity of OSIRIS, their simulation must be as realistic as possible. However, according to [129] which was developed within the JUNO simulation framework the de-excitation of ^{9}Be and ^{8}Li, the daughter nuclei of ^{9}Li and ^{8}He, are not modeled correctly in the current Geant4 versions. In reality, ^{9}Li (^{8}He) atoms decay to excited states of ^{9}Be (^{8}Li) via a β-decay, which subsequently break into a neutron and two α particles or for ^{8}Li, the excited states emit a neutron. However, the current Geant4 decay model describes the processes only with the de-excitation to the ground state via the emission of a gamma photon. Especially the neutron, which generates a delayed signal in the scintillator after the capture, plays a major role in the imitation of the coincidence signal of the searched bismuth and polonium decay. Based on the findings in [129], the decay tables of the Geant4 installation were modified to enable the realistic simulation of the decays and background events. Furthermore, the energy spectra of the initial β-decay of ^{9}Li and ^{8}He are modified due to the added different energy levels of the respective daughter nuclei. Based on the energy level the daughter nucleus is excited to, the energy of the previously emitted β-particle is limited. The resulting β-spectra of ^{9}Li and ^{8}He are thus compositions of the different spectra, as depicted in figure 6.5. The combined distributions (black line) render the visible energy in the OSIRIS detector, extracted from a simulated sample of 10^5 events. Especially the low-energetic sub-spectrum in the ^{9}Li-decay to the highly exited ^{9}Be state at 11 810 MeV has a major impact on the capability to imitate the BiPo coincidence signal, as it falls within the energy window of the bismuth decay search.

6.1.4 Simulation modes

The OSIRIS simulation framework is organized in specific run modes, which are designed for specialized tasks. The most important and newly implemented modes used within this thesis are listed below. More details on the already established modes can be found in [120].

General particle source

The *GeneralPS* mode is the default operation mode of the OSIRIS simulation software. It is based on the Geant4 *G4GeneralParticleSource* class, which allows a variable and versatile, but also user friendly event creation. Via the use of macro commands, the type of the incident particles, the starting volume and direction and the energy distribution can be adjusted. Besides the information on the detection times of the generated photons, the Monte Carlo truth is also saved in the output file. Due to a recent extension of the *GeneralPS* mode, the position and amount of energy deposition can optionally be saved, which enables the user to create response maps of the detector.

HEP event mode

The *HEPEvt* simulation mode initializes events with parameters from a separate HEP (High Energy Physics) file, which is generated via an external physics generator. In the

Table 6.3: Particles implemented in the OSIRIS simulation framework and the allocated standard physical processes, provided by Geant4. Most physical process classes are used without further constraints except for the neutron capture and scattering processes, where different process descriptions and data sets are chosen for the respective energy ranges.

Physical process	Allocated particle	Geant4 physics process class
Electro-magnetic	gamma	G4PhotoElectricEffect G4ComptonScattering G4GammaConversion
	e^-	G4eMultipleScattering G4eIonisation G4eBremsstrahlung
	e^+	G4eMultipleScattering G4eIonisation G4eBremsstrahlung G4eplusAnnihilation
	$\mu^\pm$	G4MuMultipleScattering G4MuIonisation G4MuBremsstrahlung G4MuPairProduction
	proton $\pi^\pm$	G4hMultipleScattering G4hIonisation G4hBremsstrahlung G4hPairProduction
	α ^{3}He	G4hMultipleScattering G4ionIonisation G4NuclearStopping
Hadronic	α	G4HadronElasticProcess
	neutron	G4HadronCaptureProcess $E_{kin} < 20\,\text{MeV}$: G4NeutronRadCapture $E_{kin} > 20\,\text{MeV}$: G4ParticleHPCapture G4HadronElasticProcess $E_{kin} < 4\,\text{eV}$: G4NeutronHPThermalScattering $4\,\text{eV} < E_{kin} < 20\,\text{MeV}$: G4NeutronHPElastic $20\,\text{MeV} < E_{kin}$: G4HadronElastic G4NeutronInelasticProcess $E_{kin} < 19.8\,\text{MeV}$: G4NeutronHPInelastic $19.8\,\text{MeV} < E_{kin} < 10\,\text{GeV}$: G4BinaryCascade
Decay	Bosons Leptons Mesons Baryons	G4DecayPhysics
	Ions	G4RadioactiveDecayPhysics

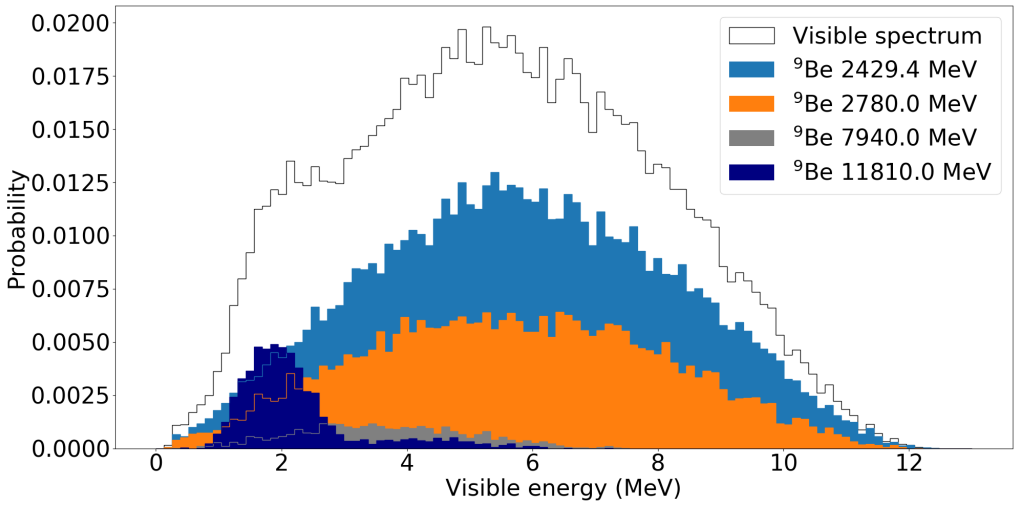

^{9}Li β-decay spectrum

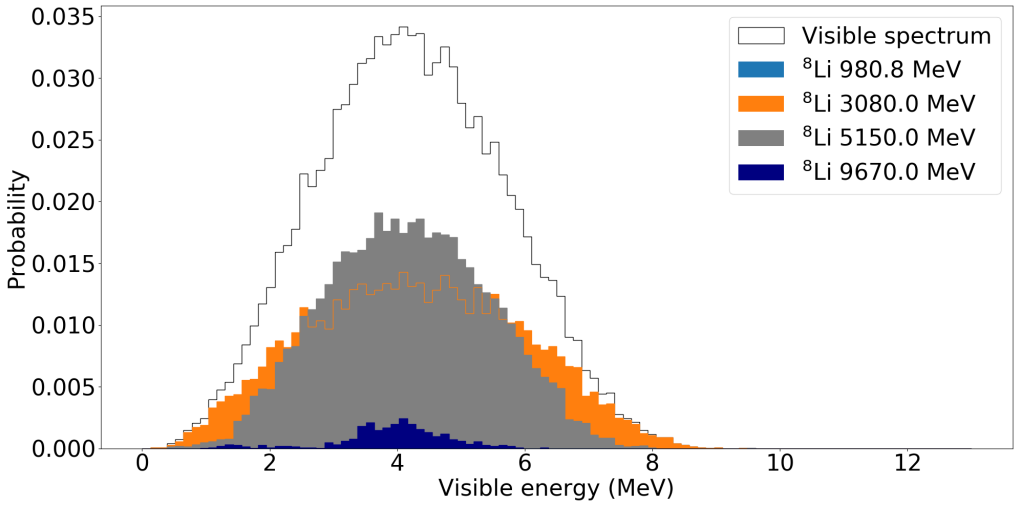

^{8}He β-decay spectrum

Figure 6.5: β-decay energy spectra of ^{9}Li and ^{8}He based on the modified decay data base. The visible energy spectrum in the OSIRIS detector is rendered with the black line and the specific sub-histograms depict the energy spectra of the ^{9}Li (^{8}He) β-decays to the respective excited states of ^{9}Be (^{8}Li).

OSIRIS framework this mode was mainly developed for the simulation of muon events, for which the input parameters are created via the parallelly developed muon generator (see section 6.2). The HEP data format has its origins in the simulation of accelerator experiments, where numerous particles with different vertices define a single event [130]. In the HEP file, the relation between mother and daughter particles is defined, together with the particle definition via the encoding compliant with the PDG standard, the initial vertex position, momentum direction and kinetic energy and the creation time of each particle. The user control of the *HEPEvt* mode is realized with a Geant4 macro file for which a separate messenger class was implemented. For the connection of the input data from the HEP file and the event generation of Geant4 an interface class is provided that creates the initial event data and passes it to the simulation environment as initial vertices. To improve the simulation performance of the cosmogenic isotope and neutron production via muons, the *HEPEvt* mode can be operated in a non-optical mode, where the production of photons via scintillation or the Cherenkov effect is disabled. Furthermore, an external physics list is used (see section 6.1.3), which describes the generation of muon-induced secondary particles more precisely and is already verified by other experiments (see section 7.1.3). For this mode, the output is extended by two additional ROOT trees that contain the truth information of the initial particle and the information about created secondary particles, the capture of neutrons and the possible decay of secondary particles.

PMT calibration mode

The timing calibration of the OSIRIS central detector and veto PMTs is realized via short laser pulses from an externally installed source. In order to reduce the number of light guiding fibers in the detector, a novel diffusor concept is installed to aim for several PMTs with one light emission point (see section 5.2). Via an external trigger to control the laser, the detection time of each PMT and the position and individual selection of the diffusors, the global timing of the detector can be calibrated. In figure 6.6, the exemplary photon distribution of a single diffusor is depicted. In order to achieve reasonable results, the majority of hits on each PMT must be resolvable as single photo electron events. For an individual PMT this can be achieved via the tuning of the laser, but since all diffusors are supplied by the same source, a homogeneous illumination of all PMTs is required. To optimize the positions of the diffusors, a separate simulation mode was established, where the beam profile of the diffusors is adjustable via an angle dependent intensity distribution. The positions and directions of the diffusors and the energy of the photons are set via an external macro file, similar to the *GeneralPS* mode. Furthermore, the compatibility of the calibration system during the detector setup when all volumes are filled with air or water

Table 6.4: Hadronic models combined in the predefined *QGSP_BERT_HP* physics list itemized by the covered particles and the energy range. The simulation of the muon-nuclear interactions is defined by the geant4 class *G4MuonNuclearProcess* (included in the physics list). Table adapted from [109].

Model	Covered particles	Energy range
Quark-Gluon String + Compound (QGSP)	protons, neutrons, π, K	$\geq 12\,\mathrm{GeV}$
Bertini Cascade	protons, π, K neutrons	$\leq 9.9\,\mathrm{GeV}$ $19.9\,\mathrm{MeV} - 9.9\,\mathrm{GeV}$
Low Energy Parameterized (LEP)	protons, neutrons, π, K	$9.5\,\mathrm{GeV} - 25\,\mathrm{GeV}$
High Precision Neutron (HP)	neutrons	$\leq 20\,\mathrm{MeV}$

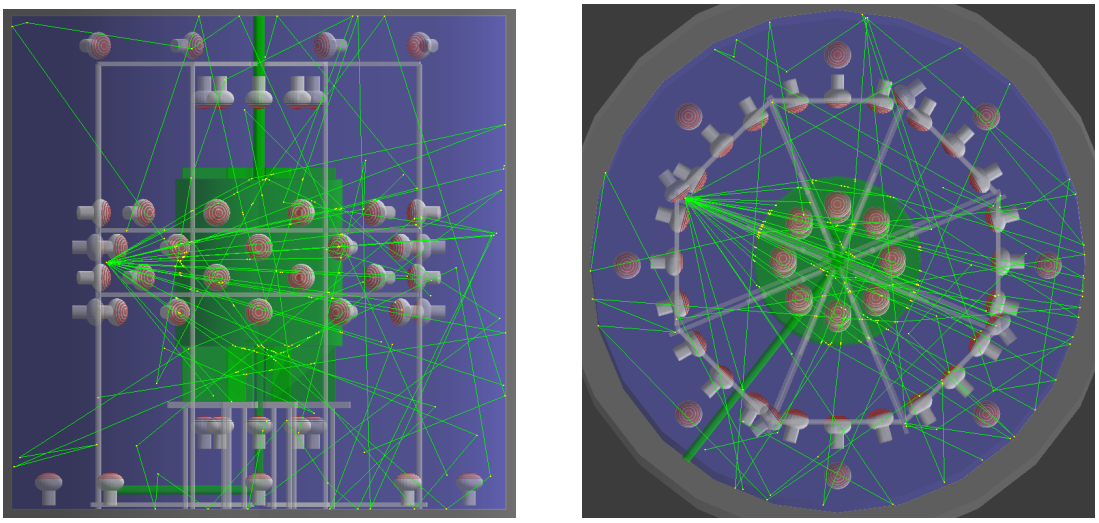

Side view Top view

Figure 6.6: Beam profile of a selected PMT calibration diffusor in the simulated geometry. 25 photons are simulated in this event, each represented by a green line. For clarity, the magnetic shielding and the optical separation are not included in the simulations. The highly reflective liner which covers the steel tank leads to several reflections of the photon beam before it is absorbed. In the top view, the lensing effect of the acrylic vessel due to different refractive indices of the materials is visible which constrains the effective beam profile of the diffusors.

could be confirmed, based on simulations.

6.2 OSIRIS muon generator

In order to simulate a realistic model of the muon flux and the muon induced background expected for the OSIRIS experiment, the actual angular and energetic distributions on site must be considered. For this purpose, the HEP event mode was implemented primarily since therefor externally generated input parameters for the initial events can be invoked. The required input files in the HEP format can be generated with the *OSIRIS-MuonGenerator*, a standalone executable within the software framework and an important part of the work described in this thesis. The major input parameters are the onsite muon flux characteristics, which are saved in a separate file adapted from the JUNO software framework and the OSIRIS volume for which the events are generated. The volume can be chosen from the acrylic vessel and the steel tank, with the additional condition whether the muons must or must not traverse the liquid scintillator volume.

6.2.1 Input data

The simulated muon flux must correspond to the real properties (energy, angular distribution) onsite as closely as possible to maintain realistic results, on which the design of the muon veto and the setup of the trigger condition essentially build upon. For the simulation framework of the JUNO experiment, simulations based on a modified Gaisser formula [131] to calculate the muon flux on the surface above the experimental hall and a high precision digital map of the landscape profile were conducted using the MUSIC [132] software package. Based on these simulations, a detailed and realistic energy and angular direction profile was generated, which is saved in a separate *txt*-file [61]. It contains 1×10^6 simulated events each with a distinct azimuthal and polar angle and kinetic energy. The spectra are shown in figure 6.7 and are a direct result of the topology of terrain above

the JUNO location. The polar angle distribution follows from the thickness of the rock volume above the detector. However, the depicted distribution does not represent the real flux in angular dependence but is weighted by the area element, which is covered by the polar angle element in the bins of the histogram. The converted angle distribution, which represents the actual polar angle dependent flux is shown in figure 6.8. The azimuth angle distribution, which reflects the surface topology above the experimental hall is not considered in the simulation, because the implemented geometry is not yet aligned with the actual orientation of the real experiment. Here, a uniform distribution is assumed. The energy distribution also depends on the thickness of the rock volume to be traversed by the muon. The mean energy of the muons is 209 GeV, according to the data set [61].

6.2.2 Event generation

For the generation of a specific muon event for the *HEPEvent* mode of the OSIRIS simulation, random azimuthal and (corrected) polar angles are sampled from the distributions (see figure 6.7), which are then translated into a three dimensional momentum direction vector. In order to reduce the simulation effort, the initial vertex of the muon tracks is located directly on the surface of the start volume. However, due to the underground location of the detector and thus the increased shielding of muons with a large horizontal component, vertical tracks entering the detector volume on the top surface are favored. For that reason, a randomly selected starting point for the muon tracks would result in a wrong simulated track distribution. To remove this bias, for each track the probability to either hit the horizontal top surface or the vertical cylinder side of the volume is calculated based on the momentum vector. For example, if the direction has a large component in z-direction, the probability that the top surface is hit is more probable than for the cylinder mantle. The probability p_{top} that a muon track hits the top surface is given by the projection which is "seen" by the muon

$$p_{top} = |\vec{d} \cdot \vec{n}_{top}| \cdot A_{top}, \tag{6.1}$$

with the direction vector of the muon $\vec{d}$, the normal vector of the horizontal surface $\vec{n}_{top} = \begin{pmatrix} 0 \\ 0 \\ 1 \end{pmatrix}$ and its area. Due to the cylindrical shape of the steel tank, the increased projected side area compared to a two dimensional surface must be considered. Thus, the probability p_{side} for a muon to hit the side of the cylinder volume is

$$p_{side} = |\vec{d} \cdot \vec{n}_{side_1}| \cdot A_{side_1} + |\vec{d} \cdot \vec{n}_{side_2}| \cdot A_{side_2}, \tag{6.2}$$

with $\vec{n}_{side_1} = \begin{pmatrix} 1 \\ 0 \\ 0 \end{pmatrix} / \begin{pmatrix} 0 \\ 1 \\ 0 \end{pmatrix}$, $\vec{n}_{side_2} = \begin{pmatrix} 1 \\ 0 \\ 1 \end{pmatrix} / \begin{pmatrix} 0 \\ 1 \\ 1 \end{pmatrix}$, $A_{side_1} = 2 \cdot r \cdot h$ and $A_{side_2} = r \cdot h$ (with radius r and height h of the cylinder volume). Based on the probability weights of the different surfaces, the initial surface of the muon track is selected randomly. The initial position of the muon track on the surface is then selected randomly.

The muon generator is implemented with several volume restrictions for the muon track, which can be chosen by the user. The basic options are muons starting on either the acrylic vessel or the steel tank with unrestricted direction. With the more sophisticated options, only muon tracks are selected that must not or must definitely traverse the liquid scintillator volume. In the case of the specific restrictions, initial positions on the surface are tested until the start position and the track direction meet the requirements. Finally the energy for the event is sampled from the given distribution and the charge of the muon is determined, based on a random selection, where the ratio is given by $R_{\mu^+} : R_{\mu^-} = 1.3 : 1$.

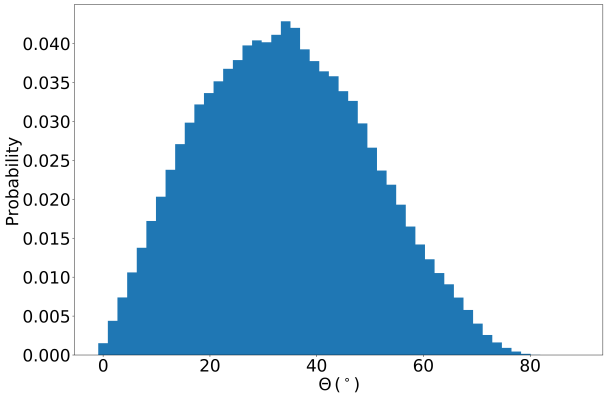

Polar angle distribution

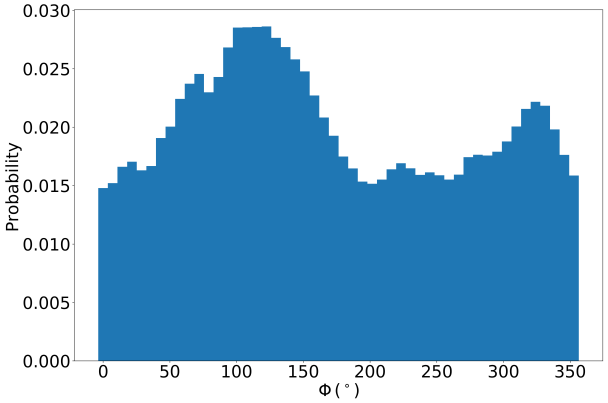

Azimuth angle distribution

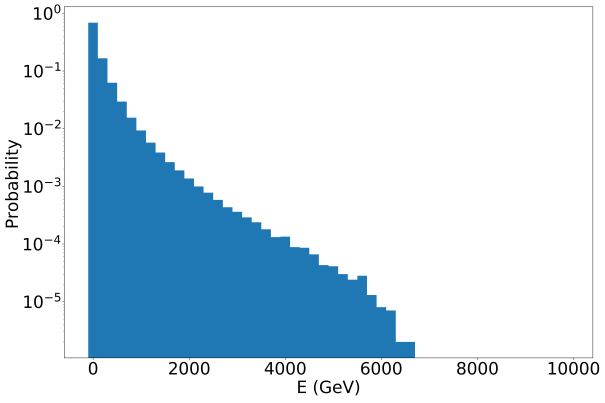

Energy distribution

Figure 6.7: Angular and energetic muon distribution for the JUNO onsite location based on MUSIC simulations. Data from [61].

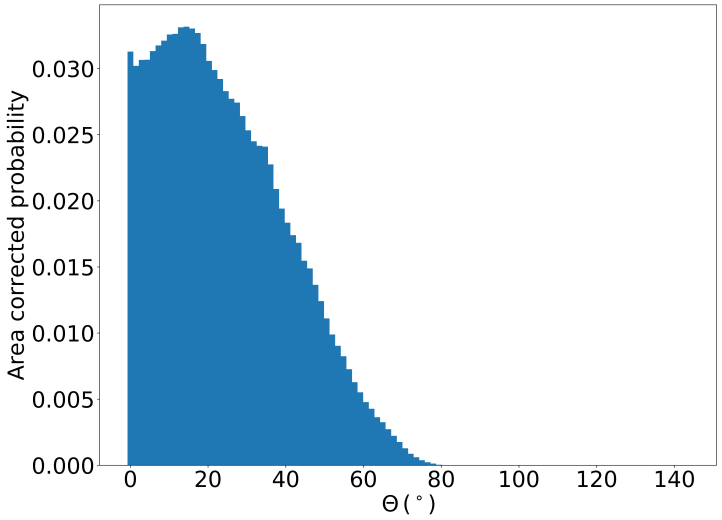

Figure 6.8: Corrected distribution of the polar muon flux distribution. The polar flux distribution from the original output of the muon flux simulation for the JUNO site (depicted in figure 6.7) is weighted with the area element covered by the polar angle.

Table 6.5: Muon flux in the different OSIRIS sub-volumes. Water only represents muon tracks that do not traverse the liquid scintillator volume.

Volume	Muon flux (Hz)
Acrylic vessel	0.04
Steel tank	0.39
Water only	0.35

The reason is that the particles of the cosmic radiation preferably interact with positively charged particles of the atmosphere and thus positive meson production is favored [133]. The initial vertex data of the muon is stored in a dedicated class object while the procedure is repeated until the number of desired events is reached. With the stored data, the HEP files are generated.

6.2.3 Muon rate in OSIRIS

The muon flux on the JUNO site is estimated with $R_{\mu,norm} \approx 0.0037\,\text{Hz}$ per horizontal square meter and a mean energy of $E_{\mu,mean} \approx 209\,\text{GeV}$. Based on the polar distribution of the events (see figure 6.7) and the geometries and dimensions of the steel tank and the acrylic vessel, the rates in the volumes can be predicted. The azimuth angular distribution is neglected in this case, as explained above. As shown in table 6.5, the muon flux in the entire OSIRIS detector can be estimated with $R_{\mu,OSIRIS} \approx 0.39\,\text{Hz}$, whereas the rate of muons, which only traverse the water volume is $R_{\mu,OSIRIS,water} \approx 0.35\,\text{Hz}$. Based on this value and the number of secondary particles from muons, which might mimic the coincidence signal OSIRIS is designed to detect, the required veto efficiency can be calculated (see section 7.3).

7. Muon induced background in OSIRIS

Cosmogenic isotopes are anticipated to create the major correlated background source in the OSIRIS detector. These cosmogenic isotopes, that also include free neutrons, are produced by cosmic muons in electromagnetic and hadronic spallation interactions with atoms of the target material, e.g. ^{12}C in the liquid scintillator. Most of these isotopes are unstable and decay via α- or $\beta^{\pm}$-decays, but also the emission of neutrons or triton nuclei in some decay branches. These are a serious background source, as a fast decay signal together with the delayed capture of a neutron can mimic the BiPo coincidence signature OSIRIS is searching for. In the following chapter, the muon induced background signals in OSIRIS are discussed. The analysis is based on extensive muon simulations with the OSIRIS simulation framework (section 7.1). In order to determine the background potential of the induced secondary particles, their signals in the detector are compared to the cut parameters which are defined for the BiPo coincidence search (section 7.2). The different cosmogenic background channels are the combination of multiple secondary neutrons, the decay of heavier isotopes with subsequent emission of a neutron (both correlated backgrounds) and the accidental coincidence of a single neutron and a gamma photon (uncorrelated background). Based on the determined background rate and the expected scintillator purity, the required muon detection efficiency of the OSIRIS muon veto is calculated (section 7.3).

7.1 Production rate and spectrum of cosmogenic isotopes

The reason for the installation of a veto system in the OSIRIS detector is, that in rare cases, cosmic muons interact with nuclei of the traversed material electromagnetically or hadronically which produces neutrons and radioactive isotopes. These showers can extend up to 3 m from the parent muon track [116], which can lead to the creation of neutrons and isotopes in the liquid scintillator volume, although the muon track itself did not traverse the acrylic vessel. In the liquid scintillator, the main target for these processes are carbon nuclei, as they are the major portion of LAB and the additives. Accordingly, the expected secondaries reach from free neutrons, knocked out from the target atom, up to ^{13}C. In water, oxygen is the main target which leads to secondaries up to ^{17}O. Interactions in the steel structures, or the glass of the PMT, where secondaries with distinctly higher atomic numbers are possible, are very rare due to the comparably small volume. In the following sections, the expected production of secondary neutrons and heavier isotopes and the ability to imitate the BiPo signals are discussed. The analysis of

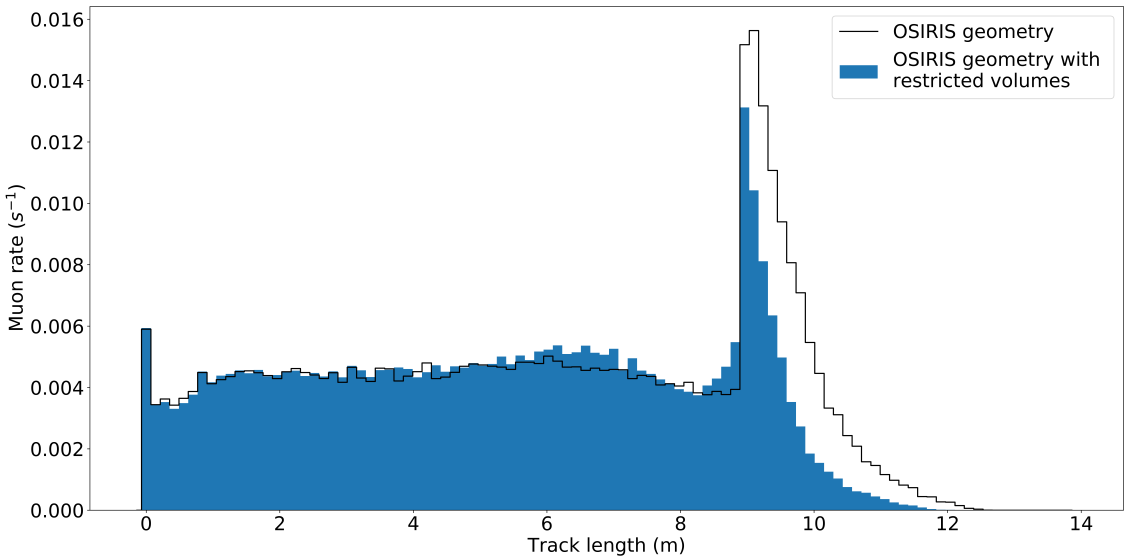

Figure 7.1: Muon track length in the water volume (blue) and for the full volume of the steel tank (black). The peak at short track lengths is caused by muons, that start close to the edge of the top lid of the tank. The second peak is associated to muons that start at the top lid and leave the tank at the bottom of the tank.

the contribution to the cosmic background of the two secondary particle types is separated due to the diverging production rate and the mechanism to mimic the BiPo signature. The results of the analyses in this chapter are the basis for the sensitivity requirements on the muon veto. For that reason and to increase the simulation efficiency, in this chapter only background from muons, which exclusively traverse the water volume is considered. The data is gathered with extensive particle simulations of muons in the OSIRIS water volume with the simulation framework (see chapter 6).

7.1.1 Simulated muon sample

The data set used for the determination of the impact of muon induced secondary particles consists of 1.1×10^8 events, which corresponds to a measurement time for OSIRIS of $\sim 10\,\mathrm{a}$. The simulation was performed on the Computer Cluster of the Physics Institute in Aachen and took $\sim 5\,\mathrm{d}$: The muon events are generated with the OSIRIS muon generator described in section 6.2 with the starting point on the steel tank and and the restriction to only traverse the water volume. To reduce the computation time in these muon simulations, no optical photons from scintillation or the Cherenkov effect are generated, but only the information about the produced secondary particles is stored. Due to the characteristic polar angle distribution of the muon flux (see figure 6.8) the majority of the tracks starts on the top lid of the cylindrical steel tank. In figure 7.1, the track length distribution of the simulated muons in the steel tank volume is shown. There are two salient features in the distribution caused by the geometry of the implemented OSIRIS setup. The sharp edge of the peak at $\sim 9\,\mathrm{m}$ can be associated with vertical muon tracks that enter the tank through the top surface and leave it through the bottom surface. With an increasing horizontal component in the muon momentum direction also the track lengths increase to a maximum of $\sim 12\,\mathrm{m}$. For comparison, the black line shows the track length distribution of a second muon simulation in the detector without volume restrictions to indicate the effect on the track length distribution. It shows the same edge at $\sim 9\,\mathrm{m}$ but the maximum is shifted towards longer track lengths, as tracks crossing the steel tank diagonally and close to the center of the detector geometry are not excluded. The peak at very short lengths is dominated by muon tracks, initialized close to the edge of the top lid with the

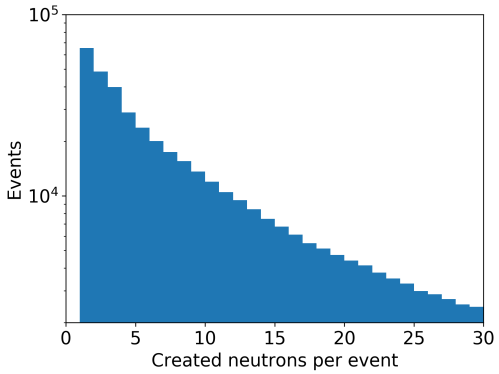

Neutron multiplicity

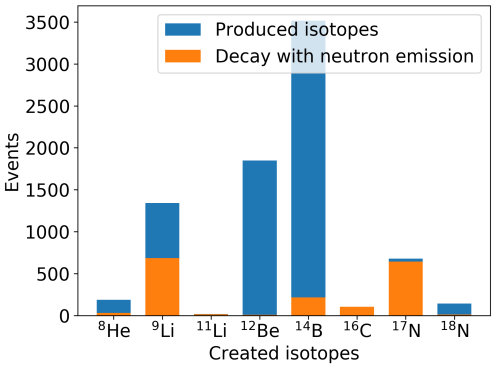

Radioactive isotopes with neutron emission

Figure 7.2: Production spectrum of muon induced secondary particles in the muon sample (1.1×10^8 simulated muon events). **Left: Neutron multiplicity:** In about 1% of the muon events neutrons are produced in the simulated detector volume. **Right: Number of events with produced radioactive isotopes** in the detector volume in the simulated muon sample. The orange bars indicate the expected ratio of branches including the emission of neutrons [116].

direction pointing away from the water volume, so the muon track only crosses the steel of the tank.

7.1.2 Simulation of muon induced particles

Neutrons are the most abundant secondary particles produced by cosmic muons. In the simulated sample with 1.1×10^8 single muon events, in around 0.96% of the events, one or more neutrons are created in the simulated detector volume with the neutron multiplicity shown in figure 7.2. The particle information of the created neutrons in an event (position, momentum, creation time) are stored separately, but assignable to the respective muon event. As depicted in figure 7.3, the majority of the produced neutrons is low energetic and only a small ratio reaches kinetic energies of more than 300 GeV. Despite the restriction on the muon tracks to the water volume, the neutrons can be generated in all physical volumes of the simulation. Neutrons that are created outside the vessel must be considered as potential contribution to the cosmogenic background, as they can travel into the sensitive volume from outside the acrylic vessel. In contrast to that, radioactive isotopes that are produced outside the acrylic vessel are not addressed further. Due to the small kinetic energy and large cross section they cannot pass the acrylic and decay in the liquid scintillator volume.

For the generation and analysis of the detector signals, induced by the muon induced secondary particles, the produced neutrons and isotopes are simulated in a second simulation step with activated optical model and photon generation. All secondary neutrons of a muon event are generated as initial particles in a new event, according to the output of the muon simulations (described in section 7.1.1). The propagation and physical interactions of the neutrons in the different OSIRIS volumes are adapted in detail in the simulations. The velocity of the neutrons is slowed in the respective materials by elastic scattering with hydrogen and carbon in the liquid scintillator and oxygen in the water volume to sub-eV energies. In the liquid scintillator, around 99% of the low energy neutrons are captured by hydrogen atoms after a mean capture time of $\tau_{capture} \approx 216\,\mu$s, followed by the emission of a 2.2 MeV gamma photon. In the case of the capture at a carbon atom, the subsequently emitted photon has an energy of 4.9 MeV [116].

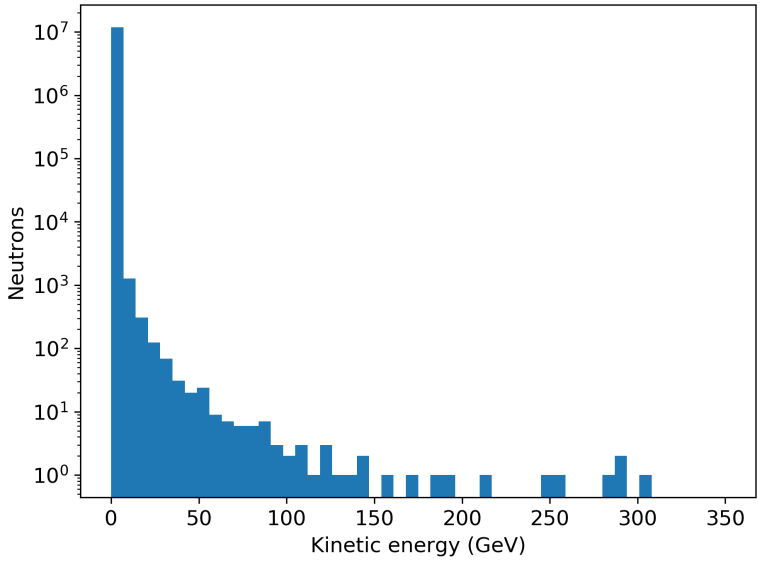

Figure 7.3: Kinetic energy of the muon induced secondary neutrons. While the majority of the produced neutrons are low energetic a small amount reaches energies of more than 300 GeV.

As shown in figure 7.2 the amount of radioactive isotopes produced in the detector volume is distinctly smaller than for neutrons. Here, the amount of all isotopes created in the simulated OSIRIS volume that contain a decay branch which includes the emission of a neutron are listed, as only these are capable to imitate coincidence events with delayed signals. The lighter isotopes up to ^{12}Be can mainly be associated with the spallation of carbon atoms in the liquid scintillator volume, whereas the heavier isotopes predominantly arise from the spallation of oxygen atoms in the water volume. The orange bars indicate the expected amount of events with a subsequent neutron emission, based on the respective branching ratios, given in [116]. Due to the small amount of produced isotopes, not the creation vertex of the isotopes from the muon simulation is used for the second simulation step, but a sample of particles of the respective isotope are placed at random positions in the liquid scintillator volume with random direction and kinetic energy sampled from the muon induced isotopes. From this large sample, the amount of decay events $r_{\text{iso, mimic}}$ is determined, for which the BiPo cuts are passed. Together with the actual number of produced secondary isotopes N_{iso} from the muon simulations, the amount of events mimicking the BiPo coincidence signal $N_{\text{iso, mimic}}$ for the different isotopes can be calculated:

$$N_{iso,mimic} = r_{iso,mimic} \cdot N_{iso} \tag{7.1}$$

The total expected rate of produced secondary isotopes is given in section 5.3.

7.1.3 Validation of the secondary particle production with Borexino results

The Borexino collaboration analyzed a large data set of muon events and the accompanying production of neutrons and radioactive isotopes, which they could reconstruct in the experiment. The secondary production yields were then compared to the respective results of the Borexino simulation framework, which is also based on geant4 [109]. Since the composition of the liquid scintillator is very close to the OSIRIS setup, their results can be transferred. Although the simulations are based on different versions of geant4 (Borexino: v9.06.01; OSIRIS: v10.02.03), the comparison of the production yields is valid, due to the minor differences in the program parts that handle the respective physics models.

In the comparison of detector and simulation data for Borexino, several distinct geant4 physics lists that combine various models and respective energy ranges are compared. In the following, only the results for Model 4, which is congruent with the OSIRIS physics list for secondary particle production are regarded and applied to the results of the present analysis. The detected and simulated production yields Y_{sec} are determined by

$$Y_{sec} = \frac{N_{sec}}{N_\mu} \cdot \frac{1}{l_\mu^{avg}} \cdot \frac{1}{\rho_{scint}}, \tag{7.2}$$

with the production rates of the secondary particles N_{sec}, the number of simulated or detected muon events N_μ, the mean muon track length l_μ^{avg} in the detector and the scintillator density ρ_{scint}. The results are shown in table 7.1. While the detected neutron production yield is in good agreement with the simulations, the comparison of the measured production of the radioactive isotopes with the simulations is aggravated. In the case of ^{9}Li the simulated yield is only 50% of the measurement, whereas the rate of measured ^{8}He is too small for a comparison with the simulation results. Therefore, in the further analysis, only the simulations for ^{9}Li are corrected accordingly. Additionally, the yields for the OSIRIS muon simulations are calculated with $N_\mu = 1.1 \times 10^8$, $l_\mu^{avg} = 5.32\,\mathrm{m}$ and $\rho_{scint} = 0.86\,\mathrm{g/cm^3}$. The ratio of the production yields is in good agreement with the results from the Borexino simulation, however the particular values are smaller. This is mainly due to the restriction that the muons only pass the water volume, whereas for Borexino also the muon tracks through the scintillator volume are considered.

Besides the total neutron capture yield per muon track, also the neutron capture multiplicity is investigated in [109]. In general, good agreement between data and simulation is found for the utilized physics list, with minor deviations for small multiplicities, where the simulations predict a decreased production of neutrons compared to the data. The direct comparison of the results in [109], where the multiplicity of the neutron capture is observed, and the multiplicity spectrum in figure 7.2, which shows the multiplicity of the neutron production in the OSIRIS simulation framework, must be treated with caution. Since not all produced neutrons are directly captured in the scintillator volume, the capture distribution is distorted towards small multiplicities.

7.2 Cosmogenic background contribution in OSIRIS

For the determination of the cosmogenic background contribution, the signal of the simulated events in the detector is analyzed with the already established BiPo coincidence cuts. By determining the number of events passing these cuts, the rate of imitating events from muon induced secondaries and thus the required veto efficiency can be defined.

Table 7.1: Comparison of the cosmogenic isotope production yield in Borexino for simulations with geant4 and measurement data. Only the relevant isotopes that can mimic the BiPo signal in OSIRIS and neutrons are considered. While the simulated neutron yield is in good agreement with the detection data, the amount of heavier isotopes deviates from the simulations. A similar yield ratio is observed in the OSIRIS simulation data, but with lower rates explainable with the higher mean muon energy. The uncertainties are derived from the simulations. Data from [109].

Secondary particles	Borexino simulation	Borexino data	OSIRIS simulation
	Yield $(10^{-4}(\mu \cdot g/cm^2)^{-1})$		
Neutrons	2.99 ± 0.03	3.10 ± 0.11	2.3369 ± 0.0007
^{8}He	$(0.18 \pm 0.05)10^{-3}$	$< 1.5 \cdot 10^{-3}$	$(0.081 \pm 0.004)10^{-3}$
^{9}Li	$(1.68 \pm 0.16)10^{-3}$	$(2.9 \pm 0.3)10^{-3}$	$(0.52 \pm 0.01)10^{-3}$

7.2.1 BiPo selection cuts

In order to identify BiPo coincidence signals and to distinguish them from accidental background events, a set of different cuts will be applied to the reconstructed event data. The selection and the limits of the cuts are based on extensive simulations of BiPo events in the liquid scintillator volume and the decay of expected radioactive contamination in the selected materials of the OSIRIS setup and the surrounding rock volume. The subsequent optimization and the resulting cut limits for the two different coincident BiPo events are shown in table 7.2 and described in detail in [120]. Following, the cuts and the respective application to the simulated events of cosmogenic secondary particles are outlined.

Fiducial volume cut

External gamma photons from the surrounding rock or parts of the OSIRIS setup like the steel tank, the PMTs or the optical separation foil (see chapter 8) are predominantly absorbed in the water volume that surrounds the acrylic vessel. Gammas that pass the water shield can deposit energy in the liquid scintillator. The majority of the gamma photons passes only small distances in the scintillator before they are absorbed, which leads to an increased event rate close to the edge of the acrylic vessel. To reduce accidental coincidences, a cylindrical fiducial volume cut is introduced, which rejects events, with reconstructed positions $r \geq 145\,\text{cm}$ and $|z| \geq 145\,\text{cm}$ [120]. Since the energy cut is very effective in rejecting background events (see below) the fiducial volume cut only excludes a small amount of the liquid scintillator volume. Especially for the ^{212}BiPo coincidence signal, where the dominant background contribution comes from radon contamination in the water shield, the fiducial volume cut has its biggest impact.

Energy cuts

In both detectable BiPo coincidence event classes (^{212}BiPo and ^{214}BiPo), an initial β-decay of the respective bismuth nucleus is followed by an α-decay of the daughter nucleus polonium. While the β-decay energy spectra show broad distributions with endpoints at around 2.3 MeV and 3.5 MeV, the α-particles are mono-energetic, resulting in a sharp peak of the detected energy at 8.954 MeV and 7.834 MeV [123]. Due to the quenching effect of the liquid scintillator, the visible energy is strongly reduced (up to a factor of 10 for α-particles).

Time difference cut

The time difference cut aims at the coincidence character of the BiPo signal. The initial β-decay is always followed by an α-decay with an exponentially distributed time difference depending on the properties of the respective isotope. Due to the short lifetimes of ^{212}Po with $\tau = 431\,\text{ns}$ and ^{214}Po with $\tau = 237\,\mu\text{s}$ [123] this cut is very effective regarding accidental coincidences of independent background events. The lower limit of the cut windows is defined by the expected computation and reconstruction time between two events and estimated conservatively to $0.2\,\mu\text{s}$ [120].

Spatial distance cut

The short lifetimes of the excited polonium events (^{212}Po and ^{214}Po) lead to an exponentially distributed distance probability between the two signals of the BiPo coincidence, which is exploited in the spatial distance cut. Random coincident background events thus can be rejected effectively as they have no spatial relation to each other. The limit of the distance cut is mainly driven by the expected imperfect position reconstruction, especially for the α-decays due to the large quenching effect.

Multiplicity cut

For the determination of potential background contributions from muon induced cosmogenic isotopes, a multiplicity cut is introduced, which rejects events with more than one coincidence signal that passes the BiPo cuts. Due to the uncorrelated character of the BiPo decays and the expected low rate, two or more simultaneous coincidence signals are excluded and can only be induced by correlated background events.

The above mentioned cuts (excluding the multiplicity cut) are all based on assumptions on the expected background activity, detection and reconstruction efficiency and the incomplete implementation of the OSIRIS geometry in the simulation framework. The final limits of the cuts will be adapted to potential changes in the design and the conditions of the completed setup.

7.2.2 BiPo coincidence event reconstruction

The event selection and reconstruction algorithms for the OSIRIS experiment as well as the implementation of the electronics response are not yet finalized in the OSIRIS simulation and analysis software. In order to still determine the potential of muon induced secondary particles to mimic the BiPo coincidence signal, the Monte Carlo truth of the simulated events must be manipulated in such a way that it is comparable to real detector data. Therefore, in the simulation data the current particle position and time are stored whenever a neutron capture or a radioactive decay of the produced isotopes is registered. Additionally, all photon hit times that are detected by any PMT are stored.

In the experiment, the position of an event will be reconstructed from the number and the hit times of the detected photo electrons. Thus the reconstructed event position is the barycenter of the particle track, weighted with the amount of energy deposited at the respective position. While in reality the energy deposition is a continuous process, in the simulation where each track is separated into steps the reconstructed position is calculated as the product of the deposited energy and the coordinates divided by the totally deposited energy. Since the vertex reconstruction is fully based on the detected scintillation photons, the accuracy is determined by photo electrons statistics. To account for this position smearing, each coordinate of the true barycenter position is shifted by a Gaussian distributed value around zero. In [120] the distribution is defined with an energy dependent standard deviation

$$\sigma = \frac{\sigma_0}{\sqrt{E_{evt}(MeV)}}, \tag{7.3}$$

Table 7.2: BiPo selection cuts. The limits of the cuts are based on simulations and results from the optimization of the expected signal to background ratio, taking into account the radioactive background sources in the OSIRIS setup and the surrounding. In parentheses, the BiPo event selection efficiencies are stated. Adapted from [120].

Cut parameter		Cut limits (Efficiency) ^{212}Bi – ^{212}Po	Cut limits (Efficiency) ^{214}Bi – ^{214}Po
Fiducial volume	r	$\leq 1.45\,\mathrm{m}$	$\leq 1.45\,\mathrm{m}$
	|z|	$\leq 1.45\,\mathrm{m}$	$\leq 1.45\,\mathrm{m}$
Energy	E_{Bi}	$[0.1375, 2.50]\,\mathrm{MeV}$ (0.98)	$[1.4, 3.50]\,\mathrm{MeV}$ (0.87)
	E_{Po}	[0.8625, 1.50]MeV (1.00)	$[0.65, 1.10]\,\mathrm{MeV}$ (0.99)
Time difference	Δt	$[0.2, 2]\,\mu\mathrm{s}$ (0.62)	$[0.2, 711]\,\mu\mathrm{s}$ (0.95)
Spatial distance	Δd	$\leq 0.725\,\mathrm{m}$ (1.00)	$\leq 0.45\,\mathrm{m}$ (0.90)

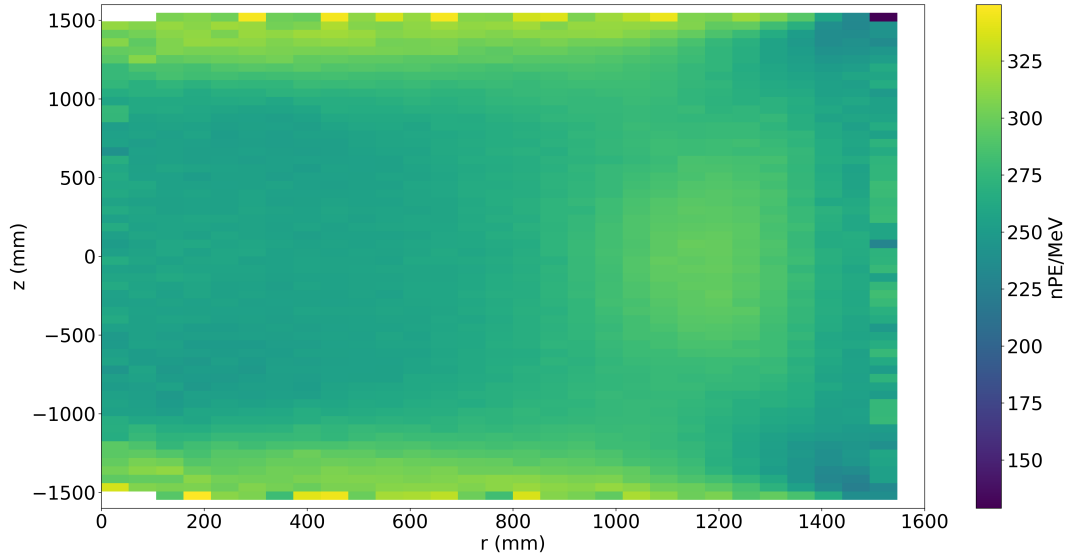

Figure 7.4: Two-dimensional illustration of the scintillation response map of OSIRIS showing the mean number of detected scintillation photons per deposited energy. The map is created via simulations of 5×10^6 2.2 MeV gamma photons in the liquid scintillator volume with random positions and directions. The specific energy value is chosen to maximize the sensitivity for the neutron capture. For the depiction, the energy response was averaged over the azimuth angle.

with E_{evt} as the true event energy and $\sigma_0 = 14\,\text{cm}$ for electrons and α-particles, estimated from scaled values of the Borexino experiment. In the case of a neutron capture, energy is deposited in the detector by the emitted 2.2 MeV gamma photon. To consider the longer path length of a photon, compared to other particles of the same energy and the consequential increased position uncertainty [134], the standard deviation of the position smearing distribution per coordinate is set to a value of $\sigma_0 = 14\,\text{cm}$ for all neutron capture events.

The absolute time of a real event is also calculated within the vertex reconstruction and tightly connected to the position reconstruction. The accuracy depends mainly on the TTS of the PMTs, but also on the event position in the detector. In OSIRIS, exclusively 20-inch Hamamatsu PMTs are used with a mean TTS of $\sigma_{TTS} = 3.3\,\text{ns}$ [74]. Distinct measurements of the OSIRIS PMTs at RWTH Aachen give a range of the TTS of $2.2\,\text{ns} \leq \sigma_{TTS} \leq 3.1\,\text{ns}$. To take this into account for the simulated events, the event time (capture or decay) is smeared accordingly with a Gaussian distribution with $\sigma = 3.1\,\text{ns}$. Compared to the time cut windows, and also to the photon detection window (see below), this correction is very small and has only minor impact on the event reconstruction.

The energy reconstruction is based on the number of detected scintillation photons in the simulation, which corresponds to the real approach. The amount of detected photo electrons does not only depend on the amount of deposited energy in the liquid scintillator, but also to the deposition position as the photon detection surface of the PMTs is not homogeneously distributed around the acrylic vessel and scintillation light is attenuated more the longer the distance to the PMT is. In order to simulate the energy reconstruction and to take into account the OSIRIS geometry, a three-dimensional response map was compiled. For this purpose, 5×10^6 gamma photons with an energy of 2.2 MeV were simulated, with the detected scintillation photons and the energy deposition at each simulation step stored in the output file. Based on this data, the mean detected photon number and the barycenter position of the energy deposition in the detector, according to the event

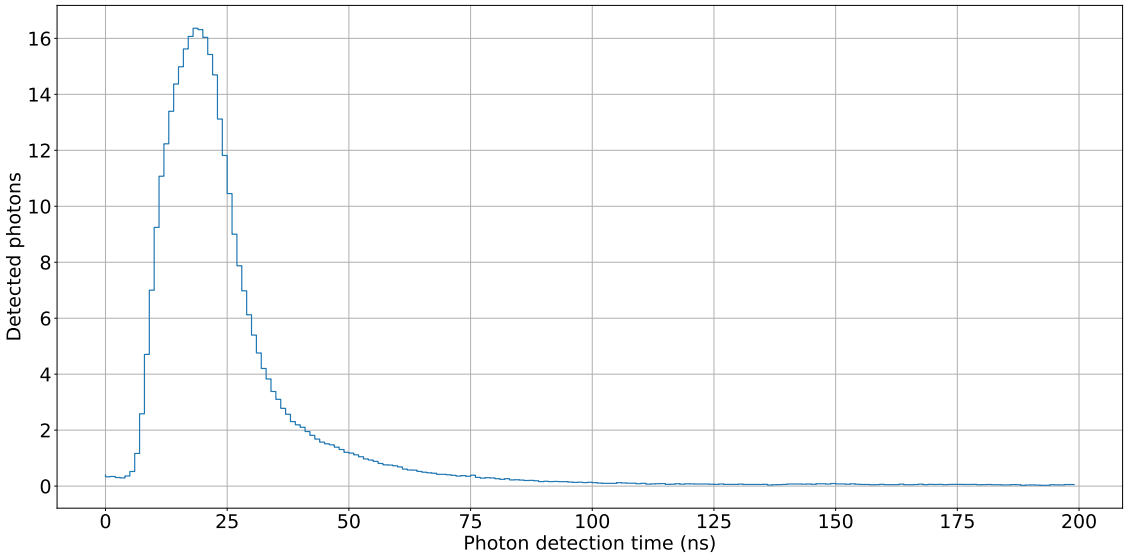

Figure 7.5: Average pulse shape of the simulated neutron capture event with the hit times of all detected photons in the time window of 200 ns after the neutron capture event. As the simulation of the PMT electronics is not yet implemented, the capture time is smeared manually to imitate the uncertainty.

vertex reconstruction (see above), are calculated and saved in a three-dimensional array with a bin size of 10 cm. In figure 7.4, the mean number of detected photons per MeV deposited energy in dependence of the event position is depicted. The non-homogeneous photon detection distribution can be explained with the increased PMT density above and below the acrylic vessel and the irregular arrangement of the side PMTs.

In the analysis of the simulated secondary particles, all photo electrons are accepted within a time window of 200 ns after the recorded time of the neutron capture or the decay event to ensure that most of the photons are either detected or absorbed. The average pulse shape is shown in figure 7.5. Based on the number of detected photons and the position of the event, the deposited energy can be reconstructed from the pre-computed detector response map.

In order to determine the rate of cosmogenic background, the BiPo coincidence cuts (see table 7.2) are applied to the reconstructed secondary particle events of each muon event.

7.2.3 BiPo coincidence signals due to secondary neutrons

For the imitation of a BiPo coincidence signal with a muon event, in which only secondary neutrons are created, at least two of the neutrons need to deposit energy in the detector via the capture at a hydrogen atom and the subsequent emission of a gamma photon. As mentioned before, not only neutrons created in the liquid scintillator volume qualify for that, but also neutrons produced in the water or rock volume, surrounding the acrylic vessel. The produced secondary neutrons are simulated as initial particles, with the activated optical model and the affiliation to the respective muon event. In figure 7.6, the multiplicity of captured neutrons in the liquid scintillator and the surrounding water volume with a distance of 25 cm to the acrylic vessel is shown. Due to the position uncertainty of the event reconstruction, also capture events in the surrounding water volume can pass the fiducial volume cut and can, caused by the proximity to the detector edge, preferentially imitate the polonium signature of the BiPo coincidence signals, as the small associated energy value is only achieved by gamma photons from neutron capture events that do not deposit the full energy in the liquid scintillator.

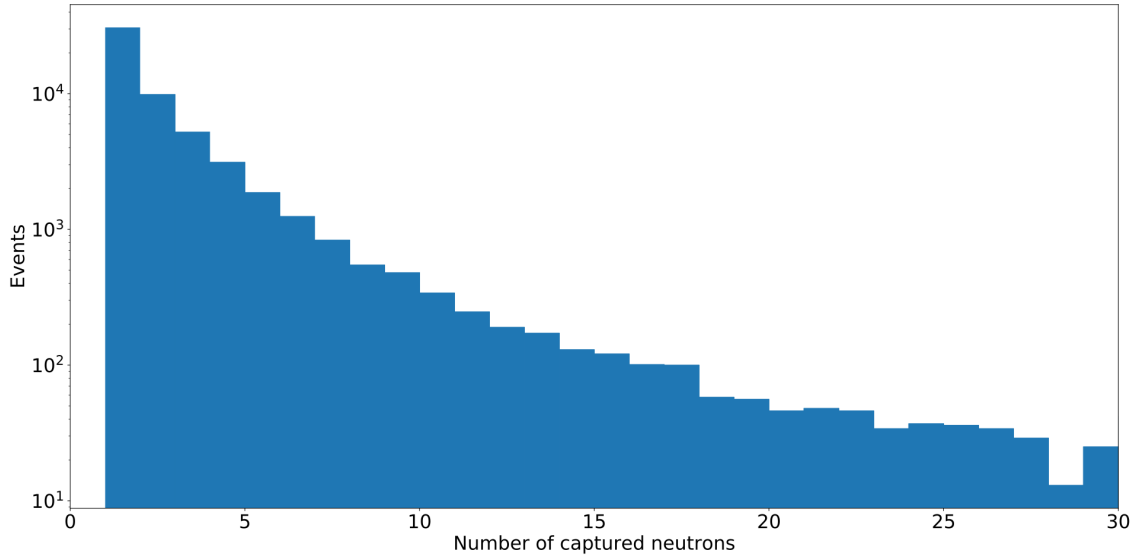

Figure 7.6: Neutron capture multiplicity on hydrogen atoms in the liquid scintillator volume and the surrounding water volume with a maximum radius of 1.75 m to the detector center.

In order to fulfill the cuts in table 7.2 and imitate the bismuth decay signal of the two BiPo coincidences, one of the emitted gamma photons must deposit its full energy in the fiducial volume. To pass the cut thresholds, a second neutron must be captured within the time difference Δt and the spatial distance Δd. Since the maximum of the energy window of the polonium decay is smaller than the energy of the gamma photon released after the neutron capture, the emitted photon of the second captured neutron must deposit only a part of its energy in the fiducial volume. This is possible for neutron captures close to the edge of the acrylic vessel.

All simulated neutrons within each event are compared pair-wise to analyze, if they meet the requirements to imitate a BiPo signal. In figure 7.7, the respective neutron event data and the cuts are depicted for the limits of the ^{214}BiPo coincidence signal. The characteristic spatial distributions (radial and axial in cylinder coordinates) origin from the properties of the muon tracks in the OSIRIS tank, which only traverse the water volume. Here, only the distributions for the first neutron of the comparison are shown, as the distributions are identical and the cut limits are the same. As the distributions show, neutron captures with radii and z-coordinates larger than the liquid scintillator measures are considered in the coincidence analysis. This accounts for capture events at hydrogen nuclei of water molecules close to the surface of the vessel, where the emitted gamma photon can enter the liquid scintillator volume. Considering the time profile, in the case of the ^{214}BiPo cuts, most events are contained in contrast to the ^{212}BiPo cut limits where the upper limit is smaller and thus most events are rejected.

The energy distributions are shown for both, the first and the second neutron capture, to indicate the two different cut limits. Both distributions show the same features which stands to reason, since the two capture events are independent of each other. The first peak at very low energies can be associated with neutron capture events outside the acrylic vessel, where the emitted gamma photon does not enter the acrylic vessel at all, or at most a very small distance. The second peak at $E_n \approx 2.2\,\mathrm{MeV}$ is connected to gamma photons, which deposit their full energy inside the liquid scintillator. As the neutrons in an event are considered independently, in some cases multiple neutron capture events occur within the time window of of photon collection, which leads to an increased energy deposition.

Table 7.3: Suppression efficiency for muon induced neutron background events based on the BiPo event cuts derived from gamma background analyses (see table 7.2). The suppression efficiency for the cuts is determined independently of the other cut parameters. For both BiPo coincidence signals, the energy cut on the polonium-like event is very effective, due to the very narrow limits, which do not contain the energy of a fully contained neutron capture event. For the ^{212}BiPo coincidence, the time difference cut is most effective, due to the exponentially distributed capture time of the neutrons after their creation.

Cut parameter		Suppression ^{212}Bi – ^{212}Po cuts	Suppression ^{214}Bi – ^{214}Po cuts
Fiducial volume	r	53.4 %	53.4 %
	|z|	15.7 %	16.5 %
Energy	E_{Bi}	51.5 %	57.3 %
	E_{Po}	96.4 %	97.5 %
Time difference	Δt	99.1 %	2.4 %
Spatial distance	Δd	79.3 %	90.9 %
Combined		99.997 %	99.966 %

The later captured neutrons are considered subsequently, so they still can contribute to the background. The domain between the two peaks, where the cut limits for the visible energy of the polonium decay are located is connected to gamma photons which only partially deposit their energy in the scintillator. The peaks at $E_{2n} \approx 4.4\,\mathrm{MeV}$ and $E_{3n} \approx 6.6\,\mathrm{MeV}$ (not visible in the histogram) are associated to multiple neutron captures within the time window of 500 ns for the energy deposition. Neutrons captured at carbon nuclei, where a 4.9 MeV gamma photon is released, are strongly suppressed and shows no visible peak in the distribution. As depicted, for most of the events the energy cut window for the bismuth decay contains the peak for one neutron capture event with full energy deposition in the detector. For the polonium decay, where the cut window is located below the first full neutron capture peak, only a minority of the events is contained, making this cut the most efficient one for the rejection of BiPo mimic events based on secondary neutrons. The same applies to the ^{212}BiPo coincidence signal, where additionally the time difference cut rejects the majority of the neutron capture events. The suppression ratios, broken down to the cut parameters, are listed in table 7.3.

In figure 7.8, the multiplicity of the detected neutron induced BiPo mimic events in the simulated sample are depicted. Although events with one coincidence signal are dominant for both BiPo-channels (^{212}BiPo: 60.2 %, ^{214}BiPo: 27.1 %), higher multiplicity events occur in a non-negligible share. However, in the context of the OSIRIS sensitivity towards $^{212/214}$BiPo coincidence signals, the higher-multiplicity BiPo mimic events can be neglected, due to the low expected true BiPo rate, which rejects two coincidence signals within the time window of one muon event. Based on the expected muon rate of $R_{\mu(OSIRIS,water)} \approx 0.35Hz$ in the water volume (see section 6.2.3) and the number of simulated muons that traverse the water volume $N_{\mu,\,sim} \approx 1.1 \times 10^8$, the simulation data represents a time span of $t_{sim} = 3637\,\mathrm{days}$. Together with the number of single imitated BiPo signals in the sample of $N_n^{212} = 34$ and $N_n^{214} = 387$ (see figure 7.8), the expected rate for muon induced coincidence signals, based on secondary neutrons, is $R_n^{212} = (0.010 \pm 0.002)\,\mathrm{counts/day}$ and $R_n^{214} = (0.113 \pm 0.006)\,\mathrm{counts/day}$.

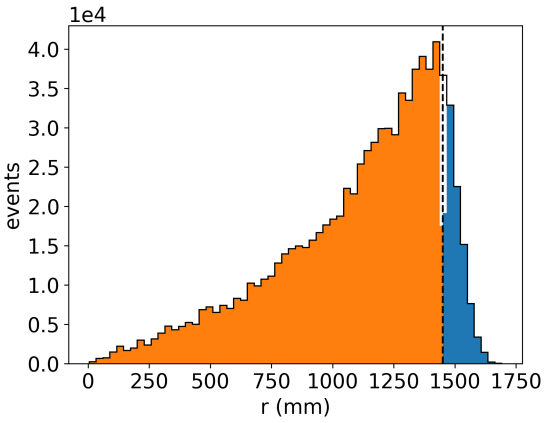

Radial distribution of first neutron capture

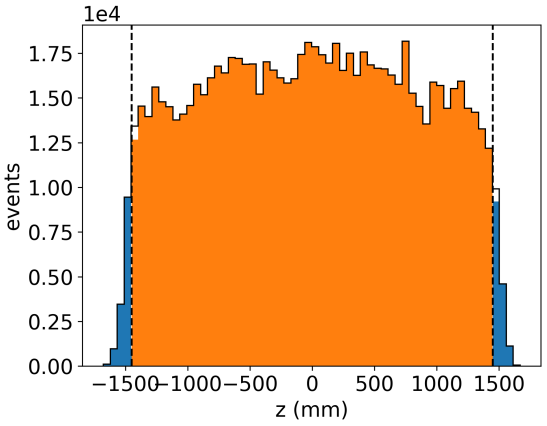

Axial distribution of first neutron capture

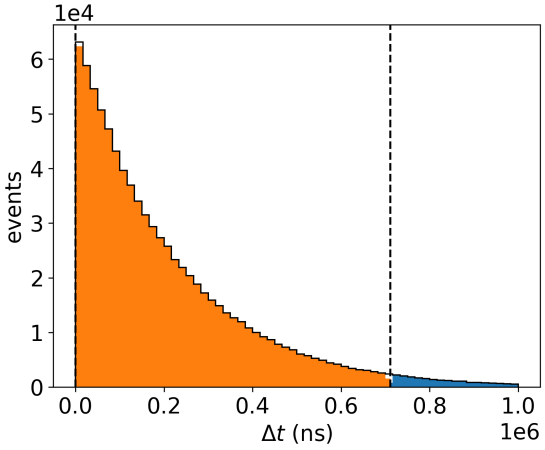

Time difference between the neutron captures

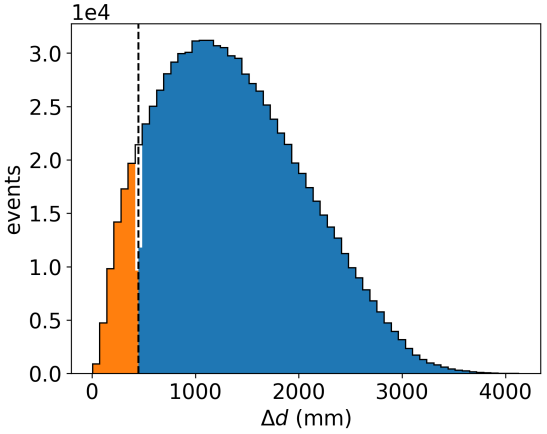

Spatial difference between the neutron captures

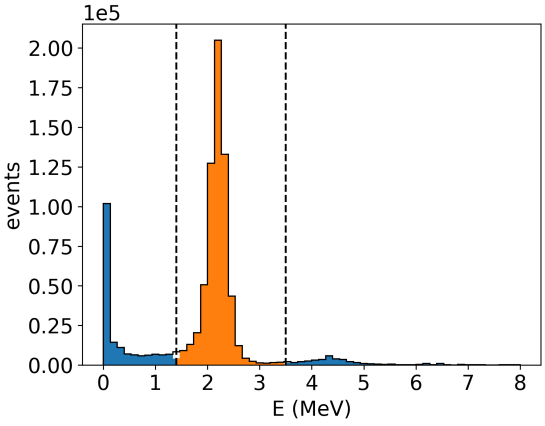

Visible energy of first neutron events

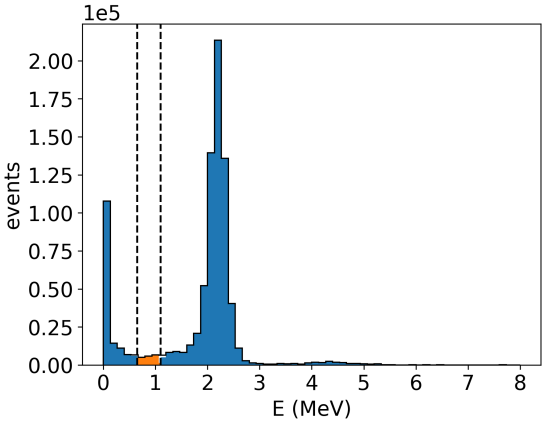

Visible energy of second neutron events

Figure 7.7: Distributions of muon induced neutrons regarding the BiPo acceptance cuts exemplary for the ^{214}BiPo coincidence signal. The cut windows are depicted with the dashed lines with events within the window in orange and outside in blue. For bins, which contain the cut value, the bin content is split up. The black line indicates the original bin height, resulting in the visible white areas below. The spatial distributions of the neutron capture position are connected to the track characteristics of the initial muon events and the cylindrical shape of the acrylic vessel. The temporal difference distribution and the energy spectra of the two independent events reflect the characteristic neutron capture properties. The spatial distance distribution renders the non-random event position distribution, caused by the common initial muon.

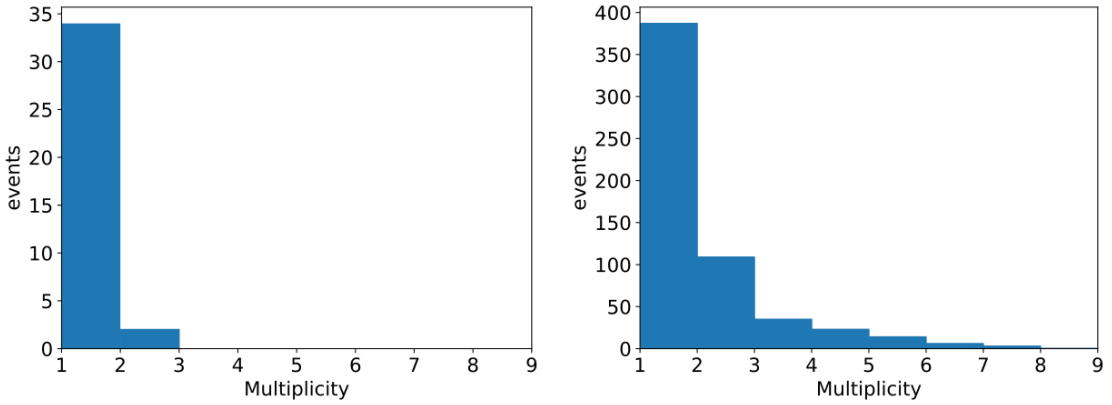

^{212}BiPo-mimic multiplicity ^{214}BiPo-mimic multiplicity

Figure 7.8: Multiplicity of BiPo imitating events from secondary neutrons for ^{212}BiPo and ^{214}BiPo in the simulated muon sample. Here only events with at least one BiPo mimic event are considered.

7.2.4 BiPo coincidence signals by heavier secondary isotopes

The imitation of the BiPo coincidence signal by muon induced secondary isotopes heavier than neutrons is restricted to decaying isotopes which can induce two signals in the liquid scintillator. In order to pass the BiPo cuts, two processes with energy deposition in the fiducial volume in a distinct time difference are required. This signature is only provided by isotopes decaying via β-decay with subsequent emission of a neutron. Furthermore, only isotopes decaying inside the liquid scintillator volume are to be considered, as the initial β particle cannot cross the acrylic material of the central detector vessel and hence no energy deposition in the liquid scintillator is possible. Since the isotopes initially produced in the water volume also can not pass the acrylic material, only isotopes created in the liquid scintillator come into question to mimic the BiPo coincidence signal.

Given these restrictions on the secondary isotopes from initial muon events, the potential background candidate distribution in figure 7.2, where all secondary isotopes produced in the simulation volume are considered, amends to the distribution in figure 7.9, where only isotopes produced in the liquid scintillator volume are taken into account. This leaves ^{8}He and ^{9}Li as potential background sources, induced by muons in the water volume. Both isotopes decay via the emission of a β^--particle, which can be followed by the emission of a neutron or a gamma photon depending on the branching ratio.

As mentioned in section 6.1.3, the implementation of the decays of ^{8}He and ^{9}Li in geant4 does not cover the branches involving the emission of a neutron. In the updated model, the neutron emission is implemented with the Q-value of ^{8}He $Q = 10.66\,\mathrm{MeV}$, the decay time $\tau = 171\,\mathrm{ms}$ and the ratio of decays including neutron emission $R = 16\,\%$. For ^{9}Li the values are $Q = 13.6\,\mathrm{MeV}$, $\tau = 257\,\mathrm{ms}$ and $R = 51\,\%$. The other decay branch consists of the prompt emission of a gamma photon after the β-decay for both isotopes [123].

The amount of generated secondary isotopes in the simulated muon sample is too small, to make a statement about the capability to pass the BiPo event cuts with statistical significance. For that reason, a sample of 10^5 single isotopes is simulated in the liquid scintillator volume with random position and momentum distribution for ^{8}He and ^{9}Li respectively. Due to the low production rate, only single isotopes are considered. The kinetic energy is sampled from the distribution of the secondary isotopes, produced in the muon simulations. The analysis of the data is analogous to the approach for the neutron based data in section 7.2.3.

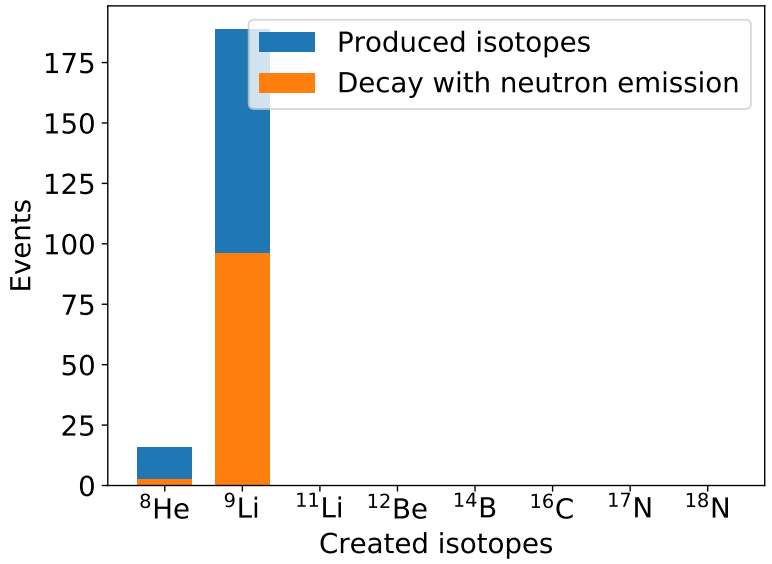

Figure 7.9: Muon induced isotopes in the liquid scintillator volume produced in 1.1×10^8 simulated muon events in the water volume. The comparison with figure 7.2 shows that isotopes from the muon interaction with oxygen nuclei in the water can not enter the liquid scintillator volume, which leaves ^{8}He and ^{9}Li as the only potential background candidates.

In the figures 7.10 and 7.11, the distributions for the initial vertex, the spatial and temporal distance and the deposited energies of the prompt and delayed events for the simulated ^{9}Li and ^{8}He events that contain the emission of a neutron are depicted. The positional distributions (radial and axial) follow the random vertex creation for the simulated events. The distributions of the spatial and temporal distance, between the initial β-decay and the delayed energy deposition after the neutron capture, are mainly driven by the thermalization process of the neutron. While the energy of the β-particle is instantly deposited in the detector, the mean neutron capture time after the emission is 216 μs. During this thermalization time, the neutron undergoes several collisions with nuclei in the volume, which explains the broad distance distribution compared to the point-like decay event. It is additionally widened by the imperfect position reconstruction for neutron capture events. The distributions of the deposited energy of the first and the second event in the detector depict the initial β-decay, indicated by the characteristic continuous spectrum for the prompt event, followed by the characteristic spectrum for the energy deposition of the emitted neutron. As indicated by the orange part of the histogram, the energy cut window for the ^{214}Bi β-decay, covers the maximum at approximately 2.0 MeV, which is characteristic for the β-decay of ^{9}Li and caused by a decay branch with an excited energy state of the daughter nucleus (see section 6.1.3). The β-decay spectrum of ^{8}He shows no distinct features. The delayed spectra show two peaks at $E_{2,\,edge} \approx 0$ MeV and $E_{2,\,n} \approx 2.2$ MeV. The first peak belongs to neutrons, that either leave the liquid scintillator volume and are captured at a hydrogen atom in the water volume or are capture close to the edge of the acrylic vessel. In both cases it is possible that none or only a part of the gamma photon energy is deposited in the scintillator volume. The latter case leads to the continuous energy distribution between the two peaks. The second peak describes the full energy deposition of the emitted gamma photon in the neutron capture in the liquid scintillator (for more details see section 7.2.3). Compared to figure 7.7, the peaks at $E_{2,\,2n} \approx 4.4$ MeV and $E_{2,\,3n} \approx 6.6$ MeV, are not present, as only one neutron accompanies the decay. As for the simulated neutron sample, the restrictions on the energy of the delayed event (polonium decay in the BiPo coincidence signature) and for ^{212}BiPo also the time difference cut are

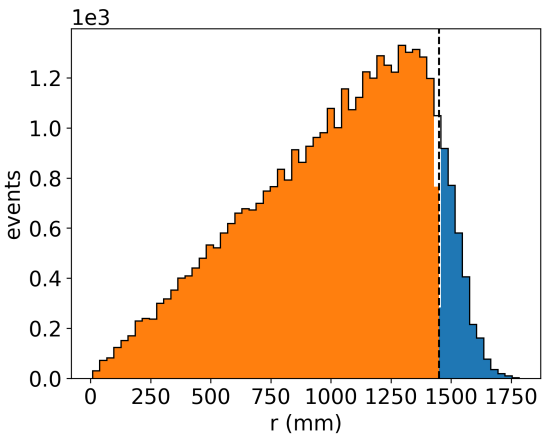

Radial distribution of decay position

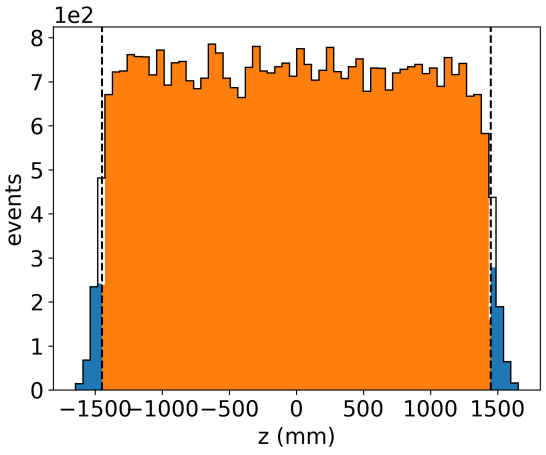

Axial distribution of decay position

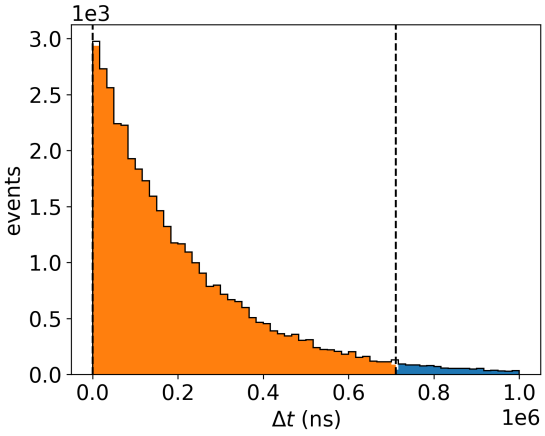

Time difference between the two events

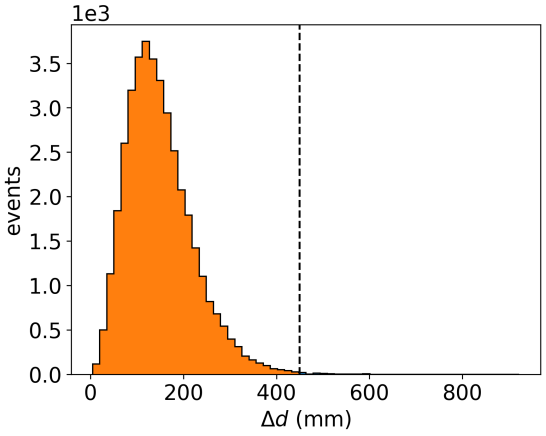

Spatial difference between the two events

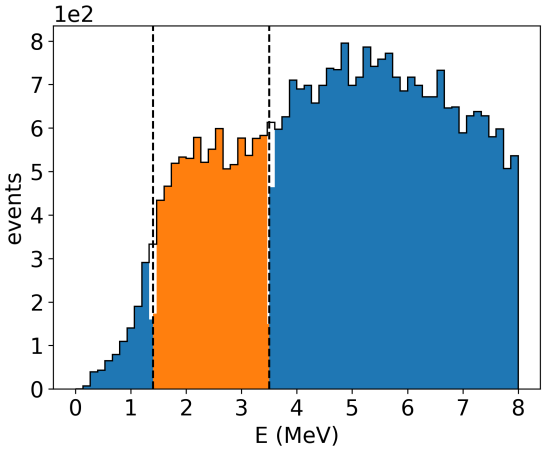

Visible energy of the prompt events

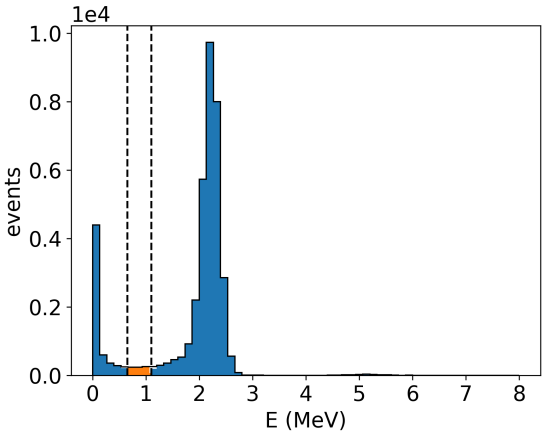

Visible energy of the delayed events

Figure 7.10: Decay signature of the simulated ^{9}Li sample with respect to the ^{214}BiPo coincidence limits. The positional distributions show the random vertex creation for the isotopes in the detector volume. The temporal and spatial difference cut limits contain the majority of the events (orange) The distributions are mainly affected by the nature of the neutron capture process as the point-like β-decay of the isotopes determines the start of the coincidence signal followed by the delayed neutron capture. The energy distribution of the first detected event represents the β-decay spectrum with the characteristic low-energetic shoulder, which is covered by the bismuth energy cut limits. The second energy spectrum shows the characteristic peaks of the neutron capture (see section 7.2.3). The polonium energy cut is apparently the most efficient cut to reject BiPo mimicking coincidences by heavier secondary isotopes (compare table 7.4).

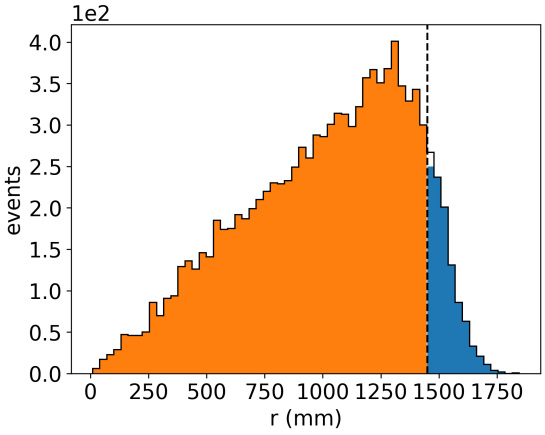

Radial distribution of decay position

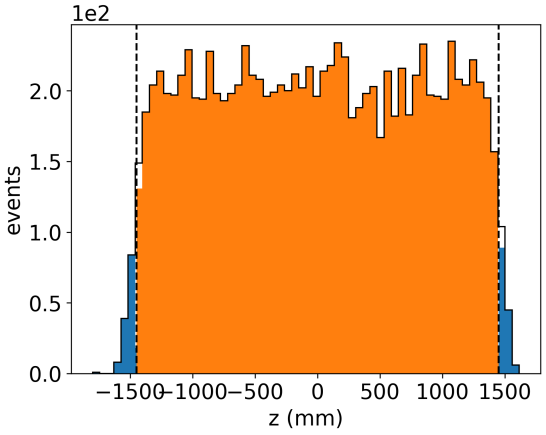

Axial distribution of decay position

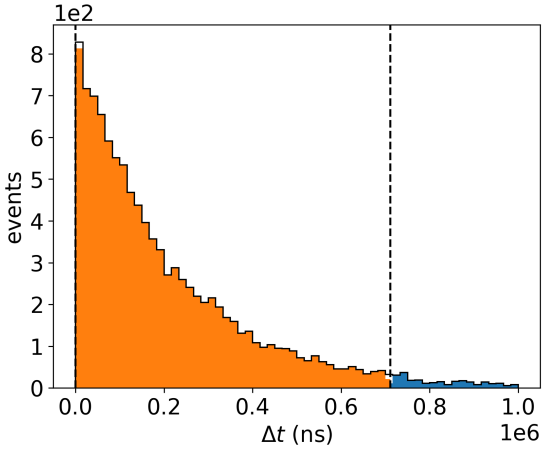

Time difference between the two events

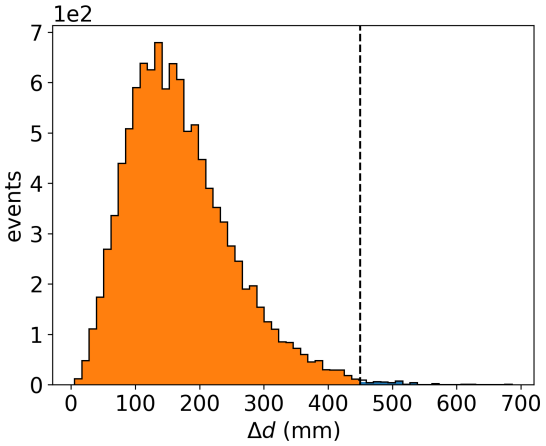

Spatial difference between the two events

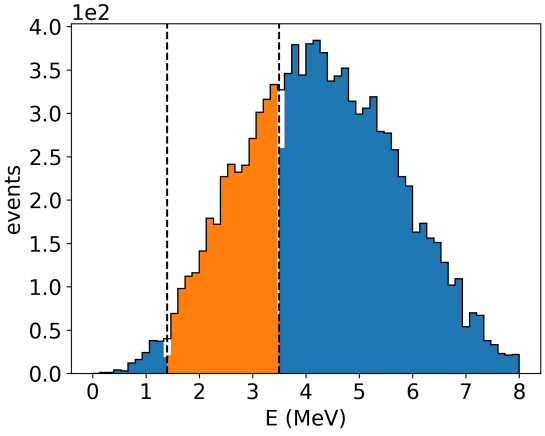

Visible energy of the prompt event

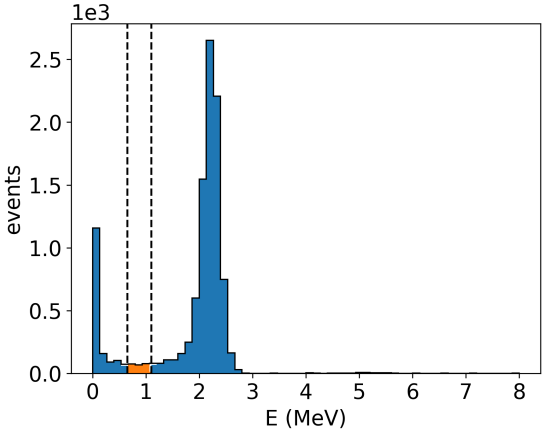

Visible energy of the delayed event

Figure 7.11: Decay signature of the simulated ^{8}He sample with respect to the ^{214}BiPo coincidence limits. The positional distributions, the temporal and spatial difference distributions and the delayed energy spectrum are similar to figure 7.10. The energy distribution of the prompt detected event represents the β-decay spectrum of ^{8}He. For ^{8}He decay events, also the polonium energy cut is the most efficient cut to reject BiPo mimicking coincidences (compare table 7.4).

Table 7.4: Suppression efficiency for muon induced ^{8}He and ^{9}Li background events based on the BiPo event cuts derived from gamma background analyses (see table 7.2). Comparable to the secondary neutron background (see table 7.3), the energy cut for the second event excludes most of the background events for both isotopes and furthermore, the time cut limits allow to discriminate the majority of the false ^{212}BiPo coincidence events. The fiducial volume cuts are not considered, as the simulated isotope events are placed randomly and not connected to the initial muon event. The combined rejection efficiency for the ^{212}BiPo coincidence signal is only stated as a lower limit, as for none of the simulated events the cut conditions are met.

		Suppression			
		^{8}He		^{9}Li	
Cut parameter		^{212}BiPo cuts	^{214}BiPo cuts	^{212}BiPo cuts	^{214}BiPo cuts
Energy	E_{Bi}	87.5 %	69.5 %	82.3 %	72.2 %
	E_{Po}	97.7 %	98.8 %	96.3 %	98.2 %
Time difference	Δt	99.5 %	46.1 %	99.6 %	51.6 %
Spatial distance	Δd	0.1 %	0.4 %	0.1 %	0.2 %
Combined		$\geq$ 99.999 %	99.993 %	$\geq$ 99.999 %	99.994 %

the dominant rejection parameters. The efficiencies of the different event cuts are listed in table 7.4.

With the simulated isotope samples, the probability for a ^{8}He and ^{9}Li decay event to pass the BiPo coincidence cuts can be calculated. While the ^{212}BiPo cuts are passed in neither of the two samples, the ^{214}BiPo are passed by seven ^{8}He and by six ^{9}Li decay events. Therefore, for the expected ^{212}BiPo mimic rate, only a upper limit can be stated. Combining the number of events passing the BiPo cut limits in the simulated sample, with the production rate of the respective isotope in the muon sample, the expected rates for mimicked BiPo signals are $R_{iso}^{212} \leq (3.8 \pm 0.3) \times 10^{-7}$ counts/day and $R_{iso}^{214} = (4.9 \pm 0.4) \times 10^{-6}$ counts/day. Applying the correction factors from the comparison of simulation and experimental results from Borexino (see section 7.1.3), the expected ^{214}BiPo mimic rates increases to $R_{iso}^{212} \leq (7.1 \pm 0.4) \times 10^{-7}$ counts/day and $R_{iso}^{214} = (9.2 \pm 0.5) \times 10^{-6}$ counts/day. Compared to the neutron based background contribution, these rates are negligible and do not influence the required veto efficiency.

7.2.5 Accidental coincidences with external gamma photons

In approximately 4.3×10^{4} of the simulated events only one neutron is captured in the liquid scintillator and surrounding water volume (see figure 7.6), which corresponds to an expected rate of $R_{n,\,single} \approx (11.69 \pm 0.06)$ counts/day. As single particles, these neutrons can not imitate a BiPo signal, but in connection with the gamma background, accidental coincidences might mimic the signal. The gamma background is analyzed in detail in [120] and is estimated with a rate of $R_{\gamma} = 35.92\,\mathrm{s}^{-1}$ or $R_{\gamma} = 6.32\,\mathrm{s}^{-1}$ respectively for gammas depositing energy in the liquid scintillator volume, depending on whether the ^{14}C is considered as background source or not (see table 5.3 and 5.4). All potential sources are considered including internal contaminations in the liquid scintillator as well as radioactive isotopes in the surrounding water and rock volumes as the main contributors. Gamma photons from ^{14}C in the liquid scintillator are low energetic and thus only are an issue for the ^{212}BiPo coincidence signal, where the energy window of the polonium decay comes within the limits of the respective gamma energies. For the analysis of random ^{214}BiPo coincidences, gammas from ^{14}C are excluded.

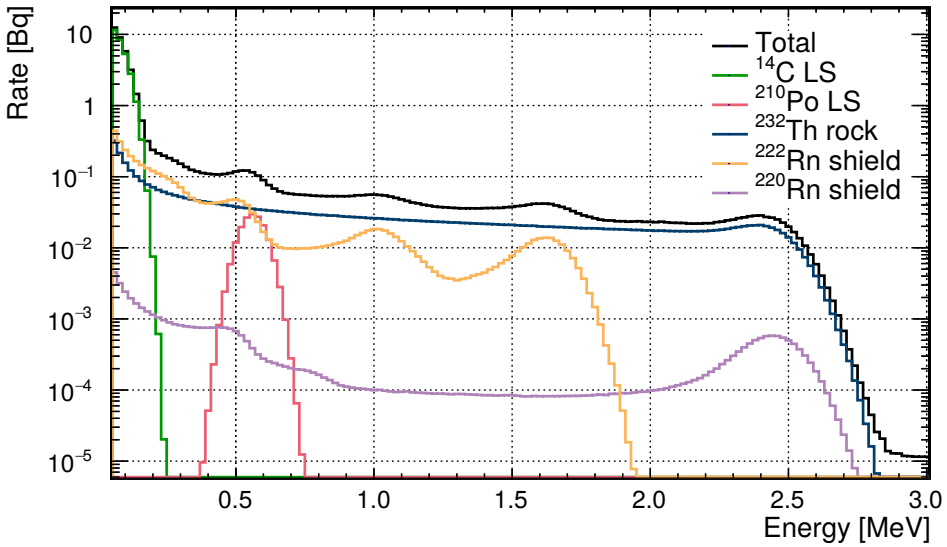

Figure 7.12: Visible energy spectrum of the expected gamma background in the liquid scintillator. The spectrum is defined by internal ^{14}C contaminations for the lower energy regions and by ^{222}Rn and ^{232}Th in the surrounding water and rock volume for higher energies. Picture from [120].

Without the application of the other BiPo cut limits, the accidental coincidence rate of single neutrons and gamma photons from external and internal sources is given by

$$R_{\gamma,n} = R_{n,\,single} \cdot R_{\gamma} \cdot \Delta t, \tag{7.4}$$

where the respective time window for the BiPo cut is applied to Δt. The expected accidental coincidence rate is $R^{212}_{\gamma,n} = (5.92 \pm 0.04) \times 10^{-4}$ counts/day for the ^{212}BiPo coincidence ($\Delta t = 1.998\,\mu$s) signal with ^{14}C gammas and $R^{214}_{\gamma,n} = (3.71 \pm 0.02) \times 10^{-2}$ counts/day for the ^{214}BiPo coincidence ($\Delta t = 711.998\,\mu$s) signal without ^{14}C gammas, which is in the same order of magnitude as the muon induced background based on secondary neutrons only.

In order to take into account the further BiPo event selection cuts, listed in table 7.2, two sets of $\approx 10^5$ single gamma events are simulated in the liquid scintillator with random position and direction distribution. The energy of the respective events is sampled from the distribution depicted in figure 7.12, once with gammas from ^{14}C and once without. To determine the rate of accidental trigger events, each event of the simulated muon sample containing a single neutron captured in the liquid scintillator is combined with 100 randomly selected events from the simulated gamma sample. The analysis shows that only a small fraction of the simulated coincidence events passes the cuts, which reduces the accidental rate to $R^{212}_{\gamma,n} = (4.7 \pm 0.1) \times 10^{-8}$ counts/day for the ^{212}BiPo coincidence signal and $R^{214}_{\gamma,n} = (4.1 \pm 0.2) \times 10^{-6}$ counts/day for the ^{214}BiPo signal. Compared to the neutron induced coincidences, where the cut condition of the polonium event is only met by specific neutrons that are captured close to the edge of the acrylic vessel, for random coincidences of gammas and single neutrons this cut is weaker as the energy distribution of the gamma background better fits the respective cut window. As the single neutrons and the gamma photons are independent events, the distance cut is most effective to reject this background, besides the time distance cut, which is already considered in the calculation of the accidental coincidence rate. The efficiencies of all cut parameters are listed in table 7.5.

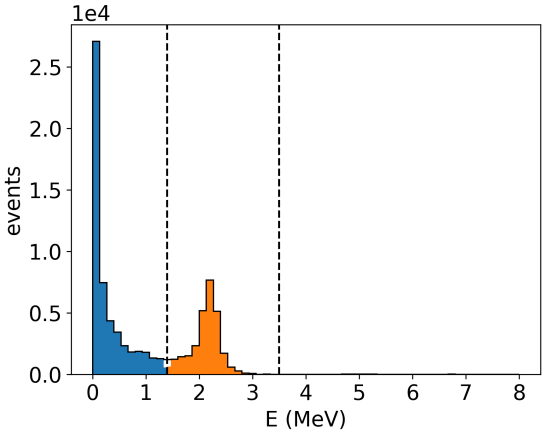

Energy distribution of the prompt event

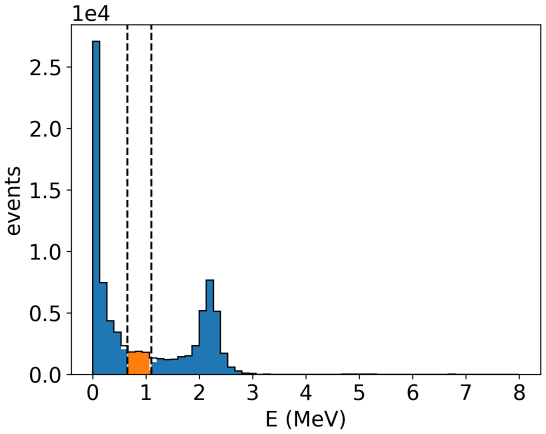

Energy distribution of the delayed event

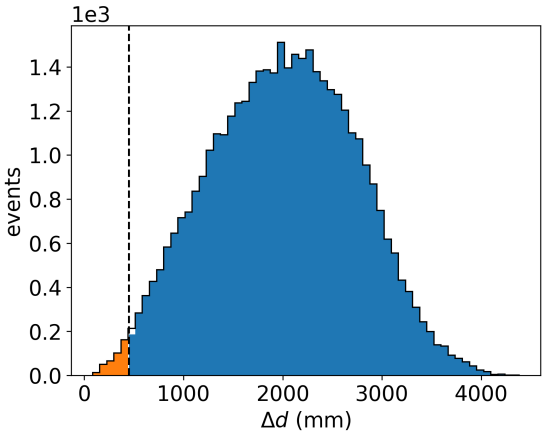

Spatial difference between the two events

Figure 7.13: Distributions of accidental coincidence events of cosmogenic neutrons and gamma photons from external and internal sources in the OSIRIS detector with respect to the ^{214}BiPo coincidence limits. The position distributions of the two different event types are identical to the distributions in figure 7.7 for neutrons and to the distributions in figure 7.10 for gamma photons.

Table 7.5: Suppression efficiency for accidental coincidences of muon induced single neutrons and gamma photons from radioactive contamination in external volumes and in the liquid scintillator. The fiducial volume cuts are combined for the background sources. Due to the independent origin of the background components, the spatial distance cut is dominant, followed by the cut on the polonium decay energy, which is rarely met by the deposited energy from a captured neutron.

Cut parameter		Suppression ^{212}Bi – ^{212}Po cuts	Suppression ^{214}Bi – ^{214}Po cuts
Fiducial volume	Neutrons	21.8 %	22.1 %
	Gamma photons	2.7 %	3.9 %
Energy	E_{Bi}	60.2 %	66.4 %
	E_{Po}	86.6 %	87.7 %
Spatial distance	Δd	97.4 %	99.3 %
Combined		99.992 %	99.98 %

7.3 Requirements on the OSIRIS muon veto efficiency

As shown in the previous sections, the muon induced background in the BiPo coincidence search is composed of different channels which are two-neutron capture events, the decay of heavier isotopes and the accidental coincidence of single neutrons and internal and external gamma photons. The simulations of these backgrounds show that the coincident signal of secondary neutrons from a joint initial muon track is the largest contribution to the background of the BiPo signal search and surpasses the other background channels by at least four orders of magnitude. With the sum of all muon induced background contributions, the total expected muon induced background rates for the two different BiPo event signatures are $R_{\mu,212} = (0.010 \pm 0.002)$ counts/day and $R_{\mu,214} = (0.113 \pm 0.006)$ counts/day.

In order to identify the neutrino mass hierarchy with JUNO by the IBD detection channel, strict limits are set on the radiopurity of the liquid scintillator. The contamination with isotopes of the ^{238}U- and ^{232}Th-chain may not exceed 1×10^{-15} g/g of liquid scintillator respectively. These limits translate to an activity of $A_{^{214}\mathrm{BiPo}} = 1.2 \times 10^{-8}$ Bq/kg for the ^{214}BiPo coincidence signal and $A_{^{212}\mathrm{BiPo}} = 0.4 \times 10^{-8}$ Bq/kg for the ^{212}BiPo coincidence signal, assuming secular equilibrium. At these activity limits, the expected number of true BiPo coincident events detected by OSIRIS are $R_{^{212}\mathrm{BiPo}} = (6.6 \pm 2.6)$ counts/day and $R_{^{214}\mathrm{BiPo}} = (19.7 \pm 4.4)$ counts/day. To pursue the solar physics program with JUNO the required contamination limit is smaller by one order of magnitude for both decay chains, which results in detection rates of $R_{^{212}\mathrm{BiPo}} = (0.7 \pm 0.8)$ counts/day and $R_{^{214}\mathrm{BiPo}} = (2.0 \pm 1.4)$ counts/day in the OSIRIS detector. By comparing these rates with the muon-induced coincidence signals, the fraction of cosmogenic background compared to the true signal rate can be determined. The results are shown in table 7.6.

The impact of muon induced background signals is larger on the ^{214}BiPo coincidence signal by one order of magnitude (see table 7.6). Therefore, assuming equal contamination of the ^{238}U and ^{232}Th chains, the required veto efficiency is determined by the ^{214}BiPo-activity and the corresponding background rate. The required efficiency ε_{veto} is calculated as follows:

$$\varepsilon_{veto} = 1 - \frac{f_{BG} \cdot A_{^{214}\mathrm{BiPo}} \cdot M_{fiducial}}{R_{\mu,214}}, \tag{7.5}$$

with the fraction of muon induced background signals to the BiPo coincidence signal f_{BG}, the fiducial mass of OSIRIS $M_{fiducial}$ (here $M_{fiducial} = 19$ t) and the muon-induced background rate in the ^{214}BiPo-channel $R_{\mu,214}$. In figure 7.14, the required veto efficiency is depicted with respect to the ^{238}U contamination for 1 %, 2 % and 5 % of muon induced background admixture to the expected signal rate. It shows that for the minimum JUNO contamination requirements of $C \leq 1 \times 10^{-15}$ g/g the influence of the muon induced background to the OSIRIS sensitivity is negligible. For a contamination of $C = 1 \times 10^{-16}$ g/g (the solar physics limit) and a contribution of muon induced background of $f_{BG} = 5\,\%$, the required rejection efficiency for muon induced background is accordingly

Table 7.6: Proportion of muon induced background signals compared to expected BiPo signals in dependence of the liquid scintillator contamination and thus the provided detection channel.

Physics	Contamination limit	Fraction of cosmogenic background ^{212}Bi – ^{212}Po	^{214}Bi – ^{214}Po
IBD	1×10^{-15} g/g	0.15 %	0.57 %
Solar	1×10^{-16} g/g	1.4 %	5.7 %

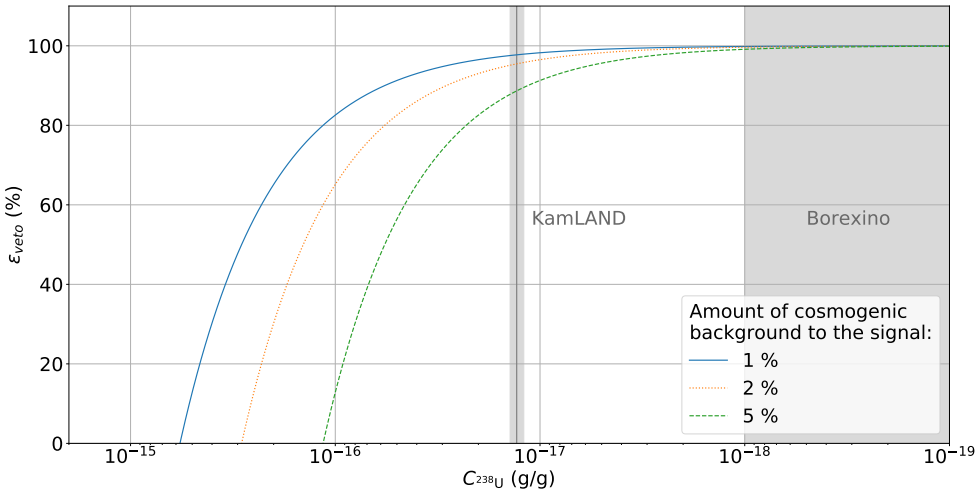

Figure 7.14: Minimum required veto efficiency in dependence of the liquid scintillator contamination for different admitted contributions of muon induced background to the expected BiPo signal. In this case the contamination of ^{238}U-chain elements is chosen, as here the proportion of cosmic background events is larger. Additionally, the respective contamination levels of the KamLAND and Borexino experiment are presented (Data from [121]).

$\varepsilon_{veto} \geq 84.5\,\%$. This value is used as benchmark for the development of the OSIRIS veto system which is presented in chapter 8. For the currently intended OSIRIS design, a veto efficiency of $\sim 95\,\%$ is expected. With this detection efficiency, the OSIRIS sensitivity to test the liquid scintillator for the solar requirements is not constrained by cosmogenic background and even smaller contamination levels in the range of $\sim 1 \times 10^{-17}$ g/g can be detected.

8. Development of the OSIRIS muon veto system with Monte Carlo simulations

The development of the veto system was incorporated to the OSIRIS design process at a stage when the main components were already defined. The volume of the water shield and the position of the detector PMTs and with them the dimensions of the steel frame were optimized with respect to reduce the flux of external gamma photons in the liquid scintillator volume from the surrounding rock and the PMTs to a minimum. For this reason, the design of the veto system is restricted by specific boundary conditions. The remaining design parameters by which the muon detection efficiency of the veto system can be optimized are the number and the positions of the veto PMTs, the optical properties of the liner which covers the steel tank and the optical separation foil which was introduced during the veto design development. The following chapter describes the work on the design of the OSIRIS muon veto and the corresponding muon detection efficiency, which are elaborated for the purpose of this work. Initially, the implementation of the veto components in the simulation framework and several veto designs are described (section 8.1). Furthermore, the necessity and realization of the optical separation are discussed (section 8.2). With the finalized model of the veto system, the performance parameters (section 8.3) and muon detection efficiency (section 8.4) are tested. Finally, the impact of the veto on the dead time and the OSIRIS sensitivity are discussed (section 8.5).

8.1 Implementation of the veto system in the simulation framework

The development of the veto design and the detection optimization are based on the use of the OSIRIS simulation framework (see chapter 6) which was further extended for this purpose. The implementation of the veto system mainly affects the geometry class of the simulation framework, where the additional detector parts are defined. The creation and placement of the geometries can be chosen optionally to allow simulation runs in the original setting. Additionally, the material and surface database classes are extended to describe the newly introduced components properly. As for the other simulation modes (see section 6.1.4) the setting of the veto system parameters is realized via an external input file.

The veto PMT system

The PMTs of the veto system are implemented in the framework as a PMT subsystem, which allows the independent setting of a different veto PMT type and also a detached

data storage of the detected photons. Together with the central detector PMT subsystem, it defines the OSIRIS PMT system, which is organized in a dedicated class object and callable at any point in the simulation and data analysis process. The positions and the orientation of each PMT are freely adjustable in the entire water volume. Additionally, the design of the magnetic shield model (see figure 6.4) can be adjusted for both PMT subsystem independently. Aside from the length of the magnetic shielding cylinder, a realistically modeled mesh grid in front of the PMT can be added. However, in the current design of the shielding, the additional mesh grid is not foreseen.

The steel tank liner

With respect to the veto performance, the steel tank liner is an important component as it mainly defines the surface of the veto volume. As only its optical properties are concerned, the implementation of the steel tank liner is realized via an optically active surface on the inner side of the steel vessel, without the introduction of an additional geometry. The optical properties are defined by the total reflectivity and its specular and diffuse components, which are registered in the separate class that contains the optical properties of the implemented materials and geometries. In order to guarantee a sufficient timing resolution of the central detector PMT system, the reflections on the tank wall must be reduced to a minimum, which requires the installation of black liner material in the initial detector design. However, as shown below, the installation of an optical separation allows the selection of a highly reflective liner material, from which the muon detection efficiency of the veto system benefits.

For the final experimental setup, the liner material will be provided by the vendor of the steel tank. The two given options differ only in the color, where black and white are presumably available. As the optical properties are not provided by the vendor, the values are estimated based on similar material, available at the University in Mainz, and the measured values of the optical separation (see below), which are assumed to be similar. In case only black liner material is available (according to the vendor the demand for the white material is very low and a custom product), but it turns out that the reflective behavior is not sufficient for the veto system, a second option is foreseen. For this alternative approach, parts of the steel tank side and bottom walls are covered with an additional foil with differing optical characteristics, as here the installation is significantly facilitated compared to the top lid of the tank. To render this option in the simulations, additional geometries are implemented as a thin film on specific parts of the liner surface to which dedicated optical properties can be assigned.

The optical separation

As will be shown in section 8.2.2, the optical separation of the detector and veto PMT subsystem is essential to exclude false trigger signals for the muon veto from actual events in the liquid scintillator. Based on simulations with electrons in an energy range of $0-5\,\mathrm{MeV}$, about $90\,\%$ of the events in the liquid scintillator induce false veto triggers. Besides that, the optical separation allows to install a high reflective steel tank liner to increase the muon detection efficiency without increasing reflections in the central detector system. In order to facilitate the design and the installation, and to maximize the water volume for the veto system, the optical separation will be realized with a foil, attached directly to the stainless steel frame. The implementation in the simulation framework is realized via thin rectangles and triangles, which are automatically adjusted in size and position to fit the dimensions of the frame and the positions of the detector PMTs, as shown in figure 8.1. Additionally, there is a second model implemented in which each side plane consists of one continuous rectangle in which the PMT positions are not omitted. With this model, the impact of the inevitable openings in the implementation of the real optical separation

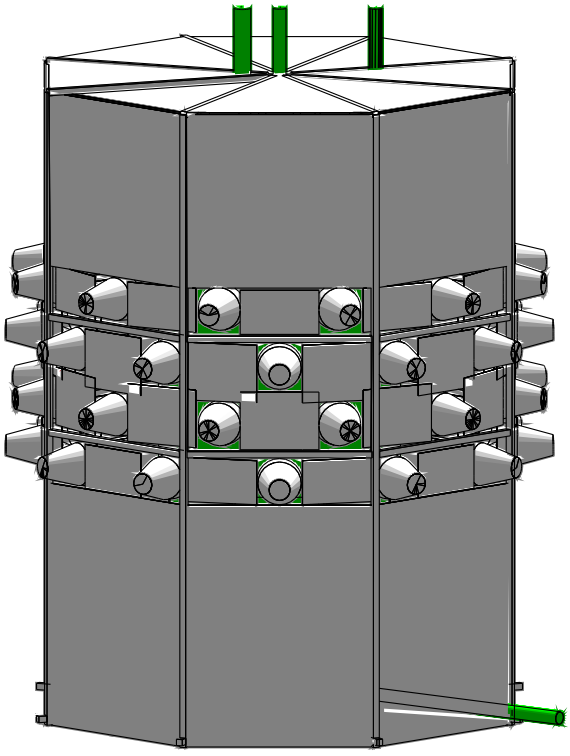

Figure 8.1: Implemented model of the optical separation in the OSIRIS simulation framework. The size and the position of the patches are calculated based on the dimensions of the steel frame and the PMT positions. The areas on top of the frame, and above and below the horizontally arranged central detector PMTs are covered with large foil pieces, while the areas between the PMTs are concealed with smaller patches which are aligned to the PMT positions. The impact of the reduced light shielding induced by the resulting gaps is studied in 8.2.3.

model can be examined. To enable different optical properties for the two sides of the separation foil, two separate volumes with half of the material thickness for each foil piece are implemented directly attached to each other. The resulting inner and the outer foil surfaces of each volume are grouped to a dedicated physical volume, which can be assigned with material and surface properties. Corresponding to the surface properties of the steel tank liner (see above), the total reflectivity as well as the specular and diffuse portion can be set.

8.2 Design studies based on Monte Carlo simulations

The decisions on the design of the OSIRIS muon veto system are mainly subordinated to maximize the number of identified muon tracks that traverse the water volume observed by the veto PMTs. Further conditions are minimizing additional background from the extra veto PMTs and the optical separation material, avoiding disruptions in the inner detector system due to the additional components and the technical feasibility. To find the ideal setting of the veto system components, dedicated simulations for the design options are performed with the respective parameters. Thereby, the initial setup is according to the geometry as depicted in figure 5.2 with the extension of a black liner covering the steel tank. Its reflective behavior is assumed to be identical to the black surface of the optical separation material (see section 8.2.3). The magnetic shielding of the PMTs is identical to the model for the inner detector PMT subsystem (see section 6.1.2), with an excess length of the shield to the PMT tip of $d = 50\,\mathrm{mm}$.

Each simulation run consists of 1×10^6 single muon events starting on random surface positions of the steel tank and exclusively traversing the water volume of the detector. The angular and energetic distributions are corresponding to the description in section 6.2. For each simulation run, the same initial starting parameters for the muon sample are used (position, direction, energy) to guarantee comparable results. For the investigation of the ideal PMT distribution (position and direction) the average number of detected Cherenkov photons per track length of the muon is used as performance parameter. After the placement of the veto PMTs and the definition of several trigger signals adjusted to the number of PMTs and their arrangement, the fraction of detected muon events is used as reference value for the veto efficiency.

8.2.1 Positions of the veto PMTs

When the development of the veto system was started, the decision on the PMT model and the acquisition were already taken. The order of 80 HamR12860HQE 20 inch contained up to 12 PMTs that were assigned to be installed in the veto system. The ensemble of the veto PMTs is positioned to maximize the mean number of detected photons in the simulated muon sample per muon path length. This is affected by the observed water volume by each PMT and possible shadowing by components of the OSIRIS setup. Besides that, the PMTs must be distributed homogeneously to maximize the coverage of the veto volume and thus the veto efficiency.

However, due to the already established basic design of OSIRIS, the PMT locations in the water volume can not be chosen freely. On the outer side of the steel frame, all positions close to a steel bar are conceivable. Locations further away from the scaffolding would require additional holding structures, which would complicate the setup and could introduce vibrations. Hence, these positions are to be avoided. Since the steel tank is covered with liner, the attachment of PMTs requires a careful sealing to avoid water leakage and following corrosion of the vessel. Such sealings are already realized on the floor of the tank, where the steel frame is attached. Therefore, the implementation of further sealings on the bottom part of the liner for potential PMT mountings are feasible for the vendor. However, mountings on the side of the cylindrical steel tank and the top lid are again to be avoided to reduce complexity of the liner production and installation.

In figure 8.2, four of the tested PMT placement schemes are depicted. The bottom PMTs, surrounding the steel frame are placed directly on the ground of the steel tank. The top PMTs are mounted on the frame, either directly on a steel bar or via extensions (Model D). In contrast to the others, model A only contains 8 PMTs, with the idea to add PMTs to the detector system to increase the OSIRIS energy resolution. It consists of four PMTs on the floor of the steel tank and four PMTs on top of the frame. The models B and C contain eight PMTs on the floor of the tank and only differ in the placement of the four top

Table 8.1: Light detection performance of the PMT placement models defined by the mean number of detected photons per muon track length and the mean number of hit PMTs. The distributions are depicted in figure 8.3.

Model	Mean detected photons per muon track length (photons/m)	Mean hit PMTs
A	39.9 ± 34.7	3.8 ± 1.4
B	75.2 ± 55.2	3.5 ± 1.8
C	72.4 ± 53.8	3.2 ± 2.0
D	62.9 ± 46.7	2.9 ± 2.1

PMTs. In model B, the top PMTs are installed centrally and directed radial to the steel tank wall. In model C (also Models A and D), the PMTs are installed inbound on the edge of the steel frame with a tilt of 30°. This has the advantage, that each top PMT observes a larger water volume and possible shadowing induced by the pipes is reduced. However, the attachment of these PMTs to the frame, requires a more sophisticated mounting. In model D, two PMTs are moved from the tank floor to the top of the steel frame to test different distributions.

In table 8.1, the mean number of detected photons per muon track length and the mean number of hit PMTs in the simulated muon sample for the respective PMT placement are listed. Additionally, the photon detection distributions are depicted in figure 8.3. Both show that the number of detected photons per muon track length strongly depends on the chosen PMT placement and that the models B and C have an increased detection efficiency. Also the mean number of hit PMTs per muon event depends on the PMT placement but with a smaller effect. Based on these results, Model B shows the best photon detection capability and thus is chosen for the further studies.

8.2.2 Veto Trigger

With the number and positions of PMTs in the veto system fixed, specific trigger conditions can be defined with the goal to maximize the detection efficiency of atmospheric muons. The goal is to detect as many muon tracks in the veto volume including tracks with short path lengths in the water volume resulting in a low number of detected Cerenkov photons. However, a too aggressive condition, where e.g. the number of to be detected photons is chosen very small, leads to accidental trigger signals, induced by the dark counts of the PMTs in the veto system. Dark counts are signals which do not originate from photon interactions with the cathode, but from the thermally induced emission of electrons from the cathode and the dynodes [63]. These two restrictions must be pondered to achieve a robust and sensitive trigger condition. Due to the installation of iPMTs (see section 5.2), each PMT can be read-out independently, which allows various combinations and logic for the trigger algorithms. Within this thesis, three conditions are defined to derive the muon detection efficiency of the veto system. In a dedicated script where the photon data of the simulated muon tracks is read-out and examined, the tested trigger conditions are:

1. Within the time window Δt at least n of the veto PMTs detect each at least m photons.
2. Within the time window Δt at least m photons are registered in total by an arbitrary number of veto PMTs.
3. Within the time window Δt at least n_1 adjacent bottom PMTs or minimum $n_{2,1}$ adjacent bottom PMTs and $n_{2,2}$ top PMTs register each at least m photons.

The third condition, which exploits the locally increased light emission close to a muon track, is more sophisticated compared to the first two, which treat all PMTs equally. With a larger time window Δt and smaller values for the number of hit PMTs n and photon detection threshold m, the sensitivity of the trigger conditions increases but also the rate of accidental trigger events caused by dark counts of the PMTs.

According to [74], the dark count rate R_{DC} for the Hamamatsu PMTs in OSIRIS is typically at 20 kHz but can also reach up to 50 kHz. Internal tests at the RWTH Aachen University indicate that none of the OSIRIS PMTs exceeds a dark count rate of $R_{DC} = 15$ kHz, which will be applied in the following calculations. As the occurrence of a dark count event in a PMT is totally random, the probability P to register x dark count events

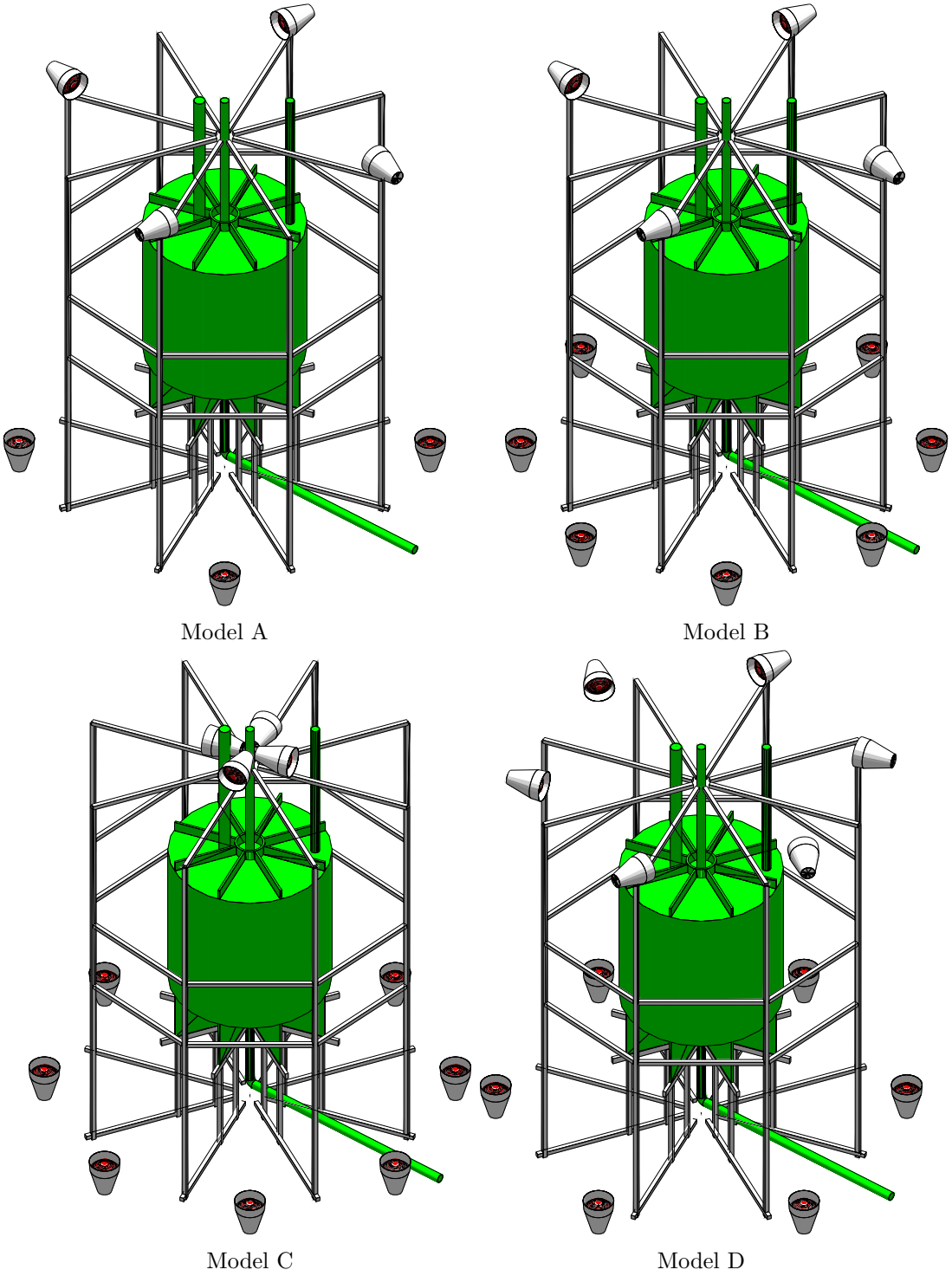

Figure 8.2: Illustration of four possible veto PMT position models in the simulation. The acrylic vessel and the pipes are show in green. For reason of visibility, the detector PMTs and the optical separation are not shown. The veto PMT placement in figure 5.2 corresponds to model B.

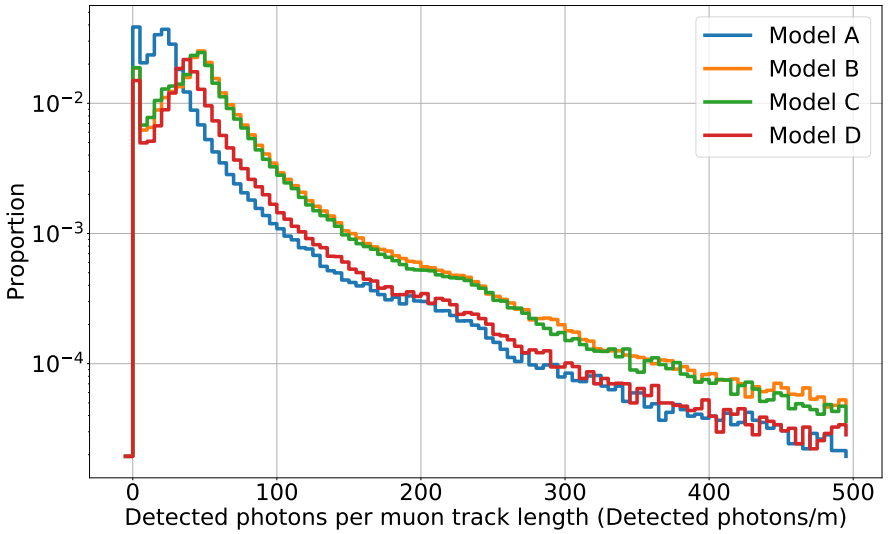

Figure 8.3: Number of detected photons with the tested PMT placement models for the simulated muon sample. Corresponding to the calculated mean values (listed in table 8.1), models B and C show a higher photon detection efficiency compared to the other models.

within a given time window Δt is Poisson distributed and given by

$$p(x) = \frac{(\Delta t \cdot R_{DC})^x}{x!} \exp(-\Delta t \cdot R_{DC}). \tag{8.1}$$

As stated above, one parameter of the trigger conditions is the photon detection threshold m per PMT. The probability to undercut this threshold with dark counts is given by $P_0 = \sum_{x=0}^{m-1} p(x)$. Accordingly, the probability to pass the threshold is $P_1 = 1 - P_0$. For the first condition, the rate of false veto triggers solely by dark count events is given by

$$R_{DC,trigger} = N \cdot R_{DC} \sum_{i=n-1}^{N-1} \binom{N-1}{i} \cdot P_0^{N-i-1} \cdot P_1^i, \tag{8.2}$$

with N as the number of PMTs in the veto system.

For trigger condition two, where the sum of detected photo electrons by all veto PMTs is considered, the case that a single PMT can detect more than one dark count event (equation 8.3) must be regarded. The probability that one PMT detects k or more dark counts within the time window Δt is given by $p_x = \sum_{x=k}^{\infty} p(x)$. By combining all cases with m or more detected dark counts by the veto system within one trigger window, the trigger rate is given by:

$$
\begin{aligned}
R_{DC,trigger} = N \cdot R_{DC} \Bigg(& \sum_{i=0}^{N-2} \binom{N-1}{1} \cdot p_m \cdot \binom{N-1}{i} \cdot p_1^i \cdot p_0^{N-i-1} \\
& + \sum_{i=0}^{N-3} \binom{N-1}{2} \cdot (p_{m-1} \cdot p_1 + p_{m-2} \cdot p_2 + ...) \cdot \binom{N-1}{i} \cdot p_1^i \cdot p_0^{N-i-1} \\
& + \sum_{i=0}^{N-4} \binom{N-1}{3} \cdot (p_{m-2} \cdot p_1^2 + p_{m-3} \cdot p_2 \cdot p_1 + ...) \cdot \binom{N-1}{i} \cdot p_1^i \cdot p_0^{N-i-1} \\
& + ... \\
& + \sum_{i=0}^{N-m-1} \binom{N-1}{i} \cdot p_1^{m+i} \cdot p_0^{N-m-i-1} \Bigg).
\end{aligned} \tag{8.3}
$$

It must be considered that terms of the sum with invalid expressions (e.g. m>N, negative indices for p) are neglected. Due to the decreased probability for more than one dark count detection by a PMT, terms with only PMTs with one hit (only p_1) are dominant. For that reason, trigger models 1 and 2 have similar dark count rates for comparable trigger parameters (see table 8.2).

For trigger model 3, where only adjacent hit PMTs are considered, the calculation of the dark count induced trigger rate must be divided into two cases. If n_1 adjacent PMTs on the bottom ring are considered, the rate is given by

$$
\begin{aligned}
R_{DC,trigger} = & N_{bottom} \cdot R_{DC} \\
& \cdot \sum_{i=n_1-1}^{N_{bottom}-1} \binom{N_{bottom}-1}{i} \cdot P_0^{N_{bottom}-2-i} \cdot \left(\frac{2}{N_{bottom}-1-i} \right) \cdot P_1^{i+1},
\end{aligned} \tag{8.4}
$$

with $n_1 > 1$ and in the case of $n_{2,1} (n_{2,1} > 1)$ adjacent bottom PMTs and $n_{2,2}$ top PMTs by:

$$
\begin{aligned}
R_{DC,trigger} = & 2 \cdot N_{bottom} \cdot N_{top} \cdot R_{DC} \\
& \cdot \left(\sum_{i=n_{2,1}-1}^{N_{bottom}-1} \left[\binom{N_{bottom}-1}{i} P_0^{N_{bottom}-2-i} \left(\frac{2}{N_{bottom}-1-i} \right) P_1^{i+1} \right] \right) \\
& \cdot \left(\sum_{i=n_{2,2}-1}^{N_{top}-1} \binom{N_{top}-1}{i} P_0^{N_{top}-1-i} P_1^i \right).
\end{aligned} \tag{8.5}
$$

In order to reduce the false trigger rate of the veto and thus the dead time of the OSIRIS detector to a minimum and to keep simultaneously the veto efficiency at a reasonable level, the allowed trigger rate induced by the dark count rate of the PMTs is limited to $R_{DC,trigger} \leq 10^{-5}$ Hz which corresponds to 0.86 false veto triggers per day. The required thresholds are listed for several cases in table 8.2.

Based on these trigger conditions, the veto efficiency of the chosen veto PMT distribution (B) in section 8.2.1 can be determined from the simulations. In table 8.3, the fraction of muon tracks from the simulated sample detected by the veto system is listed for the

Table 8.2: Minimum muon veto trigger conditions to suppress dark count induced triggers to below 10^{-5} Hz.

Trigger model	Description	Trigger parameters			
		$\Delta t = 10\,\text{ns}$	$\Delta t = 50\,\text{ns}$	$\Delta t = 100\,\text{ns}$	$\Delta t = 50\,\text{ns}$
1	$\geq n$ PMTs detect each $\geq m$ photons	$n = 5$ m=1	$n = 6$ m=1	$n = 7$ m=1	$n = 4$ m=2
2	$\geq m$ photons detected by all PMTs	$m = 5$	$m = 6$	$m = 7$	$m = 4$
3.1	$\geq n_1$ adjacent bottom PMTs detect each $\geq m$ photons	$n_1 = 3$ $m = 1$	$n_1 = 4$ $m = 1$	$n_1 = 5$ $m = 1$	$n_1 = 3$ $m = 2$
3.2	$\geq n_{2,1}$ adjacent bottom and $\geq n_{2,2}$ top PMTs detect each $\geq m$ photons	$n_{2,1} = 3$ $n_{2,2} = 1$ m=1	$n_{2,1} = 3$ $n_{2,2} = 1$ m=1	$n_{2,1} = 4$ $n_{2,2} = 1$ m=1	$n_{2,1} = 2$ $n_{2,2} = 1$ m=2

different trigger models for the time window $\Delta t = 50\,\text{ns}$ and the number of detected photons $m = 1$. The results show that trigger model 2 is most sensitive for the muon detection and it is the only model that meets the required sensitivity. However, these considerations are made for a basic detector design, where additional components in the veto, like the optical separation and reflective surfaces are neglected. In the following sections, the trigger models are tested for several design options and also for background signals from external gammas.

8.2.3 Optical separation and steel tank liner

Besides the accidental trigger of the muon veto induced by dark counts, the trigger conditions could also be met by physical events in the liquid scintillator volume as the veto PMTs have direct sight to the fiducial volume. While in comparable detector designs (e.g. JUNO [30], Double Chooz [40]) the central detector and veto PMTs are optically separated, in the OSIRIS detector they share the same water volume, without an optical separation. Inversely, also the central detector trigger condition could be imitated by the Cherenkov photons of a muon traversing the water volume.

In figure 8.4 the number of detected photons of the central detector and veto PMT system for muon events in the water volume and for electron events in the liquid scintillator volume are depicted. The electron data sample consists of 10^5 simulated electron events randomly placed in the liquid scintillator volume with an energy of $0 - 5\,\text{MeV}$. The distributions show a clear overlap indicating the potential for false trigger signals in either of the PMT

Table 8.3: Veto efficiency for muons in the water volume depending on the chosen trigger model with $\Delta t = 50\,\text{ns}$ and $m = 1$ ($m = 6$ for model 2, compare table 8.2) for the PMT setup of Model B (see figure 8.2).

Trigger model	Veto efficiency
1	78.5 %
2	92.5 %
3	80.3 %

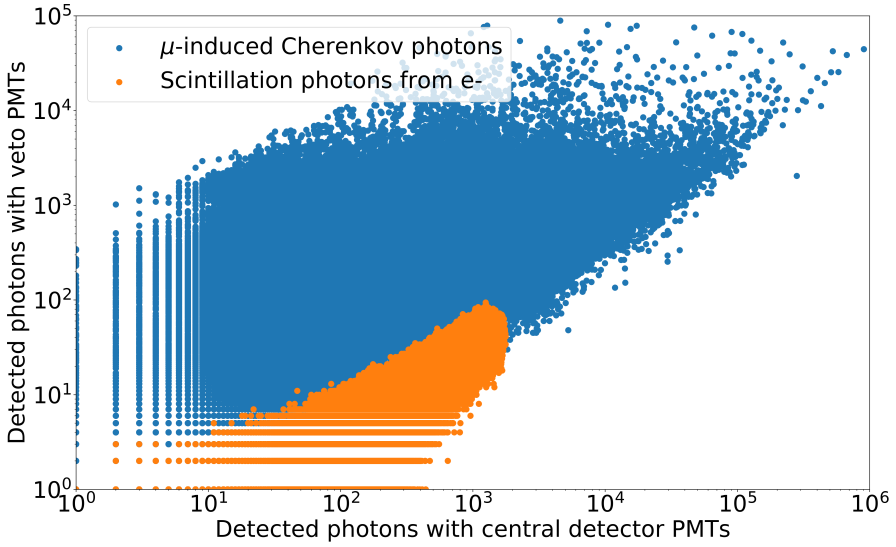

Figure 8.4: Photon detection distribution in the central detector and the veto PMT systems for muons and electrons. The event categories contain muons that only traverse the water system (blue) and electrons in the liquid scintillator volume with an energy of $0 - 5\,\mathrm{MeV}$ (orange). The scatter plot shows the detected light in the two sub-systems for simulated events without an optical separation. Each point represents a single event. The overlap of the two distributions indicates the potential of false trigger events in either of the sub-systems, which augments the necessity of the installation of the optical separation foils.

systems. For the central detector PMT system this problem might be resolved with pulse-shape analysis, to identify signals from muon events. However, due to the small number of PMTs, this approach is not applicable for the veto system. Furthermore, the veto triggers from section 8.2.2 are applied to the simulated electron events. In table 8.4, the fractions of events that trigger the veto depending on the trigger model are listed. As the fractions of $\sim 90\,\%$ for all models would imply large dead-time to the detector system and the rejection of searched events, the installation of an optical separation between the two detector systems is necessary.

Shielding capability of the optical separation

As depicted in figure 8.1, the implemented model of the optical separation in the simulation framework consists of multiple foil sheets attached to the steel frame. In the region where the horizontal detector PMTs are mounted, the installation of various small pieces leads

Table 8.4: Fraction of events in the liquid scintillator volume which trigger the muon veto, depending on the trigger model and the optical separation (OS) design. The simulation consists of 10^5 electrons in the liquid scintillator volume with an energy of $(0 - 5)\,\mathrm{eV}$.

	Veto triggering events (%)		
Trigger model	without OS	realistic OS	idealized OS
1	89.6	0.04	≤ 0.01
2	90.9	0.06	≤ 0.01
3	88.8	0.04	≤ 0.01

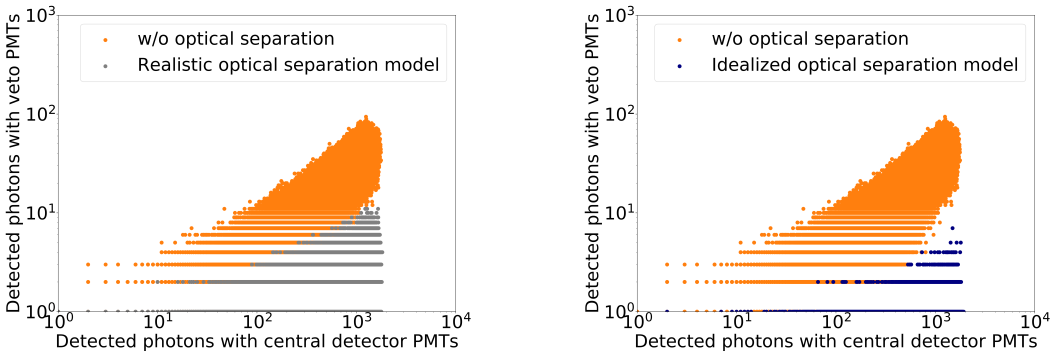

Realistic optical separation model Idealized optical separation model

Figure 8.5: Shielding capability for the implemented optical separation models for simulated electrons in the liquid scintillator with an energy of $(0-5)\,\mathrm{MeV}$, comparable to the simulations for figure 8.4. The orange distribution indicates the number of detected photons in the two PMT sub-systems for the case without the implementation of an optical separation. The simulations are repeated with two different implementations of the optical separation foils, the realistic model (left), with gaps in the separation, due to the installation of the central detector PMTs and the idealized model, where these gaps are entirely closed (right). The distinctly reduced number of detected photons in the veto PMTsystem proofs the efficiency of the optical separation model in general and indicates that light leakage in the realistic model is apparent, but decisive for false triggers in the veto.

to gaps between the sheets. In order to investigate the impact of the imperfect shielding in the PMT area and if an improved design is required, a second model of the optical separation is implemented. In this model, the entire area between two respective legs of the steel frame is covered by a continuous piece of optical separation foil, regardless of the PMTs which are intersected by the plane in the simulation. However, the light detection capability of the PMTs is unimpaired. By comparing the shielding capability of the two models, only the impact of the gaps in the PMT area are regarded. 10^5 electrons with an energy of $0-5\,\mathrm{MeV}$ with random positions in the liquid scintillator volume are simulated for each geometry option. Figure 8.5 indicates that the number of detected photons by the veto system is reduced for both implementations, however, the additional shielding by the closed model is visible. Additionally, the amount of muon veto triggers induced by the liquid scintillator events is deduced. The results for both optical separation designs are listed in table 8.4. For the realistic model, the amount of veto triggering events in the liquid scintillator is $0.06\,\%$ for trigger model 2 and $0.04\,\%$ for the trigger models 1 and 3, which generally substantiates the efficiency of the separation design. The comparison with the analysis of the closed design, where the amount of false trigger events is $\leq 0.01\,\%$ for all trigger models shows that the separation capability of the currently implemented and designated optical separation model is not perfect, but prevents false trigger signals in the veto efficiently.

Implementation of the optical properties in the simulation framework

In order to make realistic statements about the veto system performance based on simulations, the optical properties of the surfaces that define the veto volume (the steel tank and the PMT frame which is covered with the optical separation foil) must be well known and implemented in the simulation carefully. In the geant4 simulation framework, the propagation and behavior at transitions between dielectric materials is defined by the energy dependent refractive index of the material. In case this is not known or useful, optical

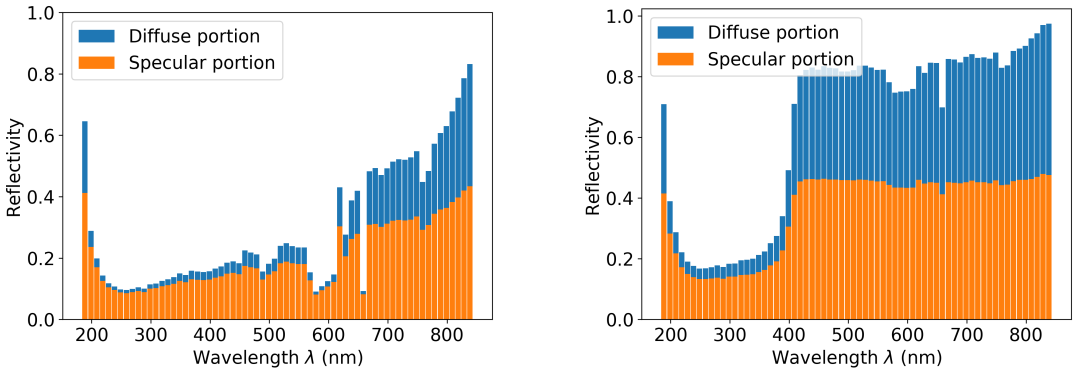

Black side White side

Figure 8.6: Measured reflection probabilities of the optical separation material depending on the wavelength of the photon for the two sides with the partition in diffuse (blue) and specular (orange) ratio.

properties can be assigned to the surface of logical volumes which are defined by the *UNIFIED* model that enables the realistic description of optical surfaces, including reflections, absorption and transmission [135].

For the optical separation foil, the liner and the contingently installed reflectors, only absorption and diffuse and specular reflection are considered. In the *UNIFIED* model, this behavior is described by the *dielectric-metal* material transition for a *ground* surface. The reflection probability of photons arriving at the specified surface is defined by energy-dependent values. Non-reflected photons are absorbed. Which characteristic reflection type is applied to the photon is defined via energy dependent probability values. The applied reflection models are specular lobe and lambertian reflection (diffuse) with respect to the surface normal [135]. As the exact values for the proposed materials are not fully available, the implemented values in the simulation are by now based on the comparison to known materials and preliminary measurements.

Optical separation material

A sample of the bichromatic LDPE foil was sent to Mainz University to determine the optical properties, regarding the requirements of the simulation framework. Due to insufficient reference materials, the final values are not yet determined but based on first measurements with Teflon material as a reference sample, rough estimations could be made which are implemented in the simulation. The reflectivity values are implemented energy dependent as shown in figure 8.6. The specular reflection is implemented as specular lobe component, as specular spike reflection is used for mirrors, which appears improper by a visual inspection of the foil.

Steel tank liner material

At the time of writing, the final decision about the installed liner and its color is not taken. Furthermore, no sample and also no reflectivity values are available, so the implemented values are based on images of the liner material which are compared to the available optical separation material. The absolute reflectivity values are adapted thereof, however the diffuse reflection component is increased to 80 %, as the material appears matter on the images.

Table 8.5: Gamma induced single PMT signal, based on simulation results. The initial position of the gamma photons is randomly chosen in the PMT shield or frame volumes. The conversion probability states the chance that a gamma photon induces the respective gamma signal in the PMT. Together with the expected contamination in the materials, the signal rate per PMT is calculated.

	^{238}U		^{232}Th		^{40}K	
PMT signal	Conversion probability	Signal rate (s^{-1})	Conversion probability	Signal rate (s^{-1})	Conversion probability	Signal rate (s^{-1})
$\geq 1\,PE$	0.047	7.71	0.070	5.56	0.142	0.34
$\geq 2\,PE$	0.032	5.25	0.051	4.05	0.089	0.23
$\geq 3\,PE$	0.023	3.77	0.044	3.49	0.072	0.17
$\geq 4\,PE$	0.017	2.79	0.032	2.54	0.054	0.13
$\geq 5\,PE$	0.013	2.13	0.027	2.14	0.041	0.10
$\geq 6\,PE$	0.010	1.64	0.024	1.91	0.032	0.08

Reflector material

As the decision about the final liner color was not yet taken and the information about the improbable availability of white material raised only recently, the design and the material choice of the additionally installed reflectors is still in progress. Currently, sheets of white Tyvek material are the preferred option as it is well known and often used in particle physics experiments, has a low density ($39\,\mathrm{g/cm^2}$ for a single-layered sheet [136]) and thus a small weight which facilitates the installation and the processing of the material. As the detailed Tyvek type is not finally set, the optical behavior regarding reflections is adapted from published measurements of other groups. As shown in [137], it must be considered that the optical properties of Tyvek strongly deviate if placed in water. In particular, the total reflectivity and the specular portion are increased compared to the deployment in air. The reflection model values implemented in the OSIRIS simulation are based on measurements of the respective reflectivity components of Tyvek 1082D in water, described in [138], where the results are compared to the identical optical simulation model. The mean total reflectivity is stated with 98 % and the mean specular lobe portion of the reflectivity with 85 % resulting in a mean diffuse component of 15 % (averaged over the wavelength dependent values).

8.2.4 Background induced false triggers signals

With the currently targeted OSIRIS veto design implemented in the simulation software, not only the expected muon detection efficiency can be determined, but also the response to external gamma background. It can induce correlated and uncorrelated PMT signals which lead to false veto triggers imitating a muon traversing the veto volume. In this context, uncorrelated trigger signals are based on the detected PMT signal induced by gamma photons originating from the same PMT. The accidental coincidence of multiple PMTs can fulfill the trigger requirements. Correlated trigger signals are induced by the PMT response of all PMTs induced by a single gamma photon in the water volume. In the case of abundant false veto triggers due to background, the parameters of the trigger algorithms (see table 8.2) must be adapted. Gamma photons from radioactive isotopes can Compton-scatter off electrons, which subsequently can emit Cherenkov radiation in the water volume. As stated in section 5.3, the main contributors to the gamma background are isotopes from the ^{238}U and ^{232}Th decay chains and ^{40}K in the surrounding rock volume and the PMTs including the magnetic shielding and the steel frame. Additionally, a potential radon contamination is expected in the water volume which leads to an additional gamma

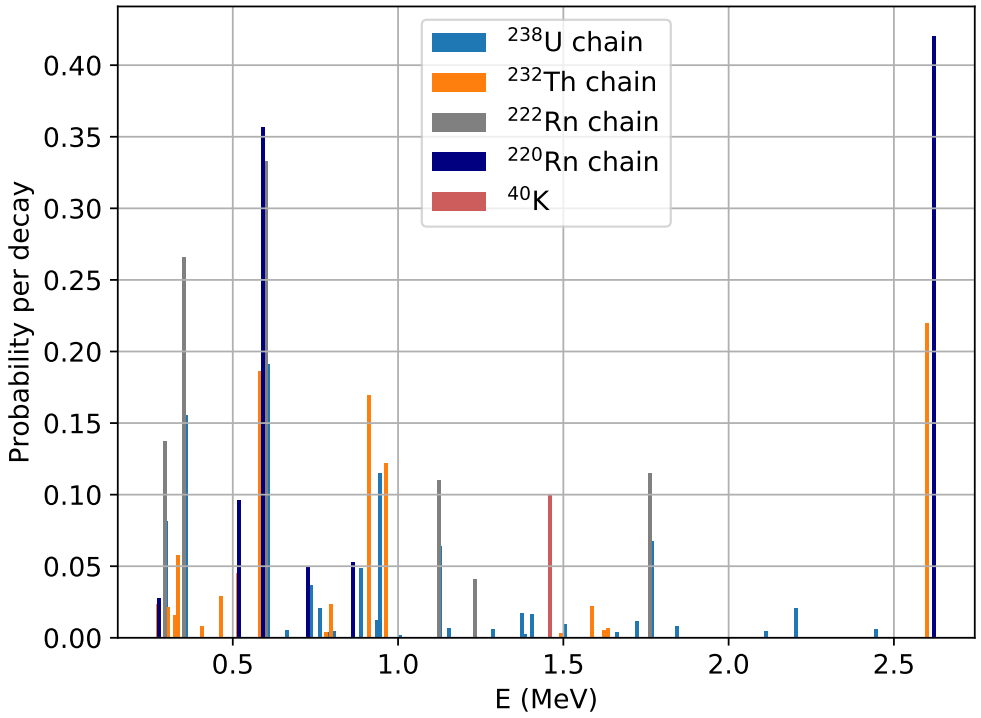

Figure 8.7: Input gamma spectrum for dominant gamma decay chains and isotopes in the simulation. The isotopes of the uranium and thorium chains are dominant in the rock and the PMTs (with shield and steel frame). In the water volume of OSIRIS, the isotopes ^{220}Rn and ^{222}Rn are expected to be dominant, however their actual accumulation from emanation can not be predicted precisely. Data from [120].

photon background. In order to investigate the impact on the muon veto with respect to accidental non-muonic trigger coincidences, an extensive set of gamma photon simulations was computed. For each isotope and decay chain in the mentioned volumes, a sample of 10^8 gamma photons was simulated with the initial energy spectrum depicted in figure 8.7. The mono-energetic gamma photons of the ^{40}K decay, which are emitted in $\sim 10\,\%$ of the decays are simulated with the initial energy $E_{\gamma,\,^{40}\mathrm{K}} = 1.46\,\mathrm{MeV}$. For the gamma flux of the ^{238}U and ^{232}Th decay chains, three or four photons are considered respectively along the decay chain per initial decay [120]. The contribution of the specified volumes (rock, PMTs, frame) to the total gamma flux is dominant compared to the further detector components as shown in table 5.3. For the determination of the uncorrelated contribution from accidental gamma coincidences of multiple PMTs, a further simulation data set was computed which contains events with gamma photons originating from only one isolated PMT (including shield) with which the individual PMT signal for a single gamma can be investigated. According to the definition in section 8.2.2, a PMT contributes to the veto trigger if the chosen photo electron (PE) threshold is exceeded in the time window of $\Delta t = 50\,\mathrm{ns}$. The fraction of events for which the conditions are fulfilled express the probability that a gamma photon can produce a veto PMTsignal of $\geq n$ PE. In the following it is called conversion probability and the values are stated in table 8.5, together with the expected single PMT rate.

False triggers induced by uncorrelated coincidences

The uncorrelated fraction of the gamma induced false veto trigger rate is based on the independent detection of photons induced by a gamma photon with multiple PMTs. It can be calculated analogous to the dark count rate calculations in section 8.2.2. As the

Table 8.6: Veto trigger rate induced by accidental coincidences of gamma photon events in individual PMTs. Due to the definition of trigger model 2, the trigger condition can be fulfilled by a high PE multiplicity in a single PMTwhich leads to the high rate of accidental coincidences compared to the trigger models 1 and 3 and the trigger rates induced by dark counts (see section 8.2.2). The trigger rates for the models 1 and 3 are distinctly lower than for dark counts, due to the reduced individual PMT signal rate (see table 8.5).

Trigger model	Accidental trigger rate (Hz)
1	1.2×10^{-20}
2	95.9
3	2.8×10^{-23}

trigger models 1 and 3 consider $\geq 1\,\mathrm{PE}$ per time window and PMT, the individual PMT rate is the sum of the first row of table 8.5 with 13.61 Hz. Trigger model 2 is directly impacted by the correlated PE multiplicity, where multiple signals per PMT are created by a single gamma photon. According to the dark rate calculations (equations 8.2 - 8.5), the accidental trigger rate for the different trigger models is calculated based on the individual signal rates of the PMTs. The results are given in table 8.6. Due to the relatively low rates and conversion probabilities, the expected accidental false veto triggers for the models 1 and 3 due to gamma background are small compared to the dark count rate background. However, the rate for trigger model 2 is increased, due to the correlated character of multi-PE events which have a higher probability than for uncorrelated dark count events. Independent of the correlated background (see following paragraph), the increased rate requires adaptions of the trigger parameters of model 2.

False triggers induced by correlated coincidences

Correlated false trigger events are events where one gamma photon leads to signals in multiple PMTs and thus imitates the veto coincidence signal. To determine the contribution to the false trigger rate, the simulation data of the specified volumes (rock, PMTs, frame) and isotopes is analyzed with the veto trigger conditions defined in section 8.2.2. Based on the results, the probability for a gamma photon of one of the respective volumes and isotopes/chains to pass the veto trigger requirements can be determined. The results stated in table 8.7 show increased trigger rates for the models 2 and 3 when compared to the results from the uncorrelated gamma signal (see table 8.6) and dark counts (see section 8.2.2), especially by gamma photons from the rock. This can be explained with the spatial dependence of the two models where a local energy deposition of a gamma photon can lead to an increased signal rate in adjacent PMTs. For the same reason trigger model 1 is not affected as the minimum required number of PMTs detecting a photon are distributed over a large distance. The histograms in figure 8.8, where the total charge and the PMT multiplicity for muon and gamma events are depicted show that the signal of a gamma photon in the water volume is spatially limited. For muon events, the total charge reaches up the order of $1 \times 10^3\,\mathrm{PE}$, while for gamma events the charge is limited to $< 60\,\mathrm{PE}$. Similarly, the PMT multiplicity for gamma events is limited to < 5, while for most muon events, larger multiplicities are observed.

As the calculated false trigger rates are not acceptable because they would lead to a detector dead-time of 100 %, the trigger parameters in table 8.2 must be adjusted. In order to find trigger conditions to suppress gamma induced trigger events to the level induced by dark counts, the PE thresholds (m) are adjusted step-wise. For trigger model 2, the PE threshold has to be increased from 6 to 60, and for trigger model 3 from 1 to 2. The drastic enhancement of the trigger thresholds has a distinct impact on the veto detection efficiency and qualifies the results from table 8.3, where for trigger model 1 the lowest performance

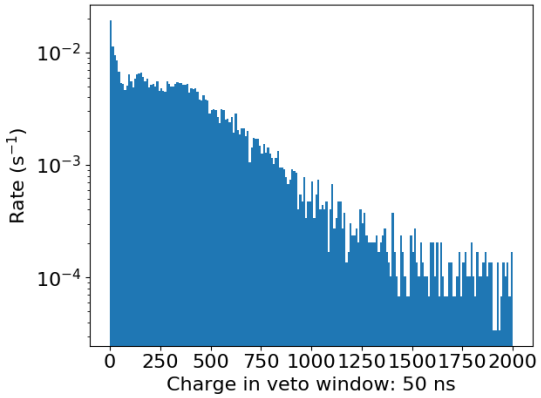

Charge distribution for muon events

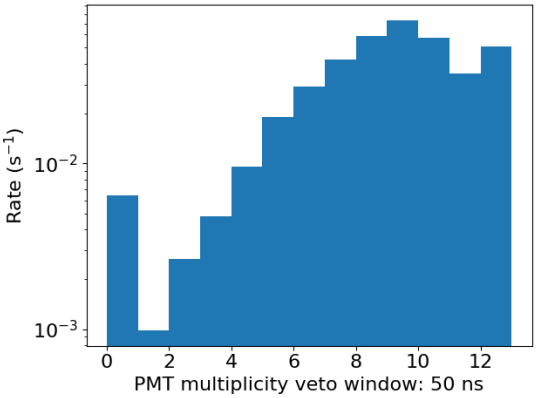

PMT multiplicity for muon events

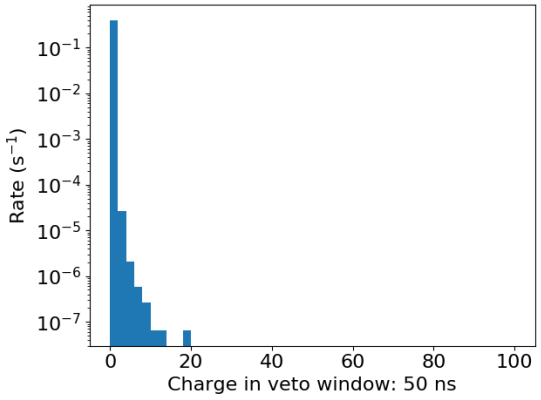

Charge distribution for gammas in water

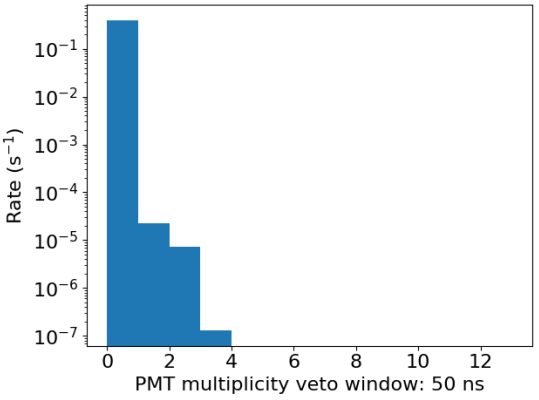

PMT multiplicity for gammas in water

Figure 8.8: Charge and PMT multiplicity in the veto system for muon (top) and gamma (bottom) events for a veto time window of 50 ns. The distributions show that for muon events distinctly more photons are detected by a larger number of PMTs compared to external gammas.

Table 8.7: Gamma and corresponding veto trigger rate depending on the original volume. The activities are based on the expected contamination stated in table 5.3 and in the text in section 5.3. The veto trigger rates are calculated for single gamma photons inducing a signal in multiple PMTs. The results indicate that the photon emission of an initial gamma event is confined, as trigger model 1 with a required PMT multiplicity of $n = 6$ is not affected, while the trigger rate for model 2, where a single PMT with sufficient PE multiplicity can trigger the veto, is strongly increased.

Volume	Activity (Bq)			Veto trigger rate (Hz)		
	^{238}U	^{232}Th	^{40}K	Model 1	Model 2	Model 3
Rock	2.64×10^8	3.05×10^8	1.36×10^8	$< 1.0 \times 10^{-9}$	4790.0	16.8
PMTs	1.83×10^3	6.03×10^3	4.15×10^3	$< 1.0 \times 10^{-9}$	53.7	7.8×10^{-3}
Frame	1.75×10^3	1.51×10^4	1.04×10^4	$< 1.0 \times 10^{-9}$	65.6	0.02
	^{220}Rn		^{222}Rn	Model 1	Model 2	Model 3
Water	298.0		2.11	4.62×10^{-7}	3.41×10^{-2}	2.62×10^{-4}

is expected. The detection efficiencies for the adjusted trigger conditions in the basic veto setup are listed in table 8.8. In the following, the increased trigger parameters are applied to the analysis of the muon samples. However, in the actual setup, the true gamma flux might be lower than expected here as the rock contamination with radioactive isotopes is estimated conservatively in the simulations and the actual rate might be overestimated. Additionally, in the simulation the rock volume is directly attached to the steel tank (see figure 6.1) which leads to an increased gamma flux in the detector volume compared to the realistic setup where the detector is located in the underground hall and the contaminated rock volume is more apart.

In the muon veto of the GERDA experiment, a low-multiplicity excess was identified which could not be explained with muons [139]. In the analysis of the detector data, also gamma photons were taken into account. However, the impact on the performance of the GERDA veto is smaller than in OSIRISat comparable gamma fluxes [140, 30]. The setup of the GERDA veto system with 66 8-inch PMTs leads to a more homogeneous PMT distribution for the Cherenkov photon detection. Thus, the PMT multiplicity for a muon track is much larger compared to a relatively small electron track induced by a gamma photon. With the less, but larger PMTs in the OSIRIS veto system, the multiplicity difference for the two event types is smaller, which explains the stronger impact of gamma photons on the false trigger rate of the OSIRIS veto system.

Table 8.8: Veto efficiency with adjusted trigger conditions for the basic veto design without optical separation and reflective surfaces (comparable to table 8.3) for the PMT setup of Model B (see figure 8.2).

Trigger model	Veto efficiency
1	78.5 %
2	84.7 %
3	73.7 %

8.3 Influences on the performance of the muon veto system

8.3.1 Optical surface conditions in the veto system

The predicted veto efficiencies of the different options that might be selected eventually will be reviewed in this section. All veto designs have in common that the PMT holding steel frame is covered with the bichromatic foil, described in section 8.2.3, that acts as an optical separation and the veto PMT arrangement described as model B (see figure 8.2). The color of the steel tank liner is not yet decided. However, the introduction of the optical separation allows to install a white liner foil, which increases the light collection efficiency of the muon veto system without impact on the inner detector performance.

In order to identify the ideal surface properties for the muon veto, different designs with black liner, white liner and several surfaces covered with reflectors are tested (see table 8.9). In simulations with 10^5 muon events traversing the water volume, the veto efficiency of the designs to identify the detection efficiency is examined. The results in table 8.9 show that only the trigger models 1 and 3 deliver the minimum veto efficiency requirement of 84 % (see section 7.3), whereby the latter is only valid for the design proposal with reflectors on the floor and the side walls of the tank which is also the favorable design for trigger model 1. In contrast to the results in table 8.3, the efficiency for trigger model 2 is reduced due to the increased PE threshold and can not pass the efficiency requirements, independently of the surface properties. The simulation results show that highly reflective liner material is required to ensure the sufficient muon detection efficiency despite the reduced water volume which is observed by the veto caused by the optical separation. In case only the black liner material is available, the muon detection efficiency is severely restricted and the installation of Tyvek foil on the bottom and side walls of the steel tank has to be considered. The better performance of the black liner design option with reflectors on the side walls and the bottom, compared to the white liner option (see table 8.9), can be explained with the conservatively implemented optical properties and, compared to the Tyvek foil, less reflecting white liner material. Until no further information is available, the comparison is imprecise. At this juncture, the option with black liner and additional reflectors on the side walls and the bottom is favored and applied in the following analyses and simulations.

8.3.2 Redundancy

In order to ensure the stable muon detection efficiency and thus the rejection of cosmogenic background in OSIRIS, the muon veto system is required to work reliably for the foreseen

Table 8.9: Muon detection efficiency depending on the optical properties of the steel tank surface for the implemented veto trigger models. The muon simulations are performed with the realistic optical separation model. The increased muon detection efficiency for the setup with black liner and white reflectors on the bottom and side walls compared to the white liner setup can be explained with the higher reflectivity values of the reflector material.

	Muon veto efficiency (%)		
Setup	Trigger model 1	Trigger model 2	Trigger model 3
Black liner	45.6	68.9	28.5
+ side reflectors	89.5	77.5	80.5
+ bottom reflectors	47.8	68.9	30.1
+ side & bottom reflectors	94.7	78.2	86.2
White liner	92.6	76.7	80.3

project duration of about ten years. Regarding the persistence of the system, the PMTs are the determining component, as they are the only active element. Since the installed PMTs are of the same type as for the JUNO detector, they are designed to outlive the experiment on average, however individual failures are not fully avoidable. In the case of the OSIRIS muon veto, possible losses have a more severe impact compared to the inner detector systems of JUNO and OSIRIS as the total number of installed PMTs is smaller. In the Borexino detector, over a period of 6 years which also includes the filling and commissioning, 206 of 2212 PMTs failed due to several reasons [141] which corresponds to more than 9.3 %. This translates to 1.1 failing PMTs for the OSIRIS muon veto system with its 12 PMTs.

To investigate the impact of PMT failure on the muon detection efficiency, distinct PMTs are blinded in the analysis of the simulated muon sample from section 8.3.1. The investigation only covered the veto design with black liner and additional reflectors on the side wall and the bottom of the steel tank as this is currently the most probable option. Analyses with the other design options show that a decreased PMT number leads to a comparable efficiency loss in the muon detection. Not only the number of blinded PMTs is important, but also their relative position (if more than one), especially if they are on the top or the bottom ring and, in the case of multiple blinded PMTs, if they are adjacent to each other or on opposite positions. Especially for trigger model 3, this aspect is very important and requires adaptions in the trigger conditions. Due to the cylindrical symmetry, the exact position of the blinded PMT in the coordinate system of the geometry has no impact on the result but the relative positions to each other.

In table 8.10, the efficiencies of the muon detection with blinded PMTs are listed. The number of deactivated PMTs on the top of the frame and the bottom of the tank are reduced step wise to cover different situations. In the setups with multiple deactivated PMTs, adjacent ones are selected (if not otherwise specified) to produce blind spots in the veto which appears to be the most dangerous case. However, the detection efficiencies show that the position of the "blind" PMTs plays a minor role compared to the absolute number. For most cases, trigger model 1 stays above the minimum required muon detection efficiency of 84 % and only fails for the last case, where four PMTs are deactivated. Trigger model 2 shows similar dependence on the number of PMTs but is generally below the threshold, due to the high trigger threshold. For trigger model 3, the impact of the number of veto PMTs on the bottom of the steel tank is apparent, as the respective reduction leads to a larger decrease in the veto efficiency compared to the reduction of PMTs on the top of the frame. Based on these analyses, the loss of one PMT in the veto system is compensable without strong implications.

8.3.3 Impact of water quality on the veto efficiency

The OSIRIS water volume is connected to the JUNO supply circulation. For the veto systems of both, JUNO and OSIRIS the same requirements are imposed regarding the water transparency. Material abrasion in the pipes, the malfunction of a water processing plant or leftover debris from the setup might deteriorate the water quality and thus the muon detection efficiency of the veto system as decreased water transparency reduces the amount of detected photons. In the following, the impact on the muon detection efficiency is estimated. In the OSIRIS simulation framework, the water transparency is characterized by the light attenuation length which defines the mean track length of photons in the specific material before they are absorbed or scattered depending on the energy of the photon. Hence, the reduction of the water attenuation length translates to an increased absorption of photons. The energy dependent attenuation length values are directly adapted from the JUNO simulation framework. In figure 8.9, the detection efficiency of the veto system is plotted for a reduction of the water attenuation length for

Table 8.10: Veto efficiency of the current muon veto setup with specific deactivated PMTs to simulate blinded or malfunctioning light sensors in the veto setup with black liner and additional reflectors on the bottom and side walls of the tank. The nominal configuration consists of 8 PMTs on the bottom of the tank and 4 PMTs on top of the frame. The blinded bottom PMTs are always adjacent.

Active PMTs	Deactivated PMTs	Muon detection efficiency (%) Trigger model 1	Trigger model 2	Trigger model 3
Top: 4 Bottom: 8	0	94.7	78.2	86.2
Top: 4 Bottom: 7	1	92.3	75.8	68.6
Top: 3 Bottom: 8	1	94.2	77.5	85.5
Top: 4 Bottom: 6	2	87.9	70.1	59.6
Top: 3 Bottom: 7	2	91.1	74.6	65.8
Top: 2 adjacent Bottom: 8	2	93.3	76.7	84.8
Top: 2 opposite Bottom: 8	2	93.4	76.7	84.6
Top: 3 Bottom: 6	3	85.4	68.0	57.2
Top: 2 adjacent Bottom: 7	3	89.5	73.7	64.4
Top: 2 adjacent Bottom: 6	4	82.3	67.1	55.7

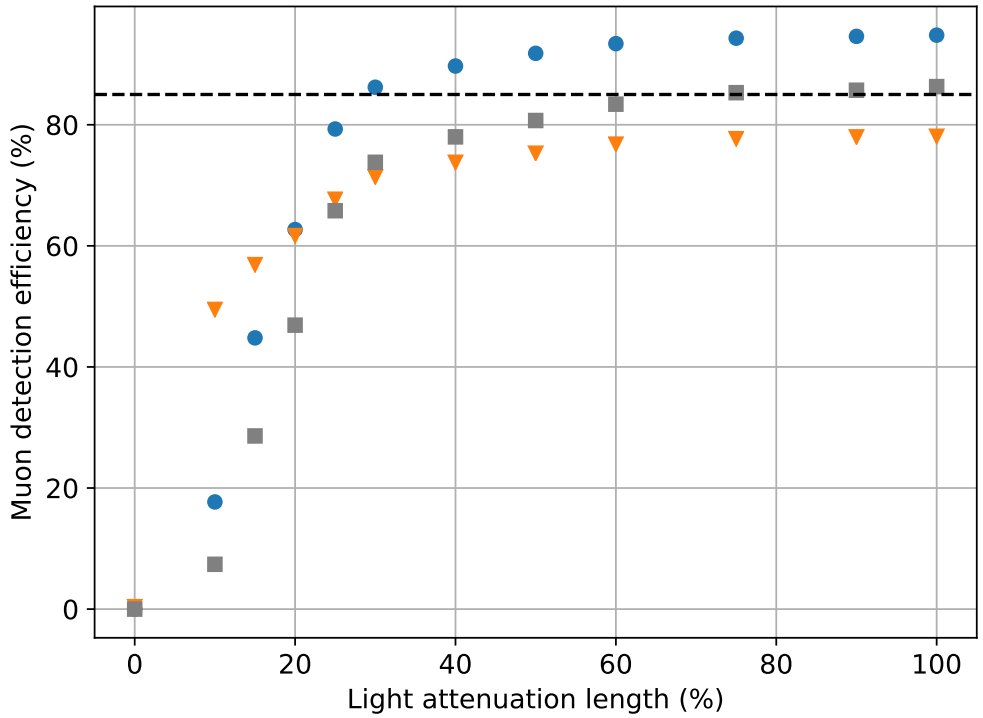

Figure 8.9: Impact on the muon detection efficiency due to a reduced light attenuation length in water for the three trigger models (see section 8.2.2). The minimum required veto efficiency of 84 % is indicated by the dashed black line. The robustness of the trigger models towards variations in the light attenuation length varies distinctly and is depending on the required minimum hit PMTs.

the three defined veto trigger models. As no detailed pollution cases are specified which impact the attenuation length depending on the photon wavelength, the attenuation length values in the simulation are reduced step wise. For the three data series, the veto efficiency shows decreasing tendency with declining light attenuation length, however with distinctly different impact for the three trigger models. As indicated by the plots, the number of minimum hit PMTs in the trigger conditions (see section 8.2.2) affects the robustness of the veto towards increased light absorption explicable with the reduced Cherenkov light range with respect to the muon track. The trigger models 1 and 3 show a similar behavior with a slow decrease of the veto efficiency in the high transparency regime and a rapid drop off at $\sim 30\,\%$. Due to the higher initial efficiency, trigger model 1 surpasses the minimum required value of 84 % for $\sim 30\,\%$ or more of the ideal water transparency, whereas trigger model 3 surpasses the threshold only for $\sim 70\,\%$ or more. Trigger model 2 shows a different behavior with a slow decrease of the veto efficiency below $\sim 50\,\%$ of the original attenuation length. As it is already below the required veto efficiency for full transparency, no limit on the water quality can be set. A reduction of the water attenuation length to 30 % is very unlikely and would require a major technical incident in the water circulation system. Thus, the risk for a failure of the OSIRIS veto system due to bad water quality is very low.

8.4 Muon detection efficiency of the veto system

For the development and the optimization of the OSIRIS muon veto design, only muon events with muon tracks exclusively in the water volume are considered. To consider the realistic muon flux onsite, in the following, a simulation sample without restrictions to

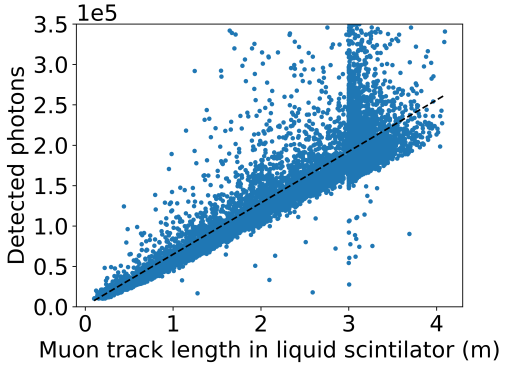

Detected photons from muon tracks in the scintillator volume.

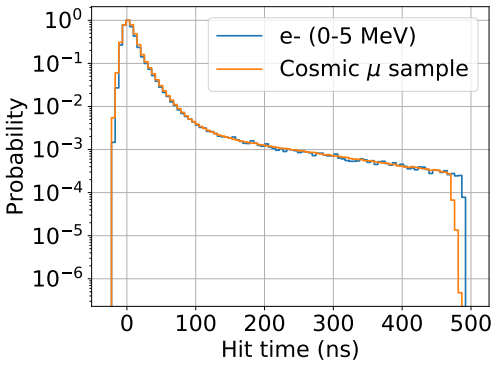

Average waveforms of simulated electrons and muons.

Figure 8.10: Photo emission of muons in the liquid scintillator. Left: Number of detected photons in dependence of the muon track length in the liquid scintillator volume. The black line represents the linear fit, which results in the detection of approximately 620 scintillation photons per cm muon track length. **Right: Average waveforms of muons and electrons in the liquid scintillator.** The additional emission of Cherenkov photons and the track-like energy deposition of the muon make the waveforms distinguishable in the region of $0 - 15\,\text{ns}$.

the traversed volumes of the muons is analyzed, especially regarding the veto efficiency. It comprises $\sim 10^5$ muon events with starting point on the steel tank surface according to the muon flux described in section 6.2. Based on the position and direction distribution of the simulated muon sample, the ratio of muons that traverse the scintillator volume and those which solely traverse the water volume can be directly compared to the predicted muon rate ratio in table 6.5 in the respective volumina. For the rate predictions, the ratio of the muon rate in the scintillator $R_{\mu_{scint}}$ and the total muon rate in OSIRIS R_μ is $r_{theo} = \frac{R_{\mu_{scint}}}{R_\mu} = \frac{0.04\,\text{Hz}}{0.39\,\text{Hz}} \approx 10.3\,\%$. In the simulated sample, the ratio of muons traversing the scintillator volume $N_{\mu_{scint}}$ and the total simulated muons N_μ is $r_{sim} = \frac{N_{\mu_{scint}}}{N_\mu} = \frac{14585}{99036} \approx 14.7\,\%$. The deviation of $\sim 4\,\%$ can be explained with additional liquid scintillator volume in the acrylic pipes that are not considered in the simulation but not in the mathematical approach.

8.4.1 Detection efficiency for muons in the liquid scintillator

In order to verify the anticipated muon flux and to compare the predicted muon detection efficiency of the veto system to the actually observed conditions in the running experiment, the expected number of detectable muons that pass the liquid scintillator volume is determined. As mentioned in section 4.2.1, muons are expected to produce approximately 1.5×10^4 scintillation photons per cm track length in the JUNO liquid scintillator and are thus the brightest events in the detector. This allows to identify the majority of muons in the acrylic vessel volume, even if they have very short track lengths. According to simulations of muons in the liquid scintillator volume, approximately 620 photons per cm muon track length are detected by the inner detector PMTs over the entire event duration (see figure 8.10a). As the trigger strategy for the central detector is not yet determined, the required amount of detected photons to identify a muon in the scintillator volume is not available. Conservatively, it is assumed here that muon events with track lengths larger than 5 cm can be identified as such. Based on the muon flux properties from section 6.2, a muon rate of 0.033 Hz in the corresponding volume is expected.

In order to identify muons in the liquid scintillator volume and to discriminate them from e.g. electrons, the different waveforms created by the emitted photons are contrasted.

Table 8.11: Muon detection efficiency for the full simulated sample depending on the chosen trigger logic. As muon tracks through the scintillator volume are likely to be detected (see table 8.12), the muon detection efficiency is larger than in table 8.9.

Trigger model	Muon detection efficiency (%)
1	96.2
2	84.9
3	89.9

The main factors which lead to differences in the waveforms are the energy deposition properties of the particle, e.g. point-like or track-like, and the fluorescence light properties of the different particles (more details in section 3.3). In the current software version of the simulation framework, the fluorescence time constants and weights for muons correspond to the implementation of electrons (see table 3.2). This leads to similar waveforms as shown in figure 8.10b, which however display small distinctions. The depicted mean waveforms are a composition of $\sim 10^5$ simulated events respectively, with the muon starting point on the steel tank surface and non-restricted direction and energy distributions and randomly distributed electrons in the scintillator volume with an energy of $0 - 5\,\mathrm{MeV}$. The mean waveforms are shifted for comparison reasons with the maximum bin at 0 ns and normalized with the height of the maximum to 1. On both sides of the maximum, the averaged photon hit time probability for the muons is slightly but significantly higher. For photon hit times smaller than zero, this is explainable with the detection of additional Cherenkov photons, produced by the muon in the water volume before it enters the acrylic vessel. On the right side of the maximum in the time window of $5 - 15\,\mathrm{ns}$, the increased photon rate is explainable with the track-like structure of the muon which causes the additional detection of photons at later times. For relativistic muons, the time span corresponds to a track length of $1.5 - 4.5\,\mathrm{m}$ which coincides with the dimension of the acrylic tank and the distance to the PMTs.

8.4.2 Veto efficiency for the realistic muon sample

In comparison with the muon sample which is restricted to tracks in water only, the unrestricted muon sample contains muon tracks which traverse the liquid scintillator volume. Due to the central position of the latter in the water volume, the muon tracks inevitably contain a segment in the veto volume (min $\sim 1\,\mathrm{m}$ for vertical muon tracks through the acrylic vessel) and can not just clip the corner of the steel tank. Thus, an increased veto detection efficiency for the realistic muon sample is expected. With the anticipated rate of 0.39 Hz of the muon flux and the 10^5 simulated muon events, the sample covers a runtime of ~ 3 days. The muon detection efficiency, depending on the trigger algorithm is presented in table 8.11. Additionally, the detection efficiency of muon tracks that at least partially traverse the liquid scintillator volume is listed in table 8.12, which explains the increased veto efficiency for the total muon sample compared to the sample without these tracks (see table 8.9).

Detection of stopping muons

For the same simulated data sample, the stopping muons are considered which have a share of $\sim 1.3\,\%$. Thereof, $\sim 4.2\,\%$ are stopped in the scintillator volume and $\sim 95.8\,\%$ in the water volume, as expected from the volume ratio. In table 8.13, the muon detection efficiency for stopping muons is given, depending on the trigger model. The detection of stopping muons is less effective than for full tracks through the detector volume, due to the reduced number of produced photons.

Table 8.12: Muon detection efficiency for simulated muon tracks through the liquid scintillator volume with the veto system and in dependence of the trigger algorithm. Due to the central position of the scintillator, the muon tracks contain a minimum path length in the veto volume of $\sim 1\,\mathrm{m}$, which increases the muon detection efficiency.

Trigger model	Muon detection efficiency (%)
1	99.995
2	98.1
3	99.7

Table 8.13: Muon detection efficiency for stopping muon tracks in the water and scintillator volumes.

	Muon detection efficiency (%)		
Trigger model	Stopped in water	Stopped in LS	Total
1	64.2	100.0	67.4
2	55.0	90.9	53.5
3	57.9	100.0	60.3

8.4.3 Characteristics of undetected muon events

As outlined in the previous sections, the muon detection efficiency of the veto system meets the design requirements. However, not every simulated muon track is recognized by the system. As the initial track parameters are known from the simulation input, the characteristics of undetected muon events can be determined. In figure 8.11a, the track lengths of detected and undetected muon tracks in the veto volume which is the water volume between the optical separation and the tank wall are depicted. The track length distribution of the detected muons ranges from very short distances up to the maximum distance in the veto volume at $\sim 10\,\mathrm{m}$ and shows three distinctive maxima. The first peak at $\sim 1\,\mathrm{m}$ can be linked with almost vertical muons starting at the top surface of the steel tank and entering the inner detector volume circumscribed by the optical separation. The broader distribution peaked at $\sim 4\,\mathrm{m}$ is defined by muon tracks entering at the side wall and leaving on the bottom of the steel tank. The small peak at $\sim 9\,\mathrm{m}$ can also be associated with vertical tracks, however not interrupted by the inner detector volume. The track lengths of undetected muon events are limited to small distances with a maximum of $\sim 3\,\mathrm{m}$. Only a few undetected muon events reach track lengths of up to 6 m.

As shown in figure 8.11b, most undetected muon events are corner clipping events at the edges of the steel tank. The figure shows the track progression of undetected muon events together with the inner detector volume (defined by the optical separation, dashed line) and the liquid scintillator volume (solid line). The muon veto system is less efficient for tracks at the bottom edge of the steel tank, which can be explained with the positioning of the veto PMTs on the bottom of the steel tank. While the upper edges of the water volume of the steel tank are observed extensively, no PMTs are directly pointing to the volume at the bottom of the steel tank. PMTs placed on the top lid of the steel tank could resolve the discrepancy, however the mounting is technically not feasible. As the detection performance of the veto system exceeds the required sensitivity, no further adaptions in the PMT positioning are planned, but for future design upgrades of OSIRIS, the installation of further veto PMTs in the respective areas might be considered.

Besides the concentration of undetected corner clipping events, further muon tracks are depicted in figure 8.11 which traverse the detector centrally but are not detected by the veto

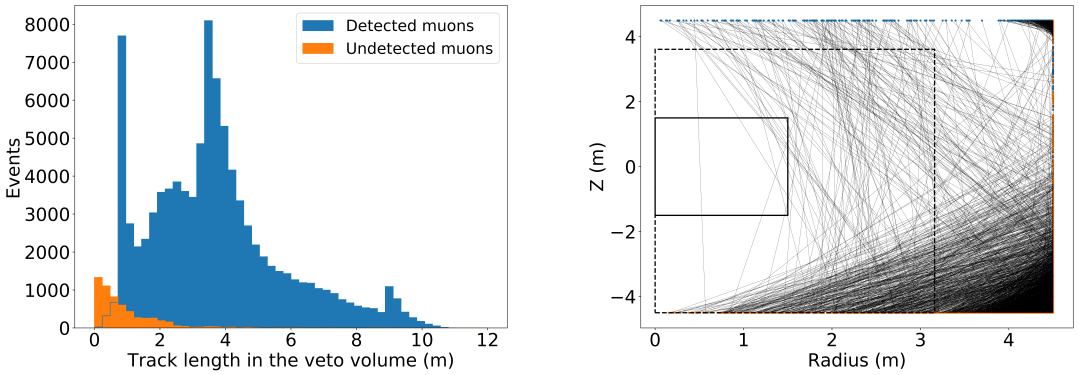

Track lengths of (un)detected muons

Track progression of undetected muons

Figure 8.11: Track distribution of undetected muon events by the veto system. **Left: Track length distributions in the veto volume** of detected (blue) and undetected (orange) muon events. The veto volume is defined by the steel tank and the optical separation. The detected events distribution shows distinct maxima which are explainable with geometrical restrictions of the tracks lengths in the veto volume. **Right: Track progression of undetected muons.** The outer boundary represents the steel tank, on which the muon entry (blue) and exit points (orange) are located. The optical separation is represented by the dashed line, the acrylic vessel by the solid line. The majority of the undetected tracks is located at the edges of the steel tank. Additionally an accumulation of flat tracks on the lower edge with relatively long track lengths in the inner detector volume is visible.

system. Most of these events have a distinct track progression in the inner detector volume. In order to include the inner detector PMTs to the muon detection, a similar trigger scheme to the veto trigger scheme 1 is defined, with a veto time window of $t_{veto} = 70\,\text{ns}$ and a PMT multiplicity of $n = 5$. These parameters are currently subject of investigation of the electronics simulation group and adopted here. With the additional PMT system and the associated increased observed volume, the results from figure 8.11 improve to those in figure 8.12. Besides the majority of the central muon tracks, also a distinct amount of tracks at the lower steel tank edge are detected with the additional PMT system, especially those with long track lengths in the inner detector volume (as also indicated in figure 8.12a). For the remaining undetected muons in the central detector with long tracks lengths in at least one of the two water volumes, the required PMT multiplicity is concisely not met, which prohibits the detection by the veto system. However, since the veto system meets the required efficiency, the few tracks are not problematic for the OSIRIS sensitivity.

8.5 Impact on the OSIRIS sensitivity

With a veto efficiency of $\sim 95\,\%$ for muons in the water volume (table 8.9) and $\sim 96\,\%$ for muon events in the entire detector volume (table 8.11), the required performance of the veto system to accomplish the OSIRIS design sensitivity for the determination of ^{238}U and ^{232}Th contamination is exceeded distinctly. As stated in chapter 7, the muon induced background imitating the ^{214}BiPo coincidence signal sums up to (0.113 ± 0.006) counts/day and is mainly driven by the accidental correlation of two captures of secondary neutrons. The reduction of muon induced background signals with $\sim 96\,\%$ by the muon veto system results in a muon induced background rate of ~ 0.005 counts/day. This rate corresponds to a BiPo signal rate in OSIRIS for a uranium contamination of $\sim 1 \times 10^{-18}\,\text{g/g}$, allowing to screen for liquid scintillator contamination with a similar sensitivity.

For the detector dead-time induced by the veto system, it is distinguished whether the

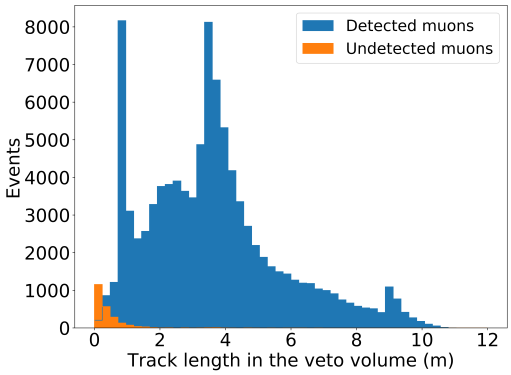

Track lengths of (un)detected muons

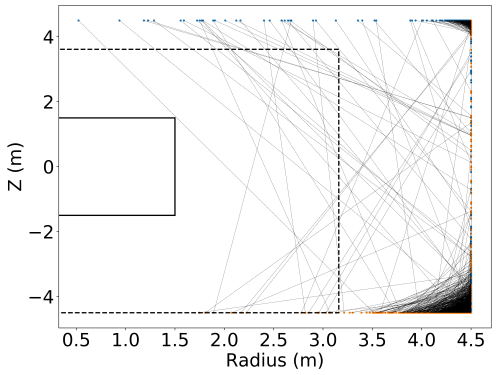

Track progression of undetected muons

Figure 8.12: Track distribution of undetected muon events by the veto system and the inner detector system. Similar to figure 8.11, but with an additional trigger condition for the inner detector system. The amount of undetected muon events is distinctly reduced, especially for tracks with long progression in the inner detector volume. The majority of undetected events is located at the edges of the steel tank.

muon track traverses the liquid scintillator volume or only the water volume. Muons that pass the scintillator volume might produce the isotopes ^{8}He and ^{9}Li (see table 5.4). The background from muon events exclusively traversing the water volume is dominated by the coincidence signal of two secondary neutron captures as indicated in section 7.2.4. Thus, according to the JUNO muon veto strategy [30] for muon events traversing exclusively the water volume, the detector is vetoed for 1.5 ms to reject accidental coincidences from neutron captures. For muon tracks through the scintillator volume which can be determined with a high accuracy due to the enhanced light production (see section 8.4.1), the detector is vetoed for 1.2 s. Based on the expected muon rates (see section 6.2.3) with 0.35 Hz in the water volume and 0.04 Hz in the scintillator volume and the veto efficiency from table 8.11 for all muon tracks, the detector dead-time is estimated with 0.05 % and 4.8 % respectively.

9. Conclusion

In the first part of this thesis, the rejection of muon induced cosmogenic background in the JUNO detector is addressed. Due to its large dimensions and relatively shallow overburden of $\sim 700\,\mathrm{m}$, the expected muon event rate in the JUNO detector is $\sim 4\,\mathrm{Hz}$. The signal of the cosmogenic isotopes produced by the muons are indistinguishable from the searched reactor antineutrino signal and thus the main background for the determination of the neutrino mass ordering. Without any counter-measures, the signal to background ratio is $\sim 1:1$, however, a total detector veto after the detection of a muon with the veto system would cause a dead-time of approximately $100\,\%$. Therefore, the JUNO veto strategy foresees the reconstruction of muon tracks with the central detector system and a partial veto of a cylindrical volume around the muon track. In order to achieve the required detector sensitivity, the number of thoroughly reconstructed muon tracks must be $\geq 99\,\%$ [30]. This includes also muon bundle events with more than one muon simultaneously in the detector which make up $\sim 10\,\%$.

Within the scope of this thesis, an algorithm for the reconstruction of the muon tracks in bundle events was established and tested with simulated muons. Contrarily to single muon events, where several established reconstruction methods are already implemented, the overlapping signals of the particular muons in a bundle require a more basic approach. Therefor, the characteristic light profile of muon tracks in the liquid scintillator detector is used which causes a high number of detected photons close to the intersection points of the muon track with the liquid scintillator volume and a conical first light front emitted around the muon track. The identification of the muon entry and exit points is realized via the search for areas with increased photon detection. The identified intersection points are then assigned with muon tracks, wherefore the track nature of muons and the parallel progression of muons in a bundle are exploited. For the determination of the reconstruction performance, extensive simulations of muon bundles with a multiplicity of up to four muons were performed using the JUNO simulation framework. Based on these, the track allocation performance and the precision of the particular track reconstruction could be determined. Considering the rates of the different bundle sizes, the algorithm reconstructs $\sim 53\,\%$ of the bundle events with an overall uncertainty on the distance of the track to the detector center $\Delta D = 177\,\mathrm{mm}$ and its direction $\alpha = 1\,^\circ$. This enables to reconstruct $96\,\%$ of all muon events assuming perfect single muon track reconstruction, which however is below the fraction anticipated by the JUNO collaboration. More sophisticated reconstruction approaches, which can be based on the results of the presented algorithm could further improve the performance and help to reach the design goal.

Besides cosmogenic background, radioactive contamination of the liquid scintillator, mainly isotopes of the ^{238}U and ^{232}Th decay chains, is a major background source in the JUNO detector. Especially the detection of solar neutrinos demands high standards on the scintillator purity. For that reason, sophisticated purification plants are developed and setup onsite to provide a maximum contamination level of 1×10^{-15} g/g (1×10^{-16} g/g for the solar neutrino program). For monitoring the radiopurity of the liquid scintillator while it is filled into the JUNO detector, the Online Scintillator Internal Radioactivity Investigation System (OSIRIS) was proposed and will be installed in the scintillator filling line. It is a 18 t liquid scintillator detector with the goal to determine the ^{238}U and ^{232}Th concentration in the scintillator via the detection of coincident decays of bismuth and polonium which are part of the decay chains. The second part of this thesis is dedicated to simulation based studies of the muon induced background characteristics and the design of an optimized muon veto system.

The simulation framework, was extended with regard to the implemented detector geometry, the physics model and the execution modes. Concerning the geometry model, the components and detector properties which determine the muon veto system were implemented such as a second PMT system with flexible positioning, optical separation models and optically active surfaces representing contemplable materials. Furthermore, details were attached to the existing model to improve the realism of the simulation results. Among them are a PMT holding frame, magnet shieldings for the PMTs and extensions to the acrylic vessel like pipes and stiffeners. The physics model was extended by the realistic light emission of muons in water and the liquid scintillator, modified decay spectra of ^{9}Li and ^{8}He and a realistic model for the production of cosmogenic isotopes by muons. Finally, dedicated simulation modes for the creation of realistic muons events, the simulation of large muon samples and a calibration mode were developed and implemented into the simulation framework.

The first application of the adapted simulation framework was to determine the impact of muon induced cosmogenic background on the OSIRIS sensitivity. Therefore, the potential of the secondary particles to imitate the bismuth-polonium (BiPo) signal, which OSIRIS is searching for, was studied based on 10^8 simulated muon events in the OSIRIS detector. The analyses showed that the accidental coincidence signals of two neutron captures, a neutron capture and a gamma photon detection, and the decays of ^{9}Li and ^{8}He in the liquid scintillator are the dominant cosmogenic candidates to pass the coincidence cuts and imitate BiPo signals. Based on the findings, the expected cosmogenic background rate could be calculated with ~ 0.1 cpd and therewith, the required detection efficiency of the muon veto in dependence of the scintillator radiopurity. The results showed that particularly for the solar physics program of JUNO, the installation of a veto system in OSIRIS is necessary and an efficiency of at least 84 % is required.

This efficiency value is used as benchmark for the development of the Cherenkov veto design which is the final aspect of the thesis. As the design process of the OSIRIS detector was already at an advanced stage, the veto system had to be fit into the existing setup. Thus, the only parameters were the positions of the twelve available veto PMTs, partially the optical properties of the steel tank liner and the optical separation. The testing of the numerous combinations revealed that for the elaborated PMT array an optical separation from the inner detector system is inevitable to avoid false signals in both systems. To compensate for the reduced veto volume due to the additionally implemented foils, the installation of a highly reflective steel tank surface is required. As the vendor could not provide the appropriate material, the tested option with white Tyvek foil on the bottom and the side walls of the steel tank will be realized. With the optimized veto system design, the trigger logic for the detection of muons was set with regard to false PMT signals from dark counts and gamma background. Concluding, stress tests for the veto

system were simulated to address contingent malfunctions, such as breaking PMTs and water pollution.

Based on simulations, the OSIRIS veto system, as proposed in this thesis, allows the detection of muons with an efficiency of $\sim 96\,\%$. This includes the detection of stopping muons with $\sim 67\,\%$. Considering cosmogenic background only, the OSIRIS detector is thus capable to determine the ^{238}U and ^{232}Th contamination of the liquid scintillator with a sensitivity of $\sim 1 \times 10^{-18}\,\mathrm{g/g}$. The assumed dead-time of the detector, due to the veto, is based on the JUNO veto strategy [30] and sums up to $4.9\,\%$. Currently, the final preparations for the setup of the detector are made and the installation started in November 2021. For the time after the commissioning of JUNO, the further utilization of the OSIRIS detector is already under investigation. One plan is the modification of the detector to tenfold the energy resolution with the goal to measure solar neutrinos [142]. According studies are currently conducted with an extended version of the simulation framework.

With the progressive installation of JUNO, the collaboration is facing an exciting time, which will give many insights into the performance and sensitivity of the detector system. Especially during the commissioning, the value of the simulation results on which the detector design and the operations are based on will be revealed. With the aimed for design specifications and successful background control, JUNO will contribute significantly to neutrino physics in many aspects and will help to get a deeper understanding of physics beyond the standard model.

List of Figures

List of Tables

List of Acronyms

ACU auxilliary calibration unit.

ALEPH Apparatus for LEP Physics.

bis-MSB p-bis-(o-methylstyryl)-benzene.

CERN European Organization for Nuclear Research.

CMB cosmic microwave background.

CNO-cycle carbon-nitrogen-oxygen cycle.

DAQ data acquisition.

DONUT Direct Observation of the NU Tau.

DSNB diffuse supernova neutrino background.

DUNE Deep Underground Neutrino Experiment.

GERDA GERmanium Detector Array.

HDPE high density polyethylen.

IBD inverse beta-decay.

IO Inverted neutrino mass ordering.

J-PARC Japan Proton Accelerator Research Complex.

JUNO Jiangmen Underground Neutrino Observatory.

KATRIN Karlsruhe Tritium Neutrino Experiment.

LAB linear alkylbenzene.

LDPE low density polyethylen.

LEGEND Large Enriched Germanium Experiment for Neutrinoless $\beta\beta$ Decay.

MCP micro-channel plate.

MUSIC MUonSImulationCode.

NNVT Northern Night Vision Technology Ltd..

NO Normal neutrino mass ordering.

OSIRIS Online Scintillator Internal Radioactivity Investigation System.

PDE photon detection efficiency.

PE photo electron.

PINGU Precision IceCube Next Generation Upgrade.

PMT photomultiplier tube.

pp-chain proton-proton-reaction chain.

PPO 2,5-diphenyloxazole.

QE quantum efficiency.

SiPMs silicon photomultipliers.

SM standard model of particle physics.

SNO Sudbury Neutrino Observatory.

SNU solar neutrino unit.

SSM standard solar model.

T2K Tokai-to-Kamioka.

TAO Taishan Antineutrino Observatory.

TTS transit time spread.

Bibliography

[1] W. Pauli. Dear radioactive ladies and gentlemen. *Phys.Today*, 31N9:27, 1978.

[2] J. Chadwick. Possible Existence of a Neutron. *Nature*, 129(3252):312–312, February 1932.

[3] E. Fermi. Versuch einer Theorie der β-Strahlen. I. *Zeitschrift für Physik*, 88(3-4):161–177, March 1934.

[4] H. Bethe and R. Peierls. The "Neutrino". *Nature*, 133(3362):532–532, April 1934.

[5] C. L. Cowan, F. Reines, F. B. Harrison, et al. Detection of the Free Neutrino: a Confirmation. *Science*, 124(3212):103–104, July 1956.

[6] G. Danby, J-M. Gaillard, K. Goulianos, et al. Observation of High-Energy Neutrino Reactions and the Existence of Two Kinds of Neutrinos. *Physical Review Letters*, 9(1):36–44, July 1962.

[7] M. L. Perl, G. S. Abrams, A. M. Boyarski, et al. Evidence for Anomalous Lepton Production in e+-e-Annihilation. *Physical Review Letters*, 35(22):1489–1492, December 1975.

[8] D. DeCamp, B. Deschizeaux, J.-P. Lees, et al. Determination of the number of light neutrino species. *Physics Letters B*, 231(4):519–529, November 1989.

[9] K.A. Olive. Review of Particle Physics. *Chinese Physics C*, 38(9):090001, August 2014.

[10] K. Kodama, N. Ushida, C. Andreopoulos, et al. Observation of tau neutrino interactions. *Physics Letters B*, 504(3):218–224, April 2001.

[11] C. S. Wu, E. Ambler, R. W. Hayward, et al. Experimental Test of Parity Conservation in Beta Decay. *Physical Review*, 105(4):1413–1415, February 1957.

[12] T. D. Lee and C. N. Yang. Question of Parity Conservation in Weak Interactions. *Physical Review*, 104(1):254–258, October 1956.

[13] B. Povh et al. *Teilchen und Kerne: Eine Einfuehrung in die physikalischen Konzepte*. Springer Berlin, Berlin, 8., Aufl edition, 2008.

[14] Mary K. Gaillard, Paul D. Grannis, and Frank J. Sciulli. The standard model of particle physics. *Reviews of Modern Physics*, 71(2):S96–S111, March 1999.

[15] M. Tanabashi, K. Hagiwara, K. Hikasa, et al. Review of Particle Physics. *Physical Review D*, 98(3), August 2018.

[16] John N. Bahcall. Solar Neutrinos: A Popular Account. *arXiv e-prints*, page physics/0411190, November 2004.

[17] B. Cleveland, T. Daily, Jr. R. Davis, et al. Measurement of the Solar Electron Neutrino Flux with the Homestake Chlorine Detector. *The Astrophysical Journal*, 496(1):505–526, March 1998.

[18] D. Vignaud. The GALLEX solar neutrino experiment. *Nuclear Physics B - Proceedings Supplements*, 60(3):20–29, January 1998.

[19] S. Fukuda, Y. Fukuda, M. Ishitsuka, et al. SolarB8 and hep Neutrino Measurements from 1258 Days of Super-Kamiokande Data. *Physical Review Letters*, 86(25):5651–5655, June 2001.

[20] B. Aharmim, S. N. Ahmed, A. E. Anthony, et al. Combined analysis of all three phases of solar neutrino data from the Sudbury Neutrino Observatory. *Physical Review C*, 88(2), August 2013.

[21] M. Gell-Mann and A. Pais. Behavior of Neutral Particles under Charge Conjugation. *Physical Review*, 97(5):1387–1389, March 1955.

[22] B. Pontecorvo. Mesonium and anti-mesonium. *Sov. Phys. JETP*, 6:429, 1957. [Zh. Eksp. Teor. Fiz.33,549(1957)].

[23] B. Pontecorvo. Inverse beta processes and nonconservation of lepton charge. *Sov. Phys. JETP*, 7:172–173, 1958. [Zh. Eksp. Teor. Fiz.34,247(1957)].

[24] Z. Maki, M. Nakagawa, and S. Sakata. Remarks on the Unified Model of Elementary Particles. *Progress of Theoretical Physics*, 28(5):870–880, November 1962.

[25] B. Pontecorvo. Neutrino Experiments and the Problem of Conservation of Leptonic Charge. *Sov. Phys. JETP*, 26:984–988, 1968.

[26] Y. Li, J. Cao, Y. Wang, and L. Zhan. Unambiguous determination of the neutrino mass hierarchy using reactor neutrinos. *Phys. Rev. D*, 88:013008, Jul 2013.

[27] K. Zuber. *Neutrino Physics*. CRC Press, Boca Raton, Fla, 2003.

[28] H. Nunokawa, S. Parke, and J. Valle. CP Violation and Neutrino Oscillations. *Prog. Part. Nucl. Phys.*, 60:338–402, 2008.

[29] B. Schwarzschild. Antineutrinos from Distant Reactors Simulate the Disappearance of Solar Neutrinos. *Physics Today*, 56(3):14–16, March 2003.

[30] Fengpeng An, Guangpeng An, Qi An, et al. Neutrino physics with JUNO. *Journal of Physics G: Nuclear and Particle Physics*, 43(3):030401, February 2016.

[31] G. Bellini, J. Benziger, D. Bick, et al. Final results of Borexino Phase-I on low-energy solar neutrino spectroscopy. *Physical Review D*, 89(11), June 2014.

[32] K. Okumura. Atmospheric Neutrino Flux Measurement. *EPJ Web of Conferences*, 208:07002, 2019.

[33] Z. Li et al. Measurement of the tau neutrino cross section in atmospheric neutrino oscillations with Super-Kamiokande. *Phys. Rev. D*, 98(5):052006, 2018.

[34] M. G. Aartsen, M. Ackermann, J. Adams, et al. Measurement of atmospheric tau neutrino appearance with IceCube DeepCore. *Physical Review D*, 99(3), February 2019.

[35] P. Dunne. Latest Neutrino Oscillation Results from T2K. `https://zenodo.org/record/3959558`, 2020. Plennary talk from Neutrino 2020.

[36] P. Vahle. New results from NOvA. *Journal of Physics: Conference Series*, 888:012003, September 2017.

[37] B. Abi et al. The DUNE Far Detector Interim Design Report Volume 1: Physics, Technology and Strategies, July 2018. arXiv e-print: 1807.10334.

[38] K. Abe et al. Hyper-Kamiokande Design Report, May 2018. arXiv e-print: 1805.04163.

[39] S. Abe et al. Precision Measurement of Neutrino Oscillation Parameters with KamLAND. *Phys. Rev. Lett.*, 100:221803, 2008.

[40] F. Ardellier et al. Double Chooz: A Search for the neutrino mixing angle theta(13), June 2006. arXiv e-print: hep-ex/0606025.

[41] J.K. Ahn et al. RENO: An Experiment for Neutrino Oscillation Parameter θ_{13} Using Reactor Neutrinos at Yonggwang, March 2010. arXiv e-print: 1003.1391.

[42] Xinheng Guo et al. A Precision measurement of the neutrino mixing angle θ_{13} using reactor antineutrinos at Daya-Bay, January 2007. arXiv e-print: hep-ex/0701029.

[43] D. Adey, F. P. An, A. B. Balantekin, et al. Measurement of the Electron Antineutrino Oscillation with 1958 Days of Operation at Daya Bay. *Physical Review Letters*, 121(24), December 2018.

[44] G. Bak, J. H. Choi, H. I. Jang, et al. Measurement of Reactor Antineutrino Oscillation Amplitude and Frequency at RENO. *Physical Review Letters*, 121(20), November 2018.

[45] L. Wolfenstein. Neutrino oscillations in matter. *Phys. Rev. D*, 17:2369–2374, May 1978.

[46] F. Capozzi, E. Di Valentino, E. Lisi, et al. Addendum to: Global constraints on absolute neutrino masses and their ordering, March 2020. arXiv e-print: 2003.08511.

[47] M.G. Aartsen et al. PINGU: A Vision for Neutrino and Particle Physics at the South Pole. *J. Phys. G*, 44(5):054006, 2017. arXiv e-print: 1607.02671.

[48] A. Ishihara. The IceCube Upgrade – Design and Science Goals. *PoS*, ICRC2019:1031, 2020.

[49] M. G. Aartsen, M. Ackermann, J. Adams, et al. Combined sensitivity to the neutrino mass ordering with JUNO, the IceCube Upgrade, and PINGU. *Physical Review D*, 101(3), February 2020.

[50] Esteban and Gonzalez-Garcia and Hernandez-Cabezudo and Maltoni and Schwetz. NuFIT 4.1 (2019). `http://www.nu-fit.org/`. Accessed on April 24th, 2020.

[51] M.C. Gonzalez-Garcia, Michele Maltoni, and Thomas Schwetz. Global analyses of neutrino oscillation experiments. *Nuclear Physics B*, 908:199–217, 2016. Neutrino Oscillations: Celebrating the Nobel Prize in Physics 2015.

[52] K. Abe et al. Constraint on the matter–antimatter symmetry-violating phase in neutrino oscillations. *Nature*, 580(7803):339–344, 2020. [Erratum: Nature 583, E16 (2020)].

[53] S. Davidson, E. Nardi, and Y. Nir. Leptogenesis. *Phys. Rept.*, 466:105–177, 2008.

[54] H. Fritzsch and Z. Xing. How to describe neutrino mixing and CP violation. *Physics Letters B*, 517(3):363 – 368, 2001.

[55] M. Agostini, G. R. Araujo, A. M. Bakalyarov, et al. Final Results of GERDA on the Search for Neutrinoless Double-β Decay. *Physical Review Letters*, 125(25), December 2020.

[56] N. Abgrall et al. The Large Enriched Germanium Experiment for Neutrinoless Double Beta Decay (LEGEND). *AIP Conf. Proc.*, 1894(1):020027, 2017.

[57] M. Dentler, Á. Hernández-Cabezudo, J. Kopp, et al. Updated Global Analysis of Neutrino Oscillations in the Presence of eV-Scale Sterile Neutrinos. *JHEP*, 08:010, 2018.

[58] S. Roy Choudhury and S. Hannestad. Updated results on neutrino mass and mass hierarchy from cosmology with Planck 2018 likelihoods, July 2019. arXiv e-print: 1907.12598.

[59] M. Aker et al. Improved Upper Limit on the Neutrino Mass from a Direct Kinematic Method by KATRIN. *Phys. Rev. Lett.*, 123(22):221802, 2019.

[60] M. Aker et al. First direct neutrino-mass measurement with sub-eV sensitivity. 5 2021.

[61] J. Xu. JUNO Muonflux update, password protected. `https://juno.ihep.ac.cn/Dev_DocDB/0025/002512/002/MuFlux_JUNONewSite.pdf`, 2017. Internal collaboration document.

[62] Yuekun Heng on behalf of JUNO Collaboration. Design and progress of the Central Detector of JUNO. `https://indico.cern.ch/event/679723/contributions/2792554/attachments/1559217/2454299/PhysicsReferenceManual.pdf`, 2018.

[63] Photomultiplier Tubes - Basics and Applications, 4th Ed. `https://www.hamamatsu.com/resources/pdf/etd/PMT_handbook_v4E.pdf`, 2017.

[64] L. Ren, J. Sun, S. Si, et al. Mass Production of MCP-PMT for JUNO and Development of 20-inch MCP-PMT with TTS Improved. In *Proceedings of the 5th International Workshop on New Photon-Detectors (PD18)*. Journal of the Physical Society of Japan, November 2019.

[65] HZC Photonics Technology Co. Ltd. Photomultiplier Tubes Product Manual. `http://www.hzcphotonics.com/products/ProductManual.pdf`, 2017.

[66] Z. Djurcic et al. JUNO Conceptual Design Report, August 2015. arXiv e-print: 1508.07166.

[67] Miao H. et al. Double calorimetry system in JUNO. *Radiation Detection Technology and Methods*, 1(2), October 2017.

[68] A. Giaz. Status and perspectives of large PMT electronics of the JUNO experiment. *Nuovo Cim. C*, 42(4):193, 2019.

[69] T. Zeng, F. Li, and K. Zhu. JUNO DAQ Readout and Event Building Research. *IEEE Trans. Nucl. Sci.*, 66(7):1217–1221, 2018.

[70] J. Xu. The JUNO double calorimetry system. *PoS*, NuFact2019:117, 2020.

[71] Z. Qin. Status of the 20-in. PMT Instrumentation for the JUNO Experiment. *Springer Proc. Phys.*, 213:285–293, 2018.

[72] X. Ding and C. Guo. Status of the JUNO Detector. Lake Louise Winter Institute 2020: Chateau Lake Louise, Canada, 2020, last accessed 08. December 2020.

[73] Z. Qin. The 20-Inch Pmt Instrumentation For The Juno Experiment, 2018.

[74] A. Tietzsch. Development, Installation and Operation of a Container-based Mass Testing System for 20-inch Photomultiplier Tubes for JUNO, 2020.

[75] N. Anfimov. Large photocathode 20-inch PMT testing methods for the JUNO experiment. *Journal of Instrumentation*, 12(06):C06017–C06017, June 2017.

[76] J. Songwadhana, K. Khosonthongkee, Y. Yan, et al. EMF Shielding of One Set of Circular Coils with Slight Distortion. *J. Phys. Conf. Ser.*, 1144(1):012022, 2018.

[77] P. Zhang. Progress of Veto Detector of JUNO. *Journal of Physics: Conference Series*, 1468:012188, February 2020.

[78] Andrea T., J.P. Athayde Marcondes de Andre, E. Baussan, et al. A Muon Telescope as Demonstrator of the JUNO Top Tracker Detector. In *Proceedings of Topical Workshop on Electronics for Particle Physics — PoS(TWEPP2019)*. Sissa Medialab, March 2020.

[79] A. Abusleme et al. Calibration Strategy of the JUNO Experiment, November 2020. arXiv e-print: 2011.06405.

[80] W. Depnering. A Liquid Scintillator Transparency Monitoring Laser System For JUNO. `https://zenodo.org/record/1300420`, 2018. Poster presentation at Neutrino 2018.

[81] M. Wurm. Measuring the Neutrino Mass Ordering in JUNO. International School of Nuclear Physics, Erice, 2017, last accessed 02. December 2020.

[82] W. Beriguete et al. Production of a gadolinium-loaded liquid scintillator for the Daya Bay reactor neutrino experiment. *Nucl. Instrum. Meth. A*, 763:82–88, 2014.

[83] H.-L. Xiao, X.-B. Li, D. Zheng, et al. Study of absorption and re-emission processes in a ternary liquid scintillation system. *Chinese Physics C*, 34(11):1724–1728, November 2010.

[84] C. Patrignani et al. Review of Particle Physics. *Chin. Phys. C*, 40(10):100001, 2016.

[85] T. Marrodán Undagoitia, F. von Feilitzsch, L. Oberauer, et al. Fluorescence decay-time constants in organic liquid scintillators. *Review of Scientific Instruments*, 80(4):043301, April 2009.

[86] G. Ranucci, A. Goretti, and P. Lombardi. Pulse-shape discrimination of liquid scintillators. *Nucl. Instrum. Meth. A*, 412:374–386, 1998.

[87] M. Grassi, J. Evslin, E. Ciuffoli, and X. Zhang. Showering cosmogenic muons in a large liquid scintillator. *Journal of High Energy Physics*, 2014(9), September 2014.

[88] M. Febbraro, R. J. deBoer, S. D. Pain, et al. New $^{13}\mathrm{C}(\alpha, n)^{16}\mathrm{O}$ Cross Section with Implications for Neutrino Mixing and Geoneutrino Measurements. *Phys. Rev. Lett.*, 125:062501, Aug 2020.

[89] R.N. Cahn, D.A. Dwyer, S.J. Freedman, et al. White Paper: Measuring the Neutrino Mass Hierarchy. In *Community Summer Study 2013: Snowmass on the Mississippi*, July 2013. arXiv e-print: 1307.5487.

[90] M. Agostini et al. Experimental evidence of neutrinos produced in the CNO fusion cycle in the Sun. *Nature*, 587:577–582, 2020.

[91] J. Liao, D. Marfatia, and K. Whisnant. Nonstandard interactions in solar neutrino oscillations with Hyper-Kamiokande and JUNO. *Phys. Lett. B*, 771:247–253, 2017.

[92] P. Bakhti and M. Rajaee. Sensitivities of future solar neutrino observatories to nonstandard neutrino interactions. *Phys. Rev. D*, 102(3):035024, 2020.

[93] K. Hirata, T. Kajita, M. Koshiba, et al. Observation of a neutrino burst from the supernova SN1987A. *Physical Review Letters*, 58(14):1490–1493, April 1987.

[94] X. Fang, Y. Zhang, G. H. Gong, et al. Capability of detecting low energy events in JUNO Central Detector. *JINST*, 15(03):P03020, 2020.

[95] D. Blum. JUNO's sensitivity for indirect dark matter search, 2021. paper in preparation.

[96] J. H. Zou, X. T. Huang, W. D. Li, et al. SNiPER: an offline software framework for non-collider physics experiments. *Journal of Physics: Conference Series*, 664(7):072053, dec 2015.

[97] I. Antcheva et al. ROOT: A C++ framework for petabyte data storage, statistical analysis and visualization. *Comput. Phys. Commun.*, 180:2499–2512, 2009.

[98] L. Lönnblad. CLHEP—a project for designing a C++ class library for high energy physics. *Computer Physics Communications*, 84(1-3):307–316, November 1994.

[99] S. Agostinelli, J. Allison, K. Amako, et al. Geant4—a simulation toolkit. *Nuclear Instruments and Methods in Physics Research Section A: Accelerators, Spectrometers, Detectors and Associated Equipment*, 506(3):250–303, July 2003.

[100] Ziyan D. Status of JUNO Simulation Software. *EPJ Web of Conferences*, 245:02022, 2020.

[101] M. Schever. Waveform Reconstruction Of Ibd And Muon Events In Juno. `https://zenodo.org/record/1300922`, 2018. Poster presentation at Neutrino 2018.

[102] H. Q. Zhang et al. Comparison on PMT Waveform Reconstructions with JUNO Prototype. *JINST*, 14(08):T08002, 2019.

[103] Q. Liu, M. He, X. Ding, et al. A vertex reconstruction algorithm in the central detector of JUNO. *Journal of Instrumentation*, 13(09):T09005–T09005, sep 2018.

[104] W. Wu, M. He, X. Zhou, and H. Qiao. A new method of energy reconstruction for large spherical liquid scintillator detectors. *Journal of Instrumentation*, 14(03):P03009–P03009, mar 2019.

[105] D. V. Forero, R. Hawkins, and P. Huber. The benefits of a near detector for JUNO, October 2017. arXiv e-print: 1710.07378.

[106] A. Abusleme et al. TAO Conceptual Design Report: A Precision Measurement of the Reactor Antineutrino Spectrum with Sub-percent Energy Resolution, May 2020. arXiv e-print: 2005.08745.

[107] J.P. Athayde Marcondes de Andre J. Xu. JUNO Muonflux update, password protected. `https://juno.ihep.ac.cn/Dev_DocDB/0059/005990/001/xujl_200630_muonrec.pdf`, 2020. Internal collaboration document.

[108] H. de Kerret et al. Yields and production rates of cosmogenic ^{9}Li and ^{8}He measured with the Double Chooz near and far detectors. *JHEP*, 11:053, 2018.

[109] G. Bellini et al. Cosmogenic Backgrounds in Borexino at 3800 m water-equivalent depth. *JCAP*, 08:049, 2013.

[110] S. Abe et al. Production of Radioactive Isotopes through Cosmic Muon Spallation in KamLAND. *Phys. Rev. C*, 81:025807, 2010.

[111] F. An et al. Cosmogenic neutron production at Daya Bay. *Phys. Rev. D*, 97(5):052009, 2018.

[112] T. Hagner, R. von Hentig, B. Heisinger, et al. Muon-induced production of radioactive isotopes in scintillation detectors. *Astroparticle Physics*, 14(1):33–47, August 2000.

[113] K. Zhang, M. He, W. Li, and J. Xu. Muon tracking with the fastest light in the JUNO central detector. *Radiation Detection Technology and Methods*, 2(1), March 2018.

[114] C. Genster, M. Schever, L. Ludhova, et al. Muon reconstruction with a geometrical model in JUNO. *Journal of Instrumentation*, 13(03):T03003–T03003, March 2018.

[115] B.S. Wonsak, C.I. Hagner, D.A. Hellgartner, et al. Topological track reconstruction in unsegmented, large-volume liquid scintillator detectors. *Journal of Instrumentation*, 13(07):P07005–P07005, July 2018.

[116] Fengpeng An et al. Neutrino Physics with JUNO. *J. Phys. G*, 43(3):030401, 2016.

[117] T. Lin, J. Zou, W. Li, et al. The Application of SNiPER to the JUNO Simulation. *Journal of Physics: Conference Series*, 898, February 2017.

[118] GEANT4 Collaboration. Physics Reference Manual. `https://indico.phys.vt.edu/event/34/contributions/753/attachments/507/612/Design_and_progress_of_the_central_detector_of_JUNO.pdf`, 2017.

[119] Y. Huan C. Yang, J. Xu. Muon bundle reconstruction in the JUNO detector, password protected. `https://juno.ihep.ac.cn/Dev_DocDB/0072/007235/001/Muon_bundle_reconstruction_in_JUNO_detector_20210713.pdf`, 2021. Paper in preparation.

[120] C. Genster. *Software and hardware development for the next-generation liquid scintillator detectors JUNO and OSIRIS*. PhD thesis, RWTH Aachen, November 2019.

[121] Genster, Hackspacher, Hu, et al. OSIRIS Conceptual Design Report, password protected. `https://juno.ihep.ac.cn/Dev_DocDB/0034/003472/004/OSIRIS_CDR_v4.pdf`, 2018.

[122] S. Zavatarelli. Borexino: new results from the high-purity phase-II data. *Journal of Physics: Conference Series*, 1056:012062, July 2018.

[123] Brookhaven National Laboratory National Nuclear Data Center. NuDat (Nuclear Structure and Decay Data), March 2008.

[124] A. Abusleme et al. The Design and Sensitivity of JUNO's scintillator radiopurity pre-detector OSIRIS, March 2021. arXiv e-print: 2103.16900.

[125] LDPE – Weich-Polyethylen. `https://www.rebel.de/service/material/ldpe.html`, 2020.

[126] OK LDPE Silofolie. `https://www.okfolien.de/kategorien/ok-ldpe-silofolie-schwarz-weiss/`, 2020.

[127] G. Bellini et al. Final results of Borexino Phase-I on low energy solar neutrino spectroscopy. *Phys. Rev. D*, 89(11):112007, 2014.

[128] L. Bieger. *Erweiterung des OSIRIS Software-Frameworks zur Analyse von Myon-induziertem Neutronenuntergrund*. Bachelor's thesis, Eberhard Karls Universität Tübingen, November 2020.

[129] C. Jollet and A. Meregaglia. ^{9}Li and ^{8}He decays in GEANT4. *Nuclear Instruments and Methods in Physics Research Section A: Accelerators, Spectrometers, Detectors and Associated Equipment*, 949:162904, January 2020.

[130] G. Altarelli, R. Kleiss, and C. Verzegnassi, editors. *Z Physics at LEP-1. Proceedings, Workshop, Geneva, Switzerland, September 4-5, 1989. Vol. 1: Standard Physics*, CERN Yellow Reports: Conference Proceedings, September 1989.

[131] M. Guan, M. Chu, J. Cao, et al. A parametrization of the cosmic-ray muon flux at sea-level, September 2015. arXiv e-print: 1509.06176.

[132] V.A. Kudryavtsev. Muon simulation codes MUSIC and MUSUN for underground physics. *Computer Physics Communications*, 180(3):339–346, March 2009.

[133] V. Khachatryan et al. Measurement of the Charge Ratio of Atmospheric Muons with the CMS Detector. *Phys. Lett. B*, 692:83–104, 2010.

[134] Q. Liu, M. He, X. Ding, et al. A vertex reconstruction algorithm in the central detector of JUNO. *JINST*, 13(09):T09005, 2018.

[135] Geant4 Collaboration. Geant4 Book For Application Developers v10.4. `http://geant4-userdoc.web.cern.ch/geant4-userdoc/UsersGuides/PhysicsReferenceManual/BackupVersions/V10.4/fo/PhysicsReferenceManual.pdf`, 2017.

[136] Tyvek-PE-Vliesfrom DuPont. `https://www.deffner-johann.de/tyvek/`, 2020.

[137] Chavarria. *A study on the reflective properties of Tyvek in air and unde rwater*. PhD thesis, Department of Physics, Duke University, May 2007.

[138] Wang, Lu, Yang, et al. Study of Tyvek reflectivity in water. *Chinese Physics C*, 36(7):628–632, July 2012.

[139] F. Ritter. *Analysis of the GERDA Muon Veto - First Light*. PhD thesis, U. Tubingen, 2011.

[140] D. Malczewski, J. Kisiel, and J. Dorda. Gamma background measurements in the Gran Sasso National Laboratory. *Journal of Radioanalytical and Nuclear Chemistry*, 295(1):749–754, July 2012.

[141] G. Alimonti, C. Arpesella, H. Back, et al. The Borexino detector at the Laboratori Nazionali del Gran Sasso. *Nuclear Instruments and Methods in Physics Research Section A: Accelerators, Spectrometers, Detectors and Associated Equipment*, 600(3):568–593, March 2009.

[142] Lukas Bieger et al. Potential for a precision measurement of solar *pp* neutrinos in the Serappis Experiment, 9 2021. arXiv e-print: 2109.10782.